5-2017

Design and characterization of plasmonic nanoprobes and interparticle interactions for surface enhanced raman scattering and biomolecular detection

Zakiya Skeete
Binghamton University--SUNY, zskeete1@binghamton.edu

DESIGN AND CHARACTERIZATION OF PLASMONIC NANOPROBES AND INTERPARTICLE INTERACTIONS FOR SURFACE ENHANCED RAMAN SCATTERING AND BIOMOLECULAR DETECTION

BY

ZAKIYA SKEETE

BS, Utica College, 2012

DISSERTATION

Submitted in partial fulfillment of the requirements for
the degree of Doctor of Philosophy in Chemistry
in the Graduate School of
Binghamton University
State University of New York
2017

Accepted in partial fulfillment of the requirements for
the degree of Doctor of Philosophy in Chemistry
in the Graduate School of
Binghamton University
State University of NY
2017

May 5, 2017

Prof. Omowunmi Sadik, Chair
Department of Chemistry, Binghamton University

Prof. Chuan-Jian Zhong, Faculty Advisor
Department of Chemistry, Binghamton University

Prof. Bruce White, Jr., Member
Department of Physics, Binghamton University

Prof. Christof Grewer, Member
Department of Chemistry, Binghamton University

Asst. Prof. Wei Qiang, Member
Department of Chemistry, Binghamton University

Asst. Prof. Amber Doiron, Outsider Examiner
Department of BioEngineering, Binghamton University

Abstract

Functional nanoparticles serve as an intriguing class of probes in medical theranostics for enabling rapid, sensitive, multiplexing, and point-of-care treatment and diagnosis. One important aspect of these applications is the exploitation of the unique plasmonic properties of certain metal nanoparticles. A key challenge is the understanding of effective harnessing of the plasmonic coupling of the nanoparticles upon interacting with the targeted biomolecular species. This thesis work focuses on investigating the interparticle interactions of chemcially-labled and bioconjugated gold and silver based nanoparticles and their influences on the plasmonic coupling for specctroscopic detection of biomolecules. Examples of the interparticle interactions include dye-mediated π–π stacking, antigen-antibody recognition, and DNA complementary binding. These molecular and biomolecular interactions lead to the formation of interparticle "hot-spot" in terms of plasmonic coupling of the nanoparticles responsible for the surface enhanced Raman scattering (SERS) and the localized surface plasmon resonance (LSPR). The interparticle plasmonic coupling induced SERS and LSPR characteristics are probed by experimental measurements and theoretical simulations for establishing the correlation between the interparticle structures and the spectroscopic properties. The results have

provided new insights for a better understanding of the design and control parameters of multifunctional nanoparticles and interparticle interactions for spectroscopic enhancements in biomolecular recognition and detection.

Acknowledgements

I would like to express my sincerest gratitude and appreciation to Dr. Chuan-Jian Zhong and Dr. Jin Luo for all of their guidance, knowledge, support, and assistance in research. They have been extremely instrumental in my growth and maturity in research, in the design and execution of the projects of interest, and allowing me to learn and use different techniques. I would like to give thanks to past and present members of the group: Haval Kareem, Jing Li, Shan Yan, Ning Kang, Dr. Jinfang Wu, Fangfang Chang, Aolin Lu, Dr. Shiyao Shan, Dr. Elizabeth Crew, Dr. Liqin Lin. Also, I would like to give special thanks those who have helped with research through support and assistance: Christian Salazar, Winny Sun, Christopher Manahan, Hannah Cronk, Yinguang Zhao, Wei Zhao, Bryan D Trimm, Pharrah Joseph, Fredrick Omenya, Natasha Chernova, and Steven Boyer.

I would like to acknowledge all of the collaborators we have worked with in the past few years, especially Prof. Quang Minh Ngo who took the time to teach me how to write codes for the theoretical simulations. Eunsoo Yoo and Daniel Goldstein from Asst. Prof. Doiron's group for their assistance with the NanoSight Tracking Analysis.

I also want to thank Dr. Alexsandra DaSilva and Dr. Yan Sun for their continual support in teaching and providing feedback for improvements in technical skills and self-

development. Additionally, I would like to thank the Department of Chemistry for all of their support and assistance throughout the years.

I also want to thank Clifford D. Clark Fellowship, Graduate Assistance in Areas of National Need (GAANN) Fellowship, and Chemistry Department for the graduate/ teaching assistantship, tuition scholarship and summer fellowship to allow me to conduct my research in the past years and the funding and grants provided by IEEC, CAMM, and NSF.

Last, but certainly not least, I wish to thank my family members, close friends, and undergraduate advisors, who have been there for me no matter what, who have always supported me, pushed me and given me extra support throughout time. I truly appreciate them for everything.

Table of Contents

Contents	Page
List of Tables	xi
List of Figures	xii
List of Schemes	xxi
List of Abbreviations and Symbols	xxiii
List of Selected Publications	xxiv
Chapter 1. Overview of Nano-structured Materials	**1**
1.1 Significance of Molecular Detection	1
1.2 Synthetic Design of Nanomaterials	8
1.3 Optical and Electrical Properties of Nanomaterials	17
1.4 Application of Bio-functional nanoprobes and assemblies	26
1.5 Current Status and Objectives of Thesis Work	43
References	47
Chapter 2. Experimental Methods and Measurements	**53**
2.1 Chemicals and Materials	53
2.2 Instrumental Measurements	54
2.3 Nanoparticle Synthesis	55
2.4 Experimental Methods	58
2.5 Methods for Theoretical Calculations	60
References	65
Chapter 3. Harnessing the interparticle J-aggregate induced plasmonic coupling for surface-enhanced Raman scattering	**67**
3.1 Introduction	67
3.2 Experimental Section	70

3.3 Result and Discussion 71
3.4 Conclusion 85
Reference 86

Chapter 4. SERS Detection of Protein Mediated Assembly of Gold Nanoparticles in Solution 88
4.1 Introduction 88
4.2 Experimental Section 90
4.3 Result and Discussion 92
4.4 Conclusion 99
Reference 101

Chapter 5. "Squeezed" Interparticle Properties for Plasmonic Coupling and SERS Characteristics of Duplex DNA Conjugated/Linked Gold Nanoparticles of Homo/Hetero-Sizes 102
5.1 Introduction 102
5.2 Experimental Section 105
5.3 Result and Discussion 107
5.4 Conclusion 119
Reference 120

Chapter 6. Assessing Interparticle Spatial Characteristics of DNA-Linked Core-Shell Nanoparticles with or without Magnetic Cores in Surface Enhanced Raman Scattering 122
6.1 Introduction 122
6.2 Experimental Section 126
6.3 Result and Discussion 128
6.4 Conclusion 152
Reference 154

Chapter 7. Summary and Future work 156

List of Tables

Table 5.3.2.1. Fitting results from fitting the simulated LSPR data in Figures 5.3.1.4A and B by exponential decay as a function of the interparticle gap (d) ($A = A_0 + A1 * \exp(-kd)$). 115

Table 5.3.2.2. Fitting results from fitting the simulated E-field intensity enhancement data in Figures 5.3.2.4B and D by exponential decay as a function of the interparticle gap (d) ($E = E1 * \exp(-kd)$). 115

Table 6.3.5.1. Long wavelength (nm) and Normalized ACS Intensity of 0.5 nm thick Au/Ag coated Magnetic NPs. 149

Table 6.3.5.2. Long wavelength (nm) and Normalized ACS Intensity of 10 nm Au/Ag coated Magnetic NPs. 149

Table 7.3.3.3. Exponential fitting of 10 nm coated magnetic NPs when magnetic core size changes (M = 1, 5, 9 nm) and when metallic shell thickness changes (A* = 0.5, 5.5, 15.5 nm). 150

List of Figures

Figure 1.2.1 Illustration of bifunctional NPs for detection and magnetic intervention of biomolecular activities in a solution. 4

Figure 1.2.1.1. (A) Seeded and aggregative growth of gold NPs. Middle panel: TEM for 30 nm seeds (a), and seed-grown 60 (b) and 90 nm (c) AuNPs. Bottom panel: Size distributions. (B) Thermally-activated processing of AuNPs capped by alkanethiolate monolayer. Middle panel: TEM of AuNPs produced by thermal processing in the presence of alkanethiols of different chain length (n): n=5 (right, 7.60 ±0.43 nm), and 15 (middle, 5.86 ±0.31 nm) and the precursor Au_{2nm}-DT (left, 2.01 ± 0.41 nm). Bottom panel: Size distributions (left) and Dependence of particle size on capping alkyl chain length (right). [47, 53, 54] 9

Figure 1.2.2.1. (A) Scheme and TEM for Fe_2O_3@Au nanoparticles produced from Au and Fe_2O_3 precursor nanoparticles by the thermally-activated processing route. (B) Scheme and TEM for Fe_3O_4@Au nanoparticles produced by combined bottom-up synthesis and thermal processing in a seeded-growth process (2* =gold precursor, reducing and capping agents, and temperature manipulation): Fe_3O_4 (5.2 ± 0.4 nm) and Fe_3O_4@Au (6.6 ± 0.4 nm). [24,45] 14

Figure 1.2.2.2. (A) Morphologies of MnZn ferrite (MZF) core-shell nanocubes: TEM/HRTEM (a-c) and ED pattern (d) for MnZn ferrite nanoparticles (size: 20.6 ± 1.8 nm, core (Fe_3O_4)/shell (($Mn_{0.5}Zn_{0.5}$)($Fe_{0.9}Mn_{1.1}$)O_4)). (Right: structural model for MZF nanocubes consisting of Fe_3O_4 core (inverse core) and MZF shell where the tetrahedral sites are doped by (0.5-δ) Zn^{2+} whereas the octahedral sites are doped by Mn^{3+}, Mn^{2+}, and the rest of Zn^{2+}. (B) EDS composition mapping for MZF@Au (left) and MZF@Ag (right) nanoparticles in terms of overlapping of Fe (red) with Au (MZF@Au) and Ag (MZF@Ag). Mn and Zn detected are not shown. (C-D) Plots showing the magnetic separation kinetics in terms of the change in absorbance of SP band at ~534 nm for a solution of MZF (a), and MZF@Au (b) (C), and ~420 nm for solutions of MZF (a), MZF@Ag (b), and mixed MZF and Ag NP (c) (D). (Insets: photos showing color changes before and after applying a magnet, leading to gradual separation (for D: t_0 = 0; t_1 = 30; t_2 = 60 min). [19,61,64] 15

Figure 1.3.2.1. SERS spectra for MBA-labeled Au_{90nm} on a Au-film substrate (A, Insert: SERS intensity at 1591 cm^{-1} vs. particle size), MBA-labeled Au_{90nm} in aqueous solution (B, Insert: SERS intensity at 1594 cm^{-1} vs. nanoparticle size), and solutions of MBA in the presence of Au_{60nm} after centrifuging at different speeds: 2000 (a), 14000 (b) rpm (C, Insert: UV-vis spectra for the corresponding solutions). [23] 22

Figure 1.3.2.2. (A) Surface plasmon resonance band wavelength l_{max} *vs*. interparticle chain length and particle size (2r, insert) for thin film assemblies of AuNPs mediated by ADTs of different chain lengths (HS-$(CH_2)_n$-SH). (B) Electrical conductivity *vs*. temperature and interparticle distance for thin film assemblies of 2-nm AuNPs mediated by ADTs of different chain lengths (HS-$(CH_2)_n$-SH). (Insert plots: activation energy *vs*. interparticle distance, and comparison of experimental (solid lines, triangle) and calculated results (dashed lines, square) for two different particle sizes). (Reproduced with permission from refs. 59, Copyright 2007 Royal Society of Chemistry, and from ref. 57, Copyright 2008 American Chemical Society.) 23

Figure 1.4.1.1. Top panel: Interparticle zwitterionic interaction, chiral recognition and hydrogen-bonding for the assembly of AuNPs by Hcys, Cys and GSH. Bottom panel: (Left): Kinetic plots of SP band absorbance (at 630 nm) for assemblies of Au_{13nm} in the presence of LL- (●), DD- (■), and DL- (▲) Cys. The dotted lines represent curve fitting by a 1st order reaction model. Insert: UV-Vis spectral evolution for the Au_{13nm} mediated assembly of LL- (a), DD- (b) and DL- (c) Cys. The arrows indicate the direction of the spectral evolution. (Right): Normalized rate or rate constant (*k*) vs. enantiomeric percentage of cysteines (%) in the presence of Au NPs of two different sizes Au_{60nm} (■) (pH = 5), Au_{13nm} (●) (pH = 6) and Au_{13nm} (▲) (pH = 7). Inactivity was also illustrated for mixing Au_{13nm} with NAC (♦). (Reproduced with permission from ref. 62, Copyright 2009 American Chemical Society.) 27

Figure 1.4.2.1. (A) Preparation of miRNA-AuNP conjugates for delivering miRNAs to cells (miRNA is labeled with fluorescent dyes (e.g., Cy5)). The sense and antisense miRNA were combined first to form miRNA duplexes which are then immobilized onto Au NP via thiol group, followed by refilling with oligoethyleneglycol thiol (OEG) to keep the miRNAs from folding and electrostatically binding. (B) Confocal/fluorescent microscopic image: MM.1S cells 48 hours after transfection was initiated with Cy5-labeled miRNA-AuNPs. (C) Plot showing the result of the functional luciferase assays for Cy5 (black bars) and Cy3 (red bars) labeled miRNA-AuNPs, and a mimic system (insert chart). (Reproduced with permission from ref. 53, Copyright 2012 American Chemical Society.) 30

Figure 1.4.2.2. (A) Schematic illustration of magnetic core@shell nanoparticles (M@Ag) as a functional antimicrobial agent in blood platelets and the magnetic separation. (B) Experimental data for the inactivation of *Bacillus cereus* (Left) and *Enterobacter cloacae* (Middle) in a PBS buffer (a), in a solution of MZF@Ag NPs (b), and in a solution of AgNPs (c); and E. coli (Right) in water (a), MZF NPs (b), and MZF@AgNPs (c) in blood platelets. (Reproduced with permission from ref. 9, Copyright 2011 American Chemical Society.) 32

Figure 1.4.3.1. Illustration of the use of surface functionalized Au and magnetic core (M)/shell (Au) nanoparticles in bio-separation and detection to study the reactivity between protein A-labeled Au nanoparticles: L-Au-A and antibody-labeled M/Au nanoparticles: Ab-M/Au. Insert (right): SERS spectra showing the assembly of Au (80 nm) nanoparticles labeled with Protein A or BSA and MBA and M@Au NPs (~8 nm) labeled with antibody (IgG). (Reproduced with permission from ref. 23. Copyright 2008 IOP.) 35

Figure 1.4.3.2. Illustration of formation of "hot-spot" upon ds-DNA assembly of *ss*-DNA/M@Au NP with RL-AuNP via molecular recognition with free complementary *ss*-DNA in the solution, and dismantling of "hot-spots" following the enzymatic cutting of the *ds*-DNA using restriction enzyme and magnetic separation characteristic. 36

Figure 1.4.3.3. AuNP-based SERS detection using a 30 bp DNA sequence where "hot-spots" form upon assembly of *ss*-DNA/AuNP with MBA/AuNP in an aqueous solution (A) ((a) bottom-DNA/AuNP mixed with MBA/AuNP; (b) bottom-DNA/AuNP and MBA/AuNP after addition of top-DNA), and *MspI* cutting of the ds-DNA/AuNPs (B) ((a) the ds-DNA/AuNPs; (b) after *MspI* addition. (Reproduced with permission from ref. 17. Copyright 2013 Royal Society of Chemistry.) 37

Figure 1.4.3.4. (A) Magnetic NPs coupled with Au NPs for SERS detection. (B) Example using a 30 bp DNA sequence where "hot-spots" form upon the assembly of ss-DNA/ MZF@Au with MBA/AuNP in an aqueous solution ((a) the mixture of MBA-Au and MZF/Au-DNA1, and (b) mixture of MZF/Au-DNA1 and MBA-Au in the presence of DNA2). (C) *MspI* cutting MBA-Au-*ds*-DNA-MZF/Au ((a) the MBA-Au-*ds*-DNA-MZF/Au solution; (b) after MspI addition). (Reproduced with permission from ref. 20. Copyright 2013 Royal Society of Chemistry.) 38

Figure 1.4.4.1. (A) Illustration of thin film of nanoparticles assembled or printed on a flexible chemiresistor device for detection of vapor molecules (VOCs, biomarkers, etc.). (B) Response profiles of relative change in resistance ($\Delta R/R=\Delta R/R_{FL}$) for a flexible device with an NDT–Au_{2nm} film in response to horizontal bending under nitrogen (a-b), ethanol (c-d), hexane (e-f), and acetone (g-h). Strains: solid lines (tensile, *ts*), dashed lines (compressive, *cs*). (C) PCA score plots in the PC1-PC2 plane (PC1: 96.8%; PC2: 2.9%.) for a chemiresistor array of thin film assemblies of Au NPs in response to several vapor samples: air (blank), acetone (210 ppm(M) in air), human breath (HB), and HB spiked with acetone. (Reproduced with permission from ref. 71. Copyright 2014 Royal Society of Chemistry, and from ref. 29, Copyright 2012 Elsevier Publishing). 42

Figure 2.5.2.1. Schematic of the NPs and its environment: single core-shell NP (A) and dimer NP (B). [37, 38] 62

Figure 2.5.2.2. Schematic of the resolution illustrating the discretized regions of the particles. [37, 38] 63

Figure 2.5.2.3. Schematic of the resolution illustrating the discretized regions of the particles (A) and the simulated EMF intensity and cross-sections of a single NP (B, C) and dimer NPs (D, E). [37, 38] 64

Figure 3.3.1.1. UV-vis spectra for Tlc (blue), AuNPs (red), and AuNPs in the presence of Tlc(green). Tlc (blue, [Tlc] = 1.23 μM), Au_{34nm} (red, [Au_{34nm}] = 0.155 nM), and Au_{34nm} + Tlc (green, [Au_{34nm}] = 0.155 nM, [Tlc] = 0.176 μM). 72

Figure 3.3.1.2. (a) Surface plasmon resonance spectral evolution for Au_{34nm} NPs in an aqueous solution ([Au_{34nm}] = 8.9×10^{-2} nM) upon addition of Tlc ([Tlc] = 2.4×10^{-2} μM) and (b) kinetic plot of the long- wavelength SP band (integrated peak area from 600 to 1000 nm) where the first-order model ($y = A_1'(1 - e^{-kt})$) yields k = 2.8×10^{-4} s^{-1}; the Avrami model ($y = A_2'(1 - e^{-kt^n})$) yields k = 2.6×10^{-5} s^{-1} and n = 1.3. (c) SERS spectra for an aqueous solution of Au_{34nm} ([Au_{34nm}] = 8.9×10^{-2} nM) upon addition of Tlc ([Tlc] = 2.4×10^{-2} μM) and (b) kinetic plot of peak intensity (at 1589 cm^{-1}) (*I*); the first-order model ($y = A_1'(1 - e^{-kt})$) yields $k = 2.6 \times 10^{-4}$ s^{-1}; the Avrami model ($y = A_2'(1 - e^{-ktn})$) yields $k = 3.2 \times 10^{-5}$ s^{-1} and $n = 1.3$. 73

Figure 3.3.1.3. SERS spectral evolution as a function of time for an aqueous solution of Au_{34nm} upon addition of Tlc. Time: 1~6000 s (from red to blue). [Au_{34nm}] = 0.089 nM; [Tlc] = 0.0238 μM. (Integration = counts/20s). (b) Kinetic plot of peak intensity (at 1589 cm^{-1}) (*I*); the first-order model ($y = A_1'(1 - e^{-kt})$) yields $k = 2.6 \times 10^{-4}$ s^{-1}; the Avrami model ($y = A_2'(1 - e^{-ktn})$) yields $k = 3.2 \times 10^{-5}$ s^{-1} and $n = 1.3$. 76

Figure 3.3.2.1. Spectral evolution of surface plasmon resonance bands and SERS intensities for solutions containing AuNPs and cyanine dyes. (a) Upon addition of 0.218 μM Tlc to 2.5 nM Au_{13nm} solution. (b) Upon addition of 0.176 μM Tlc to 0.155 nM Au_{34nm} solution. Control: 0.31 μM Tlc. (c) Plot of the normalized SERS peak intensity at 1585 cm^{-1} (integrated peak area) for J-aggregation of Tlc in the presence of AuNPs of different sizes. Note that there is a difference in particle concentration between (a) and (b) (by a factor of ~16), which is the reason for the observation of a higher degree of aggregation (as reflected by the long-wavelength SP band) for Au_{13nm} than for Au_{34nm}. 79

Figure 3.3.2.2. (a) Spectrum for a solution of Au_{13nm} (2.5 nM) upon addition of Tlc (different concentration) in terms of the surface coverages (θ_T) on the gold NPs. Control: 0.31 μM Tlc. (b) Kinetic plot of corresponding SERS peak intensity (I) at ~1585 cm^{-1} vs. Tlc concentration. The surface coverage was estimated based on 3D model of Tlc and densely packed monolayer on gold nanoparticle surface. e.g., for Au_{13nm}, surface area is $4\pi (6.5nm)^2 = 5.31x10^{-12}$ cm^2. For Tlc, which can be treated as a rectangular box with short side, long side, or flat orientation anchoring the surface. The long side is ~2.0 nm, the short side is ~1.4 nm, whereas the thickness is ~0.5 nm. For the short side orientation, the area is $0.70x10^{-14}$ cm^2 for per Tlc, yielding $5.31x10^{-12}$ cm^2 / $0.70x10^{-14}$ cm^2 = 759 Tlc/Au_{13nm}. Similarly, 531 Tlc/Au_{13nm} for short side orientation, and 190 Tlc/Au_{13nm} for flat orientation. The average of Tlc molecules on per Au_{13nm} is ~493. Experimentally, for a solution of Au13nm (2.5 nM), the addition of 0.0528 μM Tlc would yield ~21 Tlc/Au_{13nm}, which in terms of a surface coverage (θ_T would be 21/493=0.042. 80

Figure 3.3.2.3. UV-vis and SERS spectra for aqueous solutions of AuNPs in the presence of Tlc. (a) UV-Vis spectra and (b) SERS spectra for a solution of Au_{45nm} (0.0259 nM) upon addition of Tlc dyes in different concentrations: 0.0146 μM (i.e., θ_T = 0.10), 0.0293 μM

(i.e., θ_T = 0.20), and 0.146 μM (i.e., θ_T = 1.0). (c) SERS spectra for AuNPs with five different particle diameters (13 nm (2.5 nM, θ_T = 0.175), 34 nm (0.089 nM, θ_T = 0.102), 45 nm (0.0259 nM, θ_T = 0.998), 52 nm (0.0242 nM, θ_T = 0.590) and 82 nm (0.00718 nM, θ_T = 1.0)). 81

Figure 3.3.3.1. Simulated optical absorbance cross-sections and E-field enhancements upon interparticle plasmonic coupling. (a) A ‘‘core–shell’’ model of a dimer of Tlc-adsorbed AuNPs. (b) Simulated E-field enhancement vs. particle size (the refractive indices: water (1.33) and Tlc (2.40). p–p stacking distance: 0.4 nm, laser excitation: 633 nm). (c) A 3D image for simulated E-field enhancement for a dimer of Au_{30nm}. 83

Figure 3.3.3.2. Simulated optical absorbance cross sections and E-field enhancements upon interparticle plasmonic coupling. (a-b) simple dimer (a) and trimer (b) models of AuNPs (naked NPs with adsorbed Tlc defining the interparticle distance). (c) Simulated absorbance cross section for dimer and trimer of AuNPs of different sizes with interparticle distance defined by π–π stacking of Tlc (3.4 nm). (d) Wavelength (λ, nm) at SP band maximum vs. particle size for dimer and trimer. (e) absorbance (Abs.) cross section (nm^2) vs. particle size for dimer and trimer. (f) E-field intensity enhancement (in common logarithm) vs. particle size for dimer and trimer (633 nm laser excitation). (g-h) An example of 3D contour plot for the Efield enhancement for Au_{30nm} dimer (g) and Au_{30nm} trimer (h). 84

Figure 4.3.1.1. (A) SERS spectra of protein bound NPs in solution (black – MBA, red – Ab bound NPs, blue – assembly between protein and antibody bound NPs (Note: assembly addition of antibody bound NPs to a solution of protein bound NPs showed a similar trend but slightly higher peak). 92

Figure 4.3.1.2. SERS spectra (integration time 60 s) for the assembly of 52 nm MBA/Au NPs (q ≈ 200% theoretical) by protein A and antibody. Depicts evolution of 1590 cm^{-1} MBA peak in respect to protein-antibody assembly (MBA – black, with DSP – red, with capture antibody (blue), assembly with target protein in solution (cyan) and conjugated to a NP (magenta)). Proof of concept that assembly can be observed in real-time in solution. (Also observe evolution of 1575 cm^{-1} peak when protein A is introduced into the system). 93

Figure 4.3.2.1.1. UV-Vis spectra of the change in SP band as the buffer increases compared to the original solution in deionized water (black) for NPs capped with MBA alone (A) and MBA and DSP (B). Note the increase denoted by the arrow (pH: 4, 6,7, 12). 94

Figure 4.3.2.1.2. The SERS spectra (A) and the peak heights analysis (B) of the 1590 cm^{-1} peak for the NP assembly for DSP- and EDC-linked nanoprobes. DSP- ((A) solid, (B) blue) and EDC-linked ((A) dashed, (B) cyan) nanoprobes. 95

Figure 4.3.2.2.1. DSP (A-C) and EDC (D-F) linked NP-based systems before (black) and after (red) assembly in the presence of different protein concentrations (0.24, 53 – dotted

line; 0.1, 5.3e-3 – dashed line; 0.1, 5.3e-6 – solid line), before (A, D) and after (B, E) centrifugation, and peak heights at the 1590 cm^{-1} peak (C, F). 96

Figure 4.3.3.1. SERS spectra of EDC-linked protein assembly of different NP pairings: homo – sized NP dimers of 40 (black), 60 (red), and 80 (blue) (A); hetero – sized NP dimers of 4060 nm (black) and 6080 nm (red) (B). The difference in peak intensity of the 1590 cm^{-1} MBA peak before (black) and after (red) assembly (C). Note the change in intensity is the difference before and after assembly. 99

Figure 5.3.1.1. UV-Vis spectral of LSPR band for AuNPs before (solid curves) and after (dashed curves) interparticle duplex DNA linkage. (A) homo-sized AuNPs: 13 nm (black curves), 39 nm (red curves), and 62 nm (blue curves); (B) hetero-sized AuNPs: 13 nm – 39 nm (black curves), and 13 nm – 62 nm (red curves). 107

Figure 5.3.1.2. Simulated absorption cross-section spectra of ds-DNA-linked symmetrical dimer models (11 nm (A), 39 nm (B), and 62 nm (C)) as the interparticle edge-to-edge gap distance is reduced (from 12 nm to 1 nm with an interval of 0.5 nm. The red shift is shown by the direction of the arrow). 108

Figure 5.3.1.3. Simulated absorption cross-section spectra of ds-DNA-linked asymmetrical dimer models ((A) 13 – 39 nm and (B) 13 – 62 nm) as the interparticle edge-to-edge gap distance is reduced (from 12 nm to 1 nm with an interval of 0.5 nm. The red shift is shown by the direction of the arrow). 110

Figure 5.3.1.4. (A) Absorption band's wavelength vs. the gap, where symmetric NPs are 13 (a), 39 (b), and 62 nm (c). The lines represent fitting by exponential decay (Table 5.3.2.1)). (B) Absorption band's wavelength vs. the gap, where asymmetric dimers feature 13– 39 nm (a) and 13– 62 nm (b). The lines represent fitting by exponential decay (Table 5.3.2.1)). 110

Figure 5.3.2.1. SERS spectra for homo-sized AuNPs ((A) 13 nm, (B) 39 nm, and (C) 62 nm) system before (black curve) and after (red curve) the interparticle linkage by ds-DNA. 111

Figure 5.3.2.2. SERS spectra for hetero-sized AuNPs ((A) 13 – 39 nm and (B) 13 – 62 nm) system before (black curve) and after (red curve) the interparticle linkage by ds-DNA. 112

Figure 5.3.2.3. (A) SERS intensity of the peak at 1587 cm^{-1} for the (A) homo-sized NPs solutions of different sizes (13, 39, and 62 nm) and (B) hetero-sized NPs solutions of different sizes (39 – 13 nm and 62– 13 nm). Note: the intensity is normalized peak intensity at 1076 cm^{-1} over total number of NPs. 113

Figure 5.3.2.4. (A and C) 2D and 3D plots of a symmetric dimer of (A) 39 nm AuNPs and an (C) asymmetric dimer of 39 – 13 nm AuNPs, each with a gap distance (d) of 4 nm. (B and D) Plots of the change of E-field intensity enhancement at E_C as a function of the interparticle gap for (B) symmetric dimers of three different particle sizes (13 nm (a), 39 nm (b), and 62 nm (c)), and for (D) symmetric dimers (13– 39 nm (a) and 13– 62 nm (b)).

The change is measured with respect to that at 12 nm gap. The dashed lines represent fitting by exponential decay (Table 2)). 114

Figure 5.3.2.5. Normalized experimental SERS peak intensities and theoretical E-field intensity enhancements: (A) the homo-size system vs. the symmetric dimer model (from 13, 39 to 62 nm AuNPs), (B) the hetero-size system vs. the asymmetric dimer model (from 39 nm – 13 nm to 62 nm – 13 nm AuNPs), and (C) the symmetric vs. asymmetric dimer systems. (Theoretical data correspond to those at an interparticle gap of 3 nm). 115

Figure 5.3.3.1. Calculated steric repulsion, van der Waals attraction, and the total interaction potentials for symmetric dimers of AuNPs (13 nm (a), 39 nm (b), and 62 nm (c)) (A) and for asymmetric dimers of AuNPs of 13nm – 39 nm (a) and 13 nm – 62 nm (b) (B) as a function of the interparticle edge-to-edge gap. 117

Figure 6.3.1. (A-B) Dependencies of the minimum interparticle gap and total interaction energy (E_M) on effective DNA shell thickness (L') for a dimer of 40 nm NPs (Hamaker constant: – 0.83 eV and DNA monolayer thickness – 2 nm and length – 11 nm). (Dashed lines: $E_{min.} = -19.1 \times \exp(-1.6 \times L')$; $G_{min.} = 19.9 \times \exp(0.1 \times L')$) (C) Simulated EMF spectra for dimers of 39 nm AuNP dimers at L'=10 nm (gap ≈ 40 nm), 7 nm (gap ≈ 24 nm), and 2 nm (gap ≈ 3 nm). 129

Figure 6.3.2. Calculated steric repulsion and van der Waals attraction potentials for symmetric dimers of AuNPs (13 nm (A), 39 nm (B), and 62 nm (C)). Dependencies of interparticle Gap and total Energy (E_M) on effective DNA shell thickness (L') for a dimer of 13 nm (D) and 62 nm (E) NPs (Hamaker constant – 0.83 eV and DNA diameter – 2 nm. 13 nm NPs: $E_{min} = -5.1*\exp(-1.7*L')$, $G_{min} = 23.9*\exp(0.1*L') -26.7$; 62 nm NPs: $E_{min} = -30.3*\exp(-1.6*L')$, $G_{min} = 19.6*\exp(0.1*L') -20.8$. 130

Figure 6.3.1.1. Homo – sized AgNP dimers (10 nm) (A, C) and hetero – sized AgNP dimers (10 nm – 30 nm) (B, D) assembled with DNA (before (black) and after (red) assembly) while monitored using UV-Vis (A, B) and the simulated ACS (C, D) of hetero – sized AgNP dimers over a range of gap distances. 132

Figure 6.3.1.2. SERS spectra of same-sized AgNP dimers (10 nm) (A) and different sized AgNP dimers (10 nm – 30 nm) (B) assembled with DNA (before (black) and after (red) assembly) and the simulated EMF (C) of different sized AgNP dimers over a range of gap distances. 133

Figure 6.3.2.1. UV-vis spectra for an aqueous solution of *MZF@Au*-DNA1 and MBA-Au NPs before (black) and after (red) adding DNA2 (A). [*MZF@Au*-DNA1] = 6.2 nM; [DNA2] =0.56 μM; [40 nm-Au@MBA] =4.3×10^{-2} nM. (B-C) Simulated ACS spectra of AuNPs assembled to M@AuNPs (B) and AuNPs (C)) with different gap distances (12, 7, 6, 2, 1, 0 nm). 134

Figure 6.3.2.2. (A) SERS spectra for the assembly of MBA labeled AuNPs and DNA functionalized M@Au NPs (solid) (and AuNPs (dashed)) with target DNA strands (before assembly – black; after assembly – red). (B) 2D image of the simulated EMF around the Au-M@Au NPs (bottom, 9 nm magnetic core and 0.5 nm Au shell for M@Au NP) and

Au-Au NPs (top, 40 nm) at g = 2 nm; (C) Plot of the simulated EMF intensity for the Au-M@Au NPs (open squares) and Au-Au NPs (closed squares) as a function of the interparticle gap (from 1 to 10 nm). 136

Figure 6.3.2.3. Comparison of the experimental SERS intensity (black) and simulated EMF intensity (red) for the Au–M@Au NPs and the Au-Au NPs at an interparticle gap of 2 nm. 137

Figure 6.3.3.1. (A) UV-vis spectra for an aqueous solution of *MZF@Ag*-DNA1 and MBA-AuNPs before (black, bottom) and after (red, top) adding DNA2. Inset of A shows before (black) and after (red) assembly of 10 nm AgNPs and 40 nm AuNPs with DNA. (B) The simulated ACS Intensity of M@AgNPs and AuNPs when gap distance is decreased from 12 to 0 nm (arrows indicate the trend as the distance decreases: 12, 7, 6, 2, 1, and 0 nm). [*MZF@Ag*-DNA1] =3.0 nM; [DNA2] =0.56 μM; [40 nm-Au@MBA] = 4.3×10^{-2} nM). (C) The simulated EMF intensity of metallic 10 nm AgNPs assembled to 40 nm AuNPs with varying gap distances (arrows show shift from larger to smaller gaps: 12, 7, 6, 2, 1, 0 nm)). 138

Figure 6.3.3.2. (A) SERS spectrum of Magnetic Nanoparticles coated with Ag before (black) and after (red) assembly (control assembly of Ag and Au (dashed, top) and magnetic (solid, bottom)). (B) Simulated EMF spectra of the metallic AgNPs assembled to AuNPs (top) and M@AgNPs with AuNPs (bottom) at g = 2 nm. (C) The simulated EMF Intensity of 10 nm M@AgNPs (9 nm Magnetic core) and AuNPs (bottom, open circles) and Ag-Au NP dimers (top, closed circles) as gap distance decreases from 10 to 1 nm. 140

Figure 6.3.3.3. Comparison of the experimental SERS intensity (black) and simulated EMF intensity (red) for the Au-M@Ag NPs and the Au-Ag NPs at an interparticle gap of 2 nm. 141

Figure 6.3.3.4. Fractional surface coverage of DNA (black) and acrylate (red) as a function of the effective thickness (L', nm) (DNA: 11 nm height, 2 nm diameter; acrylate: 0.5 nm height, 0.5 nm diameter). 142

Figure 6.3.4.1. (A) Simulated EMF spectra of Au – M@Ag dimer at 0.1 nm gap. (B) Plots of the simulated EMF intensity of 40 nm Au NP and 10 nm NP of Au (black squares), M@Au (red circles) (B), M@Ag (blue up triangles), and Ag (lime downward triangles) at interparticle gaps below 2 nm. (C and D) Comparison of the simulated EMF and SERS intensities for heterodimers of Au – Au based NPs (C) and Au – Ag based NPs (D) above 0 nm (2 nm) and at 0 nm gap distances. 144

Figure 6.3.4.2. Comparison of EMF Intensity in the center of the hotspot region (red) and maximum intensity in the upper peripheral region of the hotspot (black) of AuNP (39 nm) – M@AuNPs (10 nm) (A) and – M@AgNPs (10 nm) (B). EMF schematic of Au – M@Ag NP at 0 nm where X_1 is the center of the hotspot and X_2 is the peripheral region. 145

Figure 6.3.5.1. Normalized simulated ACS Intensity showing the SPR changes of M@AuNP (A, B, C) and M@AgNP (D, E, F) assembled to AuNPs when the NP gap

distances is 0 nm that correspond to different core sizes when the shell thickness is 0.5 nm (A, D) (magnetic core size of 1 – black, a; 5 – red, b; 9 – blue, c), different shell thicknesses when the magnetic core is 9 nm (C, D) (shell thickness of 0.5 nm – black, a; 5.5 nm – red, b; 15.5 nm – blue, c), and 10 nm total size with different core sizes (magnetic core size of 1 – black, a; 5 – red, b; 9 – blue, c). 148

Figure 6.3.5.2. Different magnetic cores for 10 nm NPs with Au (A) or Ag (B) shell assembled to 39 nm AuNPs. (Core diameters: 1 (black, square), 5 (red, circle), and 9 (blue, triangle)). Different shell thicknesses for a 9 nm magnetic core assembled to 39 nm AuNPs: Au (C) or Ag (D) shell assembled to 39 nm AuNPs. (Shell thickness: 0.5 nm (black, square), 5.5 nm (red, circle), 15.5 nm (blue, triangle)). 150

Figure 6.3.5.3. Comparison of simulated ACS Intensity of different Fe oxide magnetic cores (Fe_2O_3 (A, B) and Fe_3O_4 (C, D)) when coated with 0.5 nm shell thickness of Au (A, C) and Ag (B, D). 151

Figure 6.3.5.4. Simulated ACS spectra of Ag coated (A-D) and Au coated (E-H) NPs with different metal cores: Co (A, D), Fe (B, E), and Ni (C, F) when gap distances are 22, 12, 2, 1, and 0 nm. 152

List of Schemes

Scheme 1.3.1. Illustration of SPR as an oscillation of surface electrons between two metallic nanoparticles. [1] 17

Scheme 1.3.2 Illustrates the ability to functionalize the surface of the NPs for various applications: Antigen, mRNA, DNA. Oligoethylene glycol, dye and more. [1] 18

Scheme 1.3.1.1. Illustrations of bioconjugation on AuNPs with: (A) thiol-containing miRNA duplexes consisting of sense and antisense miRNA (labeled with a fluorescent dye (e.g., Cy5)) along with oligoethyleneglycol thiol (OEG) to keep the miRNA from folding and electrostatically binding, (B) proteins (e.g., antibody) via a linking molecule (e.g., DSP (dithiobis (succinimidyl propionate))) along with a Raman label (RL) as a reporter, and (C) thiol-functionalized DNA. 19

Scheme 3.1.1. (top panel) Molecularly tunable interface of J-aggregated cyanine dyes for harnessing interparticle plasmonic coupling. (a) Interparticle π–π interaction of positively charged cyanine dyes (Tlc) adsorbed on gold NPs capped with negatively charged acrylate or citrate capping molecules. (b) Brickwork-like π–π stacking of Tlcs (J-aggregation). (bottom panel) Harnessing the interparticle J-aggregate induced plasmonic coupling for surface-enhanced Raman scattering 68

Scheme 4.1.1. Illustrations of an example of gold nanoparticle-based SERS detection strategy. This example uses a Protein A and goat anti-rabbit immunoglobulin G. Formation of "hot-spots" for SERS detection upon the assembly of proteins and antibodies when conjugated to MBA/AuNP. Note: The drawing with few proteins, antibodies, and MBA molecules is only to simplify the illustration 89

Scheme 5.1.1. Illustration of a dimer of AuNPs linked by two single-strand DNA (DNA1 and DNA2) through complementary binding (designed using the cyclin G promoter sequence for p53 recognition). The highlighted region indicates the area of interest in terms of plasmonic and electric field enhancements, or the center the interparticle gap (E_C). 104

Scheme 5.3.3.1. Models of three forms of double-stranded DNA (A, B, and Z forms) for a 30-bp duplex DNA derived under three different parameters (rotation/bp and increase/bp along axis: 32.7 degrees and 0.26 nm for A-form, 34.3 degrees and 0.34 nm for B-form, and 30 degrees and 0.37 nm for Z-form). 118

Scheme 6.1.1. Illustration of "hot- spot" formation of DNA – mediated dimeric assembly of core-shell nanoparticles containing magnetic cores and gold or silver nanoparticles in a solution. 125

Scheme 6.3.4.1. Proposed structures in terms of the interparticle spacing depending on the metal-metal dimer (A) and the metal-magnetic core@metal dimer (B) under an effective thickness for the DNA-capping monolayer. 146

Scheme 6.3.5.1. Manipulation of bidirectional approach for the interpretation of magnetic coated dimers (left: decrease magnetic core in a 10 nm NP (top) or a NP with 0.5 nm thick shell (bottom); right: increase metallic shell of 9 nm magnetic core). 147

List of Abbreviation and Symbols

ACS	Absorbance Cross-Section
Ab	Antibody
AgNPs	Silver Nanoparticles
AuNPs	Gold Nanoparticles
CEA	Carcinoembryonic Antigen
ds-	double-stranded
DNA	Deoxyribonucleic acids
EDS	Energy Dispersive X-ray spectroscopy
EMF	Electromagnetic Field
FTIR	Fourier Transform Infrared Spectroscopy
HR-TEM	High-Resolution Transmission Electron Microscopy
LOD	Limit of Detection
LSPR	Localized Surface Plasmon Resonance
M@Au	Gold-coated Magnetic
M@Ag	Silver-coated Magnetic
MBA	4-mercaptobenzoic acid; *p*-mercaptobenzoic acid
MHA	16-Mercaptohexadecanoic acid
MNPBEM	Metal Nanoparticle Boundary Element Method
MNP	Magnetic Nanoparticles
MUA	11-Mercaptoundecanoic Acid
MZF	Manganese Zinc Ferrite NPs
NPs	Nanoparticles
OAM	Oleylamine
OEG	Oligoethylene glycol
ProA	Protein A
ss-	single-stranded
SP	Surface Plasmon
SERS	Surface Enhanced Raman Scattering
TEM	Transmission Electron Microscopy
TGA	Thermogravimetric Analysis
TOABr	Tetraoctylammonium Bromide
UV-Vis	Ultraviolet-Visible Spectroscopy

List of Selected Publications

[1] **Skeete, Z.**; Cheng, H. W.; Li, L.; Salazar, C.; Sun, W.; Ngo, Q. M.; Luo, J.; Zhong, C. J. Assessing Interparticle Spatial Characteristics of DNA-Linked Core-Shell Nanoparticles with or without Magnetic Cores in Surface Enhanced Raman Scattering. *submitted*

[2] **Skeete, Z.**; Cheng, H.-W.; Ngo, Q. M.; Salazar, C.; Sun, W.; Luo, J.; Zhong, C.-J. "Squeezed" interparticle properties for plasmonic coupling and SERS characteristics of duplex DNA conjugated/linked gold nanoparticles of homo/hetero-sizes. *Nanotechnology* 2016, 27 (32), 325706 DOI: 10.1088/0957-4484/27/32/325706.

[3] **Skeete, Z.**; Cheng, H.; Crew, E.; Lin, L.; Zhao, W.; Joseph, P.; Shan, S.; Cronk, H.; Luo, J.; Li, Y.; et al. Design of Functional Nanoparticles and Assemblies for Theranostic Applications. *ACS Appl. Mater. Interfaces* 2014.

[4] H.W. Cheng, **Z. Skeete**, E. Crew, S. Shan, Jin Luo, C. J. Zhong, "Synthesis of Gold Nanoparticles", Chapter 2 in "*Gold Nanoparticles in Analytical Chemistry*", Edited by M. Valcarcel & A. I. Lopez-Lorente, Elsevier, 2014 (ISBN-13: 9780444632869)

[5] Chang, F.; Shan, S.; Petkov, V.; **Skeete, Z.**; Lu, A.; Ravid, J.; Wu, J.; Luo, J.; Yu, G.; Ren, Y.; et al. Composition Tunability and (111)-Dominant Facets of Ultrathin Platinum–Gold Alloy Nanowires toward Enhanced Electrocatalysis. *J. Am. Chem. Soc*. 2016, 138 (37), 12166–12175 DOI: 10.1021/jacs.6b05187.

[6] Lu, A.; Peng, D. L.; Chang, F.; **Skeete, Z**.; Shan, S.; Sharma, A.; Luo, J.; Zhong, C. J. Composition- and Structure-Tunable Gold-Cobalt Nanoparticles and Electrocatalytic Synergy for Oxygen Evolution Reaction. *ACS Appl. Mater. Interfaces* 2016, 8 (31), 20082–20091 DOI: 10.1021/acsami.6b06087.

[7] Lin, L.; Crew, E.; Yan, H.; Shan, S.; **Skeete, Z.;** Mott, D.; Krentsel, T.; Yin, J.; Chernova, N. a.; Luo, J.; et al. Bifunctional nanoparticles for SERS monitoring and magnetic intervention of assembly and enzyme cutting of DNAs. *J. Mater. Chem. B* 2013, 1 (34), 4320.

[8] Crew, E.; Yan, H.; Lin, L.; Yin, J.; **Skeete, Z.;** Kotlyar, T.; Tchah, N.; Lee, J.; Bellavia, M.; Goodshaw, I.; et al. DNA assembly and enzymatic cutting in solutions: a gold nanoparticle based SERS detection strategy. *Analyst* 2013, 138 (17), 4941–4949.

[9] Shan, S.; Wu, J.; Kang, N.; Cronk, H.; Zhao, Y.; Zhao, W.; **Skeete, Z.**; Joseph, P.; Trimm, B.; Luo, J.; et al. Nanoscale Alloying in Electrocatalysts. *Catalyst* 2015, 1465–1478 DOI: 10.3390/catal5031465.

[10] S. Shan, J. Luo, N. Kang, J.Wu, W. Zhao, H. Cronk, Y. Zhao, **Z. Skeete**, J. Li, P. Joseph, S. Yan, C.J. Zhong, "Metallic Nanoparticles for Catalysis Applications", Chapter 10 in "*Modeling, characterization, and production of nanomaterials: Electronics, photonics and energy applications*", Ed. V. Tewary, Y. Zhang, Woodhead Publishing, 2015. p. 251-288.

Chapter 1

Overview of Nano-Structured Materials

1.1. Significance of Molecular Detection

Identification and intervention of biomolecules such as amino acids, proteins, DNA, microRNA, bacteria are important for medical diagnostics. Among the various techniques for such diagnostics, the surge of interests in exploring gold or silver based nanoparticles as diagnostic probes stems largely from the unprecedented amplification of optical, spectroscopic, electrical and magnetic signals and their bio-functionality and bio-compatibility. These capabilities are further enhanced by the controllable sizes, shapes, compositions and surface properties, especially conjugation with desired biospecificity or assembly with the desired signal transduction mechanism. Therefore, the exploration of gold based nanoparticles (AuNPs) for detection, diagnostics, manipulation, targeting or transport of biomolecules is a topic of broad interest to drug delivery,[4,5] disease detection,[4] bio-sensing.[5,6] There are also increasing interests in exploiting nanoparticles' antimicrobial properties, including wound dressings, and biological responses.[7] One area of interest involves colorimetric detection of amino acids and small peptides, which are known to play different roles in heart disease, rheumatoid arthritis and AIDS.[8] For example, homocysteine is involved in the metabolism of methionine and is considered as a risk factor

for heart disease.[8] Glutathione, a tripeptide, is known to protect red blood cells from oxidative damage, and plays an important role in the detoxification of the cell, as well as the removal of harmful organic peroxides and free radicals. L-cysteine plays an important role in living systems and its deficiency is associated with a number of clinical situations (liver damage, skin lesions, AIDS, and certain neurodegenerative diseases). D-cysteine, on the other hand, is believed to interfere with many targets inside the cell. A common characteristic of these biologically relevant amino acids, such as cysteine and homocysteine, and small peptides such as glutathione is the thiol group in the structure, which has a strong affinity to gold or silver surfaces. Their conjugation to gold nanoparticles and the unique interparticle interactions provide a means for colorimetric detection of these biologically-relevant molecules.

The bio-conjugation ability of gold nanoparticles, on the other hand, enables them to function as an intriguing drug carrier or vehicle, which is an important area of current interest. Upon entering biological systems, AuNPs function as a carrier to deliver biomolecules (e.g., miRNA) in cell transfection, or as an antibacterial agent to inactivate bacteria, or potential toxic agent to damage biological functionalities (nanotoxicity). The importance of miRNA in the treatment of cancer and for the manipulation of genetic expression has been recognized. The study of AuNPs as carriers of certain miRNA (e.g., miR-130b), which express differently in glucocorticoid-sensitive versus glucocorticoid-resistant MM.1 cell lines, is one of the latest examples in cell transfection. Another area of current interest involves bacterial contamination of platelets which is the leading cause of morbidity and mortality from a transfusion transmitted infection, and bacterial inactivation which is considered as an option to reduce infection risk.[9] There is an

increasing need to understand the mechanistic details of the cell interactions of antimicrobial agents in microorganisms. Due to the high surface to volume ratio for a more efficient bacterial disinfection, nanoscale metal particles such as silver nanoparticles (AgNPs) are widely studied in antimicrobial applications. The introduction of magnetic cores in silver nanoparticles enables effective separation and delivery of the antibacterial agents in biological systems.

In comparison with the exploration of metal nanoparticles as probes, carriers or vehicles, one of the active research areas focuses on the assembly of nanoparticles. Broadly speaking, the assembly of nanoparticles is a result of the interparticle interactions leading to an association of the individual nanoparticles ranging from dimers or trimers to arrays or thin films. Such assemblies influence the collective optical or spectroscopic properties which can be harnessed for the detection of biomolecular recognition of proteins, DNA, and other biomarker molecules. There have been increasing interests in nanoparticle-based approaches to DNA analysis largely because of the potential enabling spatial multiplexing in an array format to produce simple and portable biosensor devices. Among various techniques, surface enhanced Raman scattering (SERS) technique using Au and Ag NPs has emerged as one class of the highly-sensitive spectroscopic probes for biomolecular detection.[10] It is the interparticle interaction or assembly that enables the creation of "hot-spots" for the observation of SERS effect. Theoretical calculations have shown that the SERS effect is closely related to the local electric field enhancement around nanoparticles, especially near corners, edges or gaps (so-called "hot-spots"), that are responsible for its high sensitivity and fingerprinting capability.[11-14] Recent interests in exploring magnetic nanoparticle cores with gold or silver shells largely stem from the possibility of exploiting

the unique combination of the SERS effect of Au or Ag NPs[11-13] and the nanoscale magnetic properties of magnetically-active nanoparticles for bio-specific separation, delivery, or targeting.

Indeed, the ability to impart magnetic functionality to gold or silver nanoparticles has led to increasing opportunities in the design of new strategies in theranostic applications. One important strategy for exploiting Au or Ag based nanoparticles involves an effective coupling of biomolecular detection and intervention (Figure 1.1.1).

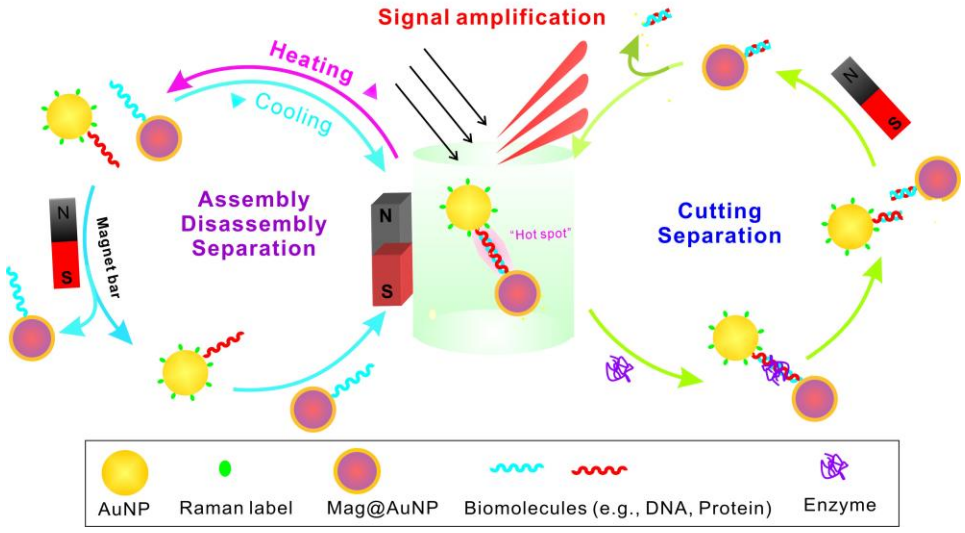

Figure 1.1.1. Illustration of bifunctional NPs for detection and magnetic intervention of biomolecular activities in a solution.

For example, this strategy can be used for the recognition of complementary single strand (*ss)*-DNA anchored to two different nanoparticles, i.e., Raman-labeled AuNPs and Au- or Ag-coated or decorated magnetic NPs, and the enzymatic cutting of the double strand (*ds)*-DNA. The creation of "hot-spot" by the interparticle plasmonic coupling as a result of double strand (*ds)*-DNA linkage provides a means for SERS detection. This ability stems from interparticle distance-dependent local electric field enhancement (i.e., "hot-spot") in between NPs linked by *ds*-DNA (e.g., dimer), as demonstrated by theoretical

modeling using discrete dipole approximation method.[13] Upon enzyme cutting of the *ds*-DNA at a specific site, the "hot-spot" can be removed. On the other hand, the incorporation of a magnetic component in the nanoparticles provides the capabilities of easy intervention and bioseparation.

This type of functional nanoprobes could enable interparticle "hot-spot" formation and bio-separation capability for monitoring DNA assembly and cutting processes in biological fluids in real time. The understanding of the effective coupling of the localized fields between particles and substrates[15] will be useful for diagnostics, drug delivery and DNA separation,[16] including cetuximab conjugated magnetic core-shell nanoparticles for early detection of colon cancer, and bioassays of DNA cleavage and binding by human p53 that may be useful for pathogen detection and disease analysis.[17] While much has been learned about the DNA-conjugated nanoparticles for assays on solid substrates,[6,18,19] relatively little is known about monitoring the detailed processes related to protein binding and cutting of DNA in a biologically-relevant solution phase.[17,20] The assembly of AuNPs by complementary-strand binding of DNA designed using the *cyclin G* promoter sequence for *p53* recognition leads to the formation of a double strand in between AuNPs, which provides a *p53* recognition site. It also provides a recognition site for a restriction enzyme that cuts the *ds*-DNA at a specific site, allowing the use of nanoparticle assembly as a probe to the interactions and relativities of the *ds*-DNA directly in a solution.[17]

The signal amplification and fingerprinting capability of SERS have led to increasing interests in studies of nanomaterials of different sizes, shapes and structures, especially gold or silver NPs for various applications.[21] The exceptionally strong confinement of electromagnetic energy around plasmonic-active metal nanoparticles exhibits

approximately fourth power of the field enhancement at the particle surface, especially in the vicinity of sharp features or small gaps in nanostructures. The synthesis of pure dimers is a challenge, but there have been several intriguing approaches to controlling the enhancement gap (e.g., gold nanogap particles[21]). Indeed, various nanostructures of Au and Ag have been extensively exploited for SERS, which has rapidly emerged as highly sensitive colorimetric and spectroscopic techniques for the detection of DNAs, proteins or enzymes.[9,11,15,17,22-25] In comparison with solid-state SERS substrates for antibody-antigen binding of AuNPs on a gold thin film,[23,24] the enhancement of SERS using nanoparticles suspended in a solution[15,23] is smaller, but understanding the interparticle plasmonic coupling ("hot-spot") as a result of the formation of small clusters of nanoparticles such as dimers and trimers[23] is useful for developing the capability for biomolecular signal transduction and activity intervention in a solution phase. Considering the limited surface modification and potential nanotoxicity of magnetic nanoparticles (MNPs, e.g., iron, nickel, or cobalt oxides) in bioseparation and controlled delivery[3], or magnetic resonance imaging (MRI),[26] there is an increased interest in introducing desired surface functionalization of MNPs using gold or silver as a shell. This type of surface chemistry has been demonstrated for biomolecular separation from solutions,[15,23-25] cancer-cell targeting,[27] and SERS detection.[28] The detection in these studies involved using solid substrates or magnetic enrichment. Recent insights into the reactivity of restriction enzyme at DNA-mediated assembly of AuNPs in a solution phase have demonstrated the possibility of the nanoprobes strategy for potential *p53* protein recognition.[26]

Another pathway for exploring the assembly of nanoparticles as functional materials involves molecularly-mediated thin film assemblies of metal nanoparticles as sensing

materials for electrical detection of volatile organic compounds (VOCs), which has potential application in the detection of breath biomarkers linked to different diseases, including diabetes[29] and lung cancers.[30] In addition to 4–5% more CO_2 and 4–5% less O_2 inhaled, vapors and trace gases include 5% H_2O, a few ppm(V) of H_2 and CO_2, NH_3 and acetone, methanol, ethanol and other VOCs.[31] The detection of biomarkers from breath samples of patients with different diseases has attracted increasing interests. One example involves detection of acetone as a breath biomarker from diabetes, which has been identified to link to the level of blood sugar. Traditionally, GC and GC–mass spectroscopy have been used in breath sample analysis for diabetes, cancer and oxidative stress in diabetes. In contrast to existing serum or urine analysis, the breath analysis features noninvasiveness and real-time monitoring. The development of nanoparticle-structured sensor arrays for breath analysis could lead to a potential point-of-care diagnostic tool.

Overall, there have been major advances in many areas exploring nanoparticles and assemblies for potential diagnostic applications, including latest examples in infectious disease detection, cancer diagnostics and imaging, and cancer biomarker detection[32] which exploit optical and spectroscopic signals due to DNA and protein adsorption and assembly[33] and interparticle spacing or aggregation. Several recent reviews have discussed different nanostructure bioconjugation and plasmonic nanoparticle based biosensing[34,35] and therapeutic applications. Rather than comprehensively describing the exploration of nanoparticles for various applications in theranostics, which have been discussed in a number of recent reviews, each focusing on a different aspect, this work focuses on harnessing functional nanoparticles and assemblies as a strategy for the creation of the structurally-tailored multifunctional properties for biomolecular detection and intervention.

In addition to describing progress in synthesis and processing of metal and magnetically-functional nanoparticles and assemblies, examples in colorimetric detection of amino acids and small peptides, SERS detection of biomolecular recognition of proteins and DNA, targeted delivery in cell transfection and bacteria inactivation, and nanostructured flexible sensor array for the detection of biomarkers of human breath will be highlighted.

1.2. Synthetic Design of Nanomaterials

1.2.1 Synthesis of gold or silver based nanoparticles

The synthesis of AuNPs generally involves wet-chemical reduction of chloroauric anions ($AuCl_4^-$) as the gold precursor. For the synthesis of AuNPs in aqueous phase, seeded growth method has been reported for controlling particle size, most of the methods have been based on the modification of Turkevich method through a two-step process (two-step process: (1) nucleation and (2) growth). For the control of size, which is often difficult, a highly-effective method was developed in our laboratory for the growth of highly-monodispersed AuNPs in the size range of 10 to 100 nm diameter,[15] which involves $AuCl_4^-$ as a starting Au-precursor and acrylates as both reducing and capping agents in a seeded "aggregative growth" process. This is in contrast to Ostwald ripening, where smaller particles dissolve preferentially with subsequent crystallization onto larger particles. Insights into the growth mechanism were gained by the determination of the size and optical properties as a function of the growth parameters such as the reaction time and the seed/precursor concentrations,[14] demonstrating the operation of the aggregation growth mechanism in this simple and reproducible growth process. AuNPs with average sizes in 10-100 nm range can be easily grown using smaller particles as seeds (Figure 1.2.1.1(A)). While the overall morphology of these nanoparticles appears spherical, faceted edges along

the outlines of nanoparticles can be observed upon close examination, which is consistent with the polycrystalline properties of the AuNPs. The size monodispersity is evidenced by narrow size distributions (Figure 1.2.1.1(A)). The relative standard deviations (RSD) are ~8% for the smaller sized (<30 nm), ~4% for the medium-sized (30~50 nm), and ~3% for the larger-sized (>50 nm) nanoparticles. The mass of the seed-grown particles is quantitatively correlated with the concentration of $AuCl_4^-$. By analysis of the correlation of nucleation parameters with the particle sizes and distributions, the growth was shown to follow a "seeded and aggregative growth" mechanism, which is consistent with the general characteristics of aggregative growth mechanism.[36]

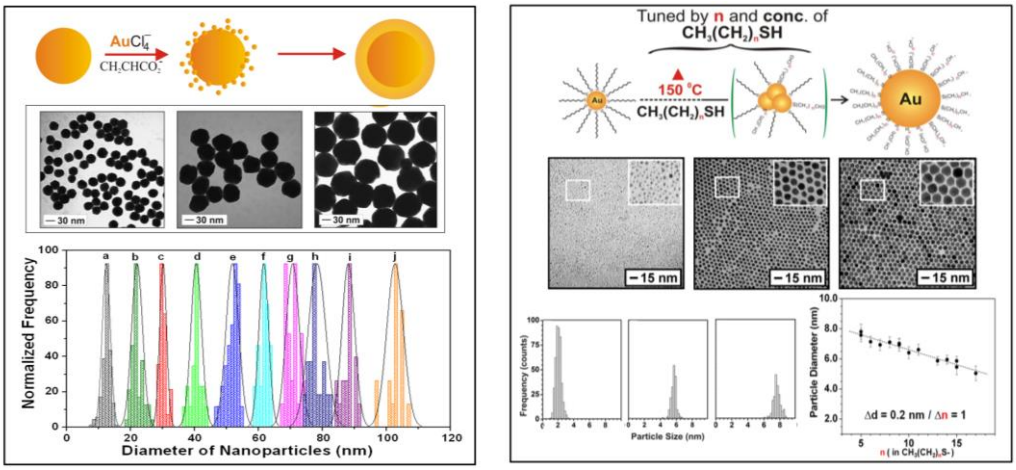

(A) (B)

Figure 1.2.1.1. (A) Seeded and aggregative growth of gold NPs. Middle panel: TEM for 30 nm seeds (a), and seed-grown 60 (b) and 90 nm (c) AuNPs. Bottom panel: Size distributions. (B) Thermally-activated processing of AuNPs capped by alkanethiolate monolayer. Middle panel: TEM of AuNPs produced by thermal processing in the presence of alkanethiols of different chain length (n): n=5 (right, 7.60 ±0.43 nm), and 15 (middle, 5.86 ±0.31 nm) and the precursor Au_{2nm}-DT (left, 2.01 ± 0.41 nm). Bottom panel: Size distributions (left) and Dependence of particle size on capping alkyl chain length (right). (Reproduced with permission from refs. 49, 55, and 56. Copyright 2006, 2010 American Chemical Society.)

For the synthesis of AuNPs in organic phase,[37] a key process in the Brust−Schiffrin Method for thiol-protected AuNPs, reported first in 1994, is to transfer $AuCl_4^-$ from aqueous phase to toluene using tetraoctylammonium bromide (TOABr), where it is reduced by sodium borohydride ($NaBH_4$) in the presence of dodecanethiol.[38] The resulting particles

are in the range of 2-5 nm. A further modification of this method by manipulating the reaction temperature and other parameters was reported by Murray *et al*., demonstrating the ability to control size down to about 1 nm with relatively high monodispersity or introducing different capping ligand structures. The smaller size characteristic is perhaps one of the main attributes in comparison with AuNPs synthesized in aqueous phases. Starting from nanoparticles synthesized by this route, one of the approaches to size control developed in our laboratory exploits the nanoscale phenomenon of melting point decrease for certain metal nanoparticles,[39,40] which is inversely proportional to the particle size and free energy reduction driven coalescence of surface-melting particles, leading to the increase of particle size. For example, alkanethiolate-capped AuNPs can be obtained by thermal activation of smaller-sized starting particles, e.g., decanethiolate (DT) capped AuNPs (Au_{2nm}-DT, 1.9 ±0.7 nm), via shell desorption, core coalescence and shell re-encapsulation in a toluene solution containing TOABr and capping molecules such as DT under controlled temperature (149 ±1.5 °C) towards larger-sized nanoparticles.[40] The size distribution is strikingly narrow, as shown in Figure 1.2.1.1(B). The uniform interparticle spacing between the nanoparticles with a predominant hexagonal packing array feature shows an edge-to-edge distance of ~1.0 nm, corresponding closely to the distance expected for an interdigitation of alkyl chains between shells of the neighboring nanoparticles (Figure 1.2.1.1(B)).[40]

The thermally-activated processing of a solution of pre-synthesized nanoparticles involves coupling of the molecular capping and re-encapsulation to the interparticle coalescence, different from simple Ostwald ripening processes. The particle size growth is shown to be a function of chain length of the capping alkanethiols ($CH_3(CH_2)_nSH$)

(Figure 1.2.1.1(B)).[35,39] The cores for nanoparticles evolved using shorter chain thiols were found to be larger than those evolved in the presence of longer thiols. For example, the AuNPs obtained using alkanethiols with n=15 (Figure 1.2.1.1(B)) an average core diameter of 5.86 ± 0.31 nm was obtained. Since our early demonstration of this strategy for producing highly-monodispersed AuNPs,[40] also showed viability for processing copper and other metal nanoparticles. Using this approach with slight modifications, gold-based alloy and other metal (e.g., copper) nanoparticles of different sizes have also been prepared.[40] The molecularly-tuned size selectivity[39] provides an important means for processing nanoparticle size and monodispersity. In addition, depending on the alkanethiol concentration, the size of the nanoparticles after the thermal treatment is linearly dependent on the chain length of alkanethiols used (Figure 1.2.1.1B), exhibiting a slope of -0.2 nm/methylene unit. This correlation demonstrates the important role played by cohesive interactions in regulating interfacial reactivities of nanoparticles for the control of particle sizes, in contrast to a chemical synthesis route from precursor molecules.[38,41] In fact, deep insights into the importance of aggregative growth mechanism for the control of AuNPs size have recently been gained in both experimental and theoretical studies of the kinetics and mechanism for the size evolution of AuNPs under the thermally-activated evolution process.[36,42] By using the well-known KJMA model for aggregative growth, a straightforward analytical method was derived for analysis of the growth kinetics. The method allows extraction of separate aggregative-nucleation, aggregative-growth, and Ostwald-ripening rate constants. The established aggregative nucleation rate and size distribution are contrasted to classical LaMer nucleation and growth, in addition to Ostwald ripening. In aggregative growth, which is a nonclassical nucleation and growth process,

the nucleation parameters can be systematically varied by conditions that influence the stability of the initial small particles, leading to controlled size and distribution.

Similar approaches have also been used for the synthesis and processing of silver and gold-silver alloy nanoparticles.[43] In the synthesis of silver and gold-silver alloy nanoparticles encapsulated with alkanethiolate monolayer,[43] two-phase reduction of $AuCl_4^-$ (in toluene) and $AgBr_2^-$ (in toluene) is used[44]. The synthesis can be carried out by separately transferring $AgBr_2^-$ and $AuCl_4^-$ from aqueous phase to organic phase using TOABr as the phase transfer reagent. Different compositions of alloy nanoparticles were synthesized by controlling the feed ratios of the two metal precursors. The size monodispersity is better than those synthesized by citrate reduction of Ag^+ in aqueous solutions. The alkanethiolate-capped Ag and AgAu nanoparticles also allow the thermally-active processing to achieve the controllability of the particle size in the range of 2 to 10 nm.

1.2.2 Synthesis of Magnetically-functionalized nanoparticles

In combination with various synthesis methods, the thermal activation strategy has also been demonstrated for controlled processing of metal, alloy and core-shell nanoparticles in solutions in terms of size and morphology under an elevation of temperatures ranging from 100 to 200 ^oC. Examples include Au, Cu, AuAg, AuCu, AuPt and Fe_2O_3 or Fe_3O_4@Au.[39,40] By a combination of the lowered melting temperature for metal nanoparticles and the un-affected melting temperature of iron oxide nanoparticles, a thermally-activated hetero-interparticle coalescence was demonstrated for fabricating core@shell type of Fe-oxide@Au) nanoparticles.[24,45] One example involves the formation of Fe_2O_3 or Fe_3O_4 and Au nanoparticles in a solution by thermally-activated hetero-

interparticle coalescence between gold and Fe_2O_3 or Fe_3O_4 nanoparticles under encapsulating environment (Figure 1.2.2.1A). The stabilization of the nanoparticles is achieved by organic ionic materials such as tetraoctylammonium bromide (TOABr) in the solution and the capping molecules such as alkanethiols (e.g., decanethiols (DT)) for Au nanoparticles and oleylamine and/or oleic acid for Fe-oxide nanoparticles. The thermal microenvironment facilitates core-shell coalescence to produce monodispersed Fe-oxide@Au nanoparticles of controlled sizes, depending on the relative ratio of the two precursors. It is the combination of the solution temperature, the composition and the capping structures, along with the competition between growing Au and Fe-oxide@Au NPs, that leads to the formation of larger-sized core@shell nanoparticles with a single or multiple Fe-oxide cores (pomegranate-like) Figure 1.2.2.1A.

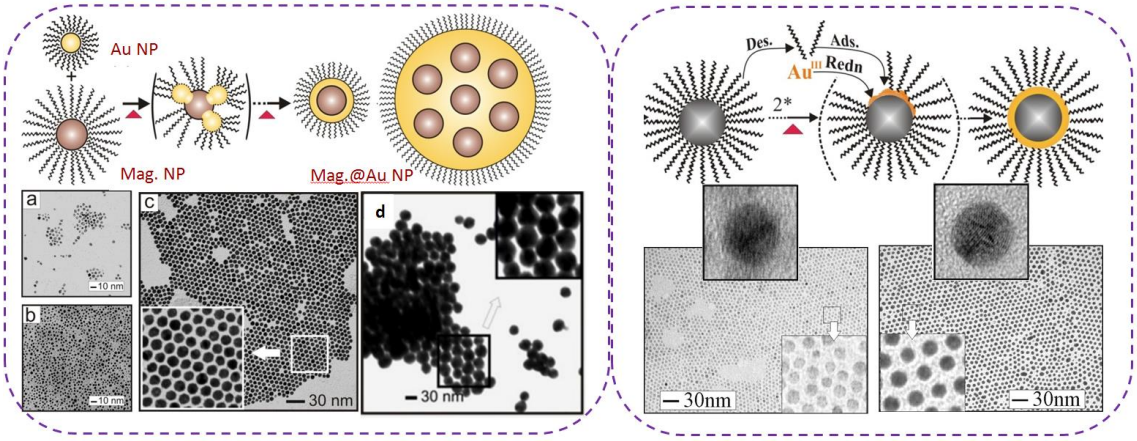

(A) (B)

Figure 1.2.2.1. (A) Scheme and TEM for Fe_2O_3@Au nanoparticles produced from Au and Fe_2O_3 precursor nanoparticles by the thermally-activated processing route. (B) Scheme and TEM for Fe_3O_4@Au nanoparticles produced by combined bottom-up synthesis and thermal processing in a seeded-growth process (2* =gold precursor, reducing and capping agents, and temperature manipulation): Fe_3O_4 (5.2 ± 0.4 nm) and Fe_3O_4@Au (6.6 ± 0.4 nm). (Reproduced with permission from refs. 24, 45. Copyright 2005 and 2007 American Chemical Society.)

The magnetic core-gold shell nanoparticles can also be prepared by combining wet-chemical synthesis and thermal processing in a seeded-growth process.[24,45,46] Figure

1.2.2.1B shows an example is the synthesis of highly-monodispersed Fe_2O_3@Au and Fe_3O_4@Au nanoparticles[45,47] using Fe_3O_4 seeds capped with oleylamine and/or oleic acid chemical reduction of $Au(CH_3COO)_3$ in the presence of capping agents at 180 °C. The formation of core-shell nanoparticles is supported by the change in particle sizes in TEM and HR-TEM images (Figure 1.2.2.1B), the observation of Au-shell specific surface chemistry, the change in magnetization and blocking temperature, and the demonstration of their use in magnetic bio-separation or as spectroscopic probes.[24,46] The latter also involved many other core-shell types of magnetic or metal nanoparticles (e.g., MnZnFeO@Au, Fe_3O_4@Au@Pt, Pt@Au, AuAg, AuPt, PtVFe, PtNiFe[23,43,46-48]).

To achieve tunable nanomagnetism, MnZn ferrite nanomaterials with a spinel structure represent an important class of tunable magnetic materials.[49] In comparison with binary MFe_2O_4 (M = Fe, Co, Mn, Zn, etc) nanoparticles,[50] MnZn ferrite nanoparticles provide an increased tunability. A novel core-shell structured nanocube of MnZn ferrite was synthesized by controlling reaction temperature and composition in the absence of conventional reducing agents in one-pot synthesis. The highly-monodispersed and cube-shaped core-shell structure consists of an Fe_3O_4 core and an $(Mn_{0.5}Zn_{0.5})(Fe_{0.9}Mn_{1.1})O_4$ shell (Figure 1.2.2.2A). The HR-TEM for the core-shell structure shows a Moiré pattern, indicating a highly-crystalline combination of core and shell with slightly different lattice constants or rotation of the core relative to the shell.[49] In Figure 1.2.2.2B, two different phases are revealed, corresponding to a core of Fe_3O_4 and a shell of MnZn ferrite $(Mn_{0.5}Zn_{0.5})(Fe_{0.9}Mn_{1.1})O_4$. They can be either antiferromagnetic or ferrimagnetic because of the antiparallel arrangement of the ions on the tetrahedral *vs*. the octahedral sites, resulting in the saturation magnetization of ~96.5 emu/g. The highest value of

magnetization, 45.6 emu/g, is close to the maximum magnetization value for Fe_3O_4 (5.2 nm) (66 emu/g).[45] The MnZn ferrite nanoparticles could also be synthesized in aqueous solutions, but the controllability over size monodispersity and shape is rather limited[46].

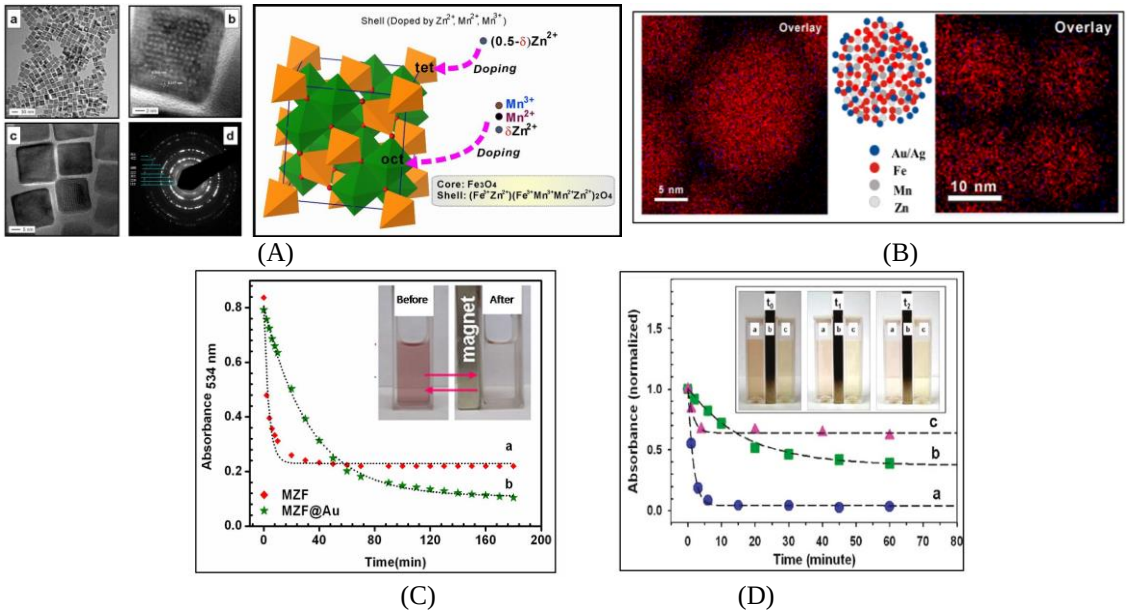

Figure 1.2.2.2. (A) Morphologies of MnZn ferrite (MZF) core-shell nanocubes: TEM/HRTEM (a-c) and ED pattern (d) for MnZn ferrite nanoparticles (size: 20.6 ± 1.8 nm, core (Fe_3O_4)/shell ($(Mn_{0.5}Zn_{0.5})(Fe_{0.9}Mn_{1.1})O_4$)). (Right: structural model for MZF nanocubes consisting of Fe_3O_4 core (inverse core) and MZF shell where the tetrahedral sites are doped by (0.5-δ) Zn^{2+} whereas the octahedral sites are doped by Mn^{3+}, Mn^{2+}, and the rest of Zn^{2+}. (B) EDS composition mapping for MZF@Au (left) and MZF@Ag (right) nanoparticles in terms of overlapping of Fe (red) with Au (MZF@Au) and Ag (MZF@Ag). Mn and Zn detected are not shown. (C-D) Plots showing the magnetic separation kinetics in terms of the change in absorbance of SP band at ~534 nm for a solution of MZF (a), and MZF@Au (b) (C), and ~420 nm for solutions of MZF (a), MZF@Ag (b), and mixed MZF and Ag NP (c) (D). (Insets: photos showing color changes before and after applying a magnet, leading to gradual separation (for D: $t_0 = 0$; $t_1 = 30$; $t_2 = 60$ min). (Reproduced with permission from refs. 9, 49 Copyright 2010 and 2011 American Chemical Society, and from ref. 20 Copyright 2013 Royal Society of Chemistry.)

The MnZn ferrite nanoparticles have been coated with Au or Ag shells of various thicknesses by either seeded growth method.[24,46] In one method,[23] 35 nm MnZn ferrite core size was coated with 1.2 nm Au shell.[24] In a recent study,[21] the thermally activated processing method was used[24] for the preparation of Au- and Ag-decorated MZF nanoparticles, by heating a concentrated toluene solution with Au-DT (or Ag-DT) and

OAM/OA-capped MZF nanoparticles in a certain ratio at 150 °C. The distributions of Fe, Mn, Zn, and Au or Ag are shown by the EDS data for MZF/Au and MZF/Ag NPs. There is clear indication that Au or Ag metals are decorated on the MZF core, as evidenced by overlapping Fe and Au in the case of MZF/Au or Fe (Figure 1.2.2.2B) and Ag in the case of MZF/Ag. The functional properties of these magnetic core-shell type NPs are also observed by a gradual decrease of the surface plasmon resonance bands of the NPs under a magnetic field (Figure 1.2.2.2C), similar to those reported recently.[9,24] For example, a gradual decrease of the SP band absorbance is observed in Figure 1.2.2.2D for MZF@Ag nanoparticles, revealing clear differences for MZF@Ag, mixed MZF and Ag, and MZF. The magnetic properties are also evidenced by the decrease of color for MZF@Ag NPs in the solutions under the magnetic field.

1.3. Optical and Electrical Properties of Nanomaterials

Nanostructured materials have found increasing applications in medical therapies and diagnostics (theranostics) many of which stem from their unique optical, electromagnetic, and catalytic properties. These materials can be manipulated in these applications by tuning their properties. For instance, metal nanomaterials like gold colloidal solutions, when excited by light undergo oscillations of their surface electrons when frequency of the electromagnetic field (EMF) matches that of the surface electrons. These oscillations that occur only on the boundaries between the NP surface and solution, produce a surface plasmon resonance (SPR) band that is unique to the metal of a particular size (Scheme 1.3.1). These oscillations can also be identified using Surface Enhanced Raman Scattering (SERS) spectroscopy, by the tracking the changes in the polarizability of the NP.[1-3]

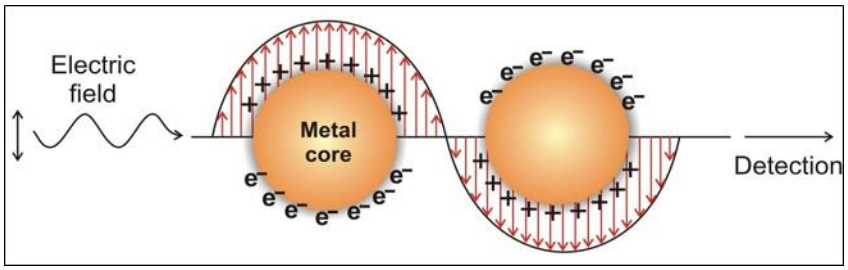

Scheme 1.3.1. Illustration of SPR as an oscillation of surface electrons between two metallic nanoparticles.[1]

A key challenge is the ability to impart the nanomaterials with structurally-tailored functional properties which can effectively target biomolecules but also provide signatures for effective detection.[4,5] The harnessing of functional nanoparticles and assemblies serves as a powerful strategy for the creation of the structurally-tailored multifunctional properties (Scheme 1.3.2). This thesis highlights important findings of recent investigations of metal (especially gold and silver), and magnetically functionalized nanoparticles, and molecularly assembled or biomolecularly conjugated nanoparticles with tunable optical, spectroscopic, magnetic, and electrical properties for applications in several areas of potential theranostic interests. Examples include colorimetric detection of amino acids and small peptides, SERS detection of biomolecular recognition of proteins and DNA, targeted delivery in cell transfection and bacteria inactivation, and chemiresistive detection of VOCs and breath sensing. A major emphasis is placed on understanding how the control of the nanostructures and the molecular and biomolecular interactions that impact these biofunctional properties, which has important implications for bottom-up designs of theranostic materials.

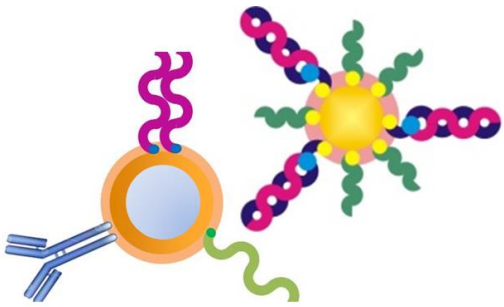

Scheme 1.3.2 Illustrates the ability to functionalize the surface of the NPs for various applications: Antigen, mRNA, DNA. Oligoethylene glycol, dye and more.[1]

1.3.1 Bio-conjugation of nanoparticles

The rich surface chemistry is one of the key attributes of Au or Ag based NPs that enables bio-conjugation of thiol-containing amino acids, small peptides, proteins, miRNA, and DNA in effective ways (Figure 1.3.1.1). Gold nanoparticles can be conjugated with microRNA (miRNA) for delivery into cells for genetic manipulation or cellular marking.[51,52] Figure 1.3.1.1A shows an example in which AuNPs are conjugated with Cy5 (or Cy3) labeled miR-130b on the AuNPs (miRNA-AuNPs).[53] The dye molecules could serve as fluorescent or SERS labels.[12,15,23] Upon conjugation, the miRNA-AuNPs, show an increased mobility in gel electrophoresis, consistent with the increased negative charge on the nanoparticle surface by miRNA. By performing ligand exchange reaction of miRNA-AuNPs with bis(*p*-sulfonatophenyl)phenylphosphine (BP), a negatively charged surfactant used for increasing the surface charge,[23] in the solution, the mobility remains unchanged, indicating that the miRNA-conjugation is quite stable.

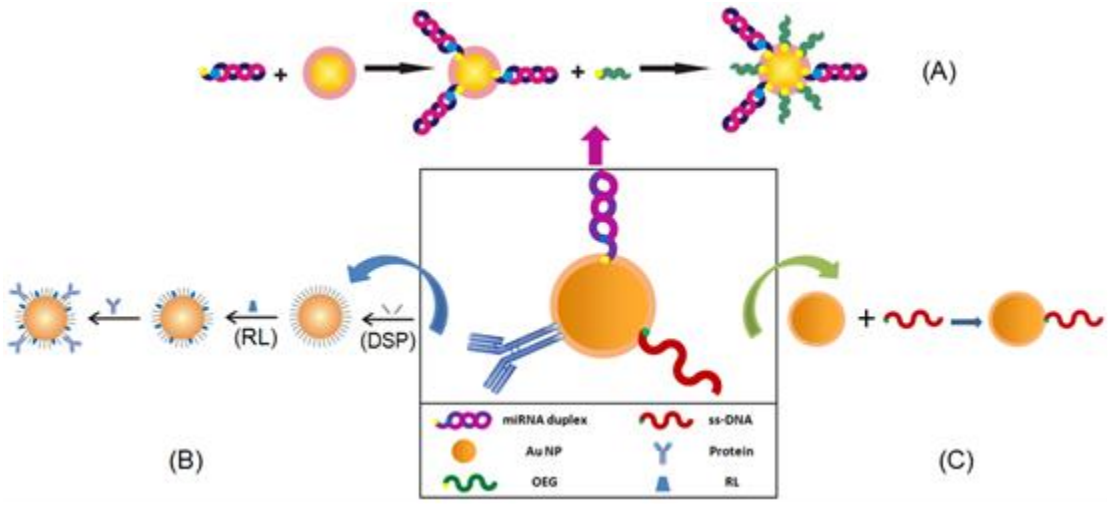

Scheme 1.3.1.1. Illustrations of bioconjugation on AuNPs with: (A) thiol-containing miRNA duplexes consisting of sense and antisense miRNA (labeled with a fluorescent dye (e.g., Cy5)) along with oligoethyleneglycol thiol (OEG) to keep the miRNA from folding and electrostatically binding, (B) proteins (e.g., antibody) via a linking molecule (e.g., DSP (dithiobis (succinimidyl propionate))) along with a Raman label (RL) as a reporter, and (C) thiol-functionalized DNA.

Effective conjugation of protein molecules (antibody or antigen) and Raman label to nanoparticle surfaces is important for SERS-based immunoassay. As shown in Figure 1.3.1.1B, AuNPs can be labeled with Raman label and protein by controlled concentrations of dithiobis(succinimidyl propionate) (DSP), mercaptobenzoic acid (MBA), and protein A. This approach is relatively simple for controlling the coverage of MBA on the surface, and also has some flexibility in terms of the sequence of immobilizing MBA and protein.[24] Similar to homocysteine-mediated assembly of AuNPs,[54] the control of salt concentration in the solution is also important in determining the stability of the nanoparticles in an aqueous system, which is dependent on the chemical nature of capping molecules and the electrical double layer charges.

DNA-based nanoparticle assembly[16,55,56] is another important area exploiting the optical properties of the nanoparticles for the detection of enzymes and proteins associated with diseases and pathogens. For example, *p53* protein, a DNA binding protein, is found

in more than 50% of all tumors. The study of *p53* recognition sites, *mdm2, p21* and *cyclin G* genes, is important for understanding the role of DNA transcription in cancer. In Figure 1.3.1.1C, the assembly of AuNPs by complimentary-strand binding of DNA, designed using the *cyclin G* promoter sequence, involves AuNPs conjugated with the top and bottom single-stranded DNA (*ss*-DNA).[17] A double strand is formed by interparticle complimentary binding of the two DNA in between AuNPs, which is a *p53* recognition site. In proof-of-concept demonstration experiments, two different DNA strands, (DNA1: 5'-/5ThioMC6-D/AGGCCAGACCTGCCCGGGCAAGCCTTGGCA-3' (bottom strand) and DNA2: 5'-/5ThioMC6-D/TGCCAAGGCTTGCCCGGGCAGGTCTGGCCT-3' (top strand)) were used.[17] For alkanethiolate-capped nanoparticles synthesized in organic phases, the bioconjugation can be achieved by transferring them to aqueous solution via ligand exchange reaction (e.g., mercaptoundecanoic acid) before conjugating with DNA or proteins.

1.3.2 Assembly of nanoparticles with tunable with optical and electrical functions

The interparticle linkage or assembly of NPs leads to changes in optical and spectroscopic properties which provide not only ways for determining their correlation with the nanoscale parameters (size and composition). Changes in absorbance and wavelength of the surface plasmon (SP) band provide a measure of particle size, shape, concentration and dielectric medium properties, which can be described by Mie theory or SERS intensity. The wavelength (λ_{max}) at maximum absorbance of the SP bands is dependent on the particle size. The increase of the λ_{max} value of the SP band with increased particle size is very comparable between the experimental and the theoretical data. Insights have been developed into the correlation among particle size, SP band, and SERS intensity.

For example, the particle size – SERS correlation has been demonstrated by comparison of SERS spectra of Raman labels on AuNPs in solution and on a solid substrate.[23] For Au thin-film substrate immobilized with AuNPs, two intense diagnostic peaks of the MBA were observed at 1081 cm^{-1} and 1591 cm^{-1}, displaying a maximum intensity for nanoparticles of 60 ~ 70 nm in size (Figure 1.3.2.1A). In contrast, the SERS intensity for MBA adsorbed on AuNPs in an aqueous solution shows a gradual increase with the particle size (Figure 1.3.2.1B). The SERS signals are clearly detectable for particle sizes greater than 40 nm. The size correlation of SERS intensity suggests the existence of a critical size range of the nanoparticles in the solution beyond which the particle-particle interaction is operative and responsible for the SERS effect. Experimentally, the nanoparticles capped with MBA in solution were first subjected to centrifugation before taking Raman spectra. Since no peak was observed prior to centrifugation, it is likely that the decrease in the interparticle distance between the particles, via formation of small clusters of nanoparticles such as dimers or trimers, allowed more effective plasmonic coupling. The adsorbed MBA molecules confined in such clusters are thus the "hot-spots" responsible for the observed SERS effect.

The formation of dimers/trimers is supported by the dependence of the SERS intensity on centrifugation speed and salt concentration. The SERS intensity is found to increase with the speed of centrifugation, which is consistent with the increase of the SP band[15,54] around ~750 nm characteristic of the nanoparticle aggregation (Figure 1.3.2.1C). Furthermore, while the dimer/trimer formation is also dependent on the salt concentration, the salt-induced aggregation of the MBA-capped nanoparticles is irreversible whereas the

centrifugation-induced aggregation of nanoparticles can lead to small clusters, which are dispersible and stable in the solution.

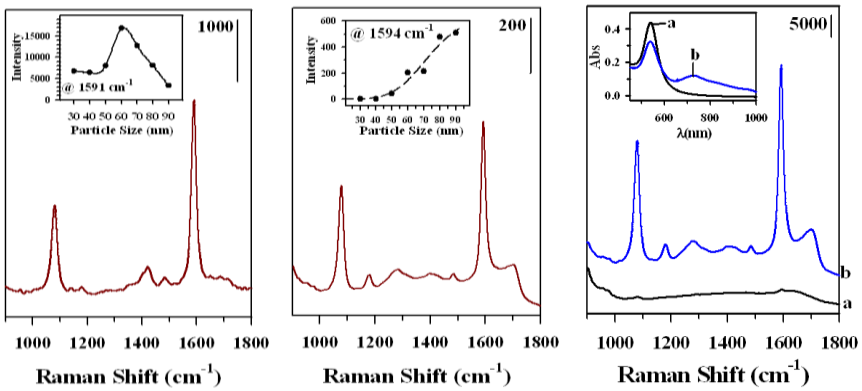

Figure 1.3.2.1. SERS spectra for MBA-labeled Au_{90nm} on a Au-film substrate (A, Insert: SERS intensity at 1591 cm^{-1} vs. particle size), MBA-labeled Au_{90nm} in aqueous solution (B, Insert: SERS intensity at 1594 cm^{-1} vs. nanoparticle size), and solutions of MBA in the presence of Au_{60nm} after centrifuging at different speeds: 2000 (a), 14000 (b) rpm (C, Insert: UV-vis spectra for the corresponding solutions). (Reproduced with permission from ref.23. Copyright 2008 IOP science.)

The controlled interparticle linkage could also lead to assembly of the nanoparticles into thin films with changes in optical and electrical properties that are dependent on particle size and interparticle spacing parameters. For example, the SP band for thin film assemblies of AuNPs of different sizes which are linked by alkyl dithiols (ADTs) or carboxylic acid-functionalized thiols (CATs) of different alkyl chain lengths are studied as a model system is shown to exhibit a red shift of the SP band (l_{max}) in comparison with the solution counterpart,[57] depending on the chain length (n) (Figure 1.3.2.2A) and the particle diameter (2r) (Figure 1.3.2.2A insert).[57] The correlation of the SP band evolution with particle size, interparticle distance, and dielectric medium properties is in agreement with Mie theory, providing information for assessing the optical properties for the nanostructured thin films.[57] Such optical properties have also been observed for molecularly-mediated assembly of AuAg[58] and Fe_3O_4@Au NPs.[45] For example, the SP band for 1,6-hexanedicarboxylic acid (HDA)-mediated assembly of $Au_{23}Ag_{77}$ NPs shifts

to longer wavelength (515 nm) in comparison to that before the assembly (460 nm).[58] The SP band shift is a common characteristic for NDT- or MUA-mediated thin film assemblies of AuNPs.

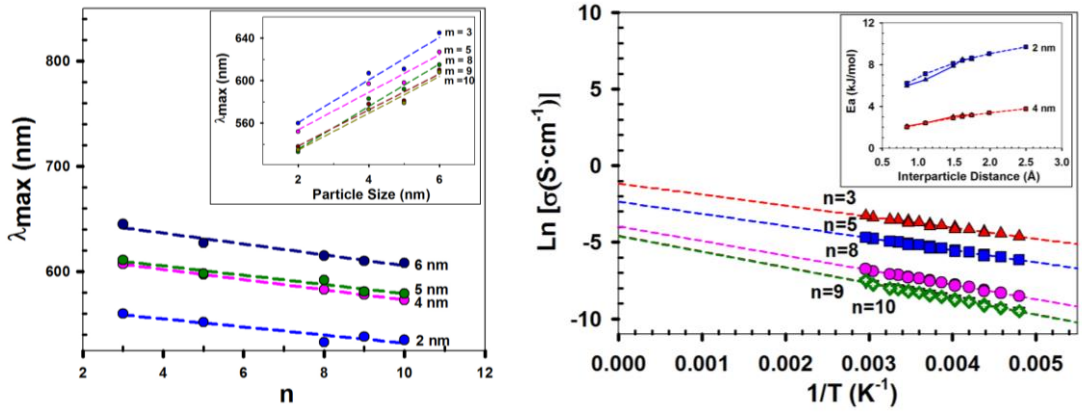

(A) (B)

Figure 1.3.2.2. (A) Surface plasmon resonance band wavelength l_{max} *vs*. interparticle chain length and particle size (2r, insert) for thin film assemblies of Au NPs mediated by ADTs of different chain lengths (HS-$(CH_2)_n$-SH). (B) Electrical conductivity *vs*. temperature and interparticle distance for thin film assemblies of 2-nm Au NPs mediated by ADTs of different chain lengths (HS-$(CH_2)_n$-SH). (Insert plots: activation energy *vs*. interparticle distance, and comparison of experimental (solid lines, triangle) and calculated results (dashed lines, square) for two different particle sizes). (Reproduced with permission from refs. 59, Copyright 2007 Royal Society of Chemistry, and from ref. 57, Copyright 2008 American Chemical Society.)

Figure 1.3.2.2B shows the experimentally determined conductivity and activation energy data for ADT-mediated thin film assemblies of AuNPs of two different sizes (2 and 4 nm) and different chain lengths (0.8 – 2 nm) on interdigitated microelectrodes (Figure 1.3.2.2B), revealing a linear dependence on interparticle distance and particle size.[59] On the basis of activated electron tunneling proposed first by Murray *et al.* in studying the electrical conductivity (σ) of monolayer-protected nanoparticles, the electrical conductivity depends on activation energy (E_A, kJ/mol), T (K), electron coupling term (β), interparticle distance (δ), and intrinsic conductivity of the nanoparticles (σ_0) as defined in Abeles's electrostatic model. The experimental data show very good agreement with the theoretical model in terms of activation energy increase with chain length and decrease

with particle size.[60] AuAg nanoparticle thin film assemblies also exhibit similar trends.[58] The detailed electron transport in the nanoparticle films depends on other factors, as evidenced by the observation of CO_2-plasticizing effect on the electrical conductivity.[60]

1.3.3 Computational modeling of NP assemblies

The application of noble metals in many areas of research have been exhaustively studied throughout the past few decades.[72-74] Many of which have been employed in biological sensors, but others have also been used as catalysts in different fuel cell devices.[74-76] Particularly, gold – and silver – based nanoparticles are commonly applied in areas of biological interest for different theranostic approaches, as previously mentioned;[72,73] however alloys of gold used in catalysts have showed promising results. For instance, Chang *et al.* demonstrated the enhancement in Pt-Au alloy nanowires over the NP counterparts in the reduction reaction of oxygen. They found that there was a synergy within the metals in the NW due to the absorption energies and decrease in atomic distance.[76] Other common noble metals, like Cu, Ni, and Fe, have been alloyed or composited with plasmonic metals to further enhance the manipulation and signal produced from these components.[77-79] Although the combination of these metals show great advancements in research, the application of these systems are limited in the design and plasmonic effect.

To further understand the role of the metals in these applications, researchers have explored the use of computational methods.[80-86] Such applications have involved different numerical approaches, like extended Mie theory, discrete dipole approximation (DDA, DDSCAT), and finite difference time domain (FDTD). All of these methods use different approaches to solve Maxwell equations and monitor the surface charges of the particles

used.[84-86] For instance, Punji *et al.* demonstrated the capabilities of numerical approaches to further substantiate the assembly of nanoparticles using the scattered intensity at a set gap distance based off a generalized Mie theory.[82] Similarly, Albella *et al.* discussed findings on the application of the numerical approach, discrete dipole approximation (DDA), to monitor the changes in the plasmonic bands of the Ag nanotip.[83] Although many of these approaches employ Mie theory to monitor the plasmonic changes, they account for the system as a whole and not as individual parts.[84-86] To accommodate for the generalized equations, a simulation toolbox was developed that discretizes the surface boundaries between different dielectric materials called boundary element method (BEM).[84-86] This method commonly used for metal NPs and focuses on the optical changes to simulate plasmonic and electromagnetic changes of metal nanomaterials (MNPBEM).[84,85,87] The implementation of this toolbox can provide an understanding of the simulated electromagnetic field enhancement observed experimentally.

1.4 Application of Bio-functional nanoprobes and assemblies

1.4.1 Colorimetric detection of amino acids and small peptides

Thiol-containing amino acids, such as cysteine (Cys) and homocysteine (Hcys), and small peptides, such as glutathione (GSH), are important biomolecules[9,24,50,54,61,62] because of their linkages to cardiovascular disease and other medical disorders. In the studies of Hcys- and Cys-mediated assembly of AuNPs,[53,54] the interparticle interaction is proposed to involve zwitterion-type electrostatic interaction of the amino acids attached via thiol group on the surface of AuNPs. The change of the SP band as a result of the interparticle interactions enables colorimetric or fluorimetric detection of the amino acids. For glutathione (GSH, a tripeptide and a reducing agent or antioxidant), the assembly of AuNPs

involves primarily hydrogen-bonding. In general, the interparticle zwitterion-type electrostatic and hydrogen-bonding interactions of these systems can be illustrated in Figure 1.4.1.1 (top panel). Cys is essential to the function of proteins and enzymes, in which the molecular chirality has important implications to medicine for specific targeting. Chiral recognition of cysteine driven by AuNPs is discovered, as shown in Figure 1.4.1.1 bottom panel.[62]

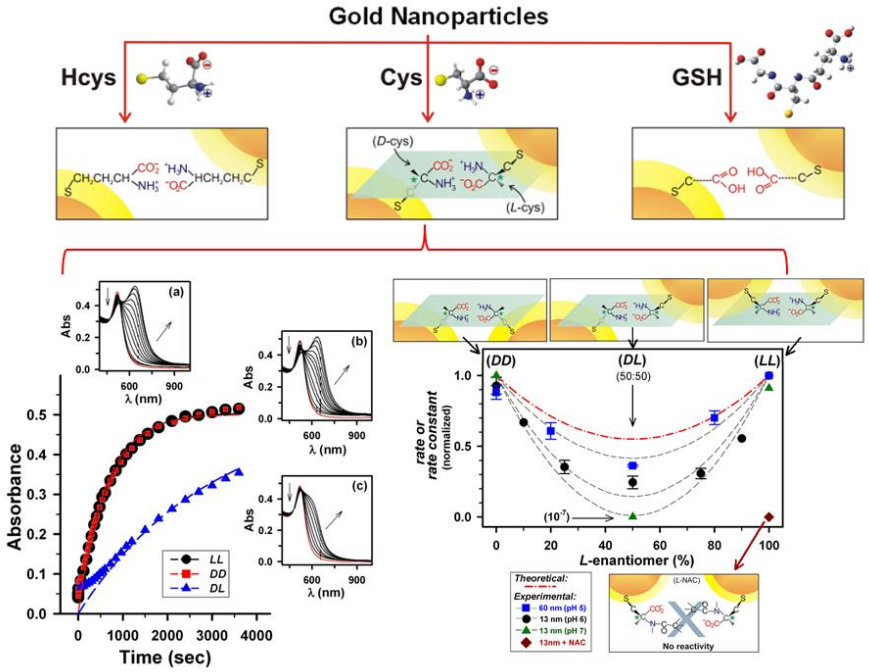

Figure 1.4.1.1. Top panel: Interparticle zwitterionic interaction, chiral recognition and hydrogen-bonding for the assembly of AuNPs by Hcys, Cys and GSH. Bottom panel: (Left): Kinetic plots of SP band absorbance (at 630 nm) for assemblies of Au_{13nm} in the presence of LL- (●), DD- (■), and DL- (▲) Cys. The dotted lines represent curve fitting by a 1st order reaction model. Insert: UV-Vis spectral evolution for the Au_{13nm} mediated assembly of LL- (a), DD- (b) and DL- (c) Cys. The arrows indicate the direction of the spectral evolution. (Right): Normalized rate or rate constant (k) vs. enantiomeric percentage of cysteines (%) in the presence of AuNPs of two different sizes Au_{60nm} (■) (pH = 5), Au_{13nm} (●) (pH = 6) and Au_{13nm} (▲) (pH = 7). Inactivity was also illustrated for mixing Au_{13nm} with NAC (♦). (Reproduced with permission from ref. 62, Copyright 2009 American Chemical Society.)

For the visualization of the nanoparticle-driven pair-wise zwitterionic interactions by enantiomeric cysteines adsorbed on AuNPs, imagine a hypothetical quasiplane for the interparticle zwitterion interaction of different chiralities (*L* and *D*) (see the structural

model), including homochiral (*LL* and *DD*) and heterochiral (*DL*) modes. There are differences between the homochiral and heterochiral interactions based on thermodynamic considerations and computational modeling results. The assembly of AuNPs by interparticle pair-wise zwitterionic interaction of the cysteines adsorbed on AuNPs can be monitored by the change of the surface plasmon (SP) resonance band of AuNPs. Upon introducing cysteines into a solution of AuNPs of 13 nm diameter (Au_{13nm}), and the SP band decreases in absorbance at 520 nm and increases in the ~630 nm region (Figure 1.4.1.1 bottom panel), displaying an isosbestic point at ~540 nm. The apparent rate constant (k) obtained by curve fitting of the SP band evolution using 1st-order kinetics (Figure 1.4.1.1 bottom panel) shows k values of ~1 order of magnitude greater for the *LL* and *DD* assemblies than that for the *DL* assembly (50% *L* and 50% *D*). By modeling the interparticle pair-wise dimerization using an idealized model, the heterochiral dimerization is found to be less favorable than the homochiral, which is indeed evidenced by the experimental data ($k_{(DL)} << k_{(LL)} \approx k_{(DD)}$), and a minimum reaction rate at an enantiomeric fraction(χ_L) of 50%. The correlation between the apparent rate (r) or k of the interparticle reactivity and the relative concentration of the enantiomer (*L*%) is shown in Figure 1.4.1.1 bottom panel for AuNPs of two different sizes, revealing a characteristic "valley" feature with the minimum appearing at 50%*L*:50%*D*. The important role of the pair-wise zwitterionic interaction in the interparticle chiral recognition and nanoparticle assembly is further supported by the inactivity for the assembly of AuNPs using *N*-acetyl-$_L$-cysteine (NAC) as a mediator.

The interparticle homochiral *vs*. heterochiral reactivities feature preferential interaction and differentiation of the enantiomeric structures, which have important

implications to the exploration of the nanoparticle-driven chiral recognition of cysteines in biomedical applications. One example involves early diagnosis and identification of elevated levels of cysteine to medical disorders (e.g., Parkinson's and Alzheimer's). Another potential application is the development of an effective route for controlling the enantiomeric specificity considering the fact that *L*-cysteine's deficiency is associated with a number of clinical situations (liver damage, skin lesions, AIDS, etc.), yet the role in the central nervous system is not well understood and *D*-cysteine interferes with many targets inside the cell. The exploration of the nanoparticle-driven chiral recognition differs from chiralities with single-crystal surfaces and chiral structures on metal NPs mainly in terms of the interparticle chiral reactivity.

1.4.2 Functional nanoprobes for cell transfection and bacteria inactivation

The explorations of functional nanoparticles for cell transfection and bacteria inactivation have attracted increasing interest in recent years due to their potential applications in drug delivery and drug discovery. One example involves miRNA-conjugated AuNPs for cell transfection, which has potential application in delivering miRNA into cells for genetic manipulation and cancer treatments, such as the resistance of multiple myeloma (MM) to glucocorticoid treatment. The use of AuNPs for the delivery of siRNA (small interfering RNA) into cells for efficient knockdown of target genes without significant cytotoxicity exploits the unique optical properties, low cytotoxicity, and enhanced lifespan in the blood stream.[63] The manipulation of genetic expression has been demonstrated recently for miR-130b which express differently in glucocorticoid-sensitive versus glucocorticoid-resistant MM.1 cell lines. Figure 1.4.2.1A shows a scheme for using miR-130b conjugated AuNPs in cell transfection. Its over-expression in the MM.1S cell

line decreases the expression of a glucocorticoid receptor protein (GR-a), inhibiting glucocorticoid-induced apoptosis of cells.

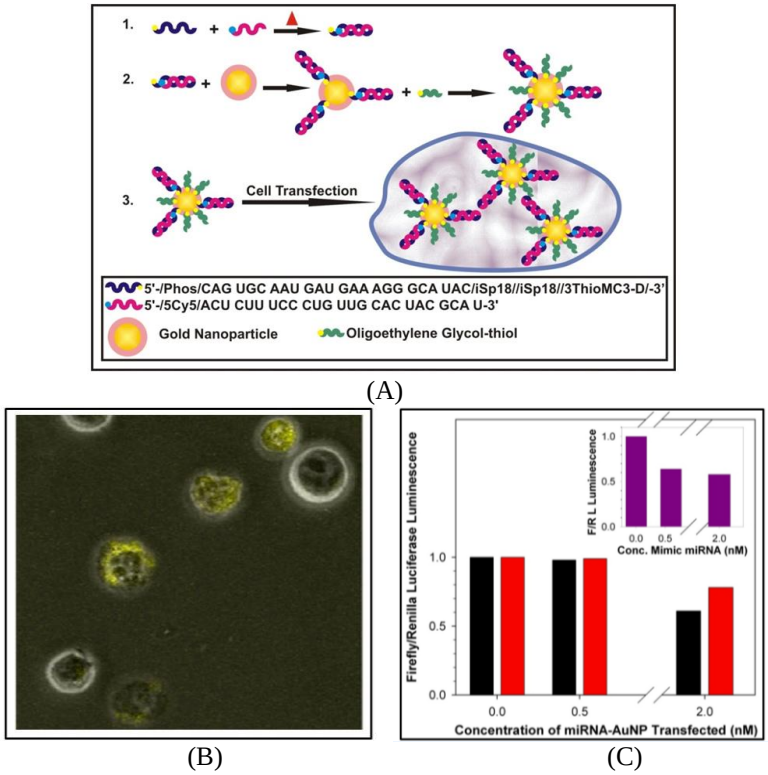

Figure 1.4.2.1. (A) Preparation of miRNA-AuNP conjugates for delivering miRNAs to cells (miRNA is labeled with fluorescent dyes (e.g., Cy5)). The sense and antisense miRNA were combined first to form miRNA duplexes which are then immobilized onto AuNP via thiol group, followed by refilling with oligoethyleneglycol thiol (OEG) to keep the miRNAs from folding and electrostatically binding. (B) Confocal/fluorescent microscopic image: MM.1S cells 48 hours after transfection was initiated with Cy5-labeled miRNA-AuNPs. (C) Plot showing the result of the functional luciferase assays for Cy5 (black bars) and Cy3 (red bars) labeled miRNA-AuNPs, and a mimic system (insert chart). (Reproduced with permission from ref. 53, Copyright 2012 American Chemical Society.)

For demonstrating miRNA-conjugated AuNPs in cell transfection, a multiple myeloma cell line (MM.1S) is used. Figure 1.4.2.1B shows the uptake of the conjugated nanoparticles Cy5-miRNA-AuNPs in the MM.1S cells, as evidenced by the clear contrast in fluorescence from the dye-labeled miRNA-AuNPs. The ability for the conjugated nanoparticles to reduce luciferase expression is further evidenced by functional luciferase assays (Figure 1.4.2.1C). Upon increasing concentration (to 2nM) of Cy5-miRNA-AuNPs, an observable reduction in gene expression is observed. Considering ~15 miRNA per

AuNP in the miRNA-AuNP solution for the luciferase knockdown and comparing the knockdown efficiencies between siRNA-AuNPs (~20% at 48 hours, ~33 siRNAs per particle [52]) and miRNA-AuNPs (~40% at 48 hours), the miRNA-AuNPs are found to be more efficient at a much lower concentration[52] for the transfection of the miRNA-AuNPs in multiple myeloma cells.

Another area of interest involves the development of functional antibacterial agents in biological fluids, which stems from the need to store platelets at room temperature where pathogen contamination can occur and pose a risk of infection associated with transfusion. It would be desirable to introduce antibacterial particles in the platelets for inactivating bacteria which can be subsequently separated out prior to transfusion. For AgNPs, the added value of incorporating magnetic function is the ability of efficient bacterial disinfection with reduced presence of Ag ions in the fluid. One intriguing approach involves the introduction of the magnetic cores (M) into the AgNPs to enable effective separation, delivery and targeting. This approach is illustrated in Figure 1.4.2.2A for developing M@Ag NPs for bacterial inactivation in blood platelets. The reduction in bacterial growth of several types of Gram-positive bacteria (e.g., *Staphylococcus aureus* and *Bacillus cereus)* and Gram-negative bacteria (e.g., *Pseudomonas aeruginosa*, *Enterobacter cloacae*, and *Escherichia coli*) has been examined to assess bacterial inactivation efficiency of the functional MZF@Ag NPs. For the growth of Gram-positive *Bacillus cereus* in saline solutions containing antimicrobial NPs over a 24-hour period and the bacterial concentration exhibits a clear reduction as a function (Figure 1.4.2.2B (Left)). For Gram-negative *Enterobacter cloacae*, an increased speed of inactivation is observed (Figure 1.4.2.2B (Middle)).

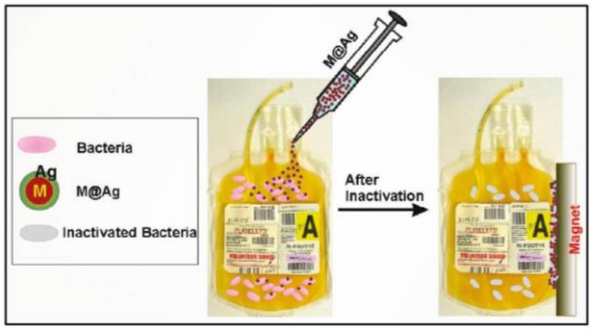

(A)

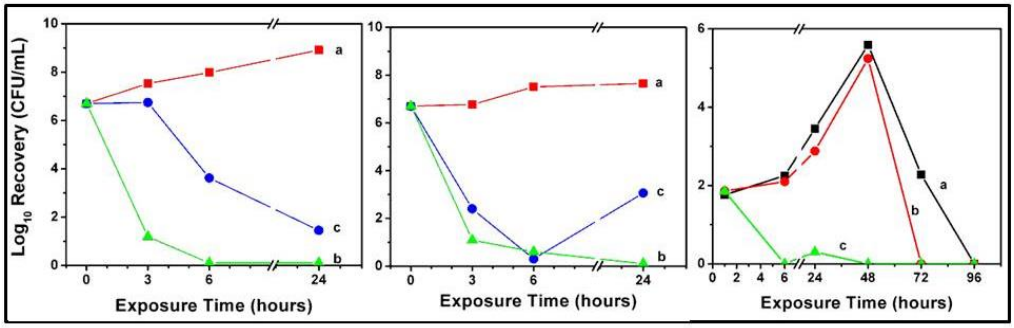

(B)

Figure 1.4.2.2. (A) Schematic illustration of magnetic core@shell nanoparticles (M@Ag) as a functional antimicrobial agent in blood platelets and the magnetic separation. (B) Experimental data for the inactivation of *Bacillus cereus* (Left) and *Enterobacter cloacae* (Middle) in a PBS buffer (a), in a solution of MZF@Ag NPs (b), and in a solution of AgNPs (c); and E. coli (Right) in water (a), MZF NPs (b), and MZF@AgNPs (c) in blood platelets. (Reproduced with permission from ref. 9, Copyright 2011 American Chemical Society.)

For blood platelet samples containing *E. coli*, the inactivation by MZF@AgNPs is also effective, as demonstrated by the drop of bacterial concentration below a detectable level after only 6 hours of exposure (Figure 1.4.2.2B (Right)). The inactivation is mainly caused by the direct contact of Ag on NPs rather than Ag ions leached into the solution. Considering the low level of the amount of silver found in the platelets, the use of MZF@Ag NPs as a functional antibacterial agent is potentially much safer when giving a transfusion after the removal of the magnetic core-shell nanoparticles. In light of the increasing use of AgNPs as antimicrobial agent in commercial products in terms of the nanotoxicity,[64] the magnetically-functional nanoparticles could offer the ability to reduce

the unwanted toxicity, which is clearly desired from the patient or the environment perspectives.

While the unique properties of metal nanomaterials enable new opportunities in theranostics, some of the nanoparticles may have unpredictable toxic potential upon being released into the environment during use or disposal, either unintentionally (such as during wear and tear), or intentionally (such as nanomedicine). There is a need to evaluate the potential toxic effects of nanoparticles. While gold-based nanoparticles have shown the least nanotoxicity towards different biological systems in comparison with various nanoparticles, there are increasing studies to understand the nanotoxicity. For example, exposure to Co and Ni NPs is shown to cause lung inflammation in rats, and oxidative stress and increased matrix metalloproteinase-2 and -9 expression and activity for human monocytes.[65] Several studies also demonstrated that exposure to some metal nanoparticles may cause genotoxic effects. For example, exposure of A549 cells to Co NPs has been shown to cause DNA damage, whereas their exposure to TiO_2 NPs does not cause DNA damage.[66] Exposure to CoNPs is shown to cause an increase in Gadd45α expression in cells which could invoke various cellular responses such as cell cycle arrest, apoptosis, and importantly, DNA repair. Understanding the potential toxic and genotoxic effects of nanoparticles is important for the development of safe nanomaterials for the various applications.

1.4.3 SERS detection of proteins and DNA via assembly, disassembly, or separation

Gold (or silver) nanoparticles and magnetically functional Au or Ag NPs have been demonstrated the viability for SERS detection of the bio-reactivity of proteins and DNA with magnetic separation capability.[23,24] The exploitation of the specific and selective

binding activity between antibodies and antigens on NPs serves as important means of sandwich-type immunoassay. SERS readout of the assay has the capability of multiplexity.[12] This type of protein recognition was recently expanded to the interparticle assembly between reporter-labeled AuNPs and magnetic core (M)@AuNPs for achieving both magnetic bio-separation and SERS-based bio-detection (Figure 1.4.3.1).[23,24] Attributes such as magnetic separation capability, enhanced stabilization of the magnetic particles, fine-tunable surface to impart biocompatibility have been demonstrated by a number of examples involving the immobilization of recognition sites on Au or M@Au NPs and spectroscopic labels for detection.[23,24] The plasmonic coupling of the localized fields between nanoparticles and substrates produces an enhanced SERS effect,[12,13] as evidenced by the size correlation of the surface plasmon resonance properties for AuNPs.[23] In particular, dimer/trimers of the NPs in the solution via interparticle interactions produce "hot-spots"[13] for the SERS effect,[15,25] which is illustrated in Figure 1.4.3.1 insert for developing SERS and magnetic nanoprobes for bio-separation and detection.

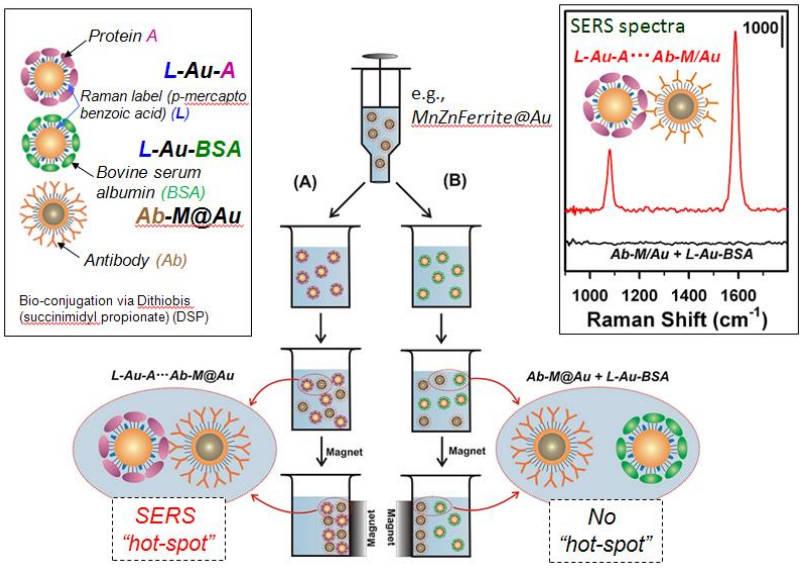

Figure 1.4.3.1. Illustration of the use of surface functionalized Au and magnetic core (M)/shell (Au) nanoparticles in bio-separation and detection to study the reactivity between protein A-labeled Au nanoparticles: L-Au-A and antibody-labeled M/Au nanoparticles: Ab-M/Au. Insert (right): SERS spectra showing the assembly of Au (80 nm) nanoparticles labeled with Protein A or BSA and MBA and M@Au NPs (~8 nm) labeled with antibody (IgG). (Reproduced with permission from ref. 23. Copyright 2008 IOP.)

As a proof-of-concept demonstration of SERS detection of the protein A-antibody binding activity, Raman label (*L* =MBA), Protein A (*A*) and antibody (*Ab*) are conjugated onto Au and M@Au (or Ag) nanoparticle surfaces.[23,24] Upon applying a magnetic field to the solution containing the reaction product between Protein A capped AuNPs with a Raman label (*L-Au-A*) and the antibody-capped M@Au NPs (*Ab-M@Au*), samples are collected and then analyzed. The reactivity with bovine serum albumin (BSA) serves as a control experiment. Diagnostic signals of the MBA are clearly detected for the separated product ((*L-Au-A*)-(*Ab-M@Au*) pair) in the SERS spectra. In contrast, there are no signals for the (*L-Au-BSA*)+(*Ab-M@Au*) combination in the control experiment using BSA. This proof-of-contrast experiment demonstrates the viability of magnetic nanoprobes for SERS bioassays, which has been supported by a number of examples.[9,23,24,54,61,62]

The creation of the SERS "hot-spot" is an important element of the nanoparticle-based strategy for the detection of DNA bioactivities (Figure 1.4.3.2).[17,20] The use of magnetic nanoparticles with gold or silver shells with a Raman label (RL) has important advantages in overcoming many of the challenging problems in bio-probing. This strategy has in fact attracted both fundamental and practical interests because of potential applications in areas such as ferrofluids, medical imaging, drug targeting and delivery, cancer therapy, separations and catalysis. A key advantage is the ability of exploiting the rich and controllable surface chemistry and spectroscopic properties of gold or silver while maintaining the magnetic properties of the cores for the desired bio-separation capabilities.

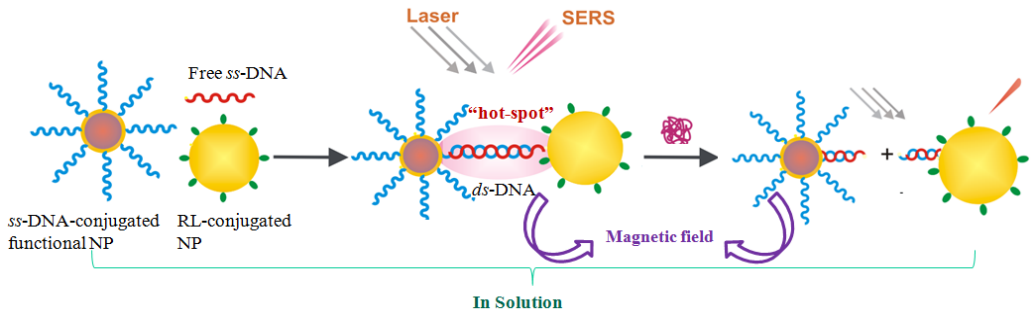

Figure 1.4.3.2. Illustration of formation of "hot-spot" upon ds-DNA assembly of *ss*-DNA/M@Au NP with RL-AuNP via molecular recognition with free complementary *ss*-DNA in the solution, and dismantling of "hot-spots" following the enzymatic cutting of the *ds*-DNA using restriction enzyme and magnetic separation characteristic.

As an expansion to the demonstration of using highly monodispersed gold NPs as SERS-active nanoprobes,[15,24] and M@Au NPs on Au substrates for sandwich-type immunoassay detection,[8,23,24] the small clusters of DNA-linked gold NPs and M@Au or Ag NPs were recently shown to be stable enough in solutions to allow SERS detection of DNA in terms of assembly and enzymatic cutting.[17,20] The later efforts, built upon our abilities to enable the nanoparticles magnetically functional and/or SERS-active,[9,49] now show promises in terms of proof-of-concept demonstration for the feasibility of the DNA detection, an area related to *p53* mutation for cancer diagnostics,[17] and miRNA detection related to cell transfection in cancer therapeutics.[9] Consider first the use of AuNPs of different sizes as nanoprobes for DNA assembly and its enzymatic cutting in an aqueous solution using two different DNA strands with a thiol modification (bottom-DNA and top-DNA, designed using the cyclin G promoter sequence for p53 recognition)[17], the complementary binding of which forms a double strand (*ds*-DNA). In one solution, AuNPs are conjugated with one of the single-stranded (*ss*), e.g., *ss*-bottom-DNA. In another solution, AuNPs are labeled with Raman reporter molecule (e.g., MBA). As shown in (Figure 1.4.3.3), by mixing the two solutions in the presence of free top DNA strand,

MBA's diagnostic bands can be detected as a result of the formation of *ds*-DNA-AuNP assemblies with an interparticle "hot-spot".

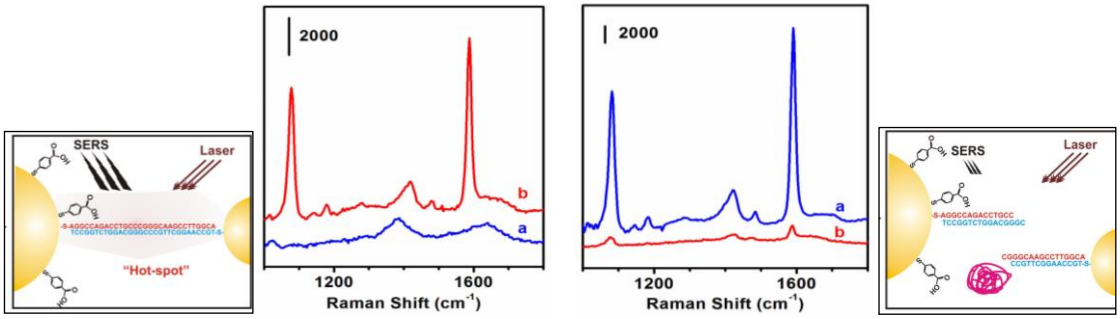

(A) (B)

Figure 1.4.3.3. Au NP-based SERS detection using a 30 bp DNA sequence where "hot-spots" form upon assembly of *ss*-DNA/AuNP with MBA/AuNP in an aqueous solution (A) ((a) bottom-DNA/AuNP mixed with MBA/AuNP; (b) bottom-DNA/AuNP and MBA/AuNP after addition of top-DNA), and *MspI* cutting of the ds-DNA/AuNPs (B) ((a) the ds-DNA/AuNPs; (b) after *MspI* addition. (Reproduced with permission from ref. 17. Copyright 2013 Royal Society of Chemistry.)

Figure 1.4.3.3A shows an example where controlled mixing of solutions of 13-nm bottom-DNA/AuNP and 39-nm MBA/AuNP in the presence of top-DNA, a gradual increase of the diagnostic Raman bands of the MBA label is observed at 1078 and 1594 cm^{-1}, corresponding to MBA's *v*(CC) ring-breathing modes. Figure 1.4.3.3B shows another example where a restriction enzyme (e.g. *MspI*) is introduced into the solution of *ds*-DNA/AuNPs assembly, which is known to cut *ss*-DNA at CCGG site. A clear decrease of the SERS intensities of the diagnostic peaks at 1078 and 1594 cm^{-1} is revealed, due to the removal of the interparticle "hot-spot" by restriction enzyme cleavage of the *ds*-DNA, demonstrating the important role of the interparticle "hot-spot" in the SERS detection.

This strategy is expanded to use gold (or silver)-decorated magnetic nanoparticles as nanoprobes for demonstrating DNA assembly and enzymatic cutting in solutions. Gold- and silver-decorated magnetic MnZn ferrite nanoparticles (MZF@Au or MZF@Ag) have been studied for demonstrating the viability.[20] The distributions of the expected

components in MZF@Au, Fe, Mn, Zn, and Au, can be identified in HRTEM and EDS. During the formation of *ds*-DNA linkage or breakage between AuNPs and MZF@Au (or MZF@Ag) NPs, interparticle "hot-spots" are formed for real-time SERS monitoring of the assembly and enzymatic disassembly processes whereas the magnetic components provide an effective means for intervention in the solution (Figure 1.4.3.4A).

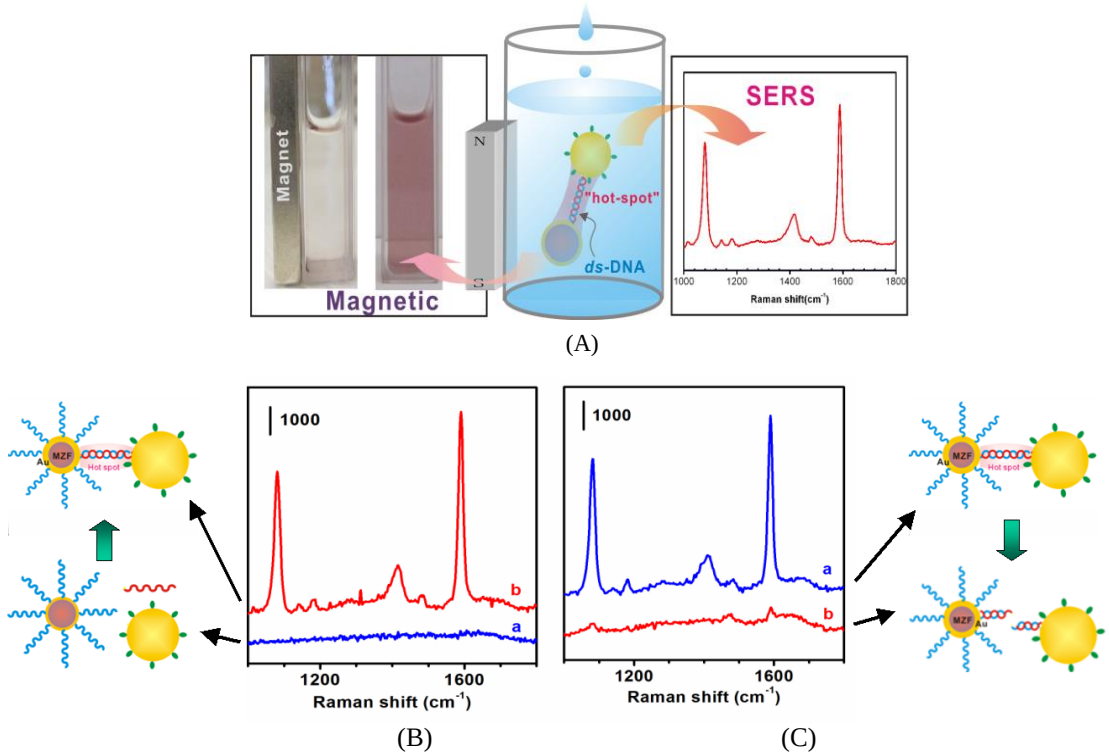

Figure 1.4.3.4. (A) Magnetic NPs coupled with Au NPs for SERS detection. (B) Example using a 30 bp DNA sequence where "hot-spots" form upon the assembly of ss-DNA/ MZF@Au with MBA/AuNP in an aqueous solution ((a) the mixture of MBA-Au and MZF/Au-DNA1, and (b) mixture of MZF/Au-DNA1 and MBA-Au in the presence of DNA2). (C) *MspI* cutting MBA-Au-*ds*-DNA-MZF/Au ((a) the MBA-Au-*ds*-DNA-MZF/Au solution; (b) after MspI addition). (Reproduced with permission from ref. 20. Copyright 2013 Royal Society of Chemistry.)

In the case of MZF/Au NPs (11 nm) and MBA-Au NPs (39 nm) forming interparticle *ds*-DNA of DNA1 and DNA2, two clear SERS peaks are observed at 1078 and 1592 cm^{-1} (Figure 1.4.3.4B), indicative of the interparticle "hot-spot" formation due to assembly of MBA-Au-DNA1/DNA2-MZF/Au, forming dimers or trimers in the solution. Upon addition of *MspI* into this solution, there is a clear reduction of the two diagnostic peaks

(Figure 1.4.3.4C). After the enzymatic cutting, the MZF/Au NPs could be separated from the solution by applying a magnetic field. Similarly, the MZF/Ag NPs were also demonstrated to be viable for SERS detection of the DNA activities and the magnetic intervention after the enzyme cutting process.[20]

In many of the examples such as thiol-containing amino acids, peptides, miRNA and bacteria, the SERS strategy could also be useful for their detection. For example, polymer-mediated assembly of AuNPs have been used for SERS detection of bacteria biomarker such as dipicolinic acid (DPA) and calcium dipicolinate (Ca-DPA),[67,68] which has application for developing rapid and accurate detection of bacteria in foods or biological fluids. In contrast to AgNPs traditionally used as SERS substrates for biomarker detection (e.g., *Bacillus subtilis*), the strong SERS effect produced by the particle-particle and particle-substrate plasmonic coupling of AuNPs was demonstrated to exhibit high sensitivity and low detection limit for SERS detection of biomarkers released from bacterial spores.[67,68]

1.4.4 Chemiresistive detection of biomarkers from human breath

Molecularly-mediated thin film assembly of AuNPs has been demonstrated as sensing materials for chemiresistive detection of breath biomarkers linked to diabetes.[29] The thin films can be prepared by a combination of mediator and template forces in one-step assembly process. This assembly technique builds upon the place-exchange reactivity[39] and expands the layer-by-layer technique.[36] The initial ligand exchange reaction is followed by interparticle linkages. Examples include thiolate-Au bonding on AuNPs, hydrogen-bonding of carboxylic acid terminal groups on AuNPs, and selective carboxylate-Ag bonding on AuAg NPs. For the linker molecules, functionalized molecules

are used, including alkyl dithiols (ADT, HS-$(CH_2)_n$-SH), carboxylic acid-functionalized thiols (HO_2C-$(CH_2)_n$-SH), and dicarboxylate acids (DCA, HO_2C-$(CH_2)_n$-CO_2H).[58,59,69] For example, 1,9-nonanedithiol (NDT)-linked thin film assembly of AuNPs involves Au-thiolate bonding at both ends of NDT.[57] These parameters determine the activation energy in a thermally-activated conduction path, and thus have an important impact to the electrical signal amplification. The array can be coupled to pattern recognition techniques to enhance selectivity.[69] The design of chemiresistive sensing arrays using the nanoparticle-structured thin films exploits the correlation between the electrical conductivity and the nanostructural parameters such as particle size, interparticle distance, and interparticle dielectric medium properties which determine the activation energy in a thermally-activated conduction path,[70] and the electrical signal amplification. For example, the correlation between the chemiresistive responses to the sorption of volatile organic compounds (VOCs) and the interparticle spatial properties[69] is established for the use of molecularly-mediated thin film assemblies of Au and AuAg nanoparticles with ADT and DCA of different chain lengths[58] as sensing array elements. Similar to the correlation of interparticle distances with the collective electrical or optical properties,[57,59,69] the balance of the interparticle chain-chain cohesive interdigitation and the nanostructure-vapor interaction is an important factor for the correlation between the sensor array's sensitivity or selectivity and the interparticle spatial properties. The interparticle spatial properties play a dominant role in the sensor response characteristics.

This work is recently expanded to flexible chemical/bio sensors for scalable thin-film assembly and printing on flexible substrates that allow exploring the unique electrical/optical properties under various device strains for detection of chemical,

biological or biomarker molecules (Figure 1.4.4.1A).[70,71] One important aspect of the flexible chemical and gauge sensors explores the unique correlation between chemical sensing and device strain characteristics under different vapor/gas atmospheres. A major finding is that an increase in resistance is observed in tensile strain (*ts*), and a decrease in the compressive strain (*cs*), displaying ΔR in the order of (hexane) > (nitrogen) ≈ (acetone) >(ethanol) (Figure 1.4.4.1B). The increase of the interparticle distance is responsible for the increase of resistance in the case of tensile strain, whereas the decrease of the interparticle distance leads to a decrease of resistance in the case of compressive strain. The overall changes reflect a combination of the interparticle spatial and dielectric properties as a result of vapor sorption in the thin film, which follow the theoretical prediction for some cases. This study demonstrated the ability to tune the interparticle interactions via capping or linking molecules that can work cooperatively with the device strains and chemical environment over the device, an important feature for multifunctional devices.

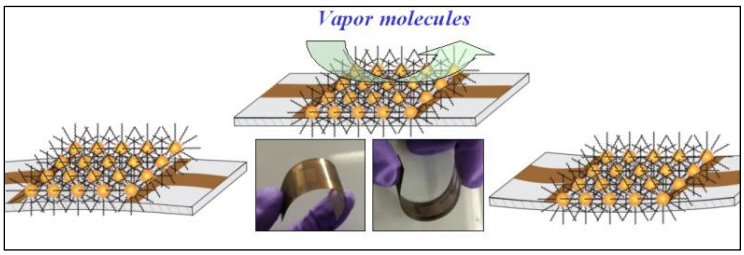

(A)

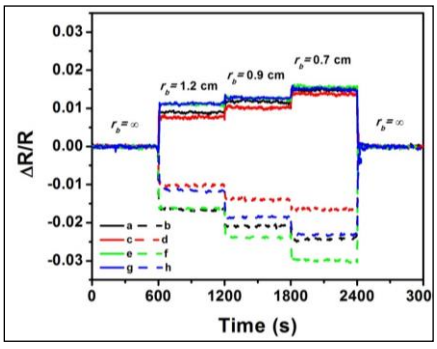

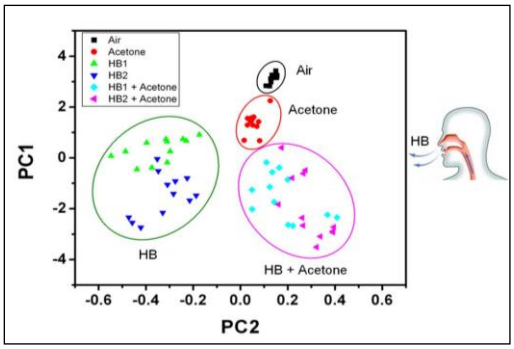

(B) (C)

Figure 1.4.4.1. (A) Illustration of thin film of nanoparticles assembled or printed on a flexible chemiresistor device for detection of vapor molecules (VOCs, biomarkers, etc.). (B) Response profiles of relative change in resistance ($\Delta R/R=\Delta R/R_{FL}$) for a flexible device with an NDT–Au_{2nm} film in response to horizontal bending under nitrogen (a-b), ethanol (c-d), hexane (e-f), and acetone (g-h). Strains: solid lines (tensile, *ts*), dashed lines (compressive, *cs*). (C) PCA score plots in the PC1-PC2 plane (PC1: 96.8%; PC2: 2.9%.) for a chemiresistor array of thin film assemblies of Au NPs in response to several vapor samples: air (blank), acetone (210 ppm(M) in air), human breath (HB), and HB spiked with acetone. (Reproduced with permission from ref. 71. Copyright 2014 Royal Society of Chemistry, and from ref. 29, Copyright 2012 Elsevier Publishing).

To explore the sensor arrays with assembled or printed nanoparticle thin films for chemical sensing of biomarkers in human breath linked to diabetes or lung cancers, a preliminary proof-of-concept experiment (Figure 1.4.4.1C) has demonstrated the viability. In addition to showing the viability for quantitative detection of acetone, the results from the array's response data to different samples of human breaths (HB1 and HB2) along with the various control experiments have demonstrated that the sensor arrays with nanostructured sensing films are viable for the detection of acetone, which is a volatile biomarker in diabetics' breath. The initial results have demonstrated the potential of the sensor arrays coupled with pattern recognition for the detection of acetone. Further optimization of the performance parameters could lead to portable and noninvasive monitoring of diabetes.[68,69,27] As shown by the PC1-PC2 plots in Figure 1.4.4.1C, air, acetone, human breath, and acetone-spiked human breath samples are clearly separated, demonstrating the feasibility of distinguishing human breath (with or without spiked acetone) from air (with or without acetone), as well as the potential of the sensor arrays coupled with pattern recognition for the detection of acetone in diabetic breath.

In these illustrated examples, the ligand-framework nanostructures are exploited in terms of electrical and mass transfer properties. For many other nanoparticle assemblies that are structurally defined for harnessing the collective nanoscale electrical, optical,

magnetic and spectroscopic properties, the basic principles are expected to operate similarly. A wide range of technological applications should benefit from further detailed delineation of the interparticle parameters in terms of size, shape, composition and surface properties to optimize the multifunctional optical, magnetic and spectroscopic properties of the molecularly-mediated thin film assembly of nanoparticles.

1.5 Current Status and Objectives of Thesis Work

The development of biosensors for detecting and targeting molecules in various bioassays has made significant advances. However, a major challenge of the design of these sensors is the limited understanding of the interparticle spatial characteristics of the NPs that dictate the formation of the hotspot and the related spectroscopic intensity. This understanding is important for using NPs as probes in detecting different molecules in solution, especially when the concentrations are very low. The overall goal of this thesis work is to understand the interparticle plasmonic coupling induced SERS and LSPR characteristics by experimental measurements and theoretical simulations for establishing the correlation between the interparticle structures and the spectroscopic properties. To this end, well-established molecular/biomolecular interactions were explored as model systems for the control of the interparticle spatial properties. This control will allow tunability of the nanoprobes for achieving sensitive and selective detection of various molecular and biomolecular activities. The specific objectives of the thesis work are outlined below.

1.5.1 To explore Interparticle π–π^* stacking of dye molecules adsorbed on nanoparticles

The aggregation of dye molecules through π–π* stacking serves as a well-defined molecular glue of nanoparticles. Such molecules display characteristic optical adsorption and Raman-active scattering bands for the spectroscopic detection. In Chapter 3, results will be shown for the characterization of the π–π* stacking of cyanine dye molecules immobilized on the surface of AuNPs, as a model system. This type of dye-induced aggregation of the NPs enables the control of the molecular distance between the NPs. The interparticle spatial characteristics upon the π–π* stacking of dye molecules will be discussed, which has provided new insights into the control of interparticle plasmonic coupling for understanding SERS and LSPR.

1.5.2 To investigate the interparticle spatial properties in nanoparticle-based immunoassays

Antigen-antibody recognition is a well-established key-lock mechanism, where every antigen has a lock that only a few antibodies have the key to open. This mechanism has been continually used in the identification of many diseases and protein biomarkers that signify the development of diseases. The ability to identify biomarkers early enough is essential for performing effective treatments. There is a clear need for the establishment of methods in the rapid and early detection of diseases, with high sensitivity, high specificity, and low detection limit. In Chapter 4, results will be shown for the SERS characterization of the interparticle interactions using antibody (goat anti-rabbit IgG) - protein A as a model system. In doing so, we focus on understanding how the interparticle distance of the biomolecule system in solution correlates with SERS intensity under different concentrations of target and capture molecules.

1.5.3 To investigate the interparticle interactions of duplex DNA-mediated assembly of gold nanoparticles for SERS detection of DNA in solution

Duplex DNA-mediated assembly of gold nanoparticles is another well-established biomolecular recognition system involving complementary binding of nucleic acids, which is important for the early detection of diseases. While NP assemblies mediated by DNA or RNA via complementary binding have been extensively studied, the correlation of SERS and LSPR properties with the interparticle spatial properties of the NPs in solutions remain elusive. This is largely due to their differences from those under dry conditions where the distance between the NPs are decreased by the desolvation of the NP and strands of DNA, thus proving a clear need to study the duplex defined interparticle distance for NPs in solution. In Chapter 5, results will be discussed for the investigation of the duplex-DNA mediated NP assembly in terms of the interparticle spatial properties and the SERS/LSPR properties. The results from both experimental measurement and computational modeling have provided new insights into the design and optimization of the functional nanoprobes for the SERS detection.

1.5.4 To understand the interparticle spatial properties of duplex DNA-mediated assembly of plasmonic nanoparticles in the presence of magnetic cores.

Plasmonic-magnetic NPs provide an intriguing nanoprobe system for SERS detection. The introduction of magnetic components into the plasmonic NPs allows for the manipulation of the location and concentration through an external magnetic field for different enhancement capabilities. While there are increasing studies of the utilization of magnetic component in a NP composite to increase the plasmonic coupling, how the magnetic component influences the interparticle interactions is not well understood,

especially in terms of the optical and electrical properties. In Chapter 6, results from our experimental and theoretical studies of magnetic core – gold or silver shell NPs will be discussed. The findings provide new insights into the design of better SERS nanoprobes for the sensitive detection of DNA and other biomolecules in solutions.

References

1. Gilmartin N.; O'Kennedy R. "Nanobiotechnologies for the detection and reduction of pathogens." Enzyme and Microbial Technology, 2012, 2(50), 87-95
2. Theron, J.; Cloete, T.; Kwaadsteniet M. "Current molecular and emerging nanobiotechnology approaches for the detection of microbial pathogens." Critical Reviews in Microbiology, 2010, 36(4), 318–339
3. Lim, I-I. S.; Njoki, P. N.; Park, H. Y.; Wang, X.; Wang, L.; Mott, D.; Zhong, C. J. Gold and Magnetic Oxide/Gold Core/Shell Nanoparticles as Bio-Functional Nanoprobes *Nanotechnology* **2008**, *19*, 305102.
4. Agasti, S. S.; Rana, S.; Park, M. H.; Kim, C. K.; You, C. C.; Rotello, V. M. Nanoparticles for Detection and Diagnosis. *Adv. Drug Delivery Rev.* **2010**, *62*, 316-328.
5. Zhang, X. Q.; Xu, X. Y.; Lam, R.; Giljohann, D.; Ho, D.; Mirkin, C. A. Strategy for Increasing Drug Solubility and Efficacy through Covalent Attachment to Polyvalent DNA-Nanoparticle Conjugates. *ACS Nano* **2011**, *5*, 6962-9670.
6. Hnilova, M.; Khatayevich, D.; Carlson, A.; Oren, E. E.; Gresswell, C.; Zheng, S.; Ohuchi, F.; Sarikaya, M.; Tamerler, C. Single-Step Fabrication of Patterned Gold Film Array by an Engineered Multi-Functional Peptide. *J. Colloid Interface Sci.* **2012**, *365*, 97-102.
7. Koch, M.; Kiefer, S.; Cavelius, C.; Kraegeloh, A. Use of a Silver Ion Selective Electrode to Assess Mechanisms Responsible for Biological Effects of Silver Nanoparticles. *J. Nanopart. Res.* **2012**, *14*, 646-657.
8. Lim, I-I. S.; Zhong, C. J. Molecularly-Mediated Processing and Assembly of Nanoparticles: Exploring the Interparticle Interactions and Structures. *Acc. Chem. Res.* **2009**, *42*, 798-808.
9. Wang, L. Y.; Luo, J.; Shan, S. Y.; Crew, E.; Yin, J.; Wallek, B.; Wong, S.; Zhong, C .J. Bacterial Inactivation using Silver-coated Magnetic Nanoparticles as Functional Antimicrobial Agents. *Anal. Chem.* **2011**, *83*, 8688-8695.
10. Wang, Y. Q.; Yan, B.; Chen, L. X. SERS Tags: Novel Optical Nanoprobes for Bioanalysis. *Chem. Rev*. **2013**, *113*, 1391-1428.
11. Kneipp, J.; Kneipp, H.; Rice, W. L.; Kneipp, K. Optical Probes for Biological Applications Based on Surface-Enhanced Raman Scattering from Indocyanine Green on Gold Nanoparticles. *Anal. Chem.* **2005**, *77*, 2381-2385.
12. Driskell, J. D.; Lipert, R. J.; Porter, M. D. Labeled Gold Nanoparticles Immobilized at Smooth Metallic Substrates: Systematic Investigation of Surface Plasmon Resonance and Surface-Enhanced Raman Scattering. *J. Phys. Chem. B* **2006**, *110*, 17444-17451.
13. Hao, E.; Schatz, G. C. Electromagnetic Fields Around Silver Nanoparticles and Dimers. *J. Chem. Phys.* **2004**, *120*, 357-366.
14. Barhoumi, A.; Zhang, D.; Tam, F.; Halas, N. J. Surface-Enhanced Raman Spectroscopy of DNA. *J. Am. Chem. Soc.* **2008**, *130*, 5523-5529.
15. Njoki, P. N.; Luo, J.; Kamundi, M. M.; Lim, I-I. S.; Zhong, C. J. Aggregative Growth in Size-Controlled Growth of Monodispersed Gold Nanoparticles. *Langmuir* **2010**, *26*, 13622-13629.
16. Stoeva, S. I.; Huo, F.; Lee, J. S.; Mirkin, C. A. Three-Layer Composite Magnetic Nanoparticle Probes for DNA. *J. Am. Chem. Soc.* **2005**, *127*, 15362-15363.
17. Crew, E.; Yan, H.; Lin, L. Q.; Skeete, Z.; Kotlyar, T.; Tchah, N.; Lee, J.; Bellavia, M.; Goodshaw, I.; Joseph, P.; Luo, J.; Gal, S.; Zhong, C. J. DNA Assembly and Enzymatic Cutting in Solutions: a Gold Nanoparticle Based SERS Detection Strategy. *Analyst* **2013**, *138*, 4941-4949.
18. Bonham, A. J.; Braun, G.; Pavel, I.; Moskovits, M.; Reich, N. O. Detection of Sequence-Specific Protein-

DNA Interactions via Surface Enhanced Resonance Raman Scattering. *J. Am. Chem. Soc*. **2007**, *129*, 14572-14573.

19. Sun, L.; Yu, C.; Irudayaraj, J. Surface-Enhanced Raman Scattering Based Nonfluorescent Probe for Multiplex DNA Detection. *Anal. Chem*. **2007**, *79*, 3981-3988.
20. Lin, L. Q.; Crew, E.; Yan, H.; Shan, S.; Skeete, Z.; Mott, D.; Krentsel, T.; Yin, J.; Chernova, N. A.; Luo, J.; Engelhard, M. H.; Wang, C.; Li, Q. B.; Zhong, C. J. Bifunctional Nanoparticles for SERS Monitoring and Magnetic Intervention of Assembly and Enzyme Cutting of DNAs. *J. Mater. Chem. B* **2013**, *1*, 4320-4330.
21. Lim, D. K.; Jeon, K. S.; Hwang, J. H.; Kim, H.; Kwon, S;. Suh, Y. D.; Nam, J. M. Highly Uniform and Reproducible Surface-Enhanced Raman Scattering from DNA-tailorable Nanoparticles with 1-nm Interior Gap. *Nat. Nanotechnol.* **2011,** *6*, 452-460.
22. Doering, W. E.; Piotti, M. E.; Natan, M. J.; Freeman, R. G. SERS as a Foundation for Nanoscale, Optically Detected Biological Labels. *Adv. Mater.* **2007**, *19*, 3100-3108.
23. Park, H. Y.; Schadt, M. J.; Wang, L.; Lim, I-I. S.; Njoki, P. N.; Kim, S. H.; Jang, M. Y.; Luo, J.; Zhong, C. J. Fabrication of Magnetic Core@Shell Fe-Oxide@Au Nanoparticles for Interfacial Bio-activity and Bio-separation. *Langmuir* **2007**, *23*, 9050-9056.
24. Yan, H.; Lim, I-I. S.; Zhang, L. C.; Gao, S. C.; Mott, D.; Le, Y.; An, D. L.; Zhong, C. J. Rigid, Conjugated and Shaped Arylethynes as Mediators for the Assembly of Gold Nanoparticles. *J. Mater. Chem*. **2011**, *21*, 1890-1901.
25. Alvarez-Puebla, R. A.; Liz-Marzán, L. M. Traps and Cages for Universal SERS Detection. *Chem. Soc. Rev.* **2012**, *41*, 43-51.
26. Hultman, K. L.; Raffo, A. J.; Grzenda, A. L.; Harris, P. E.; Brown, T. R.; O'Brien, S. Magnetic Resonance Imaging of Major Histocompatibility Class II Expression in the Renal Medulla Using Immunotargeted Superparamagnetic Iron Oxide Nanoparticles. *ACS Nano* **2008**, *2*, 477-484.
27. Jun, B. H.; Noh, M. S.; Kim, J. Y.; Kim, G. S.; Kang, H. M.; Kim, M. S.; Seo, Y. T.; Baek, J. H.; Kim, J. H.; Park, J. Y.; Kim, S. Y.; Kim, Y. K.; Hyeon, T. W.; Cho, M. H.; Jeong, D. H.; Lee, Y. S. Multifunctional Silver-Embedded Magnetic Nanoparticles as SERS Nanoprobes and Their Applications. *small* **2010**, *6*, 119-125.
28. Qian, X. M.; Zhou, X.; Nie, S. M. Surface-Enhanced Raman Nanoparticle Beacons Based on Bioconjugated Gold Nanocrystals and Long Range Plasmonic Coupling. *J. Am. Chem. Soc*. **2008**, *130*, 14934-14935.
29. Luo, J.; Luo, J.; Wang, L.; Shi, X.; Yin, J.; Crew, E.; Lu, S.; Lesperance, L. M.; Zhong, C. J. Nanoparticle-Structured Thin Film Sensor Arrays for Breath Sensing. *Sens. Actuators, B* **2012**, *161*, 845-854.
30. Peng, G.; Tisch, U.; Adams, O.; Hakim, M.; Shehada, N .; Broza, Y. Y.; Billan, S.; Abdah-Bortnyak, R.; Kuten, A.; Haick, H. Diagnosing Lung Cancer in Exhaled Breath Using Gold Nanoparticles. *Nature Nanotechnol.* **2009**, *4*, 669-673.
31. Buszewski, B.; Grzywinski, D.; Ligor, T.; Stacewicz, T.; Bielecki; Z.; Wojtas. J. Detection of Volatile Organic Compounds as Biomarkers in Breath Analysis by Different Analytical Techniques. *Bioanalysis* **2013**, *5*, 2287-2306.
32. Ye, S.; Mao, Y.; Guo, Y.; Zhang, S. Enzyme-based Signal Amplification of Surface-Enhanced Raman Scattering in Cancer-biomarker Detection. *TrAC*. **2014**, *55*, 43-54.
33. Barrow, S. J.; Funston, A. M.; Wei, X.; Mulvaney. P. DNA-Directed Self-assembly and Optical Properties of Discrete 1D, 2D and 3D Plasmonic Structures. *Nano Today* **2013**, *8*, 138-167.
34. Wang, L.; Xu, L.; Kuang, H.; Xu, C.; Kotov, N. A. Dynamic Nanoparticle Assemblies. *Acc. Chem. Res*.

2012, *45*, 1916-1926.

35. Jones, M. R.; Osberg, K. D.; Macfarlane, R. J.; Langille, M. R.; Mirkin, C. A. Templated Techniques for the Synthesis and Assembly of Plasmonic Nanostructures. *Chem. Rev*. **2011**, *111*, 3736-3827.
36. Shields, S. P.; Richards, V. N.; Buhro, W. E. Nucleation Control of Size and Dispersity in Aggregative Nanoparticle Growth. a Study of the Coarsening Kinetics of Thiolate-Capped Gold Nanocrystals. *Chem. Mater.* **2010**, *22*, 3212-3225.
37. Saha, K.; Agasti, S. S.; Kim, C.; Li, X. N.; Rotello, V. M. Gold Nanoparticles in Chemical and Biological Sensing. *Chem. Rev.* **2012**, *112*, 2739-2779.
38. Brust, M.; Walker, M.; Bethell, D.; Schiffrin, D. J.; Whyman, R. Synthesis of Thiol-Derivatized Gold Nanoparticles in a 2-Phase Liquid-Liquid System. *Chem. Commun.* **1994**, *7*,801-802.
39. Schadt, M. J.; Cheung, W.; Luo, J.; Zhong, C. J. Molecularly-Tuned Size Selectivity in Thermal Processing of Gold Nanoparticles. *Chem. Mater.* **2006**, *18*, 5147-5149.
40. Maye, M. M.; Zheng, W. X.; Leibowitz, F. L.; Ly, N. K.; Zhong, C. J. Heating-Induced Evolution of Thiolate-Encapsulated Gold Nanoparticles: a Strategy for Size and Shape Manipulations. *Langmuir* **2000**, *16*, 490-497.
41. Hostetler, M. J.; Wingate, J. E.; Zhong, C. J.; Harris, Y. E.; Vachet, R. W.; Clark, M. R.; Londono, J. D.; Green, S. J.; Stokes, J. J.; Wignall, G. D.; Glish, G. L.; Porter, M. D.; Evans, N. D.; Murray, R. W. Alkanethiolate Gold Cluster Monolayers with Radii from 7 to 26 Angstroms: Borders between Molecular and Metallic Behavior and between Two- and Three-dimensional Monolayers. *Langmuir* **1998**, *14*, 17-30.
42. Wang, F.; Richards, V. N.; Shields, S. P.; Buhro, W. E. Kinetics and Mechanisms of Aggregative Nanocrystal Growth. *Chem. Mater.* **2014**, *26*, 5-21.
43. Kariuki, N. N.; Luo, J.; Maye, M. M.; Hassan, A.; Menard, T.; Naslund, H. R.; Lin, Y.; Wang, C.; Engelhard, M. H.; Zhong, C. J. Composition-Controlled Synthesis of Bimetallic Gold-Silver Nanoparticles. *Langmuir* **2004**, *20*, 11240-11246.
44. Lahtinen, R. M.; Mertens, S. F. L.; East, E.; Kiely, C. J.; Schiffrin, D. J. Silver Halide Colloid Precursors for the Synthesis of Monolayer-Protected Clusters. *Langmuir* **2004**, *20*, 3289-3296.
45. Wang, L. Y.; Luo, J.; Fan, Q.; Suzuki, M.; Suzuki, I. S.; Engelhard, M. H.; Lin, Y.; Kim, N.; Wang, J. Q.; Zhong, C. J. Synthesis and Characterization of Monolayer-Capped PtVFe Nanoparticles with Controllable Sizes and Composition. *J. Phys. Chem. B* **2005**, *109*, 21593-21601.
46. Wang, X.; Wang, L.; Lim, I-I. S.; Bao, K.; Mott, D.; Park, H. Y.; Luo, J.; Hao, S.; Zhong, C. J. Synthesis, Characterization and Potential Application of MnZn Ferrite and MnZn Ferrite@Au Nanoparticles. *J. Nanosci. Nanotechnol.* 2009, *9*, 3005-3012.
47. Sun, S. H.; Zeng, H.; Robinson, D. B.; Raoux, S.; Rice, P. M.; Wang, S. X.; Li, G. X. Monodisperse MFe_2O_4 (M=Fe, Co, Mn) Nanoparticles. *J. Am. Chem. Soc*. **2004**, *126*, 273-279.
48. Luo, J.; Wang, L. Y.; Mott, D.; Njoki, N. P.; Lin, Y.; He, T.; Xu, Z.; Wanjana, B.; Lim, I-I. S.; Zhong, C .J. Core@Shell Nanoparticles as Electrocatalysts for Fuel Cell Reactions. *Adv. Mater.* **2008**, *20*, 4342-4347.
49. Wang, L.; Wang, X.; Luo, J.; Wanjala, B. N.; Wang, C.; Chernova, N.; Engelhard, M. H.; Bae, I. T.; Liu, Y.; Zhong, C. J. Core-Shell Structured Ternary Magnetic Nanocubes. *J. Am. Chem. Soc.* **2010**, *132*, 17686.
50. Zeng, H.; Rice, P. M.; Wang, S. X.; Sun, S. Shape-Controlled Synthesis and Shape-Induced Texture of $MnFe_2O_4$ Nanoparticles. *J. Am. Chem. Soc*. **2004**, *126*, 11458-11459.
51. Nagaraja, A. K.; Creighton, C. J.; Yu, Z. F.; Zhu, H. F.; Gunaratne, P. H.; Reid, J. G.; Olokpa, E.; Itamochi, H.; Ueno, N. T.; Hawkins, S. M.; Anderson, M. L.; Matzuk, M. M. A Link between mir-100 and

FRAP1/mTOR in Clear Cell Ovarian Cancer. *Mol. Endocrinol.* **2010**, *24*, 447-463.

52. Giljohann, D. A.; Seferos, D. S.; Prigodich, A. E.; Patel, P. C.; Mirkin, C. A. Gene Regulation with Polyvalent siRNA-Nanoparticle Conjugates. *J. Am. Chem. Soc*. **2009**, *131*, 2072-2073.

53. Crew, E.; Tessel, M. A.; Rahman, S.; Razzak-Jaffar, A.; Mott, D.; Kamundi, M.; Yu, G.; Tchah, N.; Lee, J.; Bellavia, M.; Zhong, C. J. MicroRNA Conjugated Gold Nanoparticles and Cell Transfection. *Anal. Chem.* **2012**, *84*, 26-29.

54. Lim, I-I. S.; Ip, W.; Crew, E.; Njoki, P. N.; Mott, D.; Zhong, C. J.; Pan, Y.; Zhou, S. Homocysteine-Mediated Reactivity and Assembly of Gold Nanoparticles. *Langmuir* **2007**, *23*, 826-833.

55. Jin, R.; Wu, G.; Li, Z.; Mirkin, C. A.; Schatz, G. C. What Controls the Melting Properties of DNA-Linked Gold Nanoparticles Assemblies? *J. Am. Chem. Soc.* **2003**, *125*, 1643-1654.

56. Lytton-Jean, A. K. R.; Han, M. S.; Mirkin, C. A. Microarray Detection of Duplex and Triplex DNA Binders with DNA-Modified Gold Nanoparticles. *Anal. Chem.* **2007**, *79*, 6037-6041.

57. Wang, L. Y.; Miller, D.; Fan, Q.; Luo, J.; Schadt, M.; Rendeng, Q.; Wang, G. R.; Wang, J.; Kowach, G. R.; Zhong, C. J. Assessment of Morphological and Optical Properties of Molecularly-Mediated Thin Film Assembly of Gold Nanoparticles. *J. Phys. Chem. C* **2008**, *112*, 2448-2455.

58. Kariuki, N. N.; Luo, J.; Hassan, A.; Lim, I-I. S.; Wang, L. Y.; Zhong, C. J. Assembly of Bimetallic Gold-Silver Nanoparticles via Selective Interparticle Dicarboxylate-Silver Linkages. *Chem. Mater*. **2006**, *18*, 123-132.

59. Wang, G. R.; Wang, L. Y.; Rendeng, Q.; Wang, J.; Luo, J.; Zhong, C. J. Correlation between Nanostructural Parameters and Conductivity Properties for Thin Film Assemblies of Gold Nanoparticles. *J. Mater. Chem*. **2007**, *17*, 457-462.

60. Choi, J. P.; Coble, M. M.; Branham, M. R.; DeSimone, J. M.; Murray, R. W. Dynamics of CO^{2-}Plasticized Electron Transport in Au Nanoparticle Films: Opposing Effects of Tunneling Distance and Local Site Mobility. *J. Phys. Chem. C* **2007**, *111*, 3778-3785.

61. Lim, I-I. S.; Mott, D.; Ip, W.; Njoki, P. N.; Pan, Y.; Zhou, S.; Zhong, C. J. Interparticle Interactions in Glutathione Mediated Assembly of Gold Nanoparticles. *Langmuir* **2008**, *24*, 8857-8863.

62. Lim, I-I. S.; Mott, D.; Engelhard, M.; Pan, Y.; Kamodia, S.; Luo, J.; Njoki, P. N.; Zhou, S.; Wang, L.; Zhong, C. J. Interparticle Chiral Recognition of Enantiomers: a Nanoparticle-Based Regulation Strategy. *Anal. Chem*. **2009**, *81*, 689-698.

63. Prencipe, G.; Tabakman, S. M.; Welsher, K.; Liu, Z.; Goodwin, A. P.; Zhang, L.; Henry, J.; Dai, H. J. PEG Branched Polymer for Functionalization of Nanomaterials with Ultralong Blood Circulation. *J. Am. Chem. Soc.* **2009**, *131*, 4783-4787.

64. Johnston, H. J.; Hutchison, G.; Christensen, F. M.; Peters, S.; Hankin, S.; Stone, V. A Review of the *In Vivo* and *In Vitro* Toxicity of Silver and Gold Particulates: Particle Attributes and Biological Mechanisms Responsible for the Observed Toxicity. *Crit. Rev. Toxicol.* **2010**, *40*, 328-346.

65. Wan, R.; Mo, Y.; Chien, S.; Li, Y.; Li, Y.; Tollerud, D. J.; Zhang, Q. The Role of Hypoxia Inducible Factor-1 Alpha in the Increased MMP-2 and MMP-9 Production by Human Monocytes Exposed to Nickel Nanoparticles. *Nanotoxicology*. **2011**, *5*, 568-582.

66. Wan, R.; Mo, Y.; Feng, L.; Chien, S.; Tollerud, D. J.; Zhang, Q. DNA Damage Caused by Metal Nanoparticles: Involvement of Oxidative Stress and Activation of ATM. *Chem. Res. Toxicol*. **2012**, *25*, 1402-1411.

67. Cheng, H. W.; Huan, S. Y.; Yu, R. Q. Nanoparticle-Based Substrates for Surface-Enhanced Raman Scattering Detection of Biomolecules. *Analyst* **2012**, *137*, 3601-3608.

68. Cheng, H. W.; Huan, S. Y.; Wu, H. L.; Shen, G. L.; Yu, R. Q. Surface-Enhanced Raman Spectroscopic

Detection of Biomarker Using Gold Nanoparticle Immobilized Substrates. *Anal. Chem*. **2009**, *81*, 9902-9912.

69. Wang, L. Y.; Shi, X.; Kariuki, N. N.; Schadt, M. J.; Wang, G. R.; Rendeng, Q.; Choi, J.; Luo, J.; Lu, S.; Zhong, C. J. Array of Molecularly-Mediated Thin Film Assemblies of Nanoparticles: Correlation of Vapor Sensing with Interparticle Spatial Properties. *J. Am. Chem. Soc*. **2007**, *129*, 2161-2170.

70. Yin, J.; Hu, P.; Luo, J.; Wang, L.; Cohen, M. F.; Zhong, C. J. Molecularly–Mediated Thin Film Assembly of Nanoparticles on Flexible Devices: Electrical Conductivity vs. Device Strains in Different Gas/Vapor Environment. *ACS Nano* **2011**, *5*, 6516-6526.

71. Shan, S.; Zhao, W.; Luo, J.; Yin, J.; Switzer, J. C.; Joseph, P.; Lu, S.; Poliks, M.; Zhong, C. J. Flexibility Characteristics of a Polyethylene Terephthalate Chemiresistor Coated with a Nanoparticle Thin Film Assembly. *J. Mater. Chem. C* **2014**, *2*, 1893-1903.

72. Shiohara, A.; Wang, Y.; Liz-Marzán, L. M. Recent approaches toward creation of hot spots for SERS detection. *J. Photochem. Photobiol. C Photochem. Rev.* **2014**, *21*, 2–25 DOI: 10.1016/j.jphotochemrev.2014.09.001.

73. Barrow, S. J.; Funston, A. M.; Gómez, D. E.; Davis, T. J.; Mulvaney, P. Surface Plasmon Resonances in Strongly Coupled Gold Nanosphere Chains from Monomer to Hexamer. *Nano Lett.* **2011**, *11* (10), 4180–4187 DOI: 10.1021/nl202080a.

74. Louis, C. Chemical Preparation of Supported Bimetallic Catalysts. Gold-Based Bimetallic, a Case Study. *Catalysts* **2016**, 6, 110 DOI: 10.3390/catal6080110.

75. Villa, A.; Wang, D.; Su, D. S.; Prati, L. New Challenges in Gold Catalysis: Bimetallic System. *Catal. Sci. Technol.* **2015,** 5, 55-68 DOI: 10.1039/C4CY00976B.

76. Chang, F.; Shan, S.; Petkov, V.; Skeete, Z.; Lu, A.; Ravid, J.; Wu, J.; Luo, J.; Yu, G.; Ren, Y.; Zhong, C. J. Composition Tunability and (111)-Dominant Facets of Ultrathin Platinum-Gold Alloy Nanowires toward Enhanced Electrocatalysis. *J. Am. Chem. Soc.* **2016**, 138(37), 12166-12175 DOI: 10.1021/jacs.6b05187.

77. Li, J.; Skeete, Z.; Shan, S.; Yan, S.; Kurzatkowska, K.; Zhao, W.; Ngo, Q. M.; Holubovska, P.; Luo, J.; Hepel, M.; et al. Surface Enhanced Raman Scattering Detection of Cancer Biomarkers with Bifunctional Nanocomposite Probes. *Anal. Chem.* **2015**, *87* (21), 10698–10702 DOI: 10.1021/acs.analchem.5b03456.

78. Jamshaid, T.; Neto, E. T. T.; Eissa, M. M.; Zine, N.; Kunita, M. H.; El-Salhi, A. E.; Elaissari, A. Magnetic particles: From preparation to lab-on-a-chip, biosensors, microsystems and microfluidics applications. *TrAC - Trends Anal. Chem.* **2016**, *79*, 344–362 DOI: 10.1016/j.trac.2015.10.022.

79. De Crozals, G.; Bonnet, R.; Farre, C.; Chaix, C. Nanoparticles with multiple properties for biomedical applications: A strategic guide. *Nano Today* **2016**, *11* (4), 435–463 DOI: 10.1016/j.nantod.2016.07.002.

80. Pileni, M. P. Inorganic nanocrystals self ordered in 2D superlattices: how versatile are the physical and chemical properties? *Phys. Chem. Chem. Phys.* **2010**, *12* (38), 11821 DOI: 10.1039/c0cp00456a.

81. Yang, H. T.; Hasegawa, D.; Takahashi, M.; Ogawa, T. Achieving a noninteracting magnetic nanoparticle system through direct control of interparticle spacing. *Appl. Phys. Lett.* **2009**, *94* (1), 1–3 DOI: 10.1063/1.3063032.

82. Punj, D.; Regmi, R.; Devilez, A.; Plauchu, R.; Moparthi, S. B.; Stout, B.; Bonod, N.; Rigneault, H.; Wenger, J. Self-Assembled Nanoparticle Dimer Antennas for Plasmonic-Enhanced Single-Molecule Fluorescence Detection at Micromolar Concentrations. *ACS Photonics* **2015**, *2* (8), 1099–1107 DOI: 10.1021/acsphotonics.5b00152.

83. Albella, P.; María Saiz, J.; González, F.; Moreno, F. Surface monitoring based on light scattering by metal nanosensors. *J. Quant. Spectrosc. Radiat. Transf.* **2011**, *112* (13), 2046–2058 DOI: 10.1016/j.jqsrt.2011.05.003.

84. U. Hohenester, Comput. Phys. Commun., 2014, 185, 1177

85. Hohenester, U.; Trügler, A. MNPBEM - A Matlab toolbox for the simulation of plasmonic nanoparticles. *Comput. Phys. Commun.* **2012**, *183* (2), 370–381 DOI: 10.1016/j.cpc.2011.09.009.

86. Nguyen, B. H.; Ngo, Q. M. Plasmonic enhancement by metallic spherical nanoparticles. *Adv. Nat. Sci. Nanosci. Nanotechnol.* **2014**, *5* (2), 25010 DOI: 10.1088/2043-6262/5/2/025010.

87. Garcia de Abajo, F. J.; Howie, A. Retarded field calculation of electron energy loss in inhomogeneous dielectrics. *Phys. Rev. B - Condens. Matter Mater. Phys.* **2002**, *65* (11), 1154181–11541817 DOI: 10.1103/PhysRevB.65.115418.

88. Israelachvili, J. 1992 London, Academic

89. Weddemann, A et al. 2010 Beilstein J. Nanotechnol 1 75-93

Chapter 2

Experimental Measurements and Computational Methods

2.1 Chemicals and Materials.

Hydrogen tetrachloroaurate (III) hydrate ($HAuCl_4$, 99%), sodium citrate (99%), sodium acrylate (97%), sodium chloride (NaCl, 99%), sodium phosphate (NaH_2PO_4, 99%), *p*-mercaptobenzoic acid (MBA), dithiothreitol (DTT), oleylamine (OAM, 70%), benzyl ether, 9-decanethiol (DT, 99%), 11-mercaptoundecanoic acid (MUA, 97%), tetraoctylammonium bromide (99%), sodium borohydride (99%) were purchased from Sigma-Aldrich (Milwaukee, WI) and used as received. Iron (III) acetylacetonate ($Fe(acac)_3$, 99%, Lancaster), manganese (II) acetylacetonate ($Mn(acac)_2$, 95% Strem), zinc acetylacetonate ($Zn(acac)_2$, 98%, Strem), and oleic acid (OAC, 99%, Alfa Aesar) were also used for the synthesis. Phosphate buffer (0.05 M, pH 7), carbonate/ borate buffer (0.05M, pH 10) and disodium phosphate (Na_2HPO_4, 99%) was purchased from Fisher Scientific (Pittsburgh, PA). Dithiobis (succinimidyl propionate) (DSP) and 1-ethyl-3-(3-dimethylaminopropyl)carbodiimide hydrochloride) (EDC) were purchased from ThermoFisher Scientific.

NAP-5 columns were purchased from Amersham Biosciences (Uppsala, Sweden). Pre-cast polyacrylamide gels and 10X TBE (0.89 M Tris, 0.89 M boric acid, 20mM EDTA) were purchased from Biorad Corporation (Hercules, CA).

The solvents including hexane (Hx, 99.9%), benzene (Bz, 99.0%), and toluene (Tl, 99.8%) were from Fisher and ethanol (99.9%) and acetone (99.9%) from Aldrich. Water was purified with a Millipore Milli-Q water system to achieve a final resistance of 18.2 MΩ.

Protein and antibody were purchased from Pierce Biotechnology, Inc. (Rockford, IL). DNA oligonucleotides were commercially made (Integrated DNA Technologies, Inc. Coralville, IA). DNA were dissolved in 0.2 M phosphate buffer (pH 8) at 120 μM concentrations. The sequences used are as follows: DNA1 (bottom strand): 5'-/5ThioMC6-D/AGG CCA GAC CTG CCC GGG CAA GCC TTG GCA-3' and DNA2 (top strand): 5'-/5ThioMC6-D/TGC CAA GGC TTG CCC GGG CAG GTC TGG CCT-3'.

2.2 Instrumental Measurements.

UV-Visible (UV-Vis) spectra were acquired with a Hewlett Packard 8453 spectrophotometer. The spectra were collected over the range of 200-1100 nm, using a solvent blank. A quartz cuvette with a path length of 1.0 cm was utilized.

Surface-enhanced Raman scattering (SERS) spectra were measured by an Advantage 200A Raman spectrometer (DeltaNu) and the data were collected from 200 to 3400 cm^{-1}. The laser power and wavelength were 5 mW and 632.8 nm, respectively. The integration time (counts s^{-1}) is 60 s for each set of data in this report, unless otherwise noted.

The hydrodynamic diameter of the NPs were monitored using NanoSight Tracking (NS300) by Malvern.

2.3 Nanoparticle Synthesis.

2.3.1 Citrate-Capped NPs. The citrate-capped gold and silver nanoparticles were synthesized using the reported procedure.[1] Briefly, 5 mL freshly prepared sodium citrate (38.8 mM) is added to 45 mL boiling solution containing 1 mM $HAuCl_4$ or $AgNO_3$. Upon the addition of sodium citrate to $HAuCl_4$, the color of the solution turned ruby-red, which is an indication for the formation of the gold nanoparticles. The solution is heated for an additional 30 min, then the heating mantle is removed and the nanoparticle solution was cooled to room temperature under continuous stirring. For the solution $AgNO_3$, the metal solution and sodium citrate were purged at least 10 min. prior to the reaction and changed from colorless to dark golden-yellow. The final solution is about 0.02% by weight of the metal.

2.3.2 Acrylate-Capped NPs. The acrylate-capped gold and silver nanoparticles were synthesized following a seeded growth procedure, previously reported.[2-3] Nanoparticles smaller than 30 nm in diameter were synthesized based on a reported protocol[4] with a slight modification for the control of size.[5-6] The final solutions are about 0.004% metal by weight.

Nanoparticle seeds (~10 nm) were synthesized by reacting aqueous solutions of the metal precursors and sodium acrylate at room temperature[3-7]. For example, in the synthesis of 30 nm nanoparticle seeds, an aqueous solution of $HAuCl_4$ (2.0×10^{-4} M) was mixed with sodium acrylate (12.0×10^{-3} M) and the mixture was stirred for 3 days at controlled

room temperature. The resulting solution displayed a deep-red color characteristic of the formation of gold nanoparticles.

Gold nanoparticles with diameters larger than the seeds were prepared by seeded growth via the reduction of $AuCl_4^-$ in the presence of presynthesized Au seeds[2, 6]. The basic element of the synthesis protocols involved seed formation and seeded growth using a combination of reducing and capping agents, including sodium citrates, sodium acrylates, and acrylic acids. The actual sizes of the resulting nanoparticles depend on the seed sizes and the precursor concentrations. Briefly, seeds of Au nanoparticles of between 20 and 30 nm diameter were first prepared. The seeds then underwent a seeded growth reaction in the presence of $HAuCl_4$ under a range of controlled concentrations of the reducing and capping agents to form large AuNPs (up to ~60nm). To synthesize larger AuNPs (up to ~100 nm), larger seeds (e.g., 60 nm seeds grown from seeded growth) were used in combination with controlled concentrations of $HAuCl_4$ and sodium acrylate. The particle size was controlled by varying the concentration of the seeds and the concentration of $AuCl_4^-$. In addition, control of the pH of the reaction solution and the reaction temperature is essential to the control of seeded growth. In most cases, the resulting particles displayed high monodispersity in the targeted size range. In some cases, a small fraction of particles with smaller sizes were separated by centrifugation.

Silver nanoparticles with larger NP diameters (40 nm) were prepared by the seeded growth method. The metal precursor ($AgNO_3$) was reduced in the presence of the smaller presynthesized Ag seeds and reducing agent ($NaBH_4$). The solutions were purged at least 15 min. individually, before adding together and allowing to react for 3 days under vigorous stirring.

2.3.3 Au and Ag decorated MZF NPs. The synthesis of MZF (magnesium, zinc, ferrite) nanoparticles was based on a method developed in our laboratory[8], which involved thermal decomposition of metal acetylacetonate compounds, e.g., 0.469 g $Fe(acac)_3$, 0.081 g $Mn(acac)_2$, and 0.087 g $Zn(acac)_2$) in 20 mL of benzyl ether with 2 mL of oleic acid and 2 mL of oleylamine. The mixture was refluxed for 60 min. The product was collected using a magnet.

For the preparation of MZF/Au and MZF/Ag nanoparticles, a modified strategy of the thermally activated processing protocol was used.[9] In a typical synthesis, 1.3 mL of concentrated Au-DT (or Ag-DT) and MZF nanoparticles (e.g., stock solutions of DT-capped Au (2 nm, 33 μM) and OAM/OA-capped MZF (8 nm, 2.6 μM)) in toluene with certain ratio was placed in a reaction tube. The tube was then placed in a preheated Yamato DX400 gravity convection oven at 150 °C for 3 h. Temperature variation from this set point was limited to 1.5 °C. After the thermal treatment, the reaction tube was allowed to cool down, and the particles were re-dispersed in toluene. The as-synthesized DT-capped MZF/Au and MZF/Ag particles were transferred to water by ligand exchange using mercaptoundecanoic acid (MUA).

2.3.4 DT-capped AuNPs. Gold nanoparticles of 2-nm diameter (Au_{2nm}) encapsulated with decanethiolate monolayer shells were synthesized by two-phase reduction of $AuCl_4^-$ according to Brust's two-phase protocol[10-11] and a synthetic modification.[12] The as-synthesized gold nanoparticles (DT-Au_{2nm}) exhibited an average size of 2.0 ± 0.7 nm. Gold nanoparticles with larger sizes were synthesized by a thermally-activated processing route developed in our laboratory.[13-14] Briefly, the solution containing the as-synthesized DT-Au_{2nm} nanoparticles from the synthesis was heated at 150 °C to

produce larger-sized Au nanoparticles. Gold nanoparticles of 7.0 ± 0.5 nm diameters (Au_{7nm}) produced by this method were used in this work. Details for the morphology and size distribution can be found in previous reports.[13-19]

2.4 Experimental Methods.

2.4.1 DNA mediated assembly and restriction enzyme cleavage. The detailed procedures for the assembly and the restriction enzymes cutting of the Au-DNA nanoparticle assemblies are as follows.

2.4.1.1 Molecular assembly based on complementary oligonucleotides. DNA1 and DNA2 were first dissolved in 0.1 M phosphate buffer (pH 8) at a concentration ranging from 300 to 370 μM. The disulfide bonds in DNA1 and DNA2 were cleaved using an approach similar to the reported procedure[20-24] where dithiothreitol (DTT) was added at 0.1 M (final concentration) to ~10 OD of the nucleotides in a final volume of 400 μL. The solution was allowed to react at room temperature for 2 hrs, and then put through a NAP-5 column and an aliquot of 1.1 mL phosphate buffer (pH 8) was added to the column to elute the cleaved oligonucleotide. The final concentration of the cleaved DNA was ~20 μM with an OD_{260nm} of 2.2. The exact concentrations of DNA varied slightly depending on the specific experiment.

The surface of 13 nm gold nanoparticles was functionalized with the cleaved DNA similar to the reported procedure[20-24] to form DNA-Au. Briefly, 1.45 mL of the cleaved DNA was added to 10 mL of gold nanoparticles (stock concentration 1.0 nM). The solution was left standing at room temperature for 16 hrs, after which it was diluted to 20 mM NaCl and 10 mM phosphate buffer (pH 7) and allowed to stand for another 40 hrs at room temperature. The DNA capped nanoparticles were then centrifuged and washed twice at

14,000 rpm (18,620×*g*) for 20 min (each time the solution was re-dispersed in a 20 mM NaCl/ 10 mM phosphate buffer (pH 7) solution) before being re-dispersed in its final 20 mM NaCl, 10 mM phosphate buffer (pH 7) solution and stored at room temperature.

The MBA labeled 11, 40, 60 nm gold nanoparticles were prepared as follows: sufficient volume of 0.1 mM MBA for a 50% surface coverage was added to 10 mL of gold nanoparticles (stock concentration 1.0, 0.1, 0.028 nM). The solution was left standing at room temperature overnight.

To study the assembly of the DNA capped nanoparticle solution, 20 μL of DNA2 was added to 250 μL of DNA1-Au in the presence of 500 μL of MBA labeled gold nanoparticles. Then, the solution was heated to 80 ^{o}C using a quartz cuvette, or Raman cell, with a built-in liquid flow cell connected to a temperature controller, or in a water bath, for 20 min and gradually cooled down to room temperature. The reaction monitored by UV-Vis and Raman, and the temperature of the solution was 80°C controlled by using a temperature controller (Glas-Col, Digi Trol II) with the liquid flow controlled by a mechanical pump.

2.4.2 Protein-mediated assembly. Acrylate – capped gold nanoparticles (51.6 ± 2.0 nm) were synthesized following a seeded growth procedure.[2, 5, 6] Protein A (proA) was dissolved in deionized water at a concentration of 1.3 mM and the antibody (goat anti-rabbit immunoglobulin G) was used as purchased with a concentration of 9.6e-5 M. The conjugation of AuNPs with the antibody (Ab) was similar to the reported procedure[25-27] to form Ab/AuNP, and the same for the conjugation with the protein to form ProA/AuNP. The labeling of AuNPs with MBA (MBA/AuNP) was achieved by following a previously reported procedure[25-27].

Briefly, the aqueous solution of AuNPs was first reacted with the Raman label, different concentrations of MBA ranging from 1.1 - 13 μL (2 mM) and gently shaken for 2 hrs. The protein-coupling agent, DSP (7.8 μL of 1 mM) (or 10 μL of 0.1 M EDC), was then added to the solution and gently shaken for 30 min - 15 hrs. The biomolecules were then added to the solution and gently shaken overnight (5 μL of antibody (Ab; antirabbit IgG; stock 2.4 $mg{\cdot}ml^{-1}$) or 0.5 μL of protein (Protein A; stock 53 $mg{\cdot}ml^{-1}$). The resulting protein-capped nanoparticles were stored at room temperature.

Surface coverage of MBA (θ) theoretically estimated for 52-nm AuNPs was 0.07, 0.5 and 0.7. For the free protein (or antibody) assembly of gold nanoparticles in solution, 0.5 μL of protein A (10 μM) (or 5 μL of antibody (2.4 $mg{\cdot}mL^{-1}$)) was added to a solution (unless otherwise mentioned) containing 0.5 mL of Ab/AuNP (or ProA/AuNP) and gently shaken from 30 min to ~15 hrs. For the bound protein (or antibody) assembly of gold nanoparticles in solution, 0.5 mL of ProA/AuNP (0.5 mL of Ab/AuNP) was added to a solution containing 0.5 mL of Ab/AuNP (0.5 mL of ProA/AuNP) and immediately analyzed or gently shaken for ~15 hrs. Note the range of adsorption times were used to maximize adsorption of molecules and determine the lowest possible time required to obtain signal. The assembly process was monitored-using Raman spectroscopy before and after centrifugation at 14000 rpm for 15 min.

2.5 Methods for Theoretical Calculations.

2.5.1 Calculation of Interparticle Interaction Potentials. The interparticle interaction potentials were analyzed by evaluating a simplistic dimer model of the steric repulsive and van der Waals attractive forces with relation to the interaction energies and the interparticle gap using equations (1) and (2).[28-30] r, R_1, and R_2 are the particle radius of

the AuNP dimers where r is used for homo-sized dimers and R_1 and R_2 are used to denote the different size NPs in the hetero-sized dimers. The δ and σ stand for the length and the diameter of a capping molecule on the nanoparticle surface in the steric repulsive and van der Waals attractive interaction energies with respect to the interparticle gap distance (D). In the steric calculations, the length and the diameter of the capping molecule (DNA) are 10 and 2 nm, respectively.[31-33] The Boltzmann constant (k, 8.617*10^{-5} eV K^{-1}) and temperature (T, 298 K) used in this equation as well.

$$E_{steric} \approx \frac{100r\delta^3}{(D-2r)\pi\sigma^3}\, kT \exp\left(\frac{-\pi\,(D-2r)}{\delta}\right) \qquad (1)$$

$$E_{vdW,sym} = -\frac{A}{12}\left[\frac{4r^2}{D^2-4r^2} + \frac{4r^2}{D^2} + 2\ln\left(\frac{D^2-4r^2}{D^2}\right)\right] \qquad (2a)$$

$$E_{vdW,asym} = -\frac{A}{6}\left[\frac{2\frac{R_2}{R_1}}{\left(\frac{R_1+R_2+D}{R_1}\right)^2-\left(1+\frac{R_2}{R_1}\right)^2} + \frac{2\frac{R_2}{R_1}}{\left(\frac{R_1+R_2+D}{R_1}\right)^2-\left(1-\frac{R_2}{R_1}\right)^2} + \ln\left(\frac{\left(\frac{R_1+R_2+D}{R_1}\right)^2-\left(1+\frac{R_2}{R_1}\right)^2}{\left(\frac{R_1+R_2+D}{R_1}\right)^2-\left(1-\frac{R_2}{R_1}\right)^2}\right)\right] \qquad (2b)$$

For the van der Waals interactions, the size-dependent Hamaker constants were applied for the 3 different homo-sized dimers of 13, 39, and 62 nm, corresponding to 0.830212235, 0.81772784, and 0.805243446 eV, respectively.[33-36] All of the interactions were analyzed from a gap distance (D) from 0.1 to 60 nm. The interparticle potentials were also calculated in terms of the effective shell thickness (0.1 to 10 nm) to identify the minimum energy (eV) and interparticle gap distance (nm).

2.5.2 Computational Modeling of Interparticle Plasmonic Coupling and Electromagnetic Field. The metallic nanoparticle boundary element method (MNPBEM) toolbox was developed by U. Hohenester based on the BEM approach by G. de Abajo and Howie.[37] The MNPBEM toolbox determines the electrical intensity of the localized

surface plasmon resonances of the NPs to simulated the absorbance cross-section and enhancement intensity (log base 10) of the NPs when in an aqueous environment using optical constants and Maxwell equations to determine the surface charge and currents of the particles.[37, 38] The simulation codes utilize the dielectric values of the environment ($\varepsilon_1 \approx 1.77$ or 1.33^2), the metal NP spheres and NP shells (ε_2 and ε_3) (**Figure 2.5.2.1**). In these cases, the dielectric values of the metals (Au, Ag, Fe_3O_4, Co, Ni, Fe_2O_3 and Fe) in terms of energy (eV) and the respective real and imaginary parts over a range of 300 to 900 nm (1.4 to 4.1 eV).[39-42] Depending on the material used to coat the NPs, the dielectric constants of 2.12 and 2.40 were used for DNA and cyanine dye, respectively. The planes of excitation were x alone (1, 0, 0) or x and y (1, 0, 0; 0, 1, 0), with the detector in the z plane (0, 0, 1).

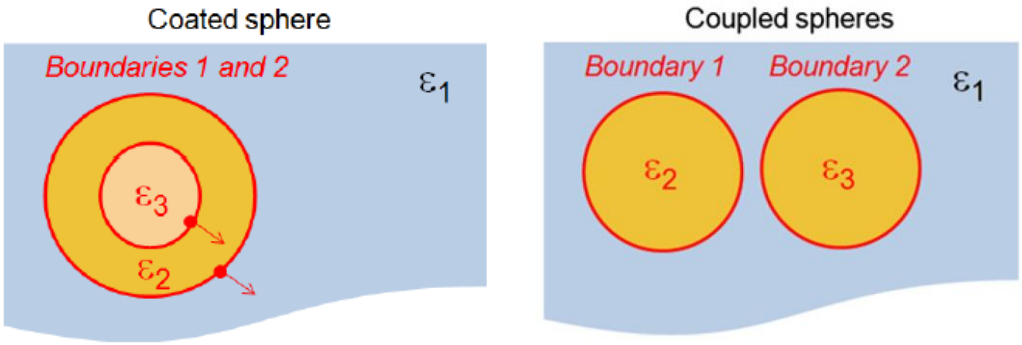

(A) (B)

Figure 2.5.2.1. Schematic of the NPs and its environmen: single core-shell NP (A) and dimer NP (B).[37,38]

For each cros-section simulation, the resolution of the spherical NPs was maintained at 150, resulting in 144 triangles on the particle for discretization (**Figure 2.5.2.2**). For the cross-section analysis, the scattering, absorption, and extinction characteristics were calculated and integrated every 1 nm.

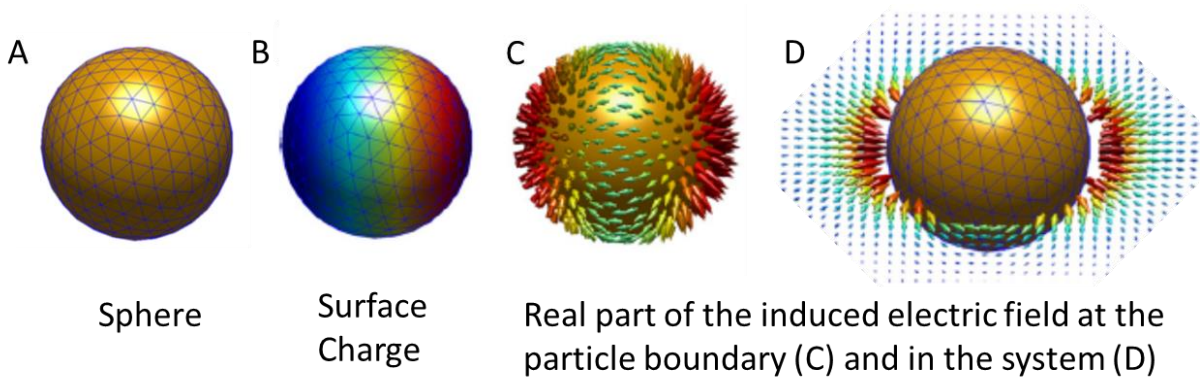

Figure 2.5.2.2. Schematic of the resolution illustrating the discretized regions of the particles.[37, 38]

Similarly for the simulated EMF enhancement the same particle resolution was used. In these modeling, the excitation wavelength used is 632 nm and the output colorbar was maintained at 3 for comparison. The resolution of the output grids to position the particles for the x axis were maintained at 2 points per grid box and 1 per grid box for the y axis (**Figure 2.5.2.3**).

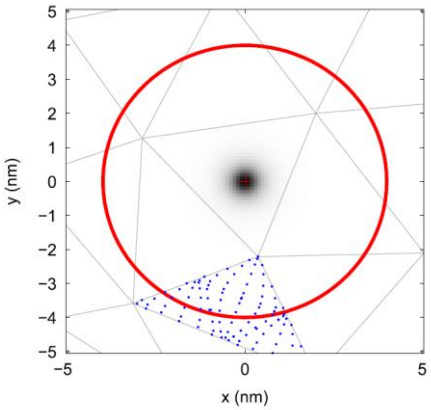

(A)

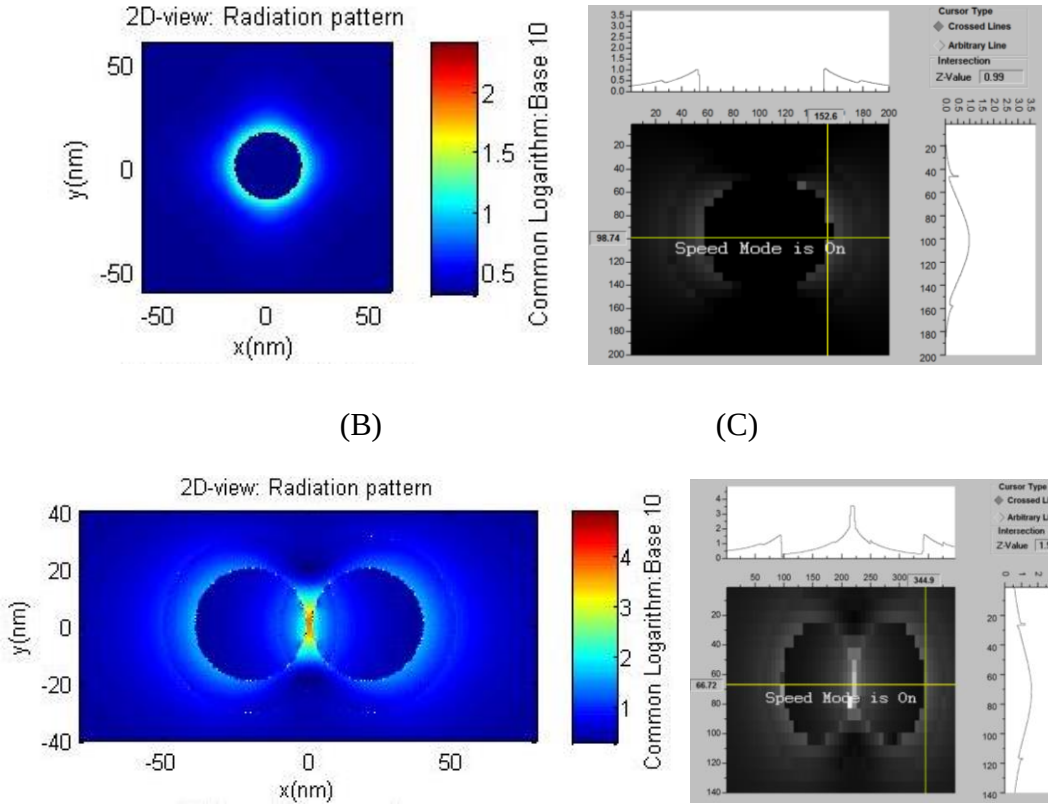

Figure 2.5.2.3. Schematic of the resolution illustrating the discretized regions of the particles (A) and the simulated EMF intensity and cross-sections of a single NP (B, C) and dimer NPs (D, E).[37, 38]

References.

1. Mbindyo, J. K. N.; Reiss, B. D.; Martin, B. R.; Keating, C. D.; Natan, M. J.; Mallouk, T. E. *Adv. Mater.*, **2001**, *13*, 249-254.
2. Njoki, P. N.; Lim, I. S.; Mott, D.; Park, H. Y.; Khan, B.; Mishra, S.; Sujakumar, R.; Luo, J.; Zhong, C. J. *J. Phys. Chem. C*, **2007**, *111*, 14664-14669.
3. P. N. Njoki, J. Luo, M. M. Kamundi, S. Lim, C. J. Zhong, *Langmuir*, **2010**, *26*, 13622-13629.
4. Hussain, I.; Brust, M.; Papworth, A. J.; Cooper, A. I. *Langmuir*, **2003**, *19*, 4831-4835.
5. Njoki, P. N.; Luo, J.; Wang, L.; Maye, M. M.; Quaizar, H.; Zhong, C. J. *Langmuir*, **2005**, *21*, 1623-1628.
6. Zhong, C. J.; Njoki, P. N.; Luo, J. U.S. Patent 7,524,354, 2009.
7. Jana, N. R.; Geatheart, L.; Murphy, C. J. *Langmuir*, **2001**, *17*, 6782-6786.
8. Wang, L.; Luo, J.; Shan, S.; Crew, E.; Yin, J.; Wallek, B.; Wong, S.; Zhong, C. J. *Anal. Chem.*, **2011**, *83*, 8688–8695.
9. Park, H. Y.; Schadt, M. J.; Wang, L.; Lim, I-I. S.; Njoki, P. N.; Kim, S. H.; Jang, M. Y.; Luo, J.; Zhong, C. J. *Langmuir*, **2007**, *23*, 9050-9056.
10. Brust, M.; Walker, M.; Bethell, D.; Schiffrin, D. J.; Whyman, R. J. *Chem. Soc., Chem. Commun.*, **1994**, 801-802.
11. Bethell, D.; Brust, M.; Schiffrin, D. J.; Kiely, C. J. *J. Electroanal. Chem.*, **1996**, *409*, 137.
12. Lewinski, N.; Colvin, V.; Drezek, R. *Small*, **2008**, *4*, 26-49.
13. Maye, M. M.; Zheng, W. X.; Leibowitz, F. L.; Ly, N. K.; Zhong, C. J. *Langmuir*, **2000**, *16*, 490-497.
14. Schadt, M. J.; Cheung, W.; Luo, J.; Zhong, C. J. *Chem. Mater.*, **2006**, *18*, 5147-5148.
15. Han, L.; Luo, J.; Kariuki, N.; Maye, M. M.; Jones, V. W.; Zhong, C. J. *Chem. Mater.*, **2003**, *15*, 29-37.
16. Luo, J.; Maye, M. M.; Han, L.; Kariuki, N.; Jones, V. W.; Lin, Y.; Engelhard, M. H.; Zhong, C. J. *Langmuir*, **2004**, *20*, 4254-4260.
17. Kariuki, N.; Han, L.; Ly, N. K.; Peterson, M. J.; Maye, M. M.; Liu, G.; Zhong, C. J. *Langmuir* **2002,** *18*, 8255-8259.
18. Luo, J.; Jones, V. W.; Maye, M. M.; Han, L.; Kariuki, N. N.; Zhong, C. J. *J. Am. Chem. Soc.* **2002**, *124*, 13988-13989.
19. Luo, J.; Jones, V. W.; Han, L.; Maye, M. M.; Kariuki, N.; Zhong, C. J. *J. Phys. Chem.* **2004**, *108*, 9669-9677.
20. Crew, E.; Rahman, S.; Razzak-Jaffar, A.; Mott, D.; Kamundi, M.; Yu, G.; Tchah, N.; Lee, J.; Bellavia, M.; Zhong, C. J. *Anal. Chem.*, **2012**, *84*, 26–29.
21. Giljohann, D. A., Seferos, D. S., Prigodich, A. E., Patel, P. C., and Mirkin, C. A. *J. Am. Chem. Soc.*, **2009**, *131*, 2072-2073.
22. Tessel, M. A.; Benham, A. L.; Krett, N. L.; Rosen, S. T.; Gunaratne, P. H. *Horm. Canc.*, **2011**, *2*, 182-189.

23. Crew, E.; Yan, H.; Lin, L.; Yin, J.; Skeete, Z.; Kotlyar, T.; Tchah, N.; Lee, J.; Bellavia, M.; Goodshaw, I.; Joseph, P.; Luo, J.; Gal, S.; Zhong, C. J. *Analyst*, **2013**, *138*, 4941-4949.

24. Lin, L.; Crew, E.; Yan, H.; Shan, S.; Skeete, Z.; Mott, D.; Krentsel, T.; Yin, J.; Chernova, N. A.; Luo, J.; Engelhard, M. H.; Wang, C.; Li, Q.; Zhong, C. J. *J. Mater. Chem. B*, **2013**, *1*, 4320-4330.

25. Lim, I-I. S.; Chandrachud, U.; Wang, L.; Gal, S.; Zhong, C. J. *Anal. Chem.*, **2008**, *80*, 6038–6044.

26. Lim, I-I. S.; Mott, D.; Engelhard, M.; Pan, Y.; Kamodia, S.; Luo, J.; Njoki, P. N.; Zhou, S.; Wang, L.; Zhong, C. J. *Anal. Chem.*, **2009**, *81*, 689–698.

27. Lim, I-I. S.; Njoki, P. N.; Park, H.-Y.; Wang, X.; Wang, L.; Mott, D.; Zhong, C. J. *Nanotechnology*, **2008**, *19(30)*, 305102.

28. Israelachvili, J. 1992 London, Academic

29. Weddemann, A et al. 2010 Beilstein J. Nanotechnol 1 75-93

30. Yockell-Lelièvre, H, Gingras, D, Lamarre, S, Vallée, R, and Ritcey, A M 2013 Plasmonics 8 1369-77

31. Griffiths, D. J. 2012 Boston, Addison-Wesley

32. Palik, E.D. 1985 London, Academic Press

33. Elhadj, S, Singh, G, and Saraf, R F 2004 Langmuir 20 5539-43

34. Pinchuk, P, and Jiang, K 2015 Proc SPIE 9549 95491J

35. Achebe, C H, and Omenvi, S N 2013 Proceedings of The World Congress on Engineering 2 1380-4

36. Sun, W, Zeng, Q, and Yu, A 2013 Langmuir 29 2175-84

37. Hohenester, U, and Trügler, A 2012 Comp. Phys. Commun. 183 370-81

38. Hohenester, U. 2014, Comp. Phys. Commun. 185 1177-87.

39. García de Abajo, F J, and Howie, A 2002 Phys. Rev. B. 65 115418

40. Griffiths, D. J. 2012 Boston, Addison-Wesley

41. Palik, E.D. 1985 London, Academic Press

42. Johnson, P. B.; Christy, R. W. 1972 Phys. Rev. B 6, 4370-4379.

Chapter 3

Harnessing the interparticle J-aggregate induced plasmonic coupling for surface-enhanced Raman scattering

3.1 Introduction

The ability to harness the nanoparticles in solution is applicable in a broad range of applications by exploiting the plasmonic and spectroscopic properties. The need to further understand the plasmonic coupling in addition to the surface plasmon resonance and surface-enhanced Raman scattering is necessary for detection of molecules with nanoparticles.

The highly conjugated p-structure characteristic of dye molecules plays a key role in various supramolecular or aggregate phenomena. One important class of such phenomena is J- or H-aggregation, which is known for a variety of interesting photochemical, photoluminescence, electroluminescence, non-linear and other optical properties.[1,2] The physical and chemical properties of an aggregate of cyanine dyes are determined by the non-covalent p-stacking interaction and molecular arrangement, which are explored as molecular building blocks in functional devices. Due to stacking geometries and molecular ordering, the absorption spectrum red-shifts upon forming J-

aggregates (brickwork- like) or blue-shifts upon forming H-aggregates (ladder-like) due to the interactions between the neighboring dipoles and the relative orientation. Cyanine dyes serve not only as an ideal system of molecular glue,[3] but also as an increasingly important class of probes for protein–ligand interactions via aggregation-related spectral singling, e.g., J-band and fluorescence, which are useful for non-covalent protein labeling and sensing.[4] One intriguing system involves J-aggregate interaction with nanomaterials, as demonstrated earlier for an assembly of gold nanoparticles via the π–π* interaction of indolenine cyanine dyes[5] and different conjugated molecules,[6] such as perylene diimides with π–π* stacking and solvophobic interactions in J- or H-type configuration,[7,8] and the J-aggregate of a thiacyanine dye.[9] There are two types of J-aggregation reported so far: one occurs on the surface of nanoparticles[9–11] and the other occurs in between nanoparticles.[5,6] Questions such as what factors control the specific interparticle π–π* stacking structure and how such a structure determines the operation of plasmonic coupling for nanoparticles in solution remain elusive.

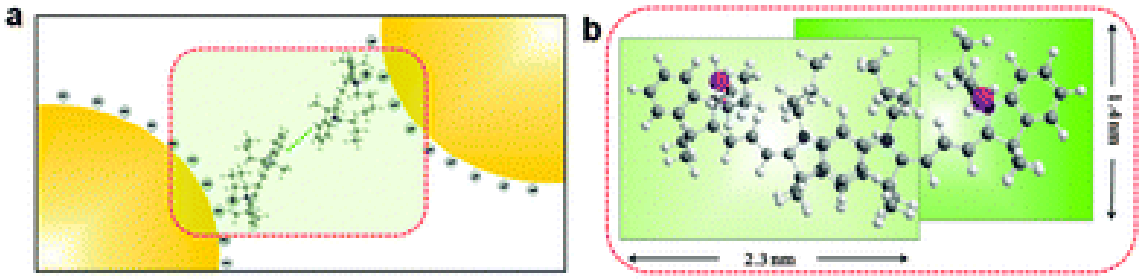

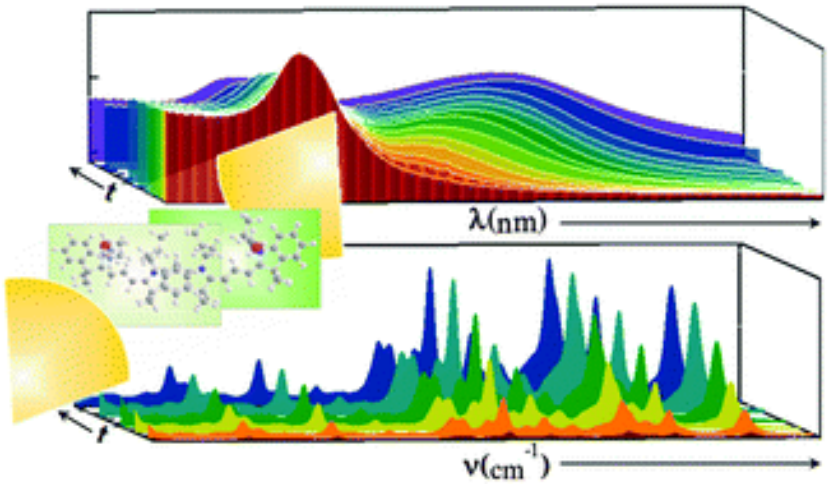

Scheme 3.1.1. (top panel) Molecularly tunable interface of J-aggregated cyanine dyes for harnessing interparticle plasmonic coupling. (a) Interparticle π–π interaction of positively charged cyanine dyes (Tlc) adsorbed on gold NPs capped with negatively charged acrylate or citrate capping molecules. (b) Brickwork-like π–π stacking of Tlcs (J-aggregation). (bottom panel) Harnessing the interparticle J-aggregate induced plasmonic coupling for surface-enhanced Raman scattering

The findings of an investigation aimed at addressing these questions through the measurement of surface plasmon resonance (SPR) and surface enhanced Raman scattering (SERS) characteristics using a combination of cyanide dyes and gold nanoparticles (AuNPs) as a model system will be discussed. AuNPs function as a nanoprobe for probing the interparticle interaction via the so-called ‘‘hot-spot’’, as demonstrated in the exploration of dye-embedded core–shell colloidal nanoparticles for multiplexed SERS detection.[12] In addition to the high SERS enhancement factor (as high as 10^{14}),[12] fluorescent dyes provide an additional 2–3 orders of magnitude amplification due to the additional resonance Raman enhancement, as demonstrated for the indocyanine green dye on colloidal silver and gold for application in living cells,[13] and the multiplexed detection of different targeted oligonucleotides with a specific sequence and Raman labels.[14] Fundamentally, the foundation for SERS is linked to local electric field enhancement (i.e., ‘‘hot-spot’’) for a dimer of NPs using the discrete dipole approximation method,[15] where the E-field enhancement is dependent on the interparticle spacing.[16–18a] Indeed, intriguing SERS

effects have been observed in studies of single gold nanoantennas, nanogaps from nano-dumbbells, and nanoparticle dimers, trimers and quadrumers,[18] and, especially, in theoretical and experimental studies of silver nanoparticles.[19] Despite the many SERS studies involving gold and silver nanoparticles, little is understood on how the SERS effect is correlated to the interparticle plasmonic coupling induced by interparticle π–π* interactions in solutions and kinetically. This correlation is determined by monitoring SPR and SERS in the process of π–π* interaction and nanoparticle assembly. As illustrated in **Scheme 3.1.1**, for a cyanine dye (i.e.,1,10-dibutyl-3,3,30,30-tetramethylindocarbocyanine iodide (Tlc)) electrostatically adsorbed on a gold nanoparticle (Au_{nm}), the π–π* interaction of the Tlc molecules defines the interparticle spatial properties, which creates opportunities to tune the interface using different molecular dye structures for harnessing the interparticle plasmonic coupling.

3.2 Experimental.

The synthesis of citrate-capped gold nanoparticles (Au_{13nm}) was performed by the reduction of $AuCl_4^-$ by citrate under boiling condition; where citrate acts as both reducing and capping agents.[1] Gold nanoparticles of larger sizes (30-100 nm) were synthesized by the growth of AuNP seeds by the reduction of $AuCl_4^-$ using acrylate at room temperature.[2] In this case, acrylate acts as both reducing and capping agents. The stock concentration of gold nanoparticles was determined using the absorbance data and the average NP size. The molar absorptivity for these nanoparticles was determined at the surface plasmon resonance band maximum.[2a]

The interparticle J-aggregation induced assembly of Au_{nm} was carried out under ambient condition. UV-Visible (UV-Vis) spectra were acquired with a HP 8453

spectrophotometer over the range of 200- 1100 nm. A quartz cuvette with a path length of 1.0 cm was utilized. Surface-enhanced Raman scattering (SERS) spectra were measured by an Advantage 200A Raman spectrometer (DeltaNu) and the data were collected from 200 to 3400 cm^{-1}. The laser power and wavelength were 5 mW and 632.8 nm, respectively.

The simulation of the surface plasmon resonance band and the electrical field was performed using MNPBEM toolbox,[3] which involved setting up the nanoparticles' boundary conditions and the dielectric environment to calculate the optical absorption and the electrical field around the nanoparticles. Two AuNPs models were used in the theoretical simulations to understand the two naked AuNPs with an Tlc-defined interparticle distance. The first provides a simplistic view of the interaction using a dimer and trimer model. The second simulates a more-complexed system using "core-shell" dimer model; which considers the adsorption of Tlc on AuNP (Tlc shell: 1.5 nm thick, refractive index is 2.40) at an interparticle π–π* stacking distance (0.4 nm).

3.3 Results and Discussion

3.3.1 J-aggregation of cyanine dyes adsorbed on gold nanoparticles. In comparison with the SPR characteristic of AuNPs, the J-aggregation of cyanide dyes is characterized by a red-shifted J-band with either a sharp peak or dip in the spectrum. In contrast to our earlier work, with a different cyanine dye in the presence of AuNPs which showed a sharp peak for the J-band at ~630 nm,[5] the Tlc dye's J-band is shown as a dip at ~606 nm in the spectrum (Figure 3.3.1.1).

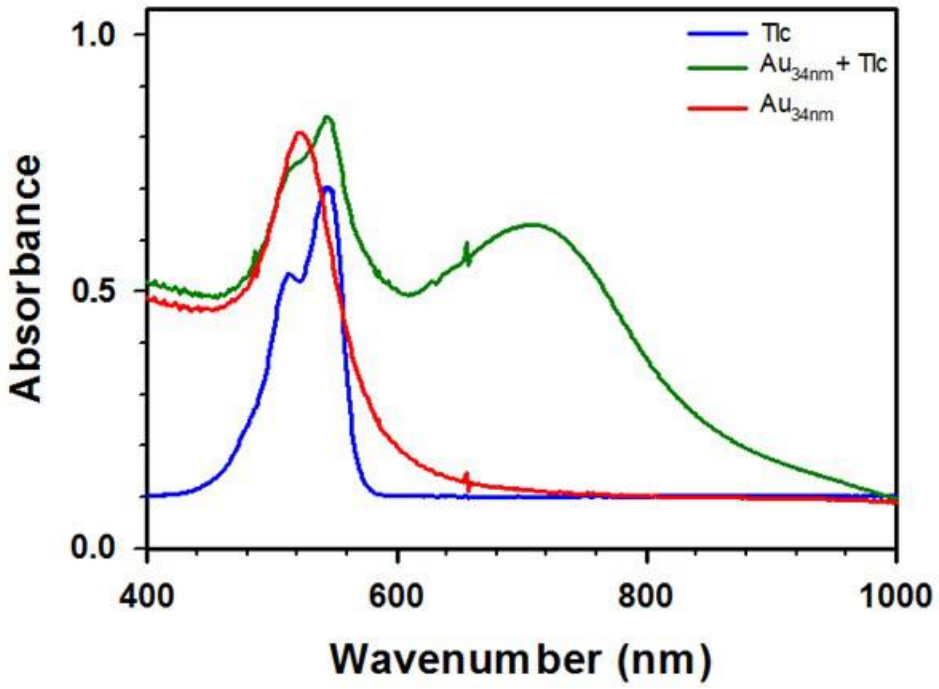

Figure 3.3.1.1. UV-vis spectra for Tlc (blue), AuNPs (red), and AuNPs in the presence of Tlc(green). Tlc (blue, [Tlc] = 1.23 μM), Au_{34nm} (red, [Au_{34nm}] = 0.155 nM), and Au_{34nm} + Tlc (green, [Au_{34nm}] = 0.155 nM, [Tlc] = 0.176 μM).

Such spectral characteristics are related to interband and intraband interactions and depend on a number of factors such as the specific structure of the dye molecules, the nanoparticle size, composition, and surface charge.[9] The model system for the NP-dye interaction incorporates a negatively charged surface due to the Citrate-/acrylate-capped gold nanoparticles (AuNPs, Au_{nm})[20] and a positively charged surface from the Tlc. Figure 3.3.1.2A shows a typical set of spectral evolutions for the surface plasmon resonance (SPR) band of AuNPs (34 nm) as time increases in an aqueous solution upon addition of Tlc. The broad emerging long-wavelength band at 600–800 nm, accompanied by a decrease of the band at 521 nm, is attributed to the SP bands of AuNPs as a result of interparticle linking by the π–π* stacking of the adsorbed Tlcs, forming small aggregates (e.g., dimers). A clear isosbestic point is observed at ~560 nm between the two bands (Figure 3.3.1.2A), indicating the involvement of two types of species (unlinked and Tlc-linked AuNPs) at

equilibrium. Overall, the spectral evolution reveals a clear increase of absorbance and broadening of the SP band, as reflected by the gradual increase in the longer-wavelength band (Figure 3.3.1.2B) and decrease in the shorter-wavelength band (Figure 3.3.1.2C).

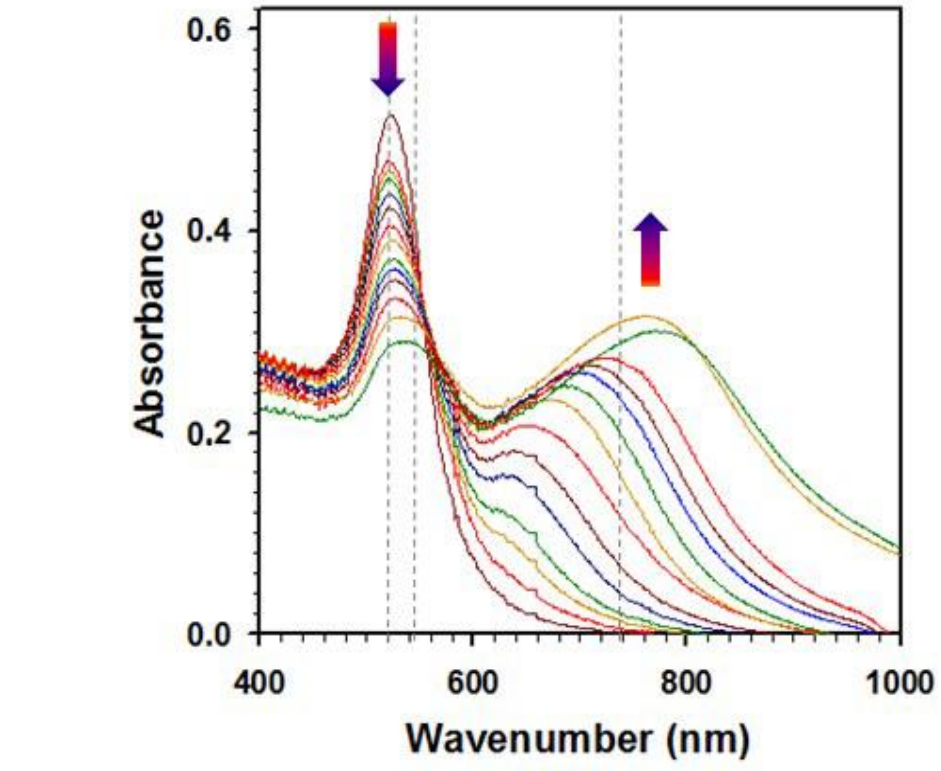

(A)

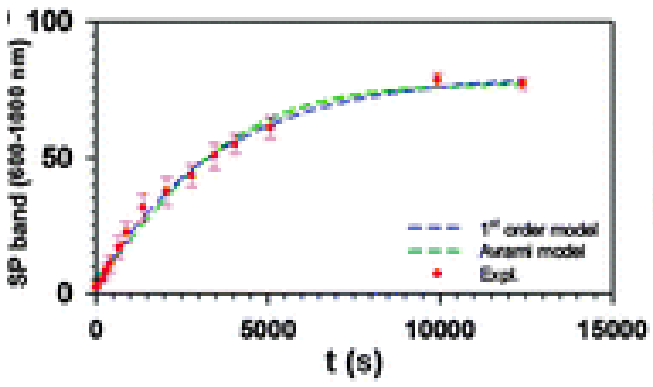

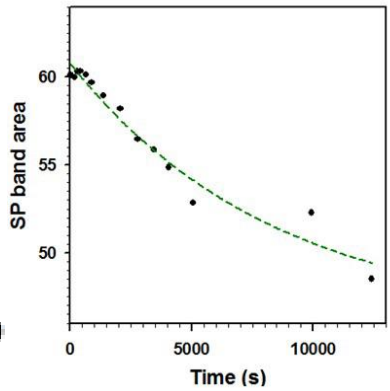

(B) (C)

Figure 3.3.1.2. (A) Surface plasmon resonance spectral evolution. (a) UV-Vis spectral evolution for Au_{34nm} NPs in an aqueous solution ($[Au_{34nm}] = 8.9 \times 10^{-2}$ nM) upon addition of Tlc ($[Tlc] = 2.4 \times 10^{-2}$ μM). (B) Kinetic plot of the long-wavelength SP band (integrated peak area from 600 to 1000 nm); the first-order model ($y = A_1'(1 - e^{-kt})$) yields $k = 2.8 \times 10^{-4}$ s^{-1}; the Avrami model ($y = A_2'(1 - e^{-ktn})$) yields $k = 3.2 \times 10^{-5}$ s^{-1} and $n = 1.3$. (C) Kinetic plot for the shorter-wavelength SP band; dotted line represent curve fitting by a 1st order reaction model ($y = A_1 + A_1' \times e^{-kt}$)) which yields $A_1 = 46.05$, $A_1' = 14.75$, $k = 1.2$ x10-4 s^{-1}.

The above SP spectral evolution is accompanied by a clear spectral evolution of the Raman bands characteristic of Tlc, as shown in Figure 3.3.1.3A. Note that these bands are not detectable in the absence of AuNPs in the solution. Upon addition of Tlc into a solution of Au_{34nm}, the intensity of the SERS peak at 1589 cm^{-1} exhibits a gradual increase as a function of time (Figure 3.3.1.3B).

An intriguing similarity is evident between the spectral evolutions of both SP bands and SERS bands, which are further analyzed by considering the adsorption of Tlc on AuNPs, which is relatively fast, and the subsequent dimerization involving the interparticle π–π^* interaction, which is relatively slow[5] and thus an apparent rate-determining step.

For a first-order reaction, the rate of the apparent rate-determining reaction is proportional to the concentration of AuNPs once a nucleus of a dimer is formed. Based on the concentration of the monomer AuNPs (i.e., $[Au_{nm}(Cit)_{m1}(Tlc)_{m2}]$), which is proportional to the absorbance of the SP band at 521 nm, and the concentration of the dimer (i.e., $[Au_{nm}\ (Cit)_{m1}(Tlc)_{m2}]_2$), which is proportional to the absorbance (A) of the broad band at 600–800 nm, the first-order reaction rate can be derived as an exponentially rising rate equation:

$$A_{(SP@4600nm)} = A_1(1 - e^{-kt}) \quad (1)$$

where A_1 is a constant related to the extinction coefficients of AuNPs, and k is an apparent rate constant. In view of the band broadening effect in the long-wavelength band region, the absorbance of the long-wavelength SP band, i.e., $A_{(SP@4600nm)}$, is best represented by the envelope in terms of the integrated peak area. The integrated area is used to substitute for A in eqn (1) based on its proportionality to the area. For the SP band spectral evolution (Figure 3.3.1.2B), the experimental data are clearly fitted very well by eqn (1), yielding an apparent rate constant (k) of 2.8×10^{-4} s^{-1} for the increase in the longer-wavelength SP band.

For the shorter-wavelength band, the fitting result (Figure 3.3.1.2C) reveals a k-value of 1.2×10^{-4} s^{-1} for the decrease in the SP band, consistent with an exponential decay function derived for the change of the concentration of the monomeric AuNPs.

In concurrence with the SPR spectral evolution, a clear increase in the Raman bands is observed in the SERS spectral evolution (Figure 3.3.1.3A). Since the Tlcs adsorbed on AuNPs are responsible for the formation of dimers or trimers, the increase in the SERS intensity can also be derived to follow an exponentially-rising rate equation (first order):

$$I_{(SERS)} = I_1(1 \times e^{-kt}) \quad (2)$$

where I_1 is a constant, and k is an apparent rate constant. As shown in Figure 3.3.1.3B, eqn (2) indeed fits the experimental data very well.

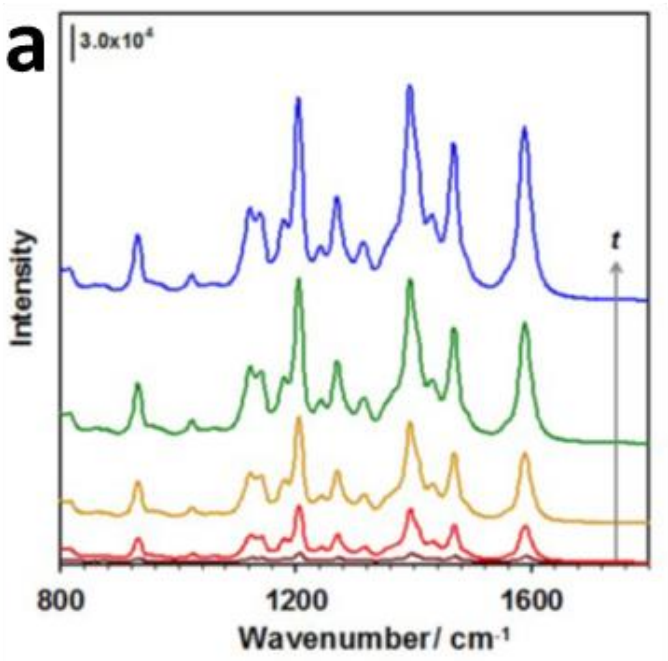

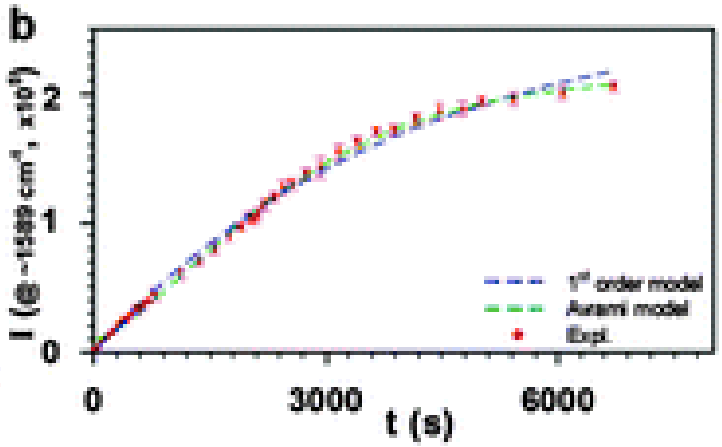

Figure 3.3.1.3. SERS spectral evolution as a function of time for an aqueous solution of Au_{34nm} upon addition of Tlc. Time: 1~6000 s (from red to blue). [Au_{34nm}] = 0.089 nM; [Tlc] = 0.0238 μM. (Integration = counts/20s). (b) Kinetic plot of peak intensity (at 1589 cm^{-1}) (*I*); the first-order model ($y = A_1'(1 - e^{-kt})$) yields $k = 2.6 \times 10^{-4}$ s^{-1}; the Avrami model ($y = A_2'(1 - e^{-ktn})$) yields $k = 3.2 \times 10^{-5}$ s^{-1} and $n = 1.3$.

The fitting yields an apparent rate constant of $k = 2.6 \times 10^{-4}$ s^{-1}. In comparison with the SP band fitting result ($k = 2.8 \times 10^{-4}$ s^{-1}), the SERS fitting result shows a very good agreement. This finding indicates that the SERS effect is directly linked to the spectral evolution of the longer-wavelength SP band, which is consistent with the theoretical calculation results for other nanoparticles.[19] In other words, the kinetic agreement demonstrates that the interparticle J-aggregation of AuNPs by Tlc molecules plays a major role in both SP and SERS spectral evolution.

Note that the first-order kinetic analyses were based on the dimer formation equilibrium (eqn (3)), which was an approximation in view of the nature of aggregative growth that could involve trimers, tetramers, etc. Considering the recent study on the growth of gold nanoparticles in organic solutions by Buhro *et al.*,[21] the aggregative growth can be well described by the Avrami model.[22] This was also confirmed by our recent study on the aggregative growth of gold nanoparticles in aqueous solutions.[20] According to the Avrami model,[20–22] the concentration of the aggregates ($C_{(aggregates)}$), which is proportional

to the intensity of the long-wavelength SP band or the intensity of the SERS peak, can be expressed as:

$$C(\text{aggregates})(\propto A_{(Abs)} \text{ or } I_{(SERS)}) = C\ (1 \times e^{-kt^n}) \quad (3)$$

where C is the proportionality constant, k is the apparent rate constant, and n is the critical growth exponent. Indeed, the use of eqn (3) for the curve fitting of the kinetic data in Figures 3.3.1.2 and 3.3.1.3 is found to be better than the first-order model. The fitting yields $k = 2.6 \times 10^{-5}$ s^{-1} and n = 1.3 for the SP band data in Figure 3.3.1.2B and $k = 3.2 \times 10^{-5}$ s^{-1} and n = 1.3 for the SERS data in Figure 3.3.1.3B, respectively. Again, similar to the first-order model fitting results, the two apparent rate constants are very close. Interestingly, the apparent rate constant from the Avrami model ($\sim 3\times10^{-5}$ s^{-1}) is about one order of magnitude smaller than the first-order model ($\sim 3\times10^{-4}$ s^{-1}), a finding consistent with the expectation of a slower rate for the formation of higher degrees of aggregation than the formation of dimers. As shown in our earlier report,[5] TEM could in principle be used to examine the formation of dimers for samples taken out of solution. However, the propensity for aggregation during the sample drying process prevented us from assessing the dimers at each aggregation stage.

3.3.2 Surface coverage and particle size dependencies. The spectral evolution characteristics were further examined under conditions of different surface coverages of dyes and different sizes of NPs to assess their changes in relation to p–p interaction. For an aqueous solution of low concentration of Tlcs, e.g., 0.218 mM in the presence of AuNPs (13 nm), the bands corresponding to the SP bands of AuNPs and the π–π* bands of Tlcs can be resolved in the spectral evolution (Figure 3.3.2.1A). Theoretically assuming a 100%

adsorption of Tlcs on AuNPs, the number of Tlc molecules at this concentration would correspond to a theoretical surface coverage (θ_T) of 0.18 in the presence of 2.5 nM Au_{13nm}. Experimentally, a clear spectral evolution at ~700 nm is observed, which is similar to that in Figure 3.3.1.2A but at a much slower rate (in 1–2 hours) (Figure 3.3.2.1A). Interestingly, the π–π* bands of Tlc, 514 and 543 nm (514 and 545 nm for Tlc only, dashed line), emerge only after the precipitation starts, as reflected by the decrease in the longer-wavelength SP band (at t ~ 1.3 h). In the presence of 0.155 nM Au_{34nm}, the data at 0.176 mM Tlc (i.e., θ_T = 0.43) showed also a similar spectral evolution of the SP bands (Figure 3.3.2.1B). In this case, the 514 and 543 nm bands are revealed at a somewhat earlier stage of the long-wavelength band appearance, which remains detectable even at the later stage of the spectral evolution and after precipitation. The depression of the π–π* bands of Tlc in the beginning of the spectral evolution is associated with the J-aggregation induced interparticle linkage of AuNPs. The overlapping with the AuNP SP band in the long-wavelength region is partially responsible for the undetectable π–π* bands of Tlc.

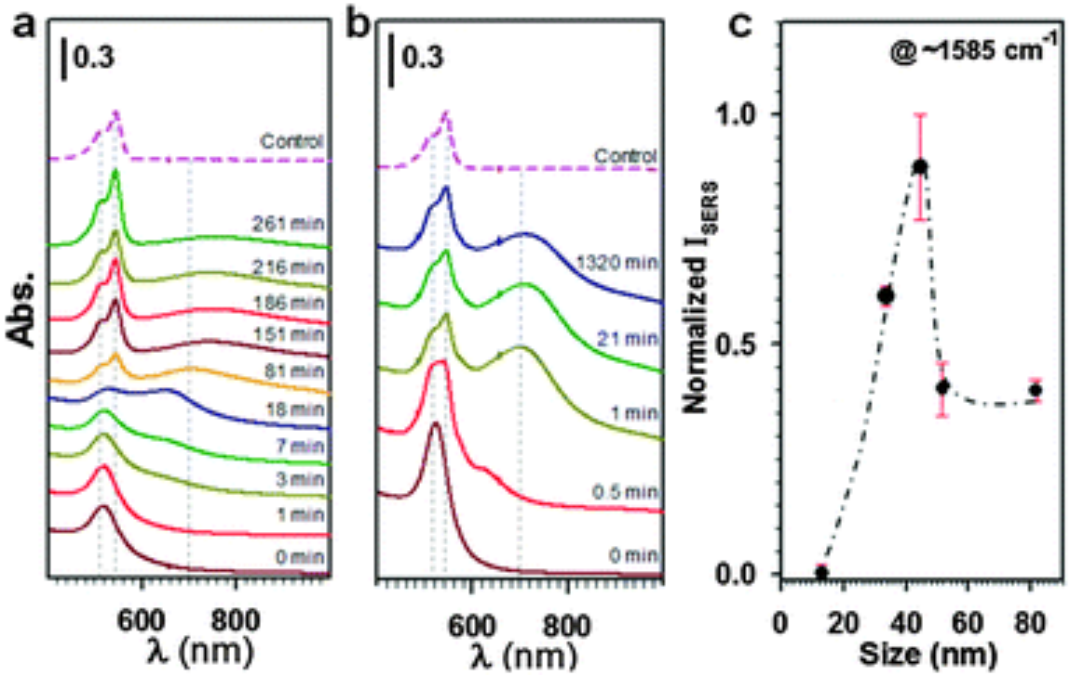

Figure 3.3.2.1. Spectral evolution of surface plasmon resonance bands and SERS intensities for solutions containing AuNPs and cyanine dyes. (a) Upon addition of 0.218 μM Tlc to 2.5 nM Au_{13nm} solution. (b) Upon addition of 0.176 μM Tlc to 0.155 nM Au_{34nm} solution. Control: 0.31 μM Tlc. (c) Plot of the normalized SERS peak intensity at 1585 cm^{-1} (integrated peak area) for J-aggregation of Tlc in the presence of AuNPs of different sizes. Note that there is a difference in particle concentration between (a) and (b) (by a factor of ~16), which is the reason for the observation of a higher degree of aggregation (as reflected by the long-wavelength SP band) for Au_{13nm} than for Au_{34nm}.

The spectral evolution of the SP bands of AuNPs also depends on the particle size. In general, for smaller size particles (Figure 3.3.2.1 and Figure 3.3.2.2), the tendency for inter-particle Tlc linkage seems to be greater, as indicated by the rapid increase in the long-wavelength SP band in comparison with the cases of larger-sized AuNPs. For smaller-sized AuNPs, e.g., Au_{13nm}, upon addition of different amounts of Tlc (Figure 3.3.2.2A), there is a clear transition from the dominance of the SP bands characteristic of AuNPs to the dominance of π–π* bands characteristic of Tlc. Interestingly, as shown by the SERS spectral evolution in terms of peak intensity vs. concentration of Tlc (Figure 3.3.2.2B), a maximum is revealed at the transition point (θ_T = 0.11).

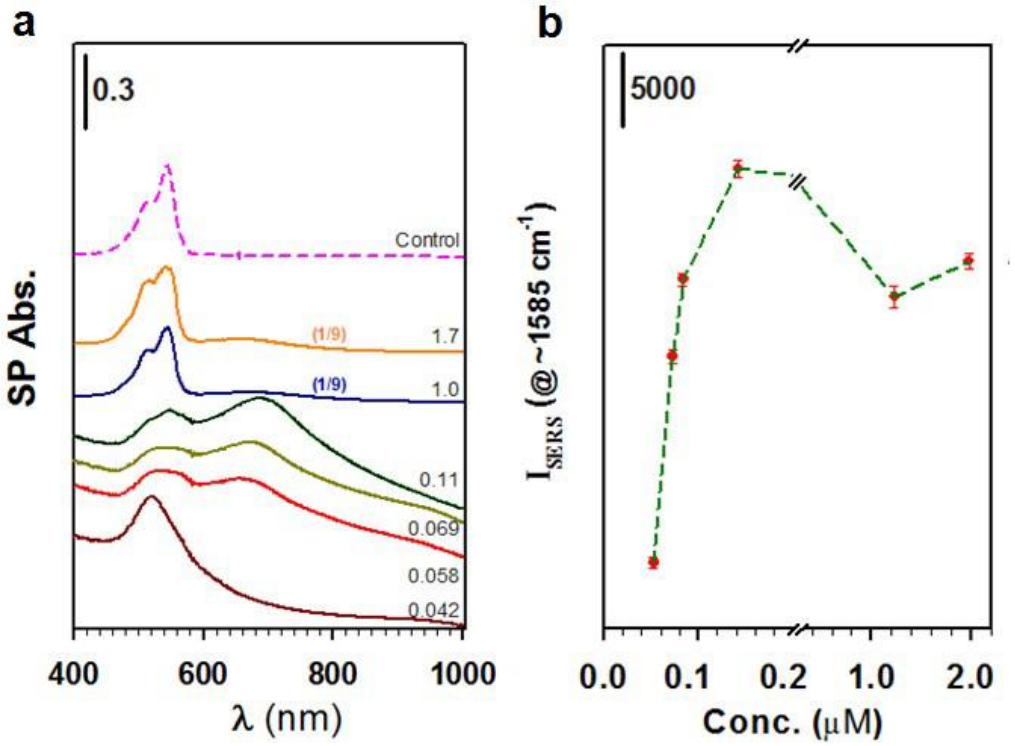

Figure 3.3.2.2. (a) Spectrum for a solution of Au_{13nm} (2.5 nM) upon addition of Tlc (different concentration) in terms of the surface coverages (θ_T) on the gold NPs. Control: 0.31 μM Tlc. (b) Kinetic plot of corresponding SERS peak intensity (I) at ~1585 cm^{-1} vs. Tlc concentration. The surface coverage was estimated based on 3D model of Tlc and densely packed monolayer on gold nanoparticle surface. e.g., for Au_{13nm}, surface area is $4\pi (6.5nm)^2 = 5.31x10^{-12}$ cm^2. For Tlc, which can be treated as a rectangular box with short side, long side, or flat orientation anchoring the surface. The long side is ~2.0 nm, the short side is ~1.4 nm, whereas the thickness is ~0.5 nm. For the short side orientation, the area is $0.70x10^{-14}$ cm^2 for per Tlc, yielding $5.31x10^{-12}$ cm^2 /$0.70x10^{-14}$ cm^2 = 759 Tlc/Au_{13nm}. Similarly, 531 Tlc/Au_{13nm} for short side orientation, and 190 Tlc/Au_{13nm} for flat orientation. The average of Tlc molecules on per Au_{13nm} is ~493. Experimentally, for a solution of Au13nm (2.5 nM), the addition of 0.0528 μM Tlc would yield ~21 Tlc/Au_{13nm}, which in terms of a surface coverage (θ_T) would be 21/493=0.042.

Similar phenomena were also observed for larger-sized particles with subtle differences in the relative spectral evolution for AuNPs and Tlc molecules (see for example Au_{45nm}) (Figure 3.3.2.3). The π–π* bands of Tlc disappear when the long-wavelength SP band appears, as a result of the interparticle π–π* stacking linkage. In this case, the J-band is likely superimposed with the longer-wavelength SP band. This assessment is substantiated by the re-emergence of the π–π* bands when the linked particles precipitate out of the solution. The increase of SERS intensity correlates very well with that of the SP band.

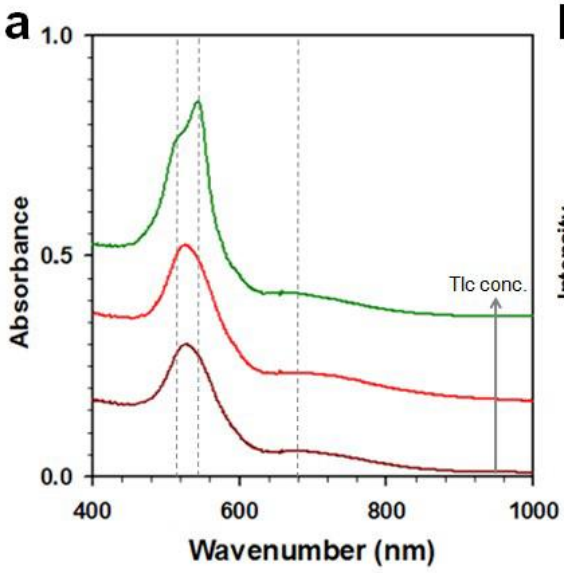

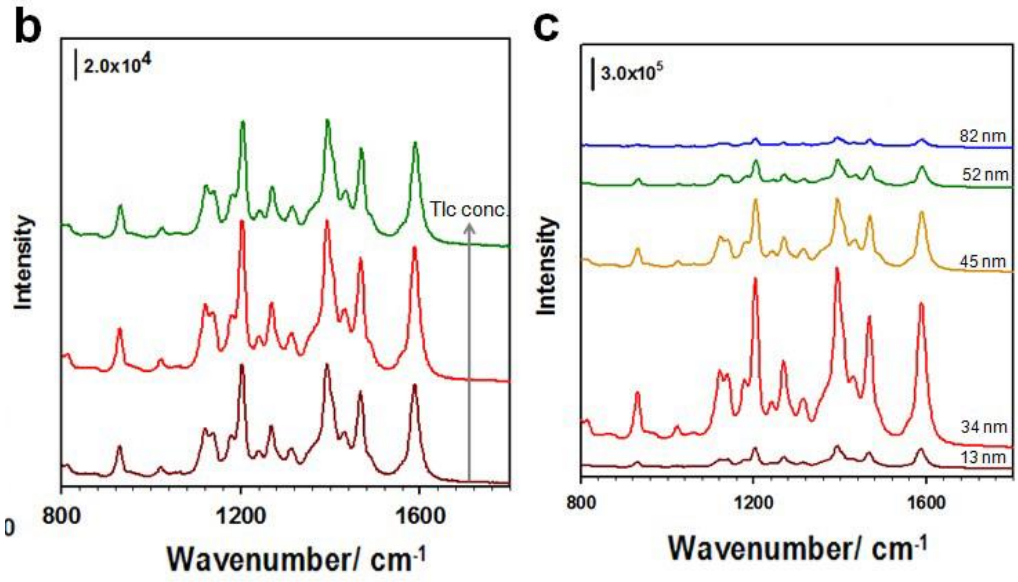

Figure 3.3.2.3. UV-vis and SERS spectra for aqueous solutions of AuNPs in the presence of Tlc. (a) UV-Vis spectra and (b) SERS spectra for a solution of Au_{45nm} (0.0259 nM) upon addition of Tlc dyes in different concentrations: 0.0146 μM (i.e., $\theta_T = 0.10$), 0.0293 μM (i.e., $\theta_T = 0.20$), and 0.146 μM (i.e., $\theta_T = 1.0$). (c) SERS spectra for AuNPs with five different particle diameters (13 nm (2.5 nM, $\theta_T = 0.175$), 34 nm (0.089 nM, $\theta_T = 0.102$), 45 nm (0.0259 nM, $\theta_T = 0.998$), 52 nm (0.0242 nM, $\theta_T = 0.590$) and 82 nm (0.00718 nM, $\theta_T = 1.0$)).

The Raman intensity of Tlc upon J-aggregation in the presence of AuNPs of different diameters is also examined (Figure 3.3.2.3). The results reveal that the intensity increases with the particle size, and interestingly also show a maximum at a particle size of ~50 nm (Figure 3.3.2.1C). This is in sharp contrast to the characteristic of a gradual increase of a plateau as observed for gold nanoparticles in solution due to other inter-particle attraction forces or linkages.[23] The size dependence reflects the red shift of the SP band via plasmonic coupling with the laser excitation (633 nm). It was shown earlier, for a gold substrate immobilized with 5,5'-dithiobis-succinimidyl-2- nitrobenzoate (reporter) labeled 60 nm AuNPs, that a strong coupling between the SP band at a wavelength of ~650 nm and the laser excitation wavelength (633 nm) is responsible for the observation of the maximum SERS effect.[24]

3.3.3 Theoretical simulations of interparticle plasmonic coupling. The plasmonic coupling as a result of interparticle J-aggregation is further assessed by theoretical simulation of the surface plasmon absorption and the electrical field enhancement using the MNPBEM toolbox,[23] which provides useful information for assessing the experimental SP and SERS characteristics. The simulation was based on the calculation of the optical absorption and the scattering of electromagnetic waves by single and dimer AuNPs with the relevant refractive indices defined by the nanoparticles, the dye molecule, and the environment (e.g., solvents), which are different for the naked AuNPs and the core–shell models. By setting up the nanoparticles' boundary conditions and the dielectric environment, the optical absorption and electrical field around the nanoparticles are calculated (Figure 3.3.3.1). In addition to using naked AuNPs with the adsorbed Tlc to define the interparticle distance as a simple model in the dimer (Figure 3.3.3.2), our simulations of dimers considered a ''core–shell'' model (Figure 3.3.3.1A). In comparison with the single AuNP, the plasmonic absorption for the dimer exhibits a new band at longer wavelength due to interparticle plasmonic coupling (Figure 3.3.3.1B). A clear red shift in the wavelength (λ_{max}) (Figure 3.3.3.1C) and an increase in the absorption intensity (Figure 3.3.3.1D) are observed as the particle size is increased; the latter displays a maximum at 55–60 nm. Theoretically a higher degree of interparticle aggregation can be simulated but it is beyond the scope of this work. The interparticle plasmonic coupling leads to more enhancements and red shifts for the plasmonic absorption band with a higher degree of aggregation than the dimer (Figure 3.3.3.2).

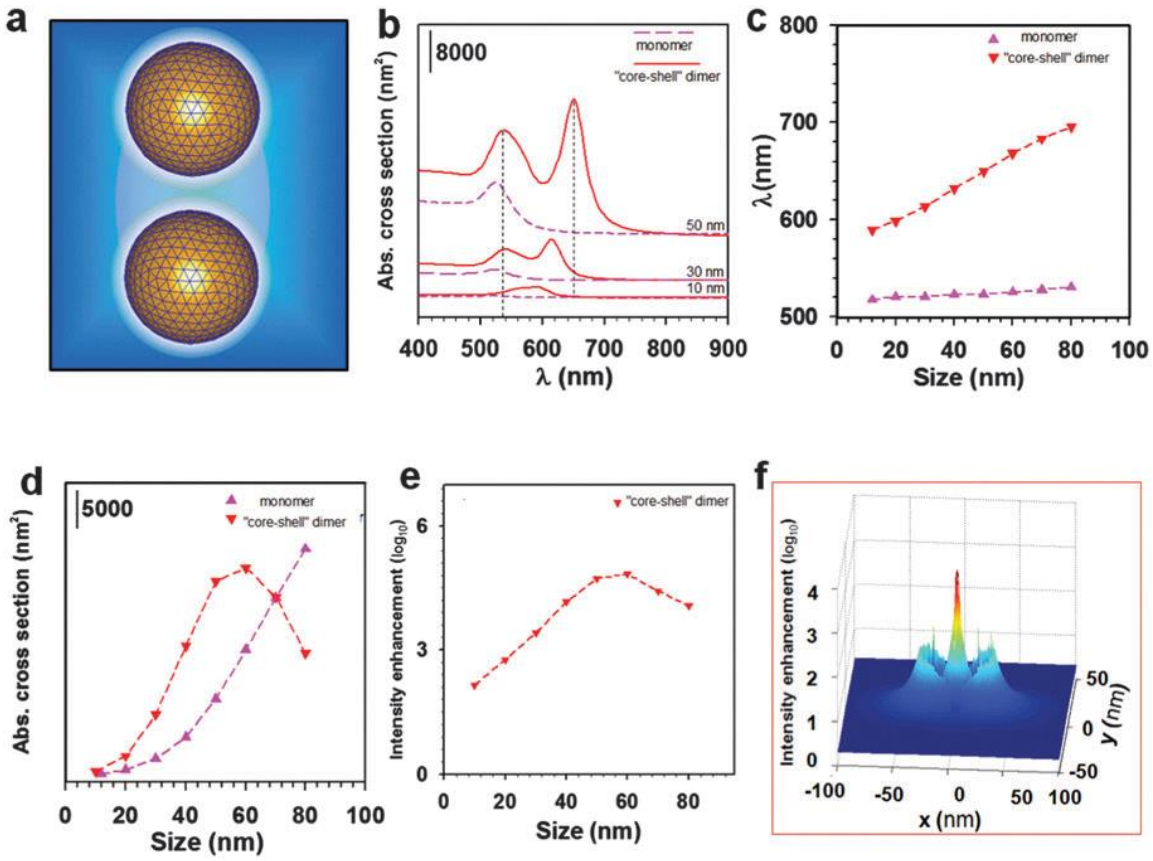

Figure 3.3.3.1. Simulated optical absorbance cross-sections and E-field enhancements upon interparticle plasmonic coupling. (a) A ‘‘core–shell’’ model of a dimer of Tlc-adsorbed AuNPs. (b) Simulated E-field enhancement vs. particle size (the refractive indices: water (1.33) and Tlc (2.40). p–p stacking distance: 0.4 nm, laser excitation: 633 nm). (c) A 3D image for simulated E-field enhancement for a dimer of Au_{30nm}.

The simulated E-field for the ‘‘core–shell’’ dimer shows a clear dependence on the particle size in terms of local intensity enhancement (Figure 3.3.3.1E). The enhanced intensity shows a clear increase with the particle size, displaying a maximum at a size of ~55 nm, which coincides with the particle size for the maximal absorption found for the simulated interparticle plasmonic band as shown in Figure 3.3.3.1D. In the vicinity of the AuNPs of the dimer, the strongest enhancement of the local electric field occurs at the center position between the AuNPs (Figure 3.3.3.1F). The core–shell model’s boundary conditions and the dielectric environment apparently reflect the dimer better. Similar but stronger enhancements can be found for a higher degree of aggregation (Figure 3.3.3.2).

This finding is in agreement with the trend observed for SERS intensity (Figure 3.3.2.1C), and qualitatively consistent with the results reported for previous simulations under relevant conditions.[15,24]

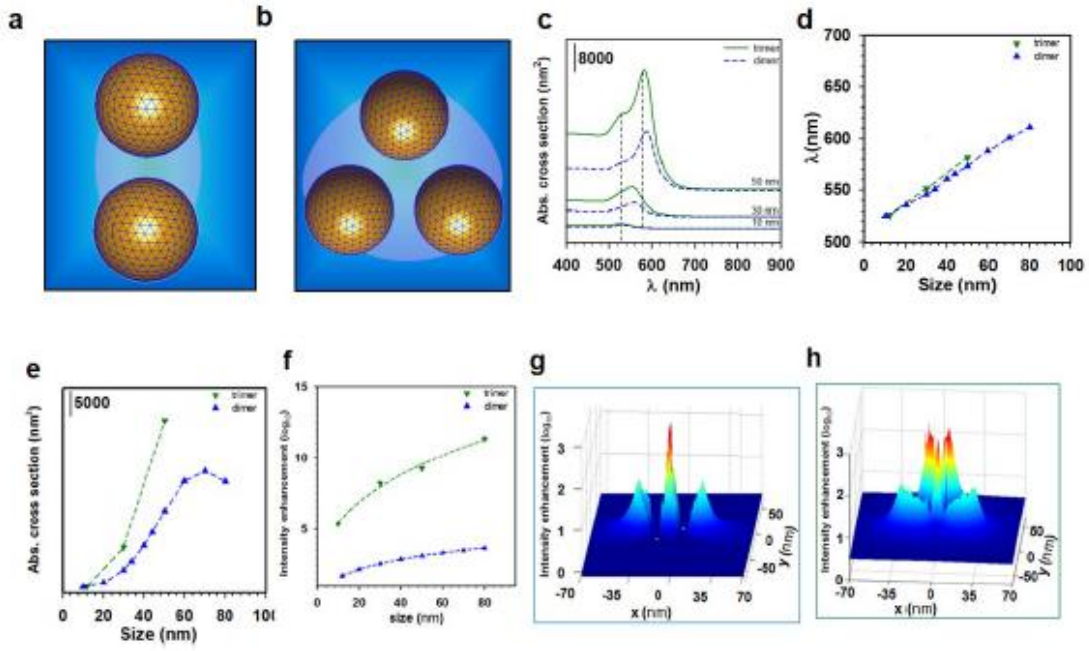

Figure 3.3.3.2. Simulated optical absorbance cross sections and E-field enhancements upon interparticle plasmonic coupling. (a-b) simple dimer (a) and trimer (b) models of AuNPs (naked NPs with adsorbed Tlc defining the interparticle distance). (c) Simulated absorbance cross section for dimer and trimer of AuNPs of different sizes with interparticle distance defined by π–π stacking of Tlc (3.4 nm). (d) Wavelength (λ, nm) at SP band maximum vs. particle size for dimer and trimer. (e) absorbance (Abs.) cross section (nm^2) vs. particle size for dimer and trimer. (f) E-field intensity enhancement (in common logarithm) vs. particle size for dimer and trimer (633 nm laser excitation). (g-h) An example of 3D contour plot for the Efield enhancement for Au_{30nm} dimer (g) and Au_{30nm} trimer (h).

3.4 Conclusion

Taken together, both experimental and the theoretical results reveal a similar dependence of the plasmonic coupling on the particle size in terms of the local E-field enhancement, demonstrating that the surface-enhanced Raman scattering work in concert with the plasmonic coupling. The latter is evidenced by their comparable apparent rate constants in terms of nanoparticle dimerization or the aggregative growth in the solution with the π–π* interaction of J-aggregates defining the interparticle spatial characteristics.

This finding is substantiated by theoretical simulations of the plasmonic coupling, revealing a direct linkage between the spectroscopic signatures. It also highlights an effective pathway for harnessing them for a broad range of applications exploiting the plasmonic and spectroscopic properties of gold nanoparticles, which were traditionally shown to be uncontrollable in most other simple mixings of linker molecules and gold nanoparticles.[22] The finding also has implications for the precise design of dye-labeled nanoprobes for the sensitive detection of chemical or biological species.[22]

References

1. V. V. Shelkovnikov and A. I. Plekhanov, in “Macro To Nano Spectroscopy”, ed. J. Uddin, 2012, pp. 317–356.
2. V. V. Prokhorov, S. I. Pozin, D. A. Lypenko, O. M. Perelygina, E. I. Mal'tsev and A. V. Vannikov, World J. Nano Sci. Eng., 2011, 1, 67.
3. O. Shklyarevskiy, P. C. M. Christianen, E. Aret, H. Meekes, E. Vlieg, G. Deroover, P. Callant, L. van Meervelt and J. C. Maan, J. Phys. Chem. B, 2004, 108, 16386 CrossRef CAS.
4. J. Kim, A. Watson, M. Henary and G. Patonay, Top. Heterocycl. Chem., 2008, 14, 31 CAS.
5. I.-I. S. Lim, F. Goroleski, D. Mott, N. Kariuki, W. Ip, J. Luo and C. J. Zhong, J. Phys. Chem. B, 2006, 110, 6673 CrossRef CAS PubMed.
6. G. Caputo and N. Pinna, J. Mater. Chem. A, 2013, 1, 2370 CAS.
7. H. Jia, X. Bai and L. Zheng, CrystEngComm, 2012, 14, 2920 RSC.
8. M. Kanehara, E. Kodzuka and T. Teranishi, J. Am. Chem. Soc., 2006, 128, 13084 CrossRef CAS PubMed.

A. Vujačić, V. Vasić, M. Dramićanin, S. P. Sovilj, N. Bibić, J. Hranisavljevic and G. P. Wiederrecht, J. Phys. Chem. C, 2012, 116, 4655 Search PubMed.

9. G. P. Wiederrecht, G. A. Wurtz and J. Hranisavljevic, Nano Lett., 2004, 4, 2121 CrossRef CAS.
10. J. Hranisavljevic, N. M. Dimitrijevic, G. A. Wurtz and G. P. Wiederrecht, J. Am. Chem. Soc., 2002, 124, 4536 CrossRef CAS PubMed.
11. W. E. Doering and S. Nie, Anal. Chem., 2003, 75, 6171 CrossRef CAS PubMed.
12. K. Kneipp, H. Kneipp and J. Kneipp, Acc. Chem. Res., 2006, 39, 443 CrossRef CAS PubMed.
13. Y. C. Cao, R. Jin and C. A. Mirkin, Science, 2002, 297, 1536 CrossRef CAS PubMed.
14. E. Hao and C. G. Schatz, J. Chem. Phys., 2004, 120, 357 CrossRef CAS PubMed.
15. L. Q. Lin, E. Crew, H. Yan, S. Shan, Z. Skeete, D. Mott, T. Krentsel, J. Yin, N. A. Chernova, J. Luo, M. H. Engelhard, C. Wang, Q. B. Li and C. J. Zhong, J. Mater. Chem. B, 2013, 1, 4320 RSC.
16. X. Lan, Z. Chen, X. Lu, G. Dai, W. Ni and Q. Wang, ACS Appl. Mater. Interfaces, 2013, 5, 10423 CAS.
17. (a)K. Lee and J. Irudayaraj, Small, 2013, 9, 1106 CrossRef CAS PubMed ; (b) S. L. Kleinman, B. Sharma, M. G. Blaber, A. Henry, N. Valley, R. G. Freeman, M. J. Natan, G. C. Schatz and R. P. Van Duyne, J. Am. Chem. Soc., 2012, 135, 301 CrossRef PubMed ; (c) D. K. Lim, K. S. Jeon, H. M. Kim, J. M. Nam and Y. D. Suh, Nat. Mater., 2010, 9, 60 CrossRef CAS PubMed ; (d) P. Nordlander and C. Oubre, Nano Lett., 2004, 4, 899 CrossRef CAS ; (e) H. Lee, J. H. Lee, S. M. Jin, Y. D. Suh and J. M. Nam, Nano Lett., 2013, 13, 6113 CrossRef CAS PubMed ; (f) L. Chuntonov and G. Haran, Nano Lett., 2011, 11, 2440 CrossRef CAS PubMed .
18. (a)Y. S. Yamamoto, Y. Ozaki and T. Itoh, J. Photochem. Photobiol., A, 2014, 21, 8 Search PubMed; (b) K. Yoshida, T. Itoh, H. Tamaru, V. Biju, M. Ishikawa and Y. Ozaki, Phys. Rev. B: Condens. Matter Mater. Phys., 2010, 81, 115406 CrossRef; (c) T. Itoh, Y. S. Yamamoto, H. Tamaru, V. Biju, S. Wakida and Y. Ozaki, Phys. Rev. B: Condens. Matter Mater. Phys., 2014, 89, 195436 CrossRef; (d) T. Itoh, Y. S. Yamamoto, H. Tamaru, V. Biju, N. Murase and Y. Ozaki, Phys. Rev. B: Condens. Matter Mater. Phys., 2013, 87, 235408 CrossRef.

19. P. N. Njoki, J. Luo, M. M. Kamundi, I.-I. S. Lim and C. J. Zhong, Langmuir, 2010, 26, 13622 CrossRef CAS PubMed.

20. S. P. Shields, V. N. Richards and W. E. Buhro, Chem. Mater., 2010, 22, 3212 CrossRef CAS.

21. (a)H. W. Cheng, J. Luo and C. J. Zhong, J. Mater. Chem. B, 2014, 2, 6904 RSC; (b) Z. Skeete, H. W. Cheng, C. Elizabeth, L. Q. Lin, S. Y. Shan, W. Zhao, H. Cronk, J. Luo, Y. J. Li, Q. W. Zhang and C. J. Zhong, ACS Appl. Mater. Interfaces, 2014, 6, 21752 CrossRef CAS PubMed.

22. (a)U. Hohenester, Comput. Phys. Commun., 2014, 185, 1177 CrossRef CAS PubMed; (b) U. Hohenester and A. Trügler, Comput. Phys. Commun., 2012, 183, 370 CrossRef CAS PubMed.

23. J. D. Driskell, R. J. Lipert and M. D. Porter, J. Phys. Chem. B, 2006, 110, 17444 CrossRef CAS PubMed.

Chapter 4

SERS Detection of Protein Mediated Assembly of Gold Nanoparticles in Solution

4.1 Introduction

Biomolecular recognition is important in diagnosis and therapeutic treatments.[1-5] This recognition requires highly sensitive and selective probes for accurate detection. One detection method is based on surface enhanced Raman scattering (SERS), which exploits the interparticle "hot-spot" accompanied with protein mediated assembly of gold nanoparticles in solution for signal amplification.

Although there have been extensive studies in the targeting and detection of antigens, many of them take a long period of time for sample preparation.[6-12] Some of the methods that were used to eliminate the time required in the sample preparation include the employment of magnetic nanomaterials and detecting the assemblies in solution.[6,11-13] Previously we reported in Lim *et al.* the development of gold based nanoprobes used for the detection of protein A (ProA), a membrane protein on the bacterium *Staphylococcus aureus*.[6] In this report, the analysis of the protein targeting was observed through the functionalization of magnetic coated Au and metallic Au nanoprobes by an increase in the SERS signal upon detection. The magnetic cores allowed for the cleaning of the

nanoprobes to remove the unbound antigens and isolation of the assemblies in a localized area for detection. Similarly to other researchers, the drying involved with the sample preparation increases the time from assembly to detection.

Although these devices have significant enhancements through sensitive and selective devices, the need to design rapid point-of-care devices is essential for the detection of protein biomarkers for disease and cancer. In this section, we describe findings from an investigation of the use of Raman-labled gold and bio-conjugated gold nanoparticles for the detection of ProA in solution as a model protein. In this system, a solution containing gold nanoparticles (AuNPs) functionalized with Raman reporter label *p*-mercaptobenzoic acid (MBA) and biomolecules (protein A or goat anti-rabbit IgG) were assembled to their complementary biomolecule, producing an interparticle "hot-spot" allowing for the monitoring of the diagnostic SERS bands (**Scheme 4.1.1)**.

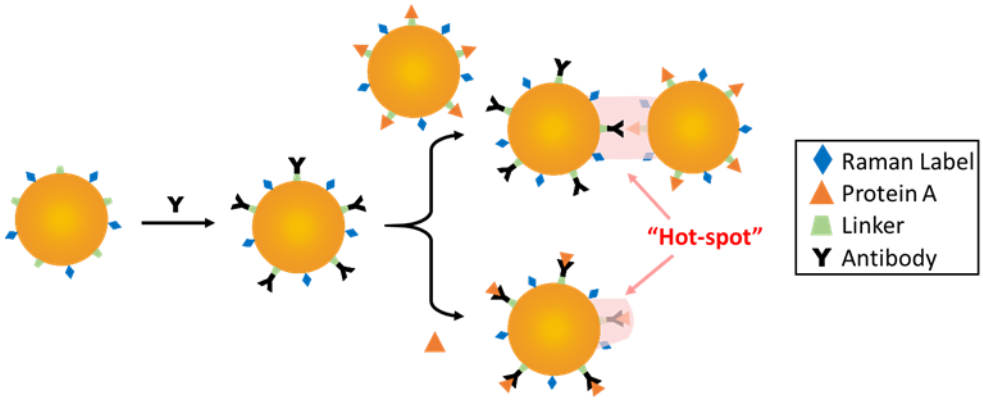

Scheme 4.1.1. Illustrations of gold nanoparticle-based SERS detection strategy. This example uses a Protein A and goat anti-rabbit immunoglobulin G. Formation of "hot-spots" for SERS detection upon the assembly of proteins and antibodies when conjugated to MBA/AuNP. Note: The drawing with few proteins, antibodies, and MBA molecules is only to simplify the illustration.

The study involves optimization of Raman labeling of gold nanoparticles and protein mediated nanoparticle assembly in solution phase for rapid SERS detection. The changes in the concentration of the Raman reporter in labeling gold nanoparticles were

studied for further control and optimization of this system. Similarly, the optimization of this system in terms of bioconjugation will be studied and the detection capability of the optimized system will be presented. The investigation aims to provide some insight into the design of nanoprobes for SERS detection of proteins in solution.

4.2 Experimental.

Chemicals and materials. Hydrogen tetrachloroaurate (III) hydrate ($HAuCl_4$), sodium citrate (99%), sodium acrylate (97%), *p*-mercaptobenzoic acid (MBA) were purchased from Sigma-Aldrich (Milwaukee, WI) and used as received. Protein and antibody were purchased from Pierce Biotechnolgy, Inc. (Rockford, IL). Water was purified with a Millipore Milli-Q water system (18.2 MΩ).

Experimental procedures Acrylate – capped gold nanoparticles (51.6 ± 2.0 nm) were synthesized following a seeded growth procedure.[10,11] Protein A (proA) was dissolved in deionized water at a concentration of 1.3e-3 M and the antibody (goat anti-rabbit immunoglobulin G) was used as purchased with a concentration of 9.6e-5 M. The conjugation of AuNPs with the antibody (Ab) was similar to the reported procedure[6] to form Ab/AuNP, and the same for the conjugation with the protein to form ProA/AuNP. The labeling of AuNPs with MBA (MBA/AuNP) was achieved by following a previously reported procedure.[6,9]

Briefly, the aqueous solution of AuNPs was first reacted with the Raman label, different concentrations of MBA ranging from 1.1 - 13 μL (2 mM) and gently shaken for a maximum of 2 hrs. The protein-coupling agent, DSP (7.8 μL of 1 mM), was then added to the solution and gently shaken from 30 min to 2 hrs. The biomolecules were then added to the solution and gently shaken from 30 min to ~15 hrs (5 μL of antibody (Ab; antirabbit

IgG; stock 2.4 mg·ml^{-1}) or 0.5 μL of protein (Protein A; stock 53 mg·ml^{-1}). Centrifuging the solution was not performed, because the nanoparticle assembly enhances SERS, making the biomolecule interaction negligible. The resulting protein-capped nanoparticles were stored at room temperature.

Surface coverage of MBA (θ) theoretically estimated for 52-nm AuNPs was 0.07, 0.5 and 0.7. For the free protein (or antibody) assembly of gold nanoparticles in solution, 0.5 μL of protein A (10 μM) (or 5 μL of antibody (2.4 mg·ml^{-1})) was added to a solution containing 0.5 mL of Ab/AuNP (or ProA/AuNP) and gently shaken for ~15 hrs or analyzed immediately. For the bound protein (or antibody) assembly of gold nanoparticles in solution, 0.5 mL of ProA/AuNP (0.5 mL of Ab/AuNP) was added to a solution containing 0.5 mL of Ab/AuNP (0.5 mL of ProA/AuNP) and analyzed in the same timeframe as the free assembly. The assembly process was monitored-using Raman spectroscopy before and after centrifugation at 14000 rpm for 15 min. The time used to conjugate the NPs through shaking were to ensure the maximum adsorption and decreased to obtain maximum signal with minimum time.

Instrumentation. SERS spectra were measured by an Advantage 200A Raman spectrometer (DeltaNu) and the data were collected from 200 to 3400 cm^{-1}. The laser power and wavelength were 5 mW and 632.8 nm, respectively. The integration time is 60 s for each set of data presented, as noted in the Figure captions. The hydrodynamic diameter was analyzed using Nanosight Tracking Analysis by Malvern NS300.

4.3 Results and Discussion

4.3.1. Determination of Surface Coverage of Raman Label on Gold NPs

The amount of molecules on the surface of the NPs are very important to control when using a mixed monolayer system for the detection of target molecules.[1] In this case, the determination of the amount of Raman Label (RL) present on the surface is essential to obtain signal but too much will compromise the addition of the capture agents. In order to optimize the signal, the coverage of the RL MBA must be determined. Figure 4.3.1.1 shows the comparison between the concentration of the RL and the intensity of the MBA 1590 cm^{-1} peak. It is clear that the coverage follows the Langmuir isotherm pattern, where a MBA coverage of 3 μM appears to exhibit full monolayer coverage of MBA (and DSP) on the AuNP surface. As far as this type of biomolecule detection, it also showed that detection was best in conditions when detecting biomolecules free in solution or when conjugated to AuNPs. In both cases, it is evident that there is a sequential effect upon the additon of biomolecules to the solution.

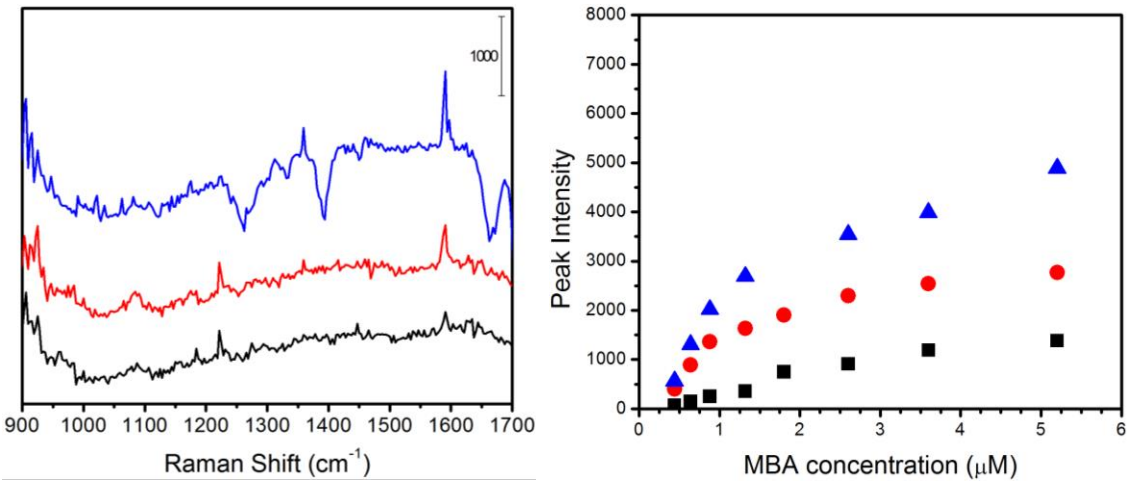

Figure 4.3.1.1. (A) SERS spectra of protein bound NPs in solution (black – MBA, red – Ab bound NPs, blue – assembly between protein and antibody bound NPs (Note: assembly addition of antibody bound NPs to a solution of protein bound NPs showed a similar trend but slightly higher peak).

Figure 4.3.1.2 shows the overall spectra for biomolecule detection using 3 μM MBA, which based on our previous data (and Figure 4.3.1.1) portrays to be optimal for this

type of biomolecule detection. This figure demonstrates the increase in signal intensity as the NP was functionalized and the assembly progressed prior to centrifugation. It is also important to note that NP conjugated with proA for detection expressed a large peak at 1575 cm^{-1}, possibly from the protein A or another smaller MBA diagnostic peak. This concentration will be used for the future concentrations in this section.

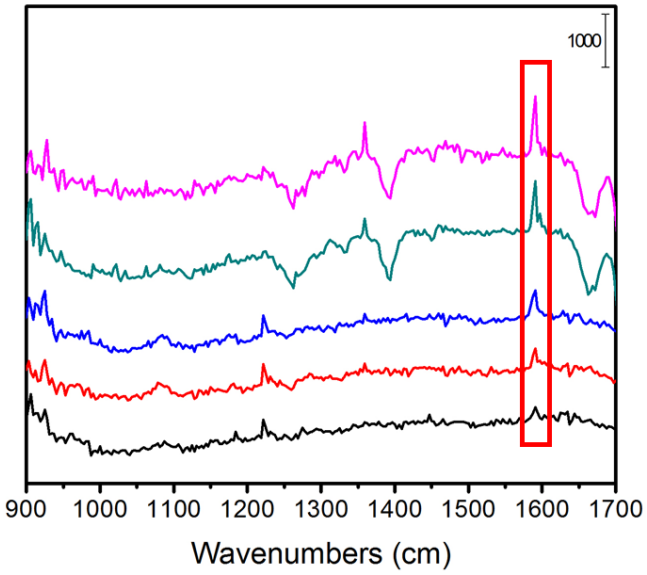

Figure 4.3.1.2. SERS spectra (integration time 60 s) for the assembly of 52 nm MBA/Au NPs ($\theta \approx 200\%$ theoretical) by protein A and antibody. Depicts evolution of 1590 cm^{-1} MBA peak in respect to protein-antibody assembly (MBA – black, with DSP – red, with capture antibody (blue), assembly with target protein in solution (cyan) and conjugated to a NP (magenta)). Proof of concept that assembly can be observed in real-time in solution. (Also observe evolution of 1575 cm^{-1} peak when protein A is introduced into the system)

4.3.2. Optimization of Protein Linkage on Gold NPs

4.3.2.1. Stability of Nanoprobes

In optimizing the NP-based sensor for detection the signal from the protein recognition was observed to determine the stability of the linkers in solution over time and in the presence of buffers. The pH of the NPs were tested before and after surface functionalization and were found to be between 6 and 8, which are reasonably neutral pH measurements. Upon resuspension in phosphate buffers of different pH (4,6,7,12), the

shifting of the SP bands were monitored using UV-Vis**.** It was found that the larger NPs (50 nm) remained suspendable in the phosphate buffer and were independent of the raman label (MBA) (Figure 4.3.2.1.1A) and protein-linker (DSP) (Figure 4.3.2.1.1B), however they showed signs of aggregation by slight color change and the formation of a secondary peak in the UV-Vis spectra (Figure 4.3.2.1.1). Although NPs greater than 50 nm were found to be suspendable in phosphate buffer, they appeared to be the most stable in deionized water, by lack of SP shifting.

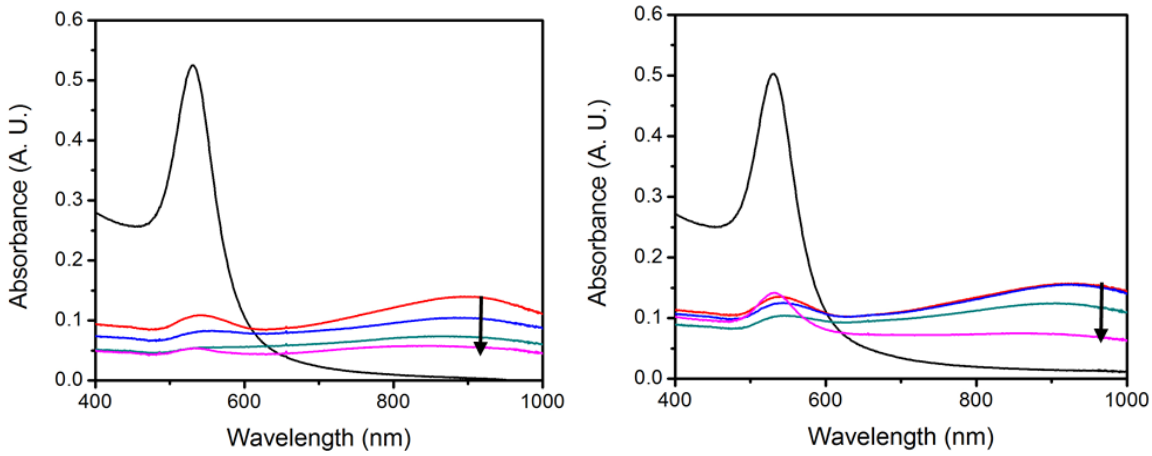

Figure 4.3.2.1.1. UV-Vis spectra of the change in SP band as the buffer increases compared to the original solution in deionized water (black) for NPs capped with MBA alone (A) and MBA and DSP (B). Note the increase denoted by the arrow (pH: 4, 6,7, 12).

The stability of the nanoprobes were considered by monitoring the SERS peak intensity before and after the NPs were assembled by protein-antibody binding and after a few days (Figure 4.3.2.1.2). The peak height of the 1590 cm^{-1} MBA peak, showed an increase in signal after the addition of protein (Figure 4.3.2.1.2(B)) as expected. However, after the NPs were assembled and reexamined over a length of time it was evident that the nanoprobes linked with EDC decreased in signal, whereas the DSP linked probes continued to increase. The decrease in signal of the EDC nanoprobes could be due to two mecahnisms:

(1) the destabilization or desorption of the molecules from the NP surface or (2) the further aggregation of the NPs by the antigen recognition which resulted in the decrease in excitation from the laser at this wavelength. The cause of the changes in intensity over time, is more likely due to the continued aggregation of the NPs requiring more energy to excite the surface electrons; however further investigation needs to be conducted.

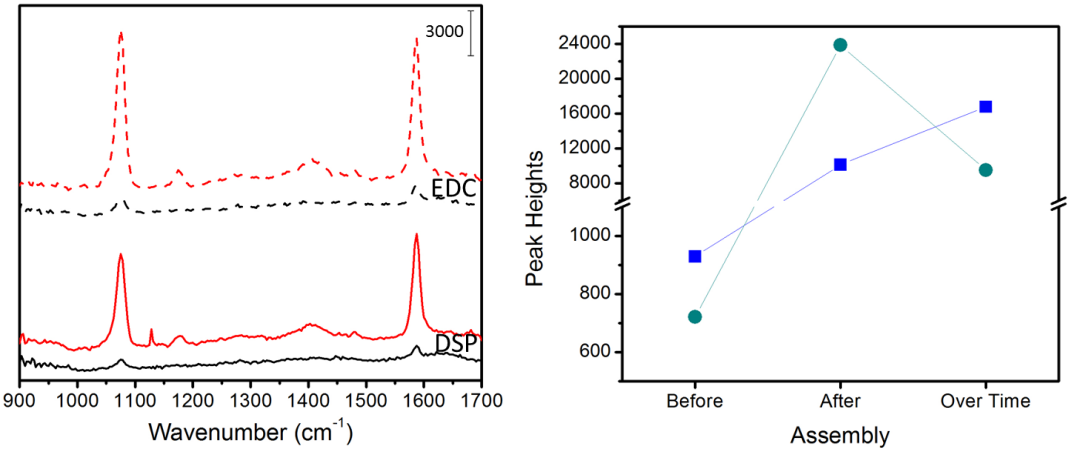

(A) (B)

Figure 4.3.2.1.2. The SERS spectra (A) and the peak heights analysis (B) of the 1590 cm^{-1} peak for the NP assembly for DSP- and EDC-linked nanoprobes after centrifuge. DSP- ((A) solid, (B) blue) and EDC-linked ((A) dashed, (B) cyan) nanoprobes.

4.3.2.2. Determination of Protein Linkage on Gold Nanoparticles

Controversy has occurred over the different protein linker available in these systems. Many researchers claim the application of DSP as a linker, result in the hydrolysis of the nanoprobes; whereas who use EDC reported more controllable results, similar to that observed in Figure 4.3.2.1.2.[1,2] To determine the best linker used in the detection of proteins using these nanoprobes, both protein linkers were tested using the optimal MBA concentration (Figure 4.3.2.2.1). This figure shows the SERS spectra of the assembly with the two protein linkers over 3 different target ProA concentrations before and after centrifugation. The assembly with DSP showed a slight increase in the SERS spectra

before centrifugation, however in post-centrifugation there were significant changes observed. These were correlated to the increase in the peak intensity at the 1590 cm^{-1} peak (Figure 4.3.2.2.1E).

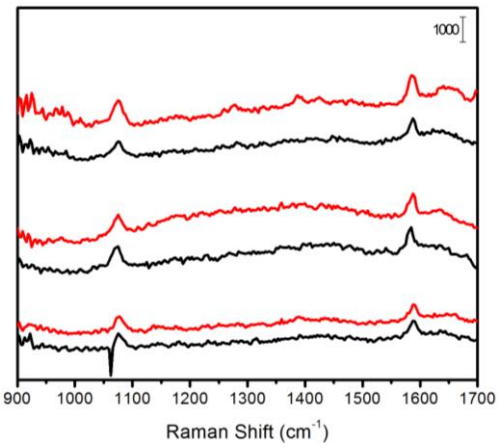

(A)

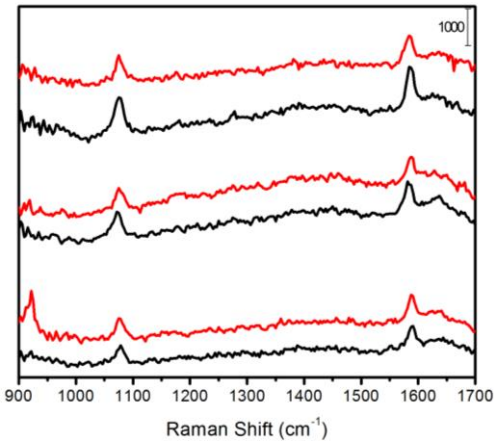

(B)

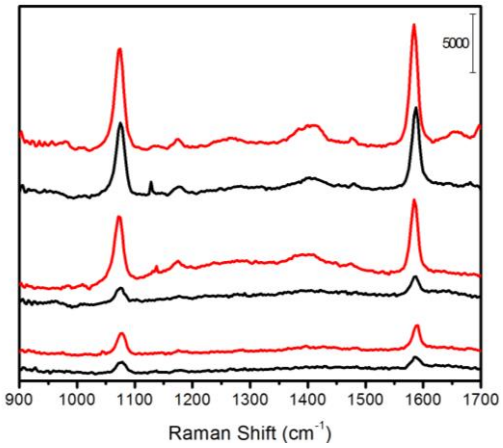

(C)

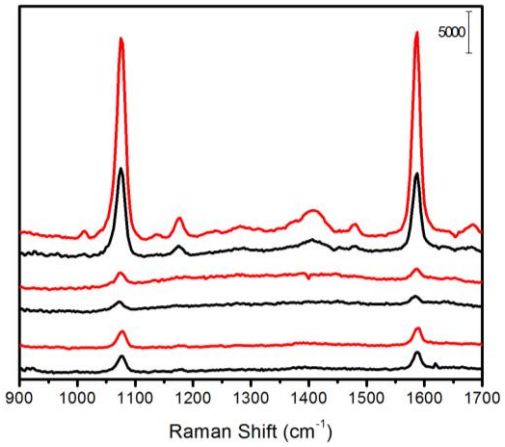

(D)

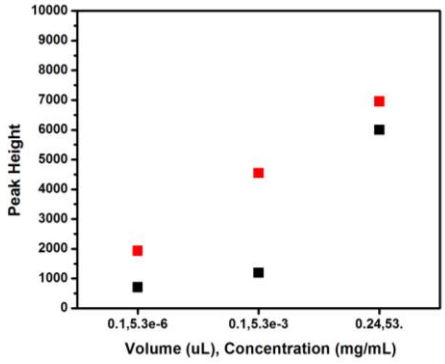

(E)

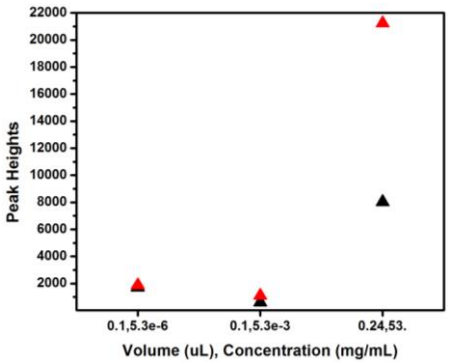

(F)

Figure 4.3.2.2.1. DSP (A, C, E) and EDC (B, D, F) linked NP-based systems before (black) and after (red) assembly in the presence of different protein concentrations (0.24, 53 – dotted line; 0.1, 5.3e-3 – dashed line; 0.1, 5.3e-6 – solid line), before (A, B) and after (C, D) centrifugation, and peak heights at the 1590 cm^{-1} peak (E, F).

Alternatively, the assembly with EDC showed the same slight increase before centrifugtation, however after centrifugation the peak intensities were significantly higher than DSP (Figure 4.3.2.2.1B, D). Based on the peak heights from the 1590 cm^{-1} peak, the change in intensity as the concentration increased showed an exponential increase (Figure 4.3.2.2.1F). The larger intensity demonstrates that the EDC assembly can detect a lower concentration of protein than DSP.

4.3.3. Nanoparticle Size Effect on SERS Intensity

The protein assembly of nanoprobes using EDC linker was analyed in SERS comparing the assembly of different NP size pairings (Figure 4.3.3.1). The NP pairings of the same size (homo – sized) dimers show an increase in signal with the introduction of the target protein, however it also shows a decrease in signal as the NP sizes were increased (Figure 4.3.3.1A). Similar findings were observed with the different size (hetero – sized) dimers (Figure 4.3.3.1B**)**, as well as in the assembly before it was centrifuged (spectra not shown). On the other hand, the difference in peak intensities before and after the assembly demonstrated that a maximum intensity is observed from the 60 nm pairings after centrifugation with 80 nm pairings exhibiting a slightly larger signal before centrifuge. The hetero – sized dimers show no significant increase before centrifuge, but after centrifugation the 4080 nm pairings exhibited a larger intensity (Figure 4.3.3.1C). In comparison, the 60 nm homo – sized pairings exhibit a larger intensity than the 4080 nm hetero – sized pairings; this effect may be due to the concentrations of the NPs used where

smaller NPs typically have a larger conentration than larger sized NPs. Considering the intensities of the NP pairings, further analysis of the NP effect on assembly needs to be considered to further determine the effect size has on the protein-protein interactions. Preliminary studies of the changes in hydrodynamic diameter of these NP assemblies with different size pairings show an increase in the hydrodynamic diameter both before and after assembly and with the different NP sizes. This strongly correlates the SERS data in that the decrease in SERS intensity of the homo – sized pairings after 60 nm, could be due to the increase in diameter after assembly where 60 nm pairings expressed 78.1 nm hydrodynamic diameter and 80 nm pairings showed 95.2 nm diameter. This further aggregation would require more energy than provided using a 633 nm laser, causing this decrease in signal. The hetero – sized NP pairings also exhibited an increase in hydrodynamic diameter (79.1 nm for 4060 and 86.2 nm for 4080), however the SERS intensity continued to increase. This unexpected result raises the assumption that NP pairings with a hydrodynamic diameter greater than 90 nm require a stronger laser to monitor NP-based protein recognitions in solution.

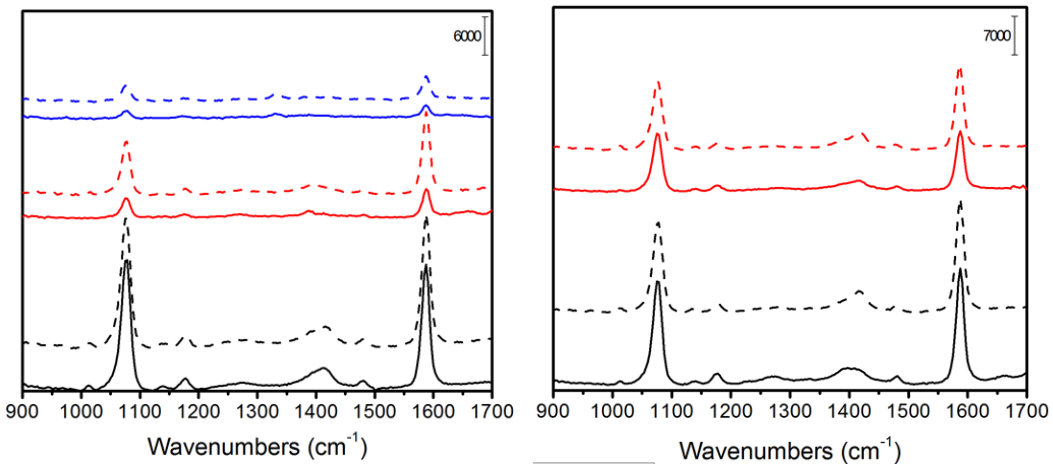

(A) **(B)**

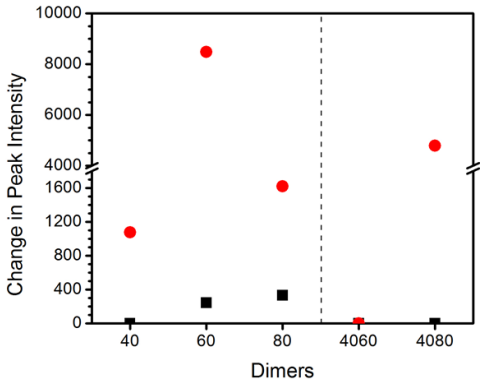

Figure 4.3.3.1. SERS spectra of EDC-linked protein assembly of different NP pairings: homo – sized NP dimers of 40 (black), 60 (red), and 80 (blue) (A); hetero – sized NP pairing of 4060 nm (black) and 4080 nm (red) (B). The difference in peak intensity of the 1590 cm^{-1} MBA peak before (black) and after (red) centrifugation (C). Note the change in intensity is the difference before and after assembly.

4.4 Conclusions

In conclusion, the formation of SERS "hot-spots" by antigen recognition with AuNPs have been demonstrated for the detection of ProA in solution. This is supported by the observed increase and decrease of the SERS signals from a Raman reporter label on gold nanoparticles of desired sizes for achieving an optimal SERS effect. However, the signals observed in many cases were limited in intensity. Also the time allotted for sample preparation in these systems were not ideal, but the findings present here show that there is room for improvement. The data presented here also demonstrates the applicability of the two protein linkers and their limitations in terms of target protein concentrations. Further research needs to be conducted to better adapt the system to solution-phase detection and then to other protein recognitions.

References

1. Lopez, A.; Lovato, F.; Oh, S. H.; Lai, Y. H.; Fillbrun, S.; Driskell, E. A.; Driskell, J.D. SERS immunoassay based on the capture and concentration of antigen-assembled gold nanoparticles. *Talanta* **2016**, 146, 388-393.

2. Pollitt, M. J., Buckton, G.; Piper, R.; Brocchimi, S. Measuring antibody coatings on gold nanoparticles by optical spectroscopy. *RSC Adv.* **2015**, *5*, 24521-24527.

3. Tan, G.; Kantner, K.; Zhang, Q.; Soliman, M.; del Pino, P.; Parak, W.; Onur, M.; Valdeperez, D.; Rejman, J.; Pelaz, B. Conjugation of Polymer-Coated Gold Nanoparticles with Antibodies—Synthesis and Characterization. Nanomaterials 2015, 5 (3), 1297–1316 DOI: 10.3390/nano5031297.

4. Crew, E.; Lim, S.; Yan, H.; Shan, S.; Yin, J.; Lin, L.; Loukrakpam, R.; Yang, L.; Luo, J.; Zhong, C. J. Biomolecular recognition: Nanotransduction and nanointervention. *ACS Symp. Ser.* **2012**, *1112*, 119–146 DOI: 10.1021/bk-2012-1112.ch005.

5. Cheng, H. W.; Luo, J.; Zhong, C. J. SERS nanoprobes for bio-application. *Front. Chem. Sci. Eng.* **2015**, *9* (4), 428–441 DOI: 10.1007/s11705-015-1536-0.

6. Lim, I.-I. S.; Njoki, P. N.; Park, H.-Y.; Wang, X.; Wang, L.; Mott, D.; Zhong, C.-J. Gold and magnetic oxide/gold core/shell nanoparticles as bio-functional nanoprobes. *Nanotechnology* **2008**, *19* (30), 305102 DOI: 10.1088/0957-4484/19/30/305102.

7. Lim, S. I.; Zhong, C.-J. Molecularly Mediated Processing and Assembly of Nanoparticles: Exploring the Interparticle Interactions and Structures. *Acc. Chem. Res.* **2009**, *42* (6), 798–808 DOI: 10.1021/ar8002688.

8. Skeete, Z.; Cheng, H.; Crew, E.; Lin, L.; Zhao, W.; Joseph, P.; Shan, S.; Cronk, H.; Luo, J.; Li, Y.; et al. Design of Functional Nanoparticles and Assemblies for Theranostic Applications. *ACS Appl. Mater. Interfaces* **2014**, *6* (24), 21752–21768 DOI: 10.1021/am502693t.

9. Driskell, J. D.; Larrick, C. G.; Trunell, C. Effect of Hydration on Plasmon Coupling of Bioconjugated Gold Nanoparticles Immobilized on a Gold Film Probed by Surface-Enhanced Raman Spectroscopy. *Langmuir* **2014**, 30, 6309-6313.

10. Crew, E.; Yan, H.; Lin, L.; Yin, J.; Skeete, Z.; Kotlyar, T.; Tchah, N.; Lee, J.; Bellavia, M.; Goodshaw, I.; et al. DNA assembly and enzymatic cutting in solutions: a gold nanoparticle based SERS detection strategy. *Analyst* **2013**, *138* (17), 4941 DOI: 10.1039/c3an00683b.

11. Park, H.-Y.; Schadt, M. J.; Wang, L.; Lim, I.-I. S.; Njoki, P. N.; Kim, S. H.; Jang, M.-Y.; Luo, J.; Zhong, C.-J. Fabrication of magnetic core@shell Fe oxide@Au nanoparticles for interfacial bioactivity and bio-separation. *Langmuir* **2007**, *23* (17), 9050–9056 DOI: 10.1021/la701305f.

12. Njoki, P. N.; Lim, I. I. S.; Mott, D.; Park, H. Y.; Khan, B.; Mishra, S.; Sujakumar, R.; Luo, J.; Zhong, C. J. Size correlation of optical and spectroscopic properties for gold nanoparticles. *J. Phys. Chem. C* **2007**, *111* (40), 14664–14669 DOI: 10.1021/jp074902z.

13. Q. Yang, J. Liang, H. H. Probing the interaction of magnetic iron oxide nanoparticles with bovine serum albumin by spectroscopic techniques. *J. Phys. Chem. B* **2009**, *113*, 10454–10458.

Chapter 5

"Squeezed" Interparticle Properties for Plasmonic Coupling and SERS Characteristics of Duplex DNA Conjugated/Linked Gold Nanoparticles of Homo/Hetero-Sizes

5.1 Introduction

The formation of interparticle duplex DNA conjugates with gold nanoparticles constitutes the basis for interparticle plasmonic coupling responsible for surface-enhanced Raman scattering signal amplification, but understanding of its correlation with interparticle spatial properties and particle sizes, especially in aqueous solutions, remains elusive. This section describes findings of an investigation of interparticle plasmonic coupling based on experimental measurements of localized surface plasmon resonance and surface enhanced Raman scattering characteristics for gold nanoparticles in aqueous solutions upon introduction of interparticle duplex DNA conjugates to define the interparticle spatial properties. Theoretical simulations of the interparticle optical properties and electric field enhancement based on a dimer model have also been performed to aid the understanding of the experimental results. The results have revealed a "squeezed" interparticle spatial characteristic in which the duplex DNA-defined distance is close or shorter than A-form DNA conformation, which are discussed in terms of the

interparticle interactions, providing fresh insight into the interparticle double-stranded DNA-defined interparticle spatial properties for the design of highly-sensitive nanoprobes in solutions for biomolecular detection.

The exploitation of the plasmonic properties of metal nanoparticles (NPs), especially gold and silver nanoparticles, has been an important focus of research interests in developing spectroscopic techniques for the detection of biomolecules, diagnostic applications, controlled delivery, and specific targeting.[1–4] One area of increasing interests involves the exploration of localized surface plasmon resonance (LSPR) and surface enhanced Raman scattering (SERS) for enhanced detection of DNA and proteins, [1, 5–10] including experimental assessments of LSPR, SERS, and synchrotron small-angle X-ray scattering characteristics by tuning the interparticle distance through the length of duplex DNA.[8, 9] There has been significant advancement in theoretical modeling to assist in the comprehension of the interactions using discrete dipole approximation method.[10–17] These studies provide useful information for understanding LSPR and SERS properties of NPs by solving Mie theory to simulate LSPR and the electromagnetic field (EMF) [14, 18–22] in terms of particle and interparticle properties. Recent examples include using finite difference time domain (FDTD) to theoretically determine the optimal SERS signals for DNA-directed gold nanodimers,[11] 3D finite element simulations of plasmonic properties in DNA detection,[12] FDTD to simulate SERS intensity of DNA origami under controlled gaps,[13] and theoretical simulation of the interaction involved in Au nanoparticle–core/Pd-shell nanospheres based LSPR sensors.[14] While the interparticle linkage by complementary binding of DNA has been widely explored for various applications, one of the long-standing issues is the lack of a clear understanding of the interparticle spacing

measured in most DNA-assembled nanoparticle systems.[23–25] While there have been studies using TEM and other imaging techniques to characterize the assembly of DNA-conjugated gold nanoparticles,[26] including our own previous work,[27] the understanding of the interparticle spatial properties is rather limited because the measurement performed under dry state for TEM may not represent the actual assemblies in solutions. Therefore, measuring the SERS characteristic with the conjugated or linked nanoparticles being suspended in the solution phase, rather than under dried phase as in most of the previous studies, should provide an insight for understanding how the SERS signals correlate with the interparticle spacing and particle size under realistic bioactive conditions. Experimentally, the "hot-spot" formation due to the assembly of gold nanoparticles conjugated by DNA strands could lead to enhanced SERS characteristics, which is illustrated in Scheme 5.1.1 for a 30-base pair (bp) ds-DNA sequence and AuNPs labeled with a Raman reporter molecule (e.g., 4-mercaptobenzoic acid (MBA)). This system provides an ideal system for the study of SERS "hot-spot" characteristics because the formation of the interparticle duplex DNA is experimentally confirmed in an earlier study by cutting using a restriction enzyme and analysis using a Southern blot method.[27]

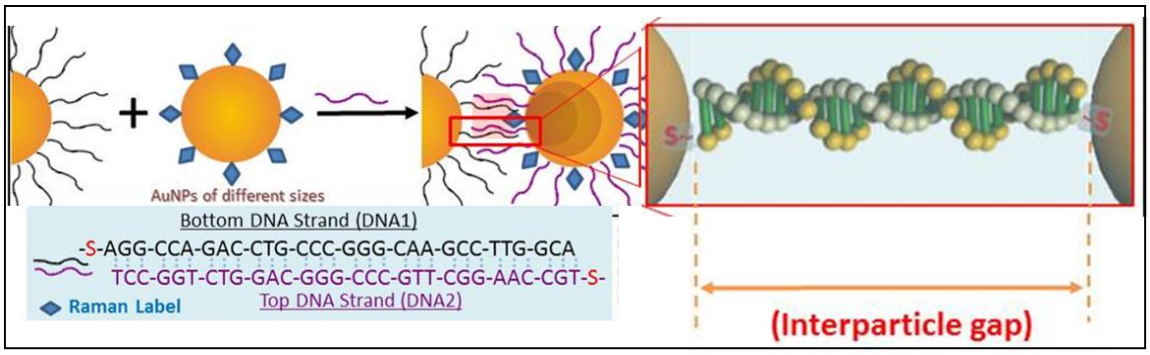

Scheme 5.1.1. Illustration of a dimer of AuNPs linked by two single-strand DNA (DNA1 and DNA2) through complementary binding (designed using the cyclin G promoter sequence for p53 recognition). The highlighted region indicates the area of interest in terms of plasmonic and electric field enhancements, or the center the interparticle gap (E_C).

In order for the DNA-conjugated or linked nanoparticle assemblies to be suspendable in the solution, the size of the aggregates must be small, such as dimers and trimers. Otherwise, they will be precipitated out from the solution. As such, while an actual solution of suspendable conjugated or linked gold nanoparticles may contain dimers, trimers or somewhat larger aggregates, a dimer model would represent a simple approach to the theoretical consideration. Herein we present the experimental results for a study of duplex DNA-linked gold nanoparticles in solution, and the understanding of their correlation with the interparticle spatial properties and particle sizes aided by theoretical simulations of the interparticle optical properties and electric field enhancement based on a dimer model. We note that the intention is not to claim that only dimers were in the solution, rather, to show that using a dimer model in the simulation provides a theoretical assessment of the experimental data, and thus shine some light into the interparticle interaction.

5.2 Experimental.

Gold nanoparticles of several monodispersed sizes, 13.3 ± 0.9 nm, 39.7 ± 1.8 nm and 62.4 ± 2.0 nm, were synthesized with either citrate or acrylate capping molecules according procedures reported earlier.[28 – 30]

SERS spectra were measured by an Advantage 200A Raman spectrometer (DeltaNu) and the data were collected from 200 to 3400 cm^{-1}. The laser power and wavelength were 5 mW and 632.8 nm, respectively. The integration time is 60 s for each set of data presented.

Two different oligonucleotides (bottom-DNA (DNA1): 5'-/5ThioMC6-D/AGG CCA GAC CTG CCC GGG CAA GCC TTG GCA-3' and top-DNA (DNA2): 5'-/5ThioMC6-D/TGC CAA GGC TTG CCC GGG CAG GTC TGG CCT-3') were used, which were dissolved in 0.1 M phosphate buffer (pH 8) at a concentration of 120 μM. The conjugation of AuNPs with the bottom-DNA1 to form bottom-DNA1/AuNP and the labeling of AuNPs with 4-mercaptobenzoic acid (MBA) was achieved using known procedure. The theoretical surface coverages were estimated to be 0.07, 0.5, and 0.7 for solutions of 13, 39, and 62 nm AuNPs where the MBA concentrations were 2, 1, and 1 μM, respectively.[5, 31, 32] DNA assembly of the conjugated and/or labeled nanoparticles were achieved by addition of DNA2 to a solution containing DNA1/AuNP (16 or 0.1 nM) and 300 μL of MBA/AuNP (16, 0.1, or 0.028 nM).

The simulation of the optical absorption and the enhancement of the electric field intensity in the dielectric environment surrounding AuNPs due to the effect of their localized surface plasmon resonances was performed using the MNPBEM toolbox based on the boundary element method (BEM).[20, 33] Using a dimer of AuNPs with specific core sizes and a shell thickness defined by DNA (11 nm) as a model, the simulation discretizes the particle boundaries of different materials then solves the Maxwell equations for the surface charge and currents.[34] The optical constants, e.g. index of refraction and absorption coefficient of AuNP and DNA, are extracted from the experimental data,[35, 36] approximating the medium environment as pure water (n = 1.33). Electric field enhancements were simulated using the same conditions as above and the laser excitation wavelength of 633 nm.

5.3 Results and Discussion

5.3.1 Optical properties. Experimentally, one of the major characteristics of interparticle linkage of AuNPs is the change of the LSPR band. For example, for homo-sized AuNPs capped with DNA in the presence of the target DNA2 strand, there is a clear red shift of the SP band (Figure 5.3.1.1A). The red shift LSPR band is clearly dependent on the size of the particles, showing a greater shift for the larger particle sizes. This is indicative of aggregation as a result of interparticle linking by the duplex DNA. In comparison with the homo-sized AuNP system, a hetero-sized system consisting of two different sized AuNPs, e.g., 13 nm DNA1/AuNP with 39 nm or 62 nm AuNPs in the presence of DNA2, was also examined. In contrast to the homo-size system, where there is a subtle decrease of the SP band intensity after the assembly, the red shift for the SP band is much smaller (**Figure 5.3.1.1**B), indicating a subtle difference between the homo-size and hetero-size systems.

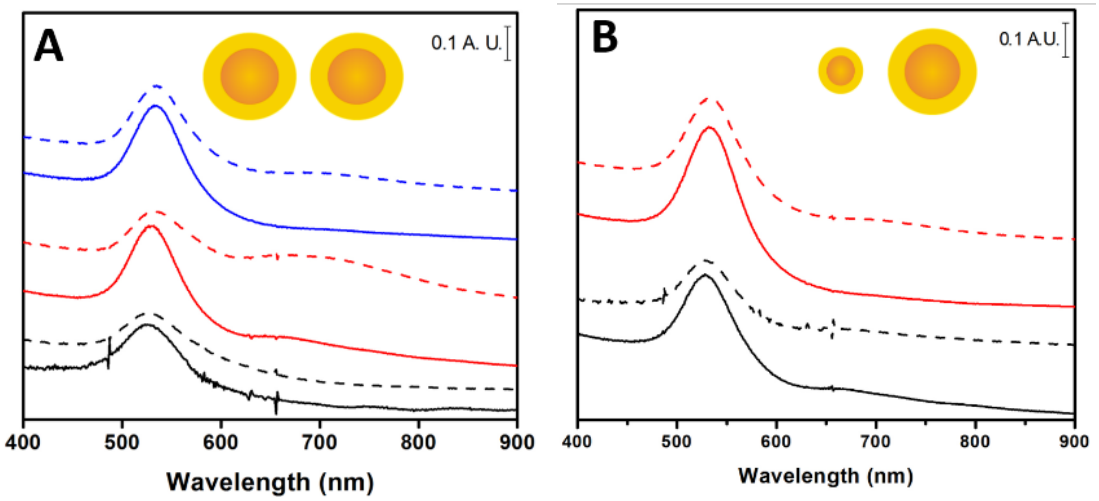

Figure 5.3.1.1. UV-Vis spectral of LSPR band for AuNPs before (solid curves) and after (dashed curves) interparticle duplex DNA linkage. (A) homo-sized AuNPs: 13 nm (black curves), 39 nm (red curves), and 62 nm (blue curves); (B) hetero-sized AuNPs: 13 nm – 39 nm (black curves), and 13 nm – 62 nm (red curves).

In view of the fact that the DNA-conjugated or linked nanoparticle assemblies are suspendable in the solution, suggesting that the size of the aggregates must be small (e.g., dimers and trimers) or they will be precipitated out from the solution, we consider here a

dimer model as a simple approach to the theoretical simulation of the evolution of the optical properties as a function of particle size and interparticle spacing. Figure 5.3.1.2A shows an example set of simulated results for a symmetric dimer of AuNPs (39 nm in diameter) as a function of interparticle gap. There is a clear trend of red shift for the overall LSPR bands as interparticle gap is reduced, showing the emergence of a new LSPR band in the long wavelength region. The red shift of the new long-wavelength LSPR band exhibits acceleration as the DNA shells become increasingly overlapped or squeezed. It is evident that the larger the particle size, the more pronounced is the red shift as a function of the interparticle gap (Figure 5.3.1.2).

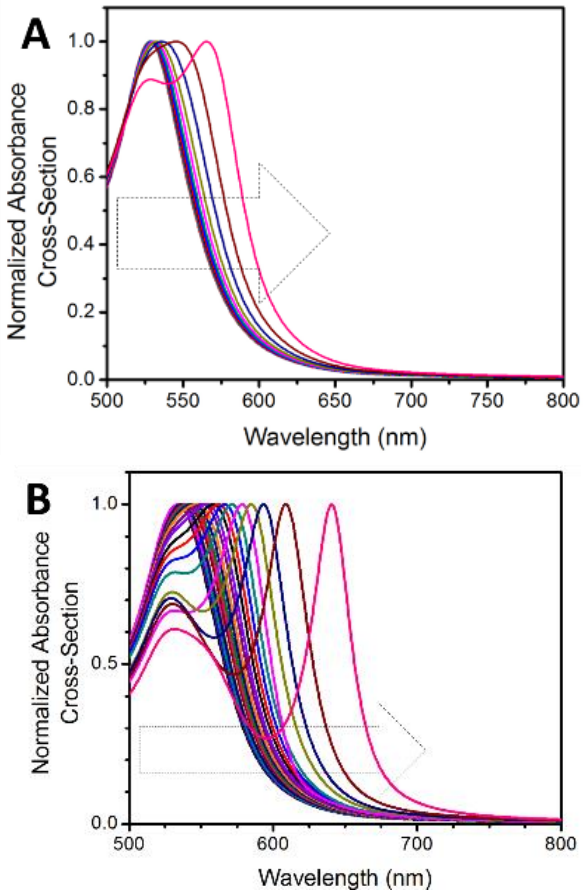

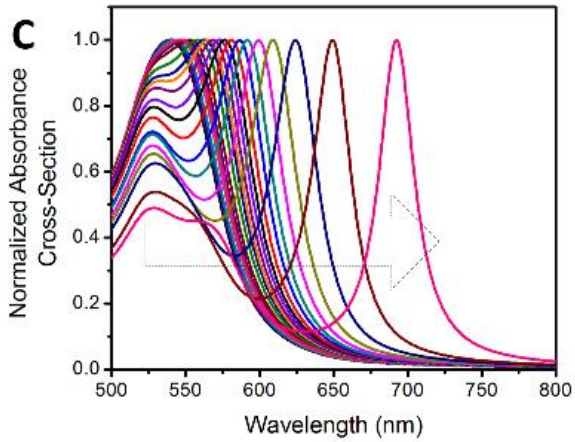

Figure 5.3.1.2. Simulated absorption cross-section spectra of ds-DNA-linked symmetrical dimer models (11 nm (A), 39 nm (B), and 62 nm (C)) as the interparticle edge-to-edge gap distance is reduced (from 12 nm to 1 nm with an interval of 0.5 nm. The red shift is shown by the direction of the arrow).

For an asymmetric dimer of nanoparticles as a model of the hetero-size nanoparticle system upon interparticle linking by duplex DNA, the LSPR is also simulated. In comparison with the simulation results for the symmetric dimers (Figure 5.3.1.2A), there is a similar red shift of the LSPR band (e.g., 13 – 39 nm and – 62 nm AuNPs, Figure 5.3.1.3(A and B)), but the extent of the shift is much smaller.

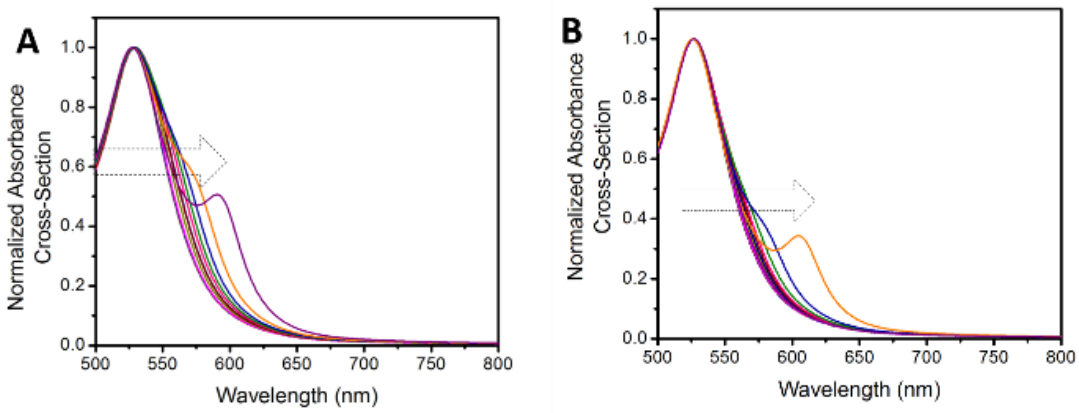

Figure 5.3.1.3. Simulated absorption cross-section spectra of ds-DNA-linked asymmetrical dimer models ((A) 13 – 39 nm and (B) 13 – 62 nm) as the interparticle edge-to-edge gap distance is reduced (from 12 nm to 1 nm with an interval of 0.5 nm. The red shift is shown by the direction of the arrow).

The trends can be fitted by exponential decay (Table 5.3.2.1), showing a smaller decay constant for the larger-sized particles, consistent with the experimental results

(Figure 5.3.1.4A). Similarly for the hetero – sized dimers the fitting results show that the larger the difference in size between the two particles, the greater is the decay constant (Figure 5.3.1.4B and Table 5.3.2.1). This finding is also consistent with experimental results (Figure 5.3.1.1B).

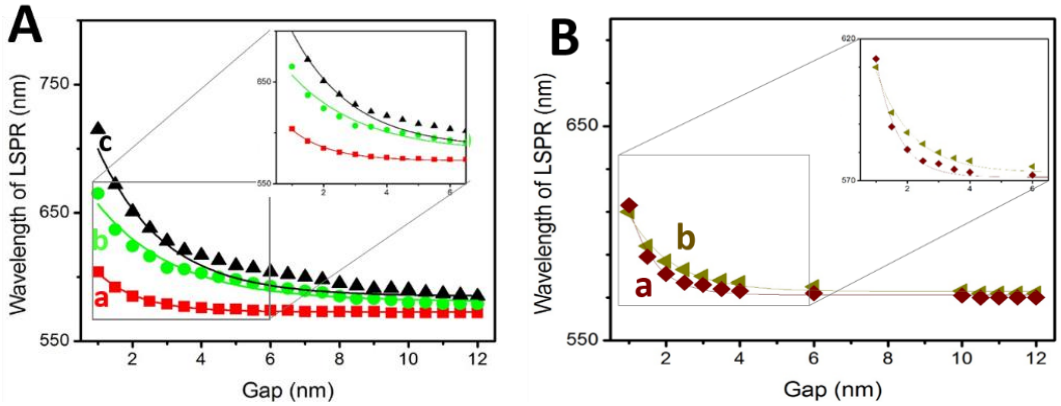

Figure 5.3.1.4. (A) Absorption band's wavelength vs. the gap, where symmetric NPs are 13 (a), 39 (b), and 62 nm (c). The lines represent fitting by exponential decay (**Table 5.3.2.1**)). (B) Absorption band's wavelength vs. the gap, where asymmetric dimers feature 13– 39 nm (a) and 13– 62 nm (b). The lines represent fitting by exponential decay **(Table 5.3.2.1**)).

5.3.2. SERS Characteristics

Experimentally, the interparticle plasmonic coupling as a result of the formation of interparticle duplex DNA conjugates with gold nanoparticles is responsible for surface-enhanced Raman scattering signal amplification. Figure 5.3.2.1 shows several sets of SERS spectra for homo-sized AuNPs of sizes 13 nm (A), 39 nm (B), and 62 nm (C) before and after duplex DNA assembly. The observation of the SERS peaks at 1075 and 1587 cm^{-1} after duplex DNA assembly, characteristic of the ring-breathing modes of MBA labels on the AuNPs, is a clear indication of SERS effect as a result of the interparticle linkage.

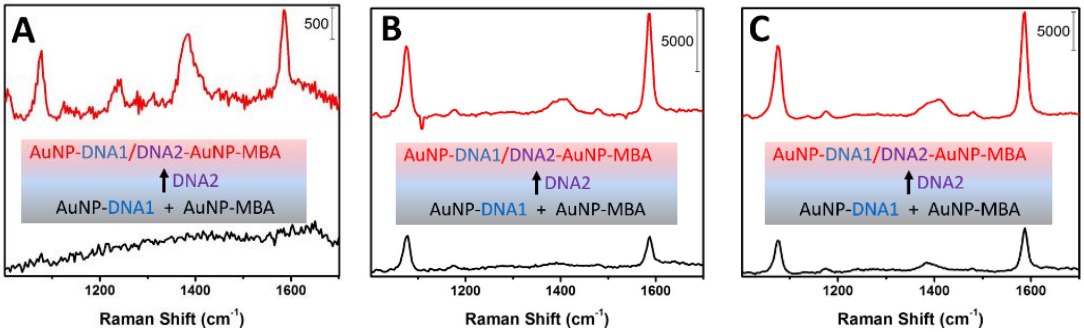

Figure 5.3.2.1. SERS spectra for homo-sized AuNPs ((A) 13 nm, (B) 39 nm, and (C) 62 nm) system before (black curve) and after (red curve) the interparticle linkage by ds-DNA.

In addition to the homo-sized AuNPs, SERS spectra for hetero-size AuNPs were also examined. Figure 5.3.2.2 shows two sets of SERS spectra for two hetero-size AuNP systems (39 – 13 nm and 62 – 13 nm),[5] showing also a clear increase of the peak intensity after duplex DNA assembly. The observation of the ring-breathing peaks of MBA labels on the AuNPs after duplex DNA assembly is again a clear indication of the interparticle linkage.

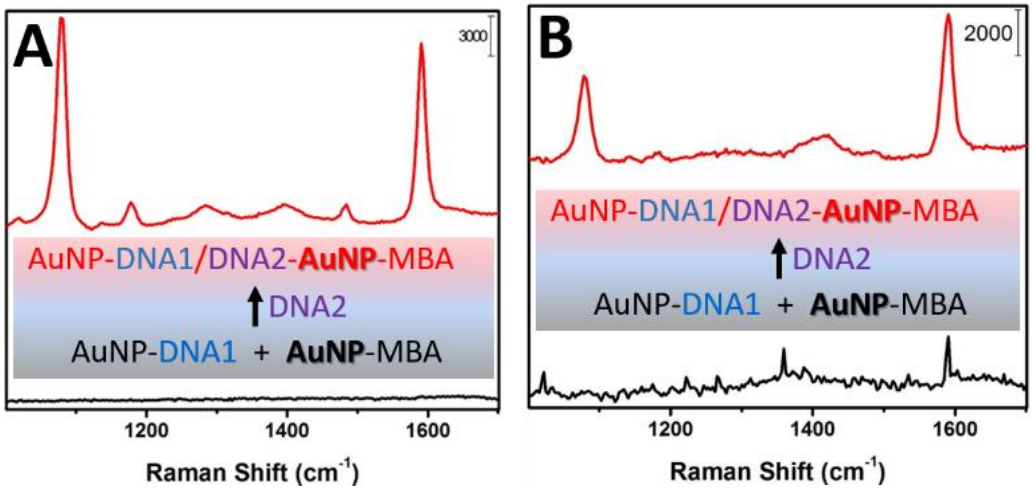

Figure 5.3.2.2. SERS spectra for hetero-sized AuNPs ((A) 13 – 39 nm and (B) 13 – 62 nm) system before (black curve) and after (red curve) the interparticle linkage by ds-DNA.

The peak intensity depends on the particle size and concentration, a comparison of the data shown in Figure 5.3.2.2A-B in terms of the normalized peak height at 1587 cm^{-1} show

that the SERS intensity increases with the particle size (Figure 5.3.2.3A). Note that our experiments and simulations of the asymmetric systems have focused on those that vary size only for one part of the dimer (e.g., 13 – 39, and 13 – 62 nm) so that the comparison can be made with only one variable. For the duplex system of 39 nm and 62 nm particles, the result indicated that it behaves similarly to the 13 – 39 nm and 13 – 62 systems, while the E-field intensity falls in between the two systems, which is consistent with intensity – size correlation (Figure 5.3.2.2A-B). A comparison of the intensities for the different particle sizes after considering concentration difference, as shown in Figure 5.3.2.3B, indicates that the intensity increases with the particle size.

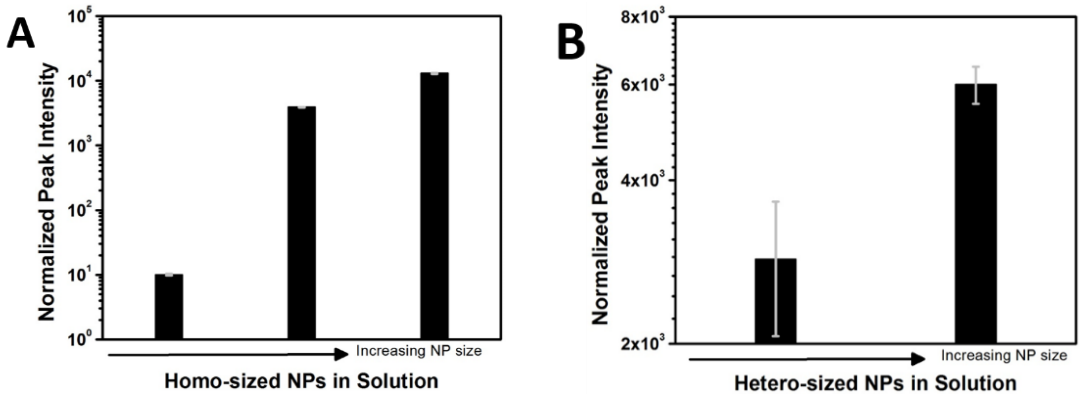

Figure 5.3.2.3. (A) SERS intensity of the peak at 1587 cm^{-1} for the (A) homo-sized NPs solutions of different sizes (13, 39, and 62 nm) and (B) hetero-sized NPs solutions of different sizes (39 – 13 nm and 62– 13 nm). Note: the intensity is normalized peak intensity at 1076 cm^{-1} over total number of NPs.

The above SERS results were further assessed by theoretical simulation of the interparticle electric field (E-field) enhancement based on a dimer model. Consider first a symmetric dimer model for the homo-size AuNP systems upon interparticle linking by duplex DNA. Figure 5.3.2.4A shows a set of simulation results in terms of the intensity enhancement for a symmetric dimer of 39 nm AuNP as a function of the interparticle gap. There is a clear enhancement of E-field around and in between the nanoparticles as the gap

decreases, with the center in between the two nanoparticles being the strongest ("hot-spot"). The enhancement clearly increases as the interparticle gap is reduced (Figure 5.3.2.4B), exhibiting a trend similar to the red shift of the simulated LSPR band (Figure 5.3.1.4A). The E-field intensity enhancement apparently shows an exponential decay with the interparticle gap, where the magnitude is strongly dependent on the particle size (Figure 5.3.2.4D). The trends of these curves are also fitted quite well by exponential decay (Figure 5.3.2.4D). The results (Table 5.3.2.2) show a smaller decay constant for the larger-sized particles, which is quite consistent with the trend revealed by the results from fitting the red shift of LSPR (Table 5.3.2.1).

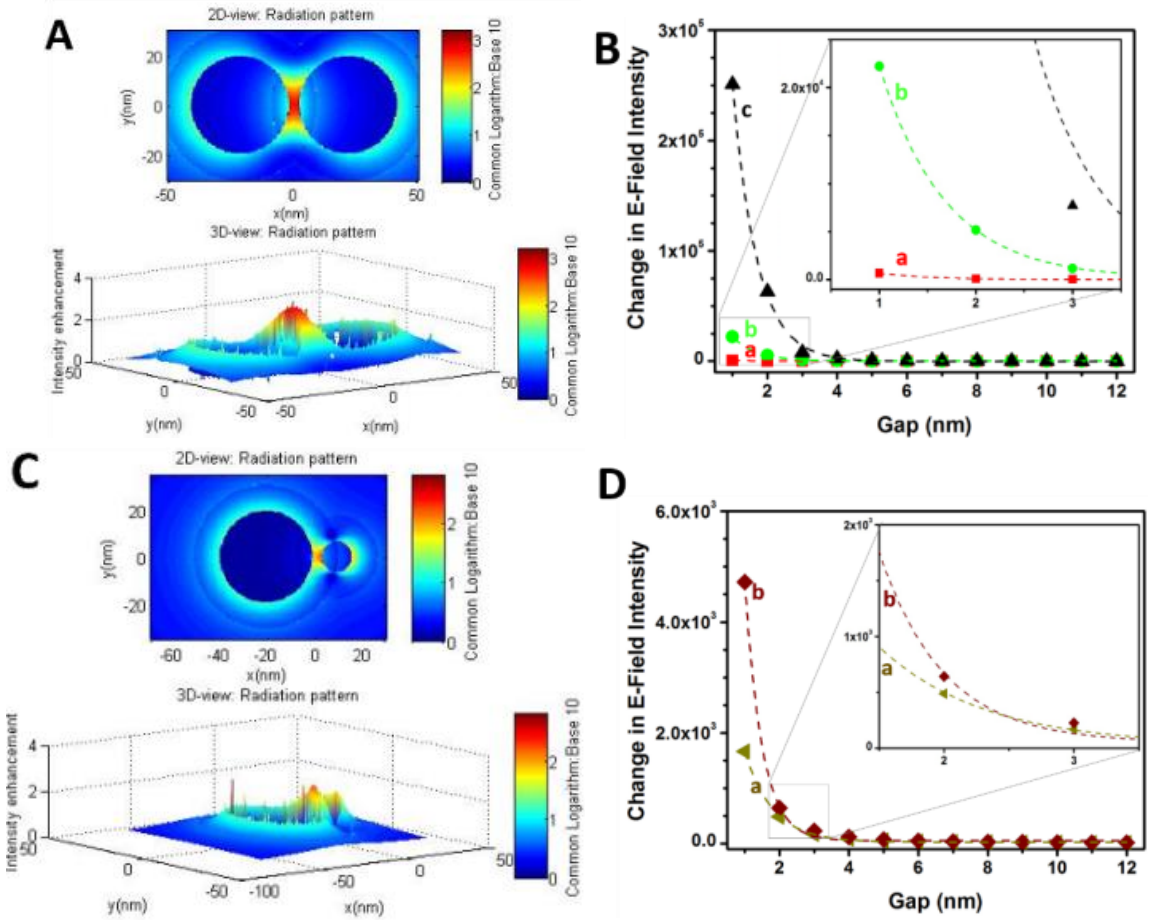

Figure 5.3.2.4. (A and C) 2D and 3D plots of a symmetric dimer of (A) 39 nm AuNPs and an (C) asymmetric dimer of 39 – 13 nm AuNPs, each with a gap distance (d) of 4 nm. (B and D) Plots of the change of E-field intensity enhancement at E_C as a function of the interparticle gap for (B) symmetric dimers of three different particle sizes (13 nm (a), 39 nm (b), and 62 nm (c)), and for (D) symmetric dimers (13– 39 nm (a) and 13–

62 nm (b)). The change is measured with respect to that at 12 nm gap. The dashed lines represent fitting by exponential decay (Table 5.3.2.2)).

Simulation based on an asymmetric dimer model was also performed for the hetero–size AuNP system upon interparticle linking, revealing a similar trend in terms of the E-field enhancement around and between the nanoparticles (Figure 5.3.2.4C). Again, the intensity enhancement is exponentially dependent on the particle size (Figure 5.3.2.4D). The change of the intensity enhancement for the asymmetric dimers is somewhat smaller by 1~2 orders of magnitude in comparison with those observed for the symmetric dimers (Figure 5.3.2.4B). Interestingly, the curve fitting results (Figure 5.3.2.4D) show again that the larger the difference in size between the two particles, the greater is the decay constant (Table 5.3.2.2); which is again very consistent with the trend revealed by fitting the red shift of LSPR (Table 5.3.2.1).

Table 5.3.2.1. Fitting results from fitting the simulated LSPR data in Figures 5.3.1.4A and B by exponential decay as a function of the interparticle gap (d) ($A = A_0 + A1 * \exp(-kd)$).

NP size	A_0	A1	k
13 nm	572.8	69.9	0.83
39 nm	581.0	117.9	0.44
62 nm	585.0	176.8	0.43
13–39 nm	572.9	84.7	0.86
13–62 nm	571.2	169.1	1.42

Table 5.3.2.2. Fitting results from fitting the simulated E-field intensity enhancement data in Figures 5.3.2.4B and D by exponential decay as a function of the interparticle gap (d) ($E = E1 * \exp(-kd)$).

NP size	E1	k
13 nm	4.3×10^2	1.87
39 nm	9.5×10^4	1.45
62 nm	1.1×10^6	1.44
13–39 nm	5.4×10^3	1.17
13–62 nm	3.2×10^4	1.93

The above experimental results for the homo-size and hetero-size AuNP systems and theoretical results for the symmetric and asymmetric dimer models are further compared (Figure 5.3.2.5). These findings are remarkable because it demonstrates that the

"hot-spot" can be tuned very effectively by manipulating the particle size and the interparticle gap.

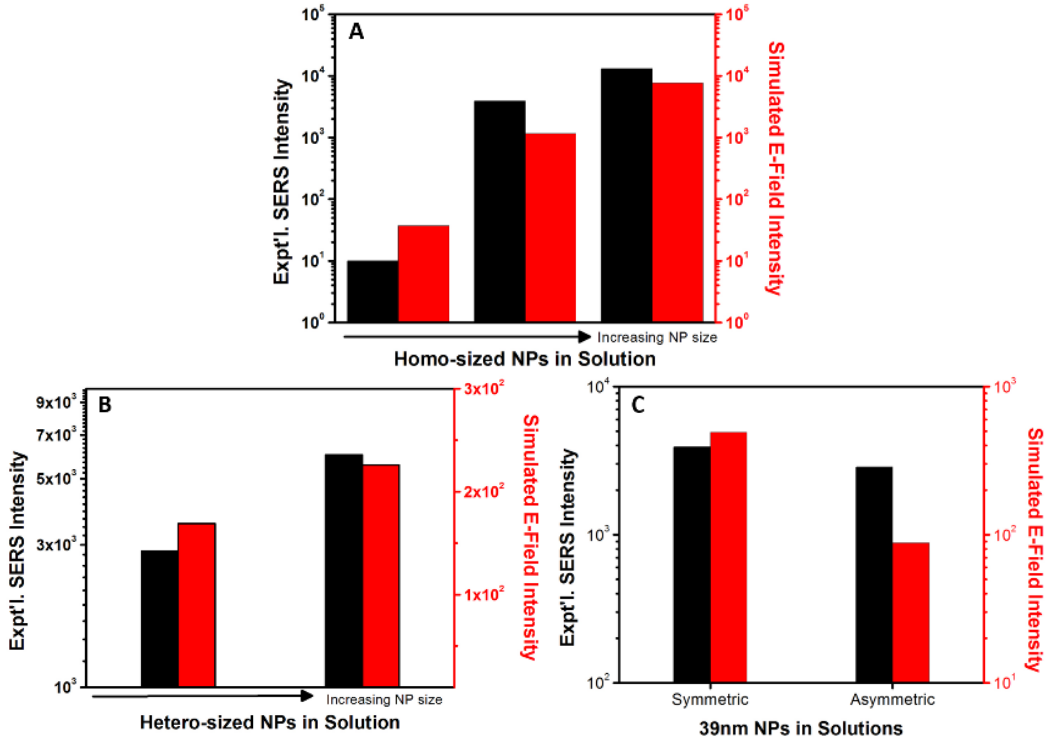

Figure 5.3.2.5. Normalized experimental SERS peak intensities and theoretical E-field intensity enhancements: (A) the homo-size system vs. the symmetric dimer model (from 13, 39 to 62 nm AuNPs), (B) the hetero-size system vs. the asymmetric dimer model (from 39 nm – 13 nm to 62 nm – 13 nm AuNPs), and (C) the symmetric vs. asymmetric dimer systems. (Theoretical data correspond to those at an interparticle gap of 3 nm).

Although the theoretical data shown correspond to a gap size of 3 nm, similar trend were also observed for other gaps, but the contrasts are relatively small for larger gaps. An interesting observation is that for a significant E-field enhancement in the dimers, the gap appears to be smaller than the length of ds-DNA (11~12 nm).

5.3.3. Discussion of Interparticle Interactions

To further understand the above theoretical results in terms of the E-field enhancement vs. the interparticle gap, we also considered the interparticle interactions on the basis of simple models for steric repulsive and van der Waals attractive interactions in terms of interaction

energies with the interparticle gap.[37–39] The calculations were based on dimer models of AuNPs (r, R1, R2 are particle radius) in which the steric repulsive and van der Waals attractive interaction energies as a function of interparticle gap (D) are calculated by the following equations (δ and σ stand for the length and the diameter of a capping molecule on the nanoparticle surface). [34-36]

$$E_{steric} \approx \frac{100r\delta^3}{(D-2r)\pi\sigma^3}\, kT \exp\left(\frac{-\pi\,(D-2r)}{\delta}\right) \qquad (1)$$

$$E_{vdW,sym} = -\frac{A}{12}\left[\frac{4r^2}{D^2-4r^2} + \frac{4r^2}{D^2} + 2\ln\left(\frac{D^2-4r^2}{D^2}\right)\right] \qquad (2a)$$

$$E_{vdW,asym} = -\frac{A}{6}\left[\frac{2\frac{R_2}{R_1}}{\left(\frac{R_1+R_2+D}{R_1}\right)^2-\left(1+\frac{R_2}{R_1}\right)^2} + \frac{2\frac{R_2}{R_1}}{\left(\frac{R_1+R_2+D}{R_1}\right)^2-\left(1-\frac{R_2}{R_1}\right)^2} + \ln\left(\frac{\left(\frac{R_1+R_2+D}{R_1}\right)^2-\left(1+\frac{R_2}{R_1}\right)^2}{\left(\frac{R_1+R_2+D}{R_1}\right)^2-\left(1-\frac{R_2}{R_1}\right)^2}\right)\right] \qquad (2b)$$

As shown in Figure 5.3.3.1, the calculated interparticle potentials are clear functions of the edge-to-edge gap between the NPs in a symmetric dimer of AuNPs. In addition to the DNA shell thickness (11 nm), the calculation also took the size-dependent Hamaker constant into considerations.[40–42]

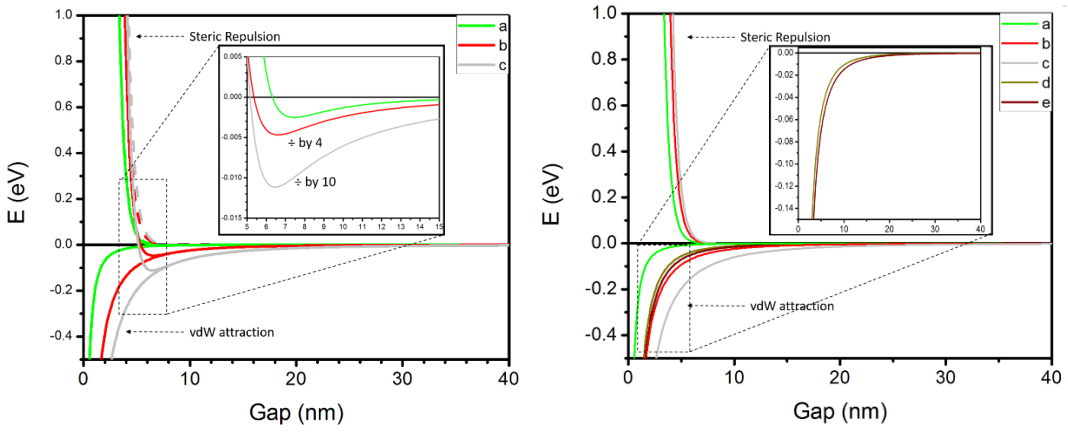

Figure 5.3.3.1. Calculated steric repulsion, van der Waals attraction, and the total interaction potentials for symmetric dimers of AuNPs (13 nm (a), 39 nm (b), and 62 nm (c)) (A) and for asymmetric dimers of AuNPs of 13nm – 39 nm (a) and 13 nm – 62 nm (b) (B) as a function of the interparticle edge-to-edge gap.

For the symmetric dimer, the minimum potential energy for the balanced interactions was found to correspond to a particle edge-to-edge distance of 6~8 nm (Figure 5.3.3.1). It showed a subtle dependence on the particle size, revealing a change from 7.8 nm to 6.5 nm as NP size increases from 13 nm to 62 nm. The trend is consistent with the increase of simulated E-field intensity enhancement with particle size, but the gap values are somewhat larger than those of simulation corresponding to a significant E-field enhancement. In comparison with the three forms of double-stranded DNA in terms of conformations (A, B, and Z forms) (Scheme 5.3.3.1), the calculated gap values somehow correspond to A-form (7.8 nm), which are usually observed with dehydration of DNA in cases such as protein binding that strips solvent off DNA.[43] Considering the length of the other types of ds-DNA being longer (10~11 nm), this finding suggests the possibility that the nanoparticles may effectively compress the interparticle double-stranded DNA by "squeezing" solvent off DNA. Interestingly, this biomolecular interparticle linkage appears to parallel an earlier finding on molecularly-mediated assembly of alkanethiolate-capped Au nanoparticles where a combination of interparticle hydrogen bonding and van der Waals interactions was proposed to lead to "squeezed" spatial property.[44] A similar result was also obtained for asymmetric dimer model (Figure 5.3.3.1B). Note that the interaction energy calculation is based on a simple model of the steric and attractive interactions at this point for a qualitative assessment of the data, in which the approximations consider that the electrostatic interaction is smaller than the steric repulsion.

Scheme 5.3.3.1. Models of three forms of double-stranded DNA (A, B, and Z forms) for a 30-bp duplex DNA derived under three different parameters (rotation/bp and increase/bp along axis: 32.7 degrees and 0.26 nm for A-form, 34.3 degrees and 0.34 nm for B-form, and 30 degrees and 0.37 nm for Z-form).

5.4 Conclusion

In summary, the experimental results on the interparticle plasmonic coupling induced localized surface plasmon resonance and surface enhanced Raman scattering characteristics of gold nanoparticles in aqueous solutions upon introduction of interparticle duplex DNA conjugates to define the interparticle spatial properties were assessed by theoretical simulations of the interparticle optical properties and electric field enhancement based on a dimer model of both homo-sized and hetero-sized AuNPs. In addition to showing a clear dependence of the LSPR and SERS characteristics on the interparticle gap and particle size, the results have revealed a "squeezed" interparticle distance that are intriguingly close to or shorter than the conformation of A-form for the duplex DNA. The findings have provided a fresh insight into the interparticle interaction and spatial properties defined by double stranded DNA linkage. A future in-depth study of the generality of this finding in many different cases of interparticle molecular/biomolecular

linkages would have important implications for the design of highly-sensitive nanoprobes in solutions.

References

1. Skeete, Z *et al.* 2014 ACS *Appl. Mater. Interfaces* 6 21752-68
2. Saha, K, Agasti, S, Kim, C, Li, X, and Rotello, V M 2012 Chem. *Rev.* **112** 2739–79
3. Khan, I, Khan, M, Umar, M N, and Oh, D H 2015 *IET Nanobiotechnol.* **9** 396-400
4. Lee, J S 2014 *Nanotechnol Rev.* **3** 499-513
5. Crew, E *et al.* 2013 Analyst *138* 4941-9
6. Punj, D, Regmi, R, Devilez, A, Plauchu, R, Moparthi, S B, Stout, B, Bonod, N, Rigneault, H, and Wenger, J 2015 ACS *Photonics 2* 1099-107
7. Ma, C, Wu, Z, Wang, W, Jiang, Q, and Shi, C 2015 J. *Mater. Chem. B 3* 2853-7
8. Guerrini, L, McKenzie, F, Wark, A W, Faulds, K, and Graham, D 2012 Chem. *Sci.* **3** 2262-9
9. Park, S J, Lazarides, A A, Storhoff, J J, Pesce, L, Mirkin, C A 2004 J. *Phys. Chem. B.* **108** 12375-80
10. Shiohara, A, Wang, Y, and Liz-Marzán, L M 2014 J. *Photochem. Photobiol. C: Photochem. Rev.* **21** 2-25
11. Yin, H J, Liu, L, Shi, C A, Zhang, X, Lv, M Y, Zhao, Y M, and Xu, H J 2015 Appl. *Phys. Lett.* **107** 193106
12. Lebedev, N, Griva, I, Dressick, W J, Phelps, J, Johnson, J E, Meshcheriakova, Y, Lomonossoff, G P, and Soto, C M 2016 Biosensors *and Bioelectronics* **77** 306-14
13. Thacker, V V, Herrmann, L O, Sigle, D O, Zhang, T, Liedl, T, Baumberg, J J, and Keyser, U F 2014 Nat. *Commun.* **5** 3448
14. Sugawa, K, Tahara, H, Yamashita, A, Otsuki, J, Sagara, T, Harumoto, T, and Yanagida, S 2015 ACS *Nano 9* 1895-904
15. Piantanida, L, Naumenko, D, and Lazzarino, M 2014 RSCAdv. **4** 15281
16. Hao, E, and Schatz, G C 2004 J. *Chem. Phys.* **120** 357-66
17. Nguyen, B H, and Ngo, Q M 2010 Adv. *Nat. Sci: Nanosci. Nanotechnol.* **5** 025010
18. Albella, P, Saiz, J M, González, F, and Moreno, F 2011 J. *Quant. Spectrosc. Radiat. Transfer 112* 2046-58
19. Chaffin, E A, Bhana, S, O'Connor, R T, Huang, X, and Wang, Y 2014 J. *Phys. Chem. B 118* 14076-84
20. Hohenester, U, and Trügler, A 2012 Comp. *Phys. Commun.* **183** 370-81
21. Abbas, A, Fei, M, Tian, L, and Singamaneni, S 2013 Plasmonics *8* 537-44
22. Wustholz, K L, Henry, A-I, McMahon, J M, Freeman, R G, Valley, N, Piotti, M E, Natan, M J, Schatz, G C, and Van Duyne, R P 2010 J. *Am. Chem. Soc.* **132** 10903-10
23. Barrow, S J, Funston, A M, Wei, X, and Mulvaney, P 2013 Nano *Today 8* 138-67
24. Sheikholeslami, S, Jun, Y W, Jain, P K, and Alivisatos, A P 2010 Nano *Lett.* **10** 2655-60
25. Barrow, S J, Funston, A M, Gómez, D E, Davis, T J, and Mulvaney, P 2011 Nano *Lett.* **11** 4180-7
26. Li, H, Carter, J D, and LaBean, T H 2009 Materialstoday 12(5) 24-32

27. Lim, I-I S, Chandrachaud, U, Wang, L, Gal, S, and Zhong, C J 2008 Anal *Chem* **80** 6038-44
28. Nicewarner-Pena, S R, Freeman, R G, Reiss, B D, He, L, Pena, D J, Walton, I D, Cromer, R, Keating, C D, Natan, M J 2001 Science 294(5540) 137-41
29. Njoki, P N, Lim, I-I S, Mott, D, Park, H-Y, Khan, B, Mishra, S, Sujakumar, R, Luo, J, and Zhong, C J 2007 J. *Phys. Chem. C* 111 14664-14669
30. Njoki, P N, Luo, J, Kamundi, M M, Lim, S, and Zhong C J 2010 Langmuir 26 13622-9
31. Lim, I-I S, Chandrachud, U, Wang, L, Gal, S, and Zhong, C J 2008 Anal. *Chem.* **80** 6038-44
32. Lim, I-I S, Njoki, P N, Park, H-Y, Wang, X, Wang, L, Mott, D, and Zhong, C J 2008 Nanotechnology 19 305102
33. García de Abajo, F J, and Howie, A 2002 Phys. *Rev. B.* **65** 115418
34. Griffiths, D. J. 2012 Boston, Addison-Wesley
35. Palik, E.D. 1985 London, Academic Press
36. Elhadj, S, Singh, G, and Saraf, R F 2004 Langmuir 20 5539-43
37. Israelachvili, J. 1992 London, Academic
38. Weddemann, A *et al.* 2010 Beilstein *J. Nanotechnol 1* 75-93
39. Yockell-Lelièvre, H, Gingras, D, Lamarre, S, Vallée, R, and Ritcey, A M 2013 Plasmonics *8* 1369-77
40. Pinchuk, P, and Jiang, K 2015 Proc *SPIE* **9549** 95491J
41. Achebe, C H, and Omenvi, S N 2013 Proceedings *of The World Congress on Engineering 2* 1380-4
42. Sun, W, Zeng, Q, and Yu, A 2013 Langmuir *29* 2175-84
43. DiMaio, F, Yu, X, Rensen, E, Krupovic, M, Prangishvili, D, and Egelman, E H 2015 Science *348* 914-7
44. Han, L, Luo, J, Kariuki, N N, Maye, M M, Jones, V W, and Zhong, C J 2003 Chem. *Mater.* **15** 29-37

Chapter 6

Assessing Interparticle Spatial Characteristics of DNA-Linked Core-Shell Nanoparticles with or without Magnetic Cores in Surface Enhanced Raman Scattering

6.1 Introduction

Surface enhanced Raman scattering (SERS) of plasmonic nanoparticles enables their use as nanoprobes for the detection of biomolecules in solutions, which exploits the "hot-spot" arisen from small aggregates of the biomolecule-linked nanoprobes for effective harnessing of the interparticle plasmonic coupling of gold nanoparticles. While a 'squeezed' interparticle spatial characteristic has been revealed from the duplex DNA-linked gold nanoparticles as dimers in solution, how this interparticle spatial characteristic is operative for plasmonic nanoparticles containing magnetic components remains unknown. We describe herein new findings of an investigation of the interparticle spatial characteristics of DNA-linked core-shell type nanoparticles consisting of magnetic cores and plasmonic gold or silver shells, focusing on theoretical-experimental correlation in terms of localized surface plasmon resonance (LSPR) and electromagnetic field (EMF) enhancement. In comparison with Au nanoprobes, the simulated results of the SERS

enhancement for the DNA-linked dimers of plasmonic-magnetic M@Au nanoprobes show a similar agreement with the experimental data in terms of the 'squeezed' interparticle spacing characteristic. Remarkably, for M@Ag nanoprobes, the same interparticle spacing characteristic does not seem to show agreement between the simulated and experimental results for DNA-linked dimers of M@Ag and Au nanoprobes. Instead, an agreement was revealed by simulations of the DNA-linked dimers of M@Ag and Au nanoprobes at an interparticle spacing of essentially zero. This finding was analyzed in terms of effective thickness of the DNA layers on the nanoparticles and the strong magnetic attraction for M@Ag nanoprobes, providing new insight into the control of nanoprobe composition and shell structure in optimizing the plasmonic coupling and spectroscopic enhancements for biomolecular detection.

Surface enhanced Raman scattering (SERS) based theranostics is a rapidly developing field, which allows for rapid and point-of-care detection in medical treatment and diagnoses.[1-4] A well-studied point of interest in the development of these systems for treatments and diagnostics, is the ability to manipulate the biomolecules in solution.[1-5] Researchers have conducted experiments that employ magnetic nanoparticles (MNPs) in biosensor systems to allow for the navigation of the biomolecules to desired locations using magnetic fields. They have found that magnetic based NPs exhibit a stronger plasmonic coupling effect, proving to be an efficient nanoprobe for biomolecule detection.[6-11] For instance, Rong *et al*. discussed the promising application of Fe_3O_4@Ag and Au@AgNRs in the capture of CEA biomolecules using SERS spectroscopy.[6] Similar findings were also observed from Fan *et al.* who determined that Ag–Fe_3O_4 nanocomposites had a positive effect on the plasmonic coupling by controlling the arrangement of the nanocomposites on

the substrate.[7] Since MNPs are composed of metals that are not typically biocompatible and have limited surface chemistry, researchers have functionalized their surfaces with gold and silver.[8] The application of dual functional NPs in molecular detection utilize the magnetic susceptibility of MNPs in combination with the unique properties from the coupling of metallic NPs, provide promising opportunities to the early detection and treatment of diseases.[9,10]

We have recently reported the study of interparticle plasmonic coupling responsible for SERS signal amplification as a result of formation of interparticle duplex DNA conjugates with gold nanoparticles, revealing a 'squeezed' interparticle spatial characteristic in which the duplex DNA-defined distance is close to or shorter than A-form DNA conformation.[12] Similar findings were also reported, like Lee *et al.* in the analysis of Au-Ag nanodimers which demonstrated a stronger intensity at a lower interparticle distance than expected.[13-16] Other studies have also found that there is a stronger NP coupling with magnetic particles due to dipolar interactions in addition to the axis orientation.[17,18] However, how this type of interparticle interaction is operative for plasmonic nanoparticles containing magnetic component is not yet established. Recent studies have employed simulation methods and SQUID technique to address this issue.[7,19] For example, Fan *et al.* showed that the SERS intensity of Ag – Fe_3O_4 nanocomposites was dependent on the external magnetic field and the gap distance between Ag and Fe_3O_4 NPs.[7] Similarly Srivastava e*t al.* analyzed the assembly of FePt or Au NPs with ferritin using SQUID technique, and found that the magnetic core of the protein increased the magnetic interaction of the nanoparticles.[19] Although there have been extensive studies on the applications of magnetic coated NPs and their orientation, there is limited understanding

of how the magnetic core of the NP plays a role in the "hot-spot" formation and how it relates to SERS detection of biomolecules. In an earlier report, [8] we demonstrated that magnetic MnZn ferrite NPs decorated with a shell of Au or Ag (M@Au or M@Ag) could be used as functional nanoprobes for SERS detection of DNA via interparticle linkage of double-strand DNA between M@Au or M@Ag NPs and AuNPs. The experimental data, along with those with interparticle double-strand DNA linked AuNPs,[20] have indicated that SERS intensity depends on particle sizes and compositions, including magnetic properties. However, little is understood on how this dependence correlates with the interparticle properties of such magnetic nanoprobes.

In this section, the interparticle spatial characteristics of DNA-linked core-shell nanoparticles consisting of magnetic cores and gold or silver nanoparticles and the formation of the SERS "hot spot" in solution phase[8] (Scheme 6.1.1) are theoretically modeled using dimers of various combinations of magnetic core – gold or silver shell nanoparticles.

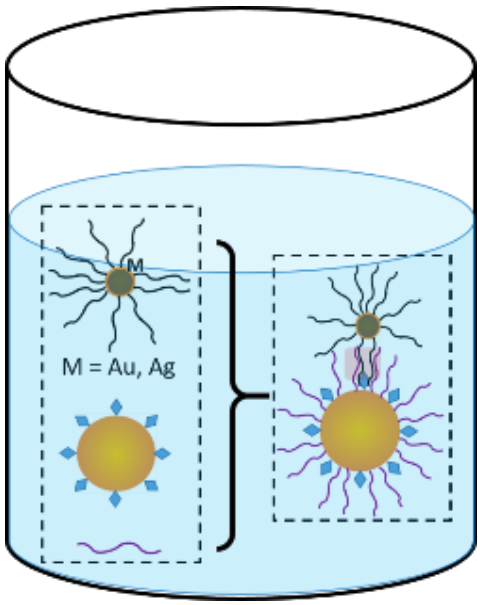

Scheme 6.1.1. Illustration of "hot- spot" formation of DNA – mediated dimeric assembly of core-shell nanoparticles containing magnetic cores and gold or silver nanoparticles in a solution.

The study focuses on the correlation between the experimental measurements and the theoretical simulations in comparison with those for gold or silver nanoparticle counterparts without magnetic cores.[12] New insights are gained into how the effective thickness of DNA layers on the nanoparticles and the interparticle interactions for magnetic core – metal shell nanoparticles operate in terms of composition and structure for optimizing the plasmonic coupling and spectroscopic enhancements.

6.2 Experimental.

Chemicals. Nanoparticle synthesis and functionalization were performed using sodium citrate (99%), sodium borohydride ($NaBH_4$, 99%), silver nitrate ($AgNO_3$, >99%), sodium acrylate (97%), hydrogen tetrachloroaurate (III) hydrate ($HAuCl_4$), dithiothreitol (DTT), and 4-mercaptobenzoic acid (MBA), which were used as purchased from Sigma-Aldrich (Milwaukee, WI). Buffers of carbonate/borate (0.05 M, pH 10) and phosphate (0.05 M, pH 7) were purchased from Fisher Scientific (Pittsburgh, PA). Thiol modified DNA (bottom-DNA: 5'-/5ThioMC6-D/AGGCCAGACCTGCCCGGGCAAGCCTTGGCA-3' and top-DNA: 5'-/5ThioMC6-D/TGCCAAGGCTTGCCCGGGCAGGTCTGGCCT-3') with standard desalting purification for DNA functionalization were purchased from Integrated DNA Technologies, Inc. (Coralville, IA). 10X TBE (0.89 M Tris, 0.89 M boric acid, 20 mM EDTA) buffer and pre-cast polyacrylamide gels purchased from Biorad Corporation (Hercules, CA) were used to purify DNA. Water (18.2 MΩ) was purified using a Millipore Milli-Q water system.

Synthesis, **Instrumentation and Simulation**.

Nanoparticle Synthesis. Using the reported procedure, citrate – capped (11.7 nm) and acrylate – capped gold nanoparticles (39.7 nm and 62.4 nm) were synthesized.[19-23] Citrate – capped (10 nm) silver nanoparticles were synthesized using the same procedure as the gold nanoparticles.[22,23] Similarly, acrylate-capped silver nanoparticles were synthesized using the same seeded growth method used for acrylate gold nanoparticles.[19-22] The bare and coated MZF nanoparticles (8 nm MZF NP, 9 nm M@AgNP, and 11 nm M@AuNP) were synthesized using the previously reported procedure and capped with 11-mercaptoundecanoic acid (MUA).[8]

DNA-linked Assemblies of Au or Ag and core@shell NPs. Two oligonucleotides, 5'-/5ThioMC6-D/AGGCCAGACCTGCCCGGGCAAGCCTTGGCA-3' ((bottom-DNA) and top-DNA: 5'-/5ThioMC6-D/TGCCAAGGCTTGCCCGGGCAGGTCTGGCCT-3' (top-DNA), were dissolved in 0.1 M phosphate buffer (pH 8) at a concentration ranging from 260 to 300 μM. The bottom-DNA (10 μM) was conjugated to acrylate–capped NPs of Au and Ag and MUA–capped MZF NPs.[8,23,24] The labeling of AuNPs with Raman Label (RL), i.e., MBA, was achieved similarly to the reported procedure.[8,23,24] Using the reported procedure, citrate – capped (10 nm) and acrylate-capped silver nanoparticles (30 nm) were synthesized.[21,22] The assembly of the NPs with DNA were monitored using UV-Vis (HP 8453) over 200-1100 nm and SERS (DeltaNu Advantage 200A – 5 mW, 632 nm) spectrophotometry over 200 - 3400 cm^{-1}. Simulations of the localized surface plasmon resonance and electrical intensity were computed using MNPBEM toolbox, which incorporates the AgNP boundaries and dielectric environments.[12]

Simulation Method. The electrical intensity of the localized surface plasmon resonances of the NPs were simulated using the MNPBEM toolbox to obtain the absorption

and enhancement (log base 10) of the NPs when in an aqueous environment.[12] The MNPBEM toolbox utilizes the optical constants and Maxwell equations to determine the surface charge and currents of the particles.

6.3 Results and Discussion

In our recent study,[12] the interparticle gap of DNA-mediated assembly of AuNPs would subject a small "squeezing" in the presence of AuNPs. However, the role of the DNA or capping ligands in the interparticle interactions remained elusive. Experimentally, for adsorption of surface species into the capping shell structure on the NP surfaces via place exchange reaction,[25] the degree of the original capping ligands being replaced by the incoming ligands depends on the competitive adsorption. Thus, there is an effective shell thickness determined by the original and incoming ligands which can impact the interparticle interaction energy, leading to different interaction potentials for different effective shell thicknesses (Figure 6.3.1A). Figure 6.3.1A-B illustrates the changes in terms of the minimum energy and interparticle gap for a dimer of 40 nm AuNPs when the effective shell thickness (L') of DNA shell is varied from 0.1 nm to 10 nm, i.e., from the original monolayer of citrate (or acrylate) capping to a full monolayer of DNA coverage.

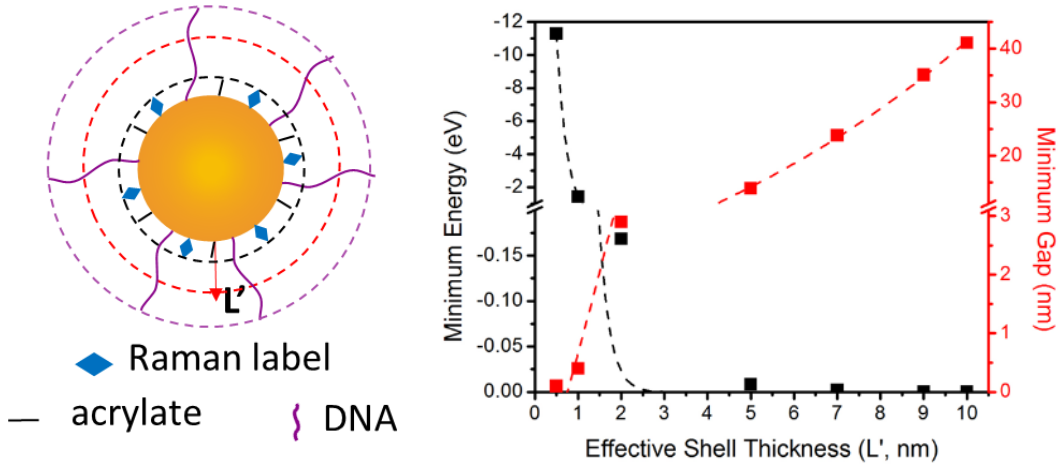

(A) **(B)**

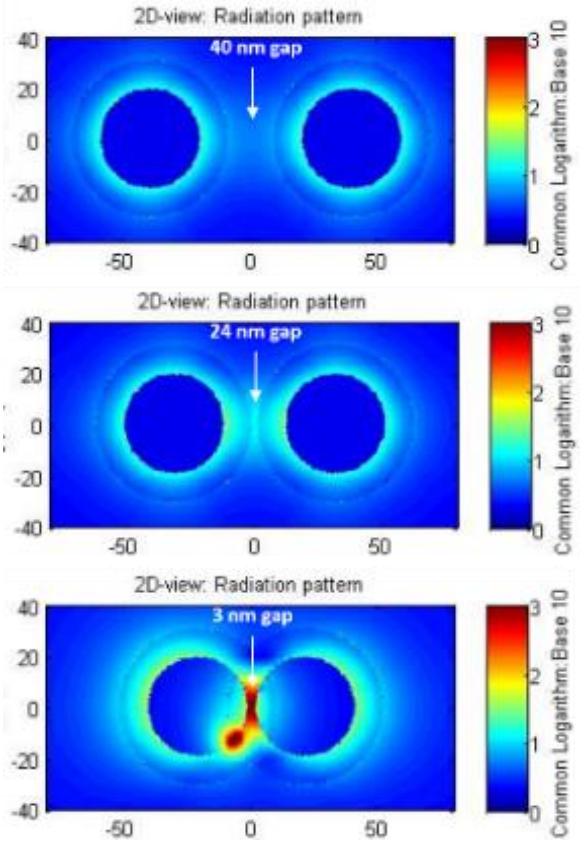

(C)

Figure 6.3.1. (A-B) Dependencies of the minimum interparticle gap and total interaction energy (E_M) on effective DNA shell thickness (L') for a dimer of 40 nm NPs (Hamaker constant: – 0.83 eV and DNA monolayer thickness – 2 nm and length – 11 nm). (Dashed lines: $E_{min.} = -19.1 \times \exp(-1.6 \times L')$; $G_{min.} = 19.9 \times \exp(0.1 \times L')$) (C) Simulated EMF spectra for dimers of 39 nm AuNP dimers at L'=10 nm (gap ≈ 40 nm), 7 nm (gap ≈ 24 nm), and 2 nm (gap ≈ 3 nm).

In this case, the effective ligand thickness would be smaller than the expected 11 nm DNA shell length as a result of squeezing in the presence of AuNPs. Based on the calculated potentials (Figure 6.3.2), under several effective thicknesses (L' = 10 nm (gap ≈ 40 nm), 7 nm (gap ≈ 24 nm), and 2 nm (gap ≈ 3 nm)) the simulated EMF intensity at the center of the dimer showed a sharp contrast between L' = 10 nm and 2 nm (Figure 1C). While the center EMF intensity for L'= 2 nm displays a clear enhancement, there is essentially no enhancement for L' = 10 nm (Figure 6.3.1).

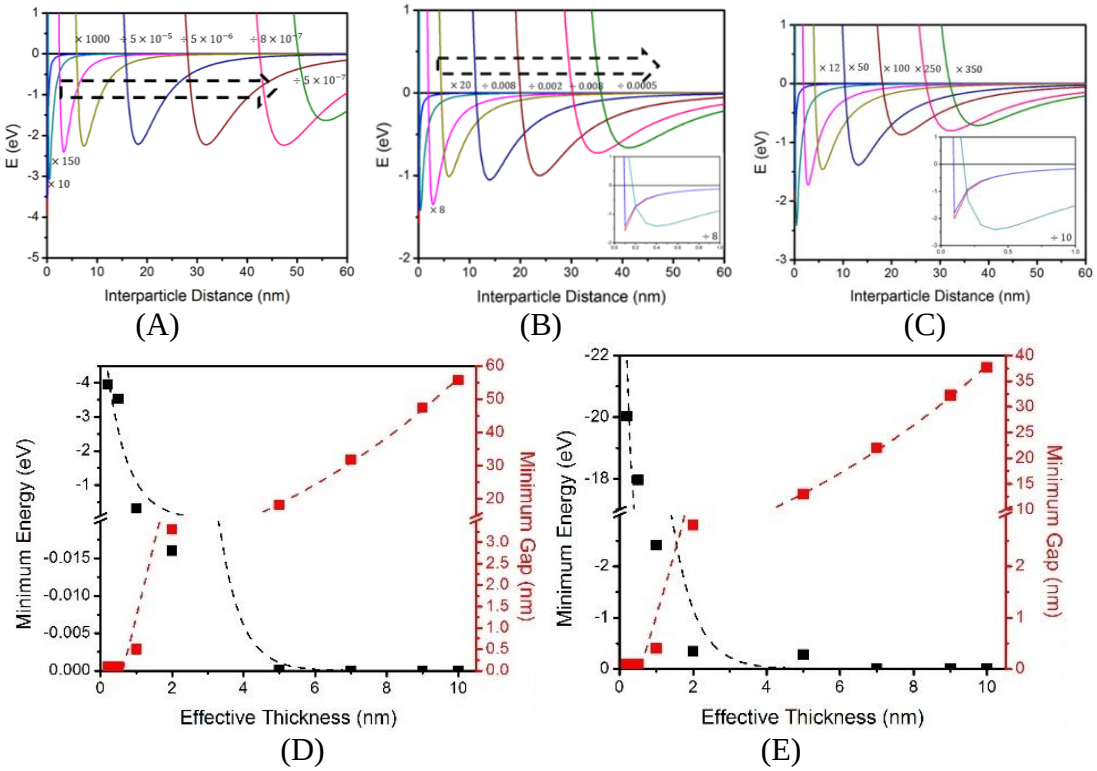

Figure 6.3.2. Calculated steric repulsion and van der Waals attraction potentials for symmetric dimers of AuNPs (13 nm (A), 39 nm (B), and 62 nm (C)). Dependencies of interparticle Gap and total Energy (E_M) on effective DNA shell thickness (L') for a dimer of 13 nm (D) and 62 nm (E) NPs (Hamaker constant – 0.83 eV and DNA diameter – 2 nm. 13 nm NPs: E_{min} = -5.1*exp(-1.7*L'), G_{min} = 23.9*exp(0.1*L') -26.7; 62 nm NPs: E_{min} = -30.3*exp(-1.6*L'), G_{min} = 19.6*exp(0.1*L') -20.8.

The center EMF intensity for L'=7 nm displays an enhancement which is almost the same as that surrounding the NPs. This finding is significant, demonstrating a clear need to assess the interparticle plasmonic coupling and SERS characteristics in terms of the effective thickness. Similar findings were observed in dimers of smaller (e.g., 13 nm) or larger (e.g., 62 nm) AuNPs (Figure 6.3.2). In view of the likelihood that part of the DNA strands are laying down on the surface of the NPs or over the original capping molecules, leading to a greatly-squeezed interparticle distance, our study focused on understanding how such smaller interparticle distance correlates with the interparticle plasmonic coupling and the SERS "hot-spot" effect, especially for nanoparticles with magnetic cores which could further squeeze the interparticle gap distance (*g*). The results

are discussed in the next few subsections on interparticle plasmonic coupling and electric field enhancement for two different combinations of NPs linked by DNA strands, i.e., Au–M@Au NPs and Au–M@Ag NPs. The control experiments of Ag–Ag NPs, Au–Au NPs, and Au–Ag NPs will also be discussed to further substantiate the results presented.

6.3.1 Combination of Ag – Ag NPs as a Control

In this section, we consider the metallic Ag-Ag combination as a control for the experimental analysis using UV-Vis and SERS. Note that most experimental observations indicate that silver–based NPs have a stronger SERS enhancement than gold-based NPs; which is further substantiated from the results presented. Combination of AgNPs of the same size (10 nm AgNPs) and different sizes (40 nm with 10 nm AgNPs) were analyzed. Experimentally, the intensity decreased after the addition of DNA; however, there was no change within the 10 nm AgNP dimer assembly but a very subtle change in the SP peak was observed in the 40 nm – 10 nm Ag-Ag NPs (Figure 6.3.1.1A-B). The insignificant change in the SP peak of the 10 nm AgNPs could due to be minimal shifting observed in the simulated ACS of the dimer combination at smaller NP gaps (Figure 6.3.1.2C-D).

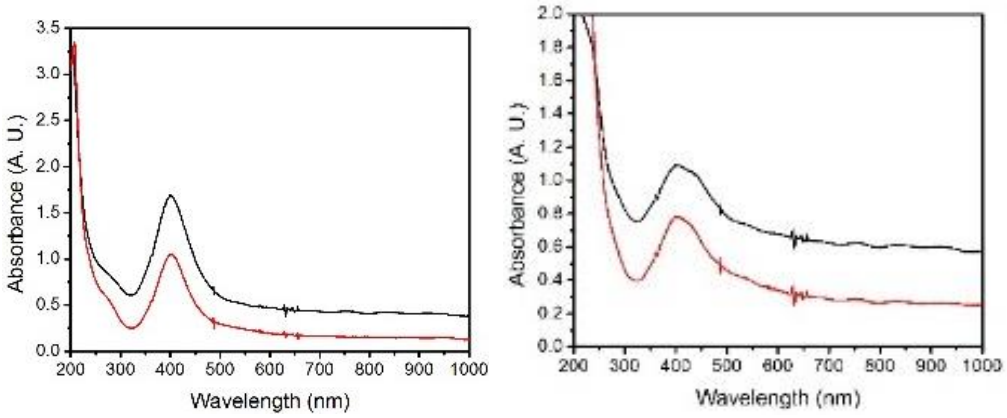

(A) **(B)**

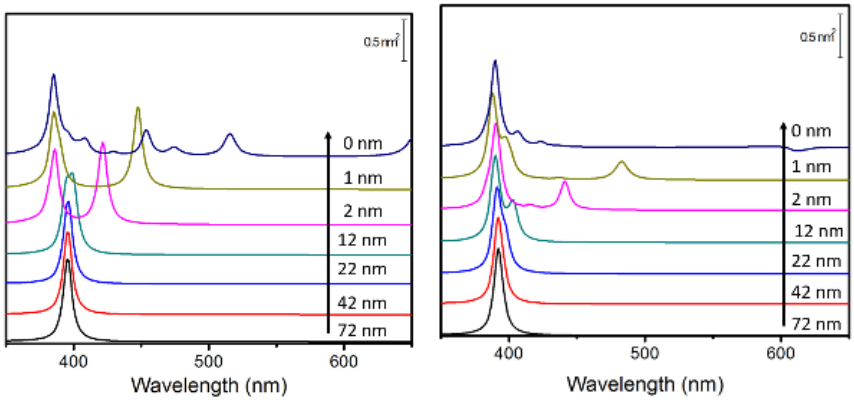

Figure 6.3.1.1. Homo – sized AgNP dimers (10 nm) (A, C) and hetero – sized AgNP dimers (10 nm – 30 nm) (B, D) assembled with DNA (before (black) and after (red) assembly) while monitored using UV-Vis (A, B) and the simulated ACS (C, D) of hetero – sized AgNP dimers over a range of gap distances.

The assembly of the two systems were analyzed using Raman. Similarly to the UV-Vis, the smaller 10 nm AgNPs were showed no increase in intensity after assembly with DNA (Figure 2A). On the other hand, the larger 10 nm and 39 nm AgNPs showed a significant increase after the addition of the target DNA (Figure 6.3.1.2B). The significance, and lack thereof for the 10 nm AgNPs, in the SERS peak are evident from the simulated ACS peaks in that the smaller NP combination does not shift as far as the 10 nm – 39 nm AgNPs (Figure 6.3.1.1C-D). Since the 10 nm – 39 nm AgNPs shift closer to 500 nm (Figure 6.3.1.1D (gap = 1nm) it can be viewed in the 632 nm Raman.

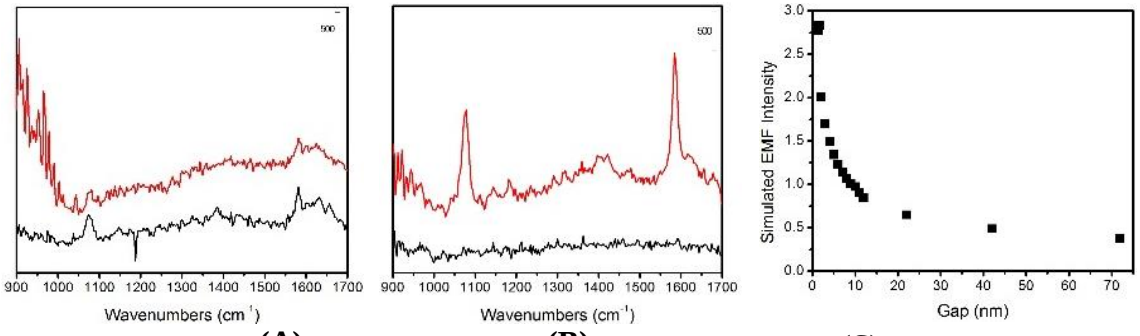

Figure 6.3.1.2. SERS spectra of same-sized AgNP dimers (10 nm) (A) and different sized AgNP dimers (10 nm – 30 nm) (B) assembled with DNA (before (black) and after (red) assembly) and the simulated EMF (C) of different sized AgNP dimers over a range of gap distances.

The simulated EMF intensity of the different size AgNP dimers were analyzed over a range of gap distances (0 to 72 nm). The intensity of dimers increase significantly below 10 nm gap distance. This is apparent from the increase in Raman signal after the addition of the DNA, which is smaller than 10 nm in length. Similarly to Chapter 5 (AuNP assembly), it is observed that larger sized NPs have a more significant shift in SP band, thus a larger EMF intensity as expected. Even though silver exhibits a stronger plasmon band than gold, signal is not apparent from smaller sized NPs unless they are paired with larger NPs.

6.3.2 Combination of Au–M@Au NPs

In this section, we describe the DNA-mediated assembly of AuNPs and M@AuNPs, i.e., Au–M@Au assembly. First we describe the surface plasmon resonance (SPR) optical characteristics based on experimental UV-Vis data and theoretical simulation of the plasmonic coupling. It is then followed by the discussion of the Surface Enhanced Raman Scattering (SERS) intensity in correlation with the theoretical simulation of the interparticle electrical field enhancement.

Experimentally, a subtle change can be detected in the SP band as shown by the UV-Vis spectra for an aqueous solution of *MZF@Au*-DNA1 and MBA-Au NPs before and after adding DNA2 (Figure 6.3.2.1A). This change is reflected by a very small red shift in the SP band.

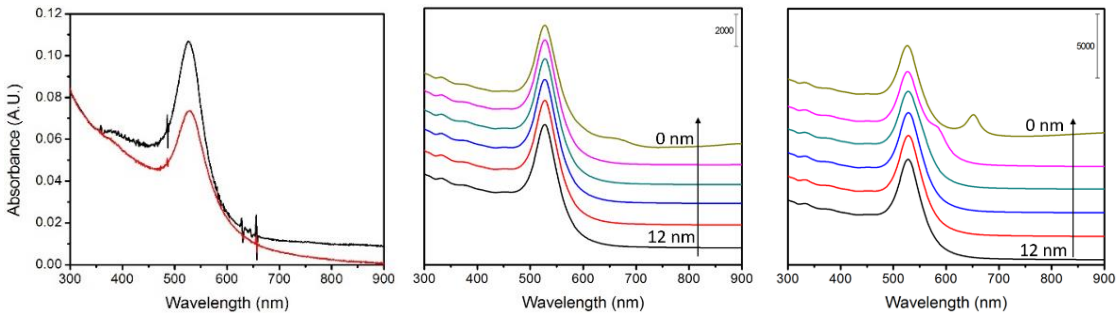

(A) **(B)** **(C)**

Figure 6.3.2.1. (A) UV-vis spectra for an aqueous solution of MZF@Au-DNA1 and MBA-Au NPs before (black) and after (red) adding DNA2. [MZF@Au-DNA1] = 6.2 nM; [DNA2] =0.56 μM; [40 nm-Au@MBA] =4.3×10^{-2} nM. **(B-C)** Simulated ACS spectra of AuNPs assembled to M@Au NPs (B) and AuNPs (C) with different gap distances (12, 7, 6, 2, 1, 0 nm).

Theoretically, the SP band characteristics of the Au–M@Au NPs were simulated in terms of absorbance cross-section spectra (ACS) as a function of g (Figure 6.3.2.1B). The general feature for the simulated ACS is similar to those observed experimentally. There is no obvious shift in the SP band. The core size is 9 nm whereas the Au shell thickness is 0.5 nm for the simulation in the above example. The insignificant shift of the simulated ACS band for the relatively larger-sized magnetic core and the relatively thinner Au shell thickness can be further analyzed through simulations (see Section 6.3.5).

In comparison with the band characteristics of the Au-M@Au NPs, the simulated ACS band Au-Au NPs showed a more red-shift as a function of *g* (Figure 6.3.2.1C). As reflected by the appearance of the longer-wavelength band, the Au-Au NP dimer exhibits a larger shift below 10 nm gap, whereas the band for the Au-M@Au NP dimer does not show any significant shift until the gap distance is below 5 nm.

An increase in SERS intensity was observed upon the M@AuNPs, as shown by the SERS spectra before and after addition of DNA2 to the solutions of DNA1-M@Au NPs and MBA-Au NPs (Figure 6.3.2.2A). The SERS intensity of the Raman labels significantly increased upon the addition of the target DNA strands. The SERS intensity was assessed by simulation of the EMF intensity using a dimer model consisting of 10 nm M@AuNP and 40 nm AuNPs as a function of *g*. **Figure 6.3.2.2**B shows the 2D images of the simulated EMF around the Au–M@Au NPs (bottom) and Au-Au NPs (top) at g = 2 nm, showing clearly an enhanced intensity at the center of the interparticle gap. The EMF

intensity for the Au–M@Au dimer measured at the center of the gap ("hot-spot") increases as the interparticle distance increases (Figure 6.3.2.2C, open squares). The EMF intensity for the Au-Au dimer is included for comparison (Figure 6.3.2.2C, closed squares).

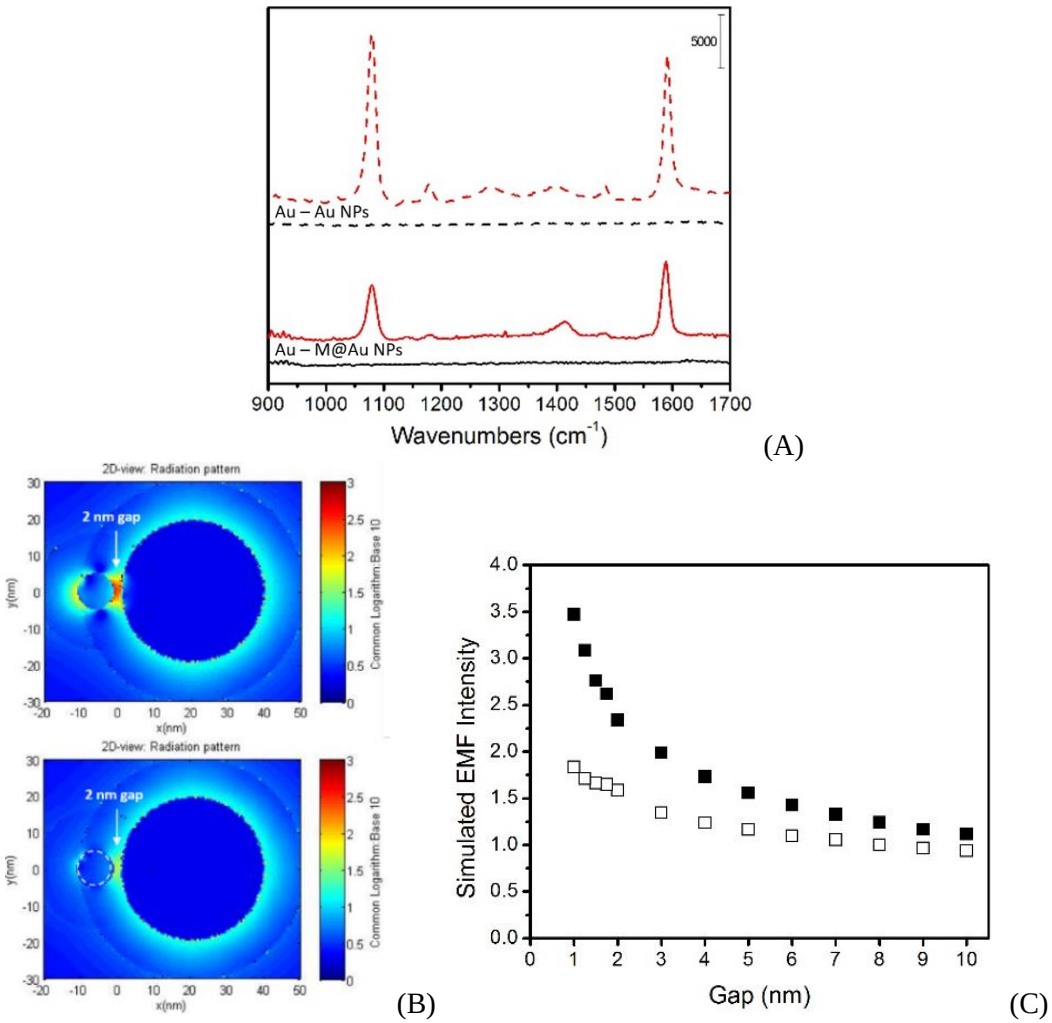

Figure 6.3.2.2. (A) SERS spectra for the assembly of MBA labeled AuNPs and DNA functionalized M@Au NPs (solid) (and AuNPs (dashed)) with target DNA strands (before assembly – black; after assembly – red). (B) 2D image of the simulated EMF around the Au-M@Au NPs (bottom, 9 nm magnetic core and 0.5 nm Au shell for M@Au NP) and Au-Au NPs (top, 40 nm) at g = 2 nm; (C) Plot of the simulated EMF intensity for the Au-M@Au NPs (open squares) and Au-Au NPs (closed squares) as a function of the interparticle gap (from 1 to 10 nm).

It is evident that the EMF intensity for Au–M@Au dimer is smaller than that for Au-Au dimer. A significant increase in EMF at the "hot-spot" is observed when the gap distance is below 3 nm (Figure 6.3.2.2C). The experimentally observed SERS intensity

enhancement is reflected by the theoretically-simulated EMF enhancement at the "hot-spot".

A comparison of the above experimental data and theoretical simulation results for the Au–M@Au NPs and the Au-Au NPs at g = 2 nm is shown in Figure 6.3.2.3. It is evident that both the SERS intensity and the EMF intensity for Au-Au NPs are higher than those for the Au–M@Au NPs, showing an excellent agreement between the experimental data and the simulation results. This agreement is also validated for the other interparticle distances. This finding is consistent with the stronger plasmonic coupling for Au-Au NPs than that for the Au–M@Au NPs, as described earlier (see Figure 6.3.2.1B-C).

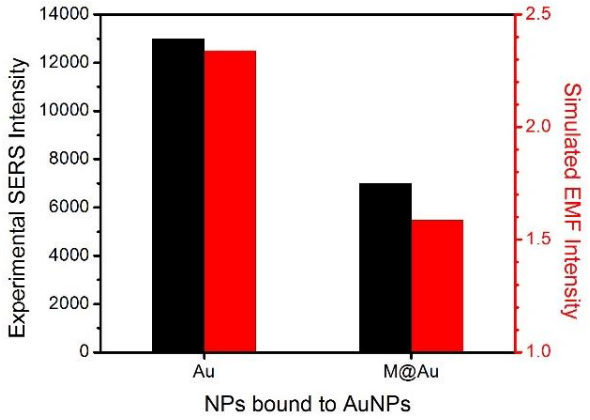

Figure 6.3.2.3. Comparison of the experimental SERS intensity (black) and simulated EMF intensity (red) for the Au–M@Au NPs and the Au-Au NPs at an interparticle gap of 2 nm.

6.3.3 Combination of Au – M@Ag NPs

Using M@Ag NPs to replace M@Au NPs, similar experiments and simulations were performed for the DNA-mediated assembly of AuNPs and M@Ag NPs, i.e., Au–M@Ag assembly. Both the SPR optical and the SERS characteristics are discussed in correlation with the theoretical simulation results.

A representative set of UV-Vis spectra for the DNA-mediated assembly of AuNPs and M@Ag NPs is shown in Figure 6.3.3.1A. In comparison with the spectral features for Au–M@Au (Figure 6.3.2.1A), there appears a stronger plasmonic coupling for the Au-M@Ag, as evidenced by the appearance of the SP band at a longer wavelength (~660 nm), demonstrating a subtle difference in plasmonic coupling between Au–M@Au and Au–M@Ag NPs.

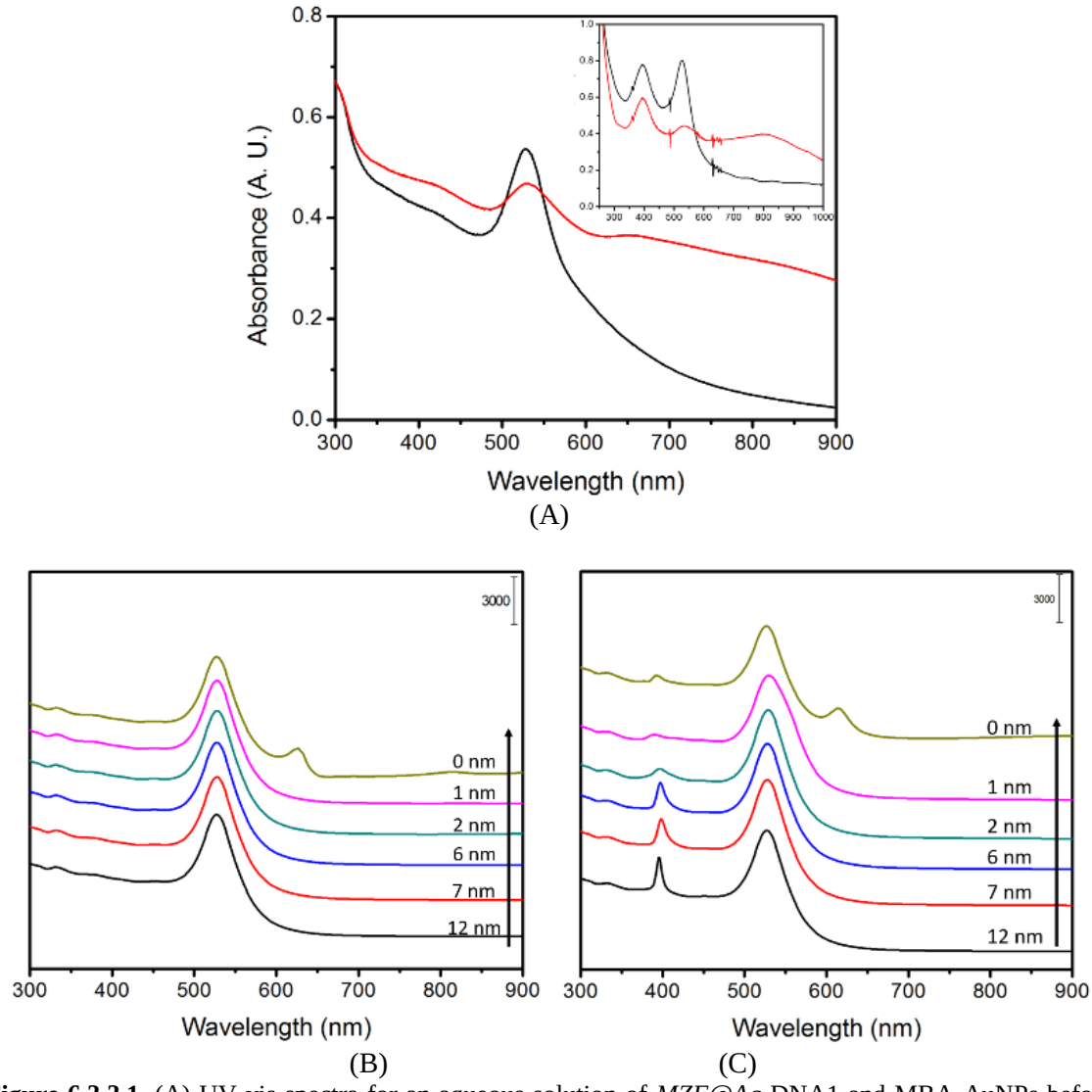

Figure 6.3.3.1. (A) UV-vis spectra for an aqueous solution of *MZF@Ag*-DNA1 and MBA-AuNPs before (black, bottom) and after (red, top) adding DNA2. Inset of A shows before (black) and after (red) assembly of 10 nm AgNPs and 40 nm AuNPs with DNA. (B) The simulated ACS Intensity of M@AgNPs and AuNPs when gap distance is decreased from 12 to 0 nm (arrows indicate the trend as the distance decreases: 12, 7, 6, 2, 1, and 0 nm). [*MZF@Ag*-DNA1] =3.0 nM; [DNA2] =0.56 μM; [40 nm-Au@MBA] = 4.3×10^{-2} nM).

(C) The simulated EMF intensity of metallic 10 nm AgNPs assembled to 40 nm AuNPs with varying gap distances (arrows show shift from larger to smaller gaps: 12, 7, 6, 2, 1, 0 nm)).

The simulated ACS spectra for Au–M@Ag NPs and the Au-Ag NPs are shown in Figure 6.3.3.1 as a function of the interparticle gap (*g*). While there is no significant shift of the main SP band, similar to the case for Au–M@Au NPs and the Au-Au NPs; the spectral feature in terms of the appearance of the longer wavelength band as the interparticle gap approaches zero, appears to be in agreement with the UV-Vis spectra.

For a further comparison, we also examined the UV-Vis spectra for the assembly of AgNPs (10 nm) functionalized with DNA and AuNPs (40nm) functionalized with MBA (Figure 6.3.3.1A insert). Interestingly, after introduction to the target DNA strand, the appearance of the red-shifted SP band at a longer wavelength (~800 nm) is evident, demonstrating a stronger plasmonic coupling for the Au-Ag NPs than Au-Au NPs, and some similarity in plasmonic coupling between Au-Ag NPs and Au–M@Ag NPs.

A representative set of SERS spectra is shown in Figure 6.3.3.2A for the DNA2 mediated assembly of DNA1-M@Ag NPs and MBA-Au NPs. The SERS for the assembly of Au-Ag NPs is also included for comparison (Figure 6.3.3.2(A) (dashed lines, top)). There is a clear increase in SERS intensity after the assemblies of both Au–M@Ag and Au-Ag NPs, which was also assessed by simulations. Similar to the simulation for the Au–M@Au NPs and Au-Au NPs, the 2D images of the simulated EMF around the Au–M@Ag NPs and Au-Ag NPs at an interparticle gap of 2 nm, also showed a clear enhancement in intensity at the center of the interparticle gap (Figure 6.3.3.2B). The EMF intensity for the Au–M@Ag dimer measured at the center of the gap (“hot-spot”) increases as the interparticle distance increases (Figure 6.3.3.2C, open circles), which is again lower than that for the Au-Ag dimer (Figure 6.3.3.2C, closed circles). The experimentally observed

SERS intensity enhancement is consistent with trend of the theoretically-simulated EMF enhancement at the "hot-spot" as a function of the interparticle gap.

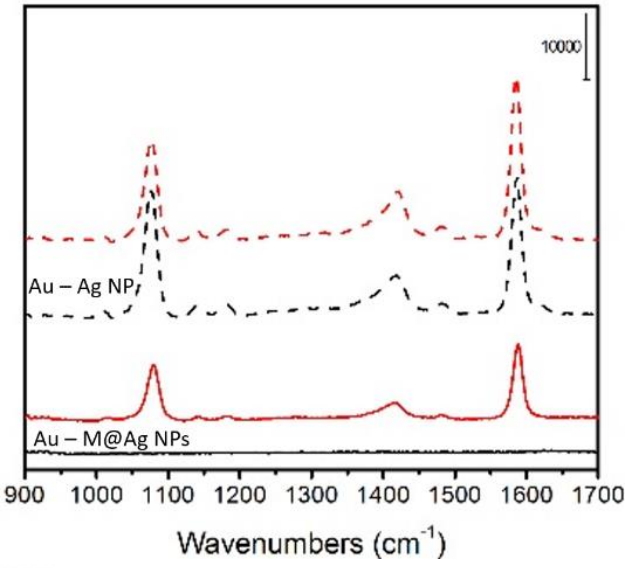

(A)

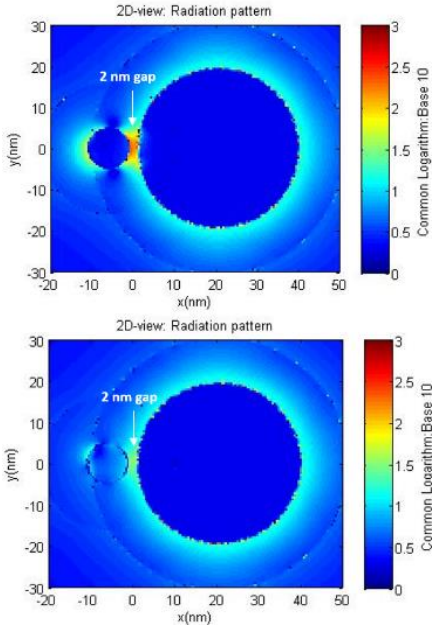

(B)

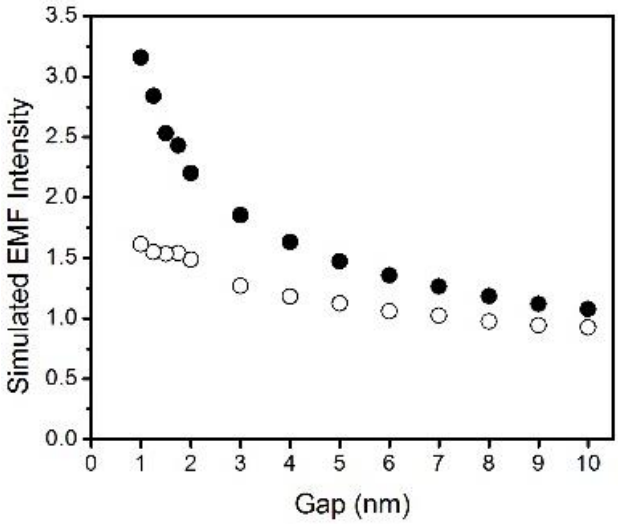

(C)

Figure 6.3.3.2. (A) SERS spectrum of Magnetic Nanoparticles coated with Ag before (black) and after (red) assembly (control assembly of Ag and Au (dashed, top) and magnetic (solid, bottom)). (B) Simulated EMF spectra of the metallic AgNPs assembled to AuNPs (top) and M@AgNPs with AuNPs (bottom) at g = 2 nm. (C) The simulated EMF Intensity of 10 nm M@AgNPs (9 nm Magnetic core) and AuNPs (bottom, open circles) and Ag-Au NP dimers (top, closed circles) as gap distance decreases from 10 to 1 nm.

In Figure 6.3.3.3, the experimental data and theoretical simulation results are compared for Au–M@Ag NPs and Au-Ag NPs at g = 2 nm. In contrast to the trend

observed for the Au–M@Au and Au-Au NPs, a discrepancy between the theoretical and experimental data is observed. While the simulated EMF intensity shows a decrease from Au-Ag NPs to Au–M@Ag NPs, the experimental SERS intensity exhibits an opposite trend, the origin of which is discussed in the next subsection.

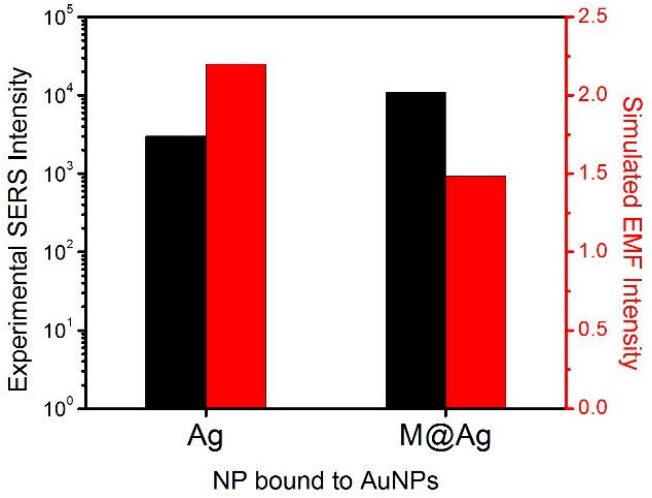

Figure 6.3.3.3. Comparison of the experimental SERS intensity (black) and simulated EMF intensity (red) for the Au-M@Ag NPs and the Au-Ag NPs at an interparticle gap of 2 nm.

6.3.4 A comparison between Au-M@Au and Au-M@Ag combinations

As shown in Figures 6.3.2.2 and 6.3.3.3 for both experimental SERS and simulated EMF at g = 2 nm, there is a clear agreement for the difference between Au-M@Au and Au-Au NPs. However, there is a disagreement for the Au-M@Ag and Au-Ag NPs. Also, the SERS intensity for Au-M@AgNPs is higher than that of the Au-M@AuNPs. Note that most experimental observations indicate that silver–based NPs have a stronger SERS enhancement than gold-based NPs. To address the experimental-theoretical disagreement, a key question that must be addressed is how the interparticle spacing is operational for plasmonic coupling of the dimeric nanoparticles in the presence of the magnetic cores and the effective monolayer capping shells.

The interparticle spacing is determined by the interparticle interaction potentials for the DNA – mediated NP assembly, which were analyzed by considering the monolayer structure in terms of the number of DNA and capping molecules on the NP surface. The approximate number of DNA and other capping molecules on the NP surface can be estimated from the model shown in Figure 6.3.3.4 (see Equations 3 and 4).

$$xA_{DNA} + yA_{cap} = 4\pi r_{NP}^2 \quad (1)$$

$$\frac{xh_{DNA}+yh_{cap}}{x+y} = L' \quad (2)$$

The estimated effective thickness (L') is dependent on the orientation of DNA strands on the smaller NP surface (Figure 6.3.3.4). When DNA stands on the surface, the thickness is approx. 11 nm, and when laying on the surface it is approx. 2 nm. At an effective thickness of 2 nm, the mixed monolayer consists of 73% DNA. This partial surface coverage provides an explanation of the finding on the small interparticle spacing for the experimental-theoretical correlation (Figures 6.3.2.2 and 6.3.3.3).

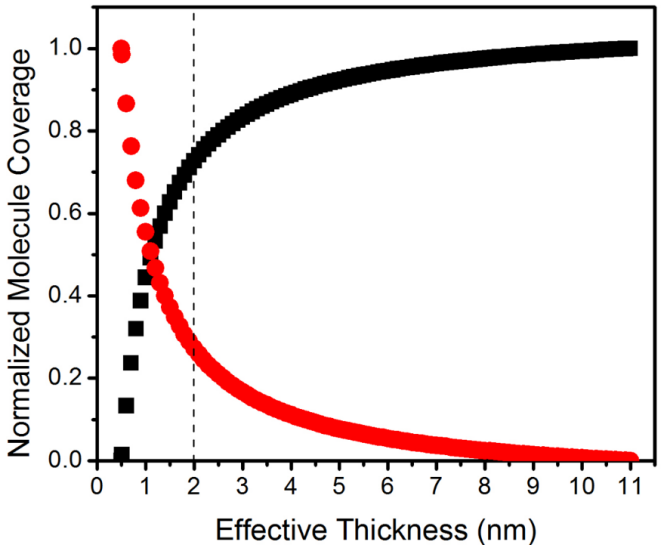

Figure 6.3.3.4. Fractional surface coverage of DNA (black) and acrylate (red) as a function of the effective thickness (L', nm) (DNA: 11 nm height, 2 nm diameter; acrylate: 0.5 nm height, 0.5 nm diameter).

6.3.4 Comparison between Au- and Ag-based NPs

We further examined the EMF intensity over the four dimer assemblies for g ≤ 2 nm (Figures 6.3.2.2 and 6.3.3.3). Figure 6.3.2.2 shows the simulated EMF spectra of Au–M@Au at g = 0.1 nm and demonstrates the change in simulated EMF intensity as gap distance decreases from 2 nm to 0 nm for Au-Au (black, squares) and Au–M@Au (red, circle). As the gap distance decreases, the EMF intensity of Au-Au NP dimers increase to a maximum at 0.5 nm gap and drops thereafter. The Au–M@Au NP dimer shows a similar trend in EMF intensity as the gap decreases, and exhibits a maximum at 0.5 nm, except the intensity is much smaller compared to the Au-Au NP dimer. When the NPs come into contact (g = 0 nm), the EMF intensity of the Au–M@AuNPs shows an increase which is practically the same in comparison with that for the Au-Au NP dimer. A similar trend is evident for the EMF intensities observed for Au-Ag and Au–M@Ag NP dimers as the gap drops from 2 nm to 0 nm (Figure 6.3.3.3). A close comparison of the data with that in Figure 6.3.4.1, the EMF intensity for the Au-Ag NP dimer showed a less sharp decrease after the maximum at 0.5 nm gap. Interestingly, when gap = 0 nm, the EMF intensity for the Au-M@Ag NP dimers shows a dramatic increase, which is much greater than that for the Au-Ag NP dimer.

The above findings are interesting because the change of the simulated EMF intensities shows sharp contrasts as a function of the interparticle gap. For gap > 0.5 nm, the Au-Au NP dimers display a higher EMF intensity than that of Au-Ag NP dimers. For gap < 0.5 nm, the two systems show similar trends but the intensity of Au-Ag NP dimers is larger than the intensity of Au-Au NP dimers. For dimers of Au–M@Au and Au–M@Ag, apparently, the intensity of Au–M@Au remains higher than Au–M@Ag when gap > 0 nm.

However at gap = 0 nm, the intensity for both Au–M@Au and Au–M@Ag dimers increase sharply; although the intensity for Au–M@Ag dimer is greater than that for Au–M@Au dimer.

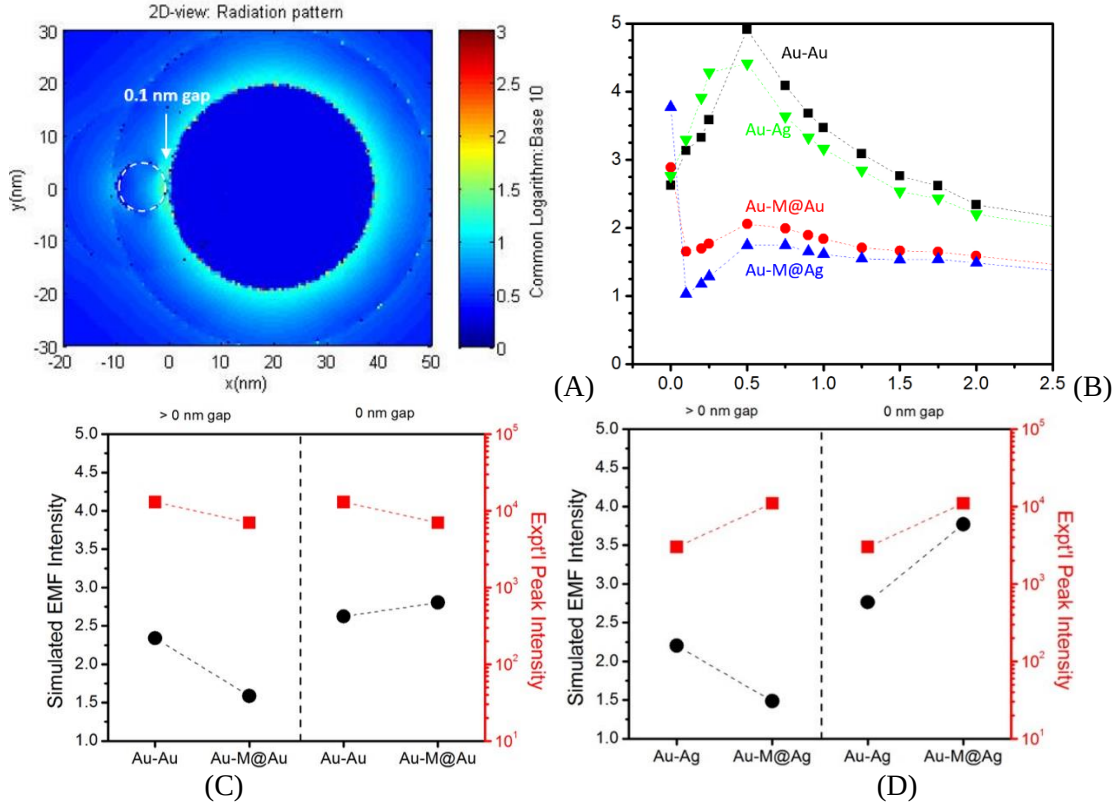

Figure 6.3.4.1. (A) Simulated EMF spectra of Au – M@Ag dimer at 0.1 nm gap. (B) Plots of the simulated EMF intensity of 40 nm Au NP and 10 nm NP of Au (black squares), M@Au (red circles) (B), M@Ag (blue up triangles), and Ag (lime downward triangles) at interparticle gaps below 2 nm. (C and D) Comparison of the simulated EMF and SERS intensities for heterodimers of Au – Au based NPs (C) and Au – Ag based NPs (D) above 0 nm (2 nm) and at 0 nm gap distances.

The simulated results are summarized in Figure 6.3.4.1C and D for an overall comparison with the experimental results. The experimental SERS (red, squares) and simulated EMF (black, circles) intensities are compared for gap > 0 nm and gap = 0 nm. For Au-Au and Au–M@Au NP dimers (Figure 6.3.4.1C), the experimental SERS intensity for Au-Au is greater than Au–M@Au dimers, which is consistent with the simulated EMF intensities of Au-Au dimer being greater than Au–M@Au for gap > 0. For gap = 0 nm,

the EMF for Au-Au is the same as or slightly lower than that of Au–M@Au. For Au-Ag and Au-M@Ag NP dimers (Figure 6.3.4.1D), a sharp contrast is revealed. For gap > 0 nm, the simulated EMF intensity for Au-Ag is higher than that for Au–M@Ag NP dimers. But at g = 0 nm, the simulated EMF intensity for Au-Ag is lower than Au–M@Ag dimer which is clearly consistent with the experimentally-observed SERS intensities for Au-Ag dimer being smaller than Au-M@Ag NP dimers.

An important implication from the above results is that the interparticle plasmonic coupling and squeezing are strongly dependent on the composition of the nanoparticles. The presence of Ag and magnetic core in the nanoparticles apparently had a stronger impact on these interparticle properties in comparison with Au. For pure metallic NPs, the effective monolayer thickness falls likely in the range of 1 – 2 nm, whereas the presence of magnetic cores appears to further squeeze the gap distance to approximately 0 nm. Squeezing of the DNA-capped NPs in the interparticle gap favors the peripheral region near the hot-spot contact region (edges of the gap), or in some cases the smaller-sized particle. In these cases, it was found that the highest intensity is not necessarily at the center between the NPs when the gap distance decreases, instead it could be in the peripheral contact region. These assessments were substantiated by a close examination of the EMF in peripheral region (Figure 6.3.4.2) for both Au–M@Au (Figure 6.3.4.2A)) and Au–M@Ag (Figure 6.3.4.2B) dimers.

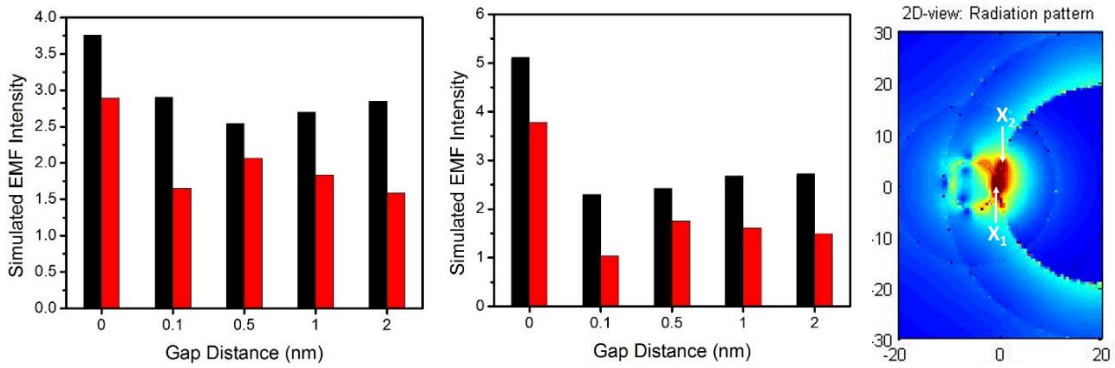

(A) **(B)** **(C)**

Figure 6.3.4.2. Comparison of EMF Intensity in the center of the hotspot region (red) and maximum intensity in the upper peripheral region of the hotspot (black) of AuNP (39 nm) – M@AuNPs (10 nm) (A) and – M@AgNPs (10 nm) (B). EMF schematic of Au – M@Ag NP at 0 nm where X_1 is the center of the hotspot and X_2 is the peripheral region.

The metallic NPs appear to exhibit a strong experimental-theoretical correlation, whereas the correlation for the metal-coated magnetic NPs is apparent only at gap distances below 0.5 nm. It is believed that the magnetic forces could have played an important role in the interparticle interactions other than van der Waals forces. This leads to further squeezing of the interparticle spacing in comparison with only van der Waals interaction, pushing the DNA to the edges of the dimer (Scheme 6.3.4.1).

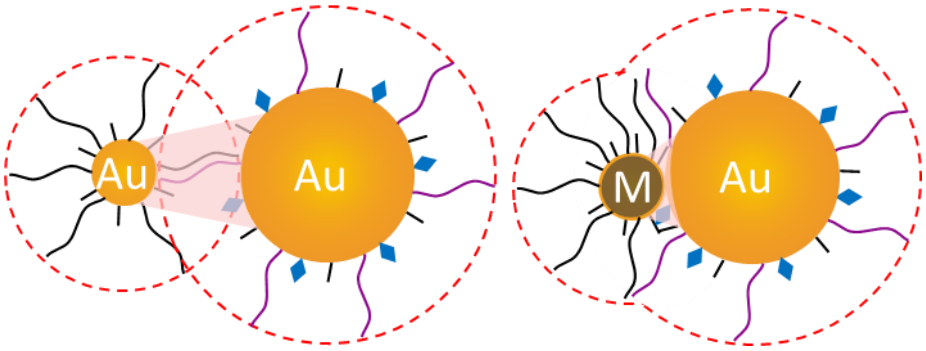

(A) (B)

Scheme 6.3.4.1. Proposed structures in terms of the interparticle spacing depending on the metal-metal dimer (A) and the metal-magnetic core@metal dimer (B) under an effective thickness for the DNA-capping monolayer.

Moreover, the NP dimers that involve Ag component appears to have a stronger plasmonic effect than those involving Au component only, even though there appeared to

be less Ag on the magnetic NP than Au. This finding could be due to a larger tendency of charge transfer from Ag than Au.[13, 14, 16] This was further supported by the simulation showing the red-shift in SP bands near 700 nm. Experimentally, since the excitation wavelength of the laser is 633 nm, the NP dimers involving Ag component exhibits a higher SERS intensity than those involving only Au component.

6.3.5 Factors that affect Magnetic NP assembly

In the experiment M@AuNPs (1.5 nm thick) have a thicker shell than M@AgNPs (0.5 nm thick) used, however M@AgNPs exhibited a larger intensity than M@AuNPs. This section examines the influence of the relative magnetic core size and metal shell thickness on plasmonic coupling to identify the reason for the increase in intensity of thin NP shells. The simulations were performed in terms of the different relative magnetic core size and metal shell thickness for the NP dimers, including (1) changing magnetic core while keeping the same metal shell thickness (0.5 nm), (2) changing shell thickness while keeping the same core size (9 nm), and (3) changing core size and shell thickness while maintaining the same overall NP size (10 nm) (Scheme 6.3.5.1).

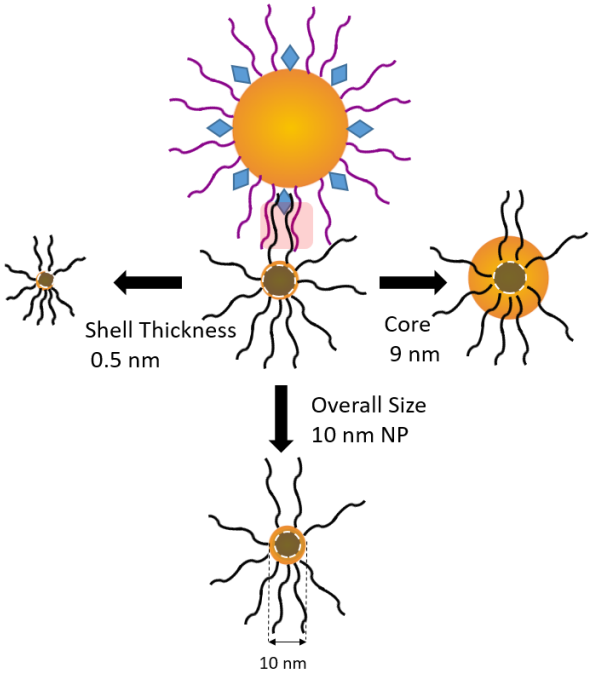

Scheme 6.3.5.1. Manipulation of bidirectional approach for the interpretation of magnetic coated dimers (left: decrease magnetic core in a 10 nm NP (top) or a NP with 0.5 nm thick shell (bottom); right: increase metallic shell of 9 nm magnetic core).

As shown by the SP data (Figures 6.3.5.1) and the EMF (Figure 6.3.5.2) data, subtle changes in intensities of SP and EMF, as well as the wavelength of SP were observed (Tables 6.3.5.1-3). Increasing the magnetic core size for Au–M@Au and Au–M@Ag dimers appeared to increase the red-shift of the SP band. Similar trends were found when increasing the metal shell thickness of the dimers, except the SP bands initially far-red shifted and slowly shifted back towards the original SP band of the metal. Increasing the shell thickness and magnetic core size for an overall 10 nm sized NP, the SP band showed a slight red-shift and decreased intensity. Overall, while the SP band showed slight differences, the Au–M@Ag NP dimer's red-shift was smaller than that for Au–M@Au NP dimer, and remained near 700 nm which is close to the laser's wavelength (633 nm).

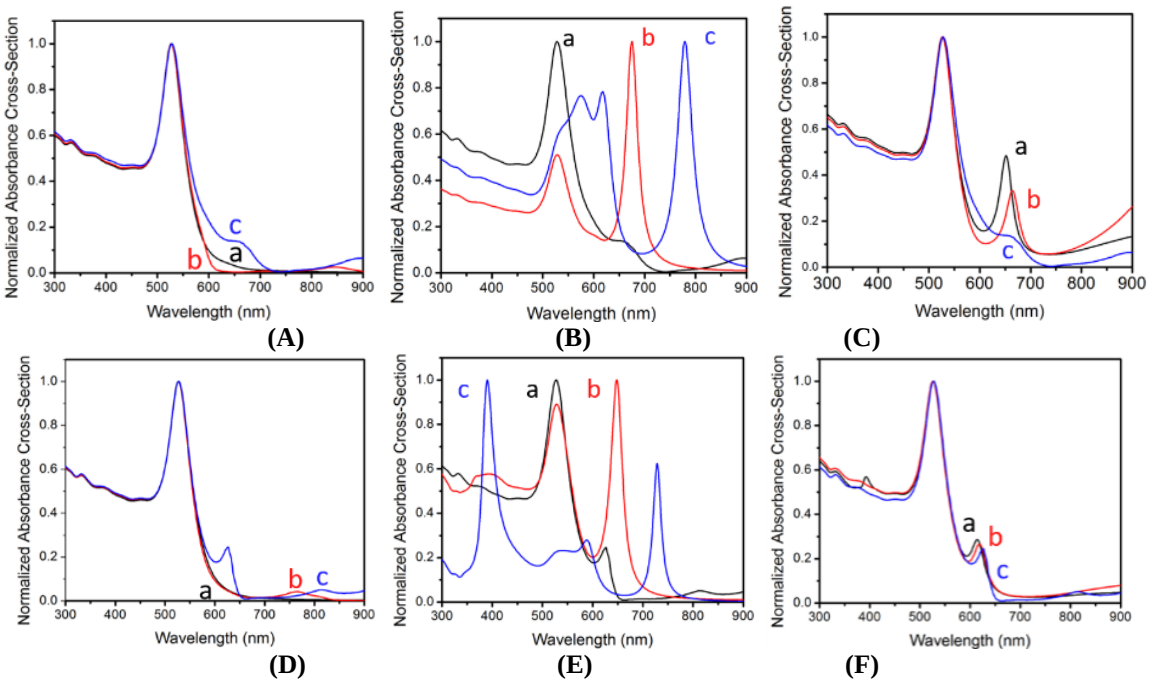

Figure 6.3.5.1. Normalized simulated ACS Intensity showing the SPR changes of M@AuNP (A, B, C) and M@AgNP (D, E, F) assembled to AuNPs when the NP gap distances is 0 nm that correspond to different core sizes when the shell thickness is 0.5 nm (A, D) (magnetic core size of 1 – black, a; 5 – red, b; 9 – blue, c), different shell thicknesses when the magnetic core is 9 nm (C, D) (shell thickness of 0.5 nm – black, a; 5.5 nm – red, b; 15.5 nm – blue, c), and 10 nm total size with different core sizes (magnetic core size of 1 – black, a; 5 – red, b; 9 – blue, c).

Table 6.3.5.1. Long wavelength (nm) and Normalized ACS Intensity of 0.5 nm thick Au/Ag coated Magnetic NPs.

Core, Shell NP		Au		Ag	
M	A*	nm	Intensity	nm	Intensity
1	0.5	527.3	1.000	526.3	1.000
5	0.5	844.8	0.026	764.7	0.043
7	0.5	527.3	1.000	527.3	1.000
12	0.5	806.8	0.020	730.7	0.032
9	0.5	896.9	0.064	813.8	0.051
9	5.5	674.6	1.000	648.5	1.000
9	15.5	778.4	1.000	728.7	0.62

Table 6.3.5.2. Long wavelength (nm) and Normalized ACS Intensity of 10 nm Au/Ag coated Magnetic NPs.

Core, Shell		Au		Ag	
M	A*	nm	Intensity	nm	Intensity
1	4.5	651.5	0.484	614.5	0.286
5	2.5	664.6	0.333	618.5	0.267
9	0.5	660.6	0.136	813.8	0.051

Similar trends were observed for the EMF intensities upon changing the shell thicknesses for an overall NP size of 10 nm (Figure 6.3.5.2). A maximum EMF intensity was shown at gap = 0.5 nm for all three cases. Increasing the shell thickness leads to an increase in the simulated EMF intensity.

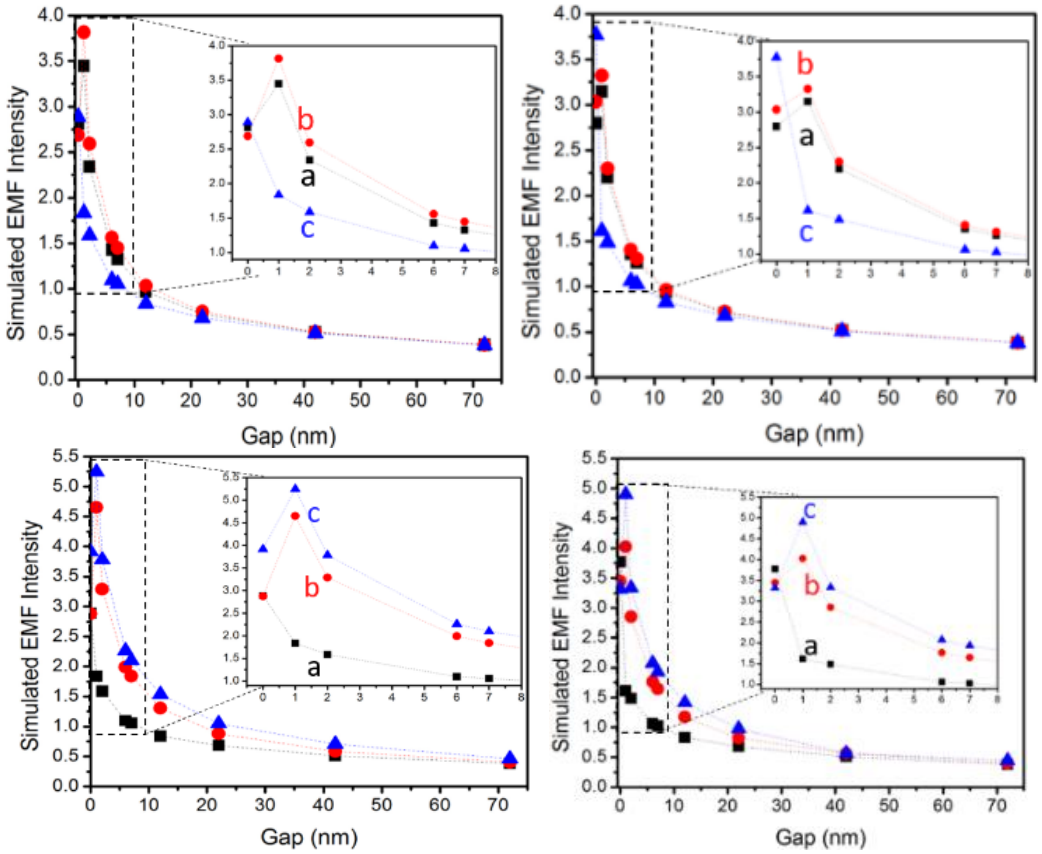

Figure 6.3.5.2. Different magnetic cores for 10 nm NPs with Au (A) or Ag (B) shell assembled to 39 nm AuNPs. (Core diameters: 1 (black, square), 5 (red, circle), and 9 (blue, triangle)). Different shell thicknesses for a 9 nm magnetic core assembled to 39 nm AuNPs: Au (C) or Ag (D) shell assembled to 39 nm AuNPs. (Shell thickness: 0.5 nm (black, square), 5.5 nm (red, circle), 15.5 nm (blue, triangle)).

Table 6.3.5.3. Exponential fitting of 10 nm coated magnetic NPs when magnetic core size changes (M = 1, 5, 9 nm) and when metallic shell thickness changes (A* = 0.5, 5.5, 15.5 nm).

$$y = y0 + A*\exp(R0*x)$$

Core, Shell		Au			Ag		
M	A*	y0	A	R0	y0	A	R0
1	0.5	0.578	3.288	-0.224	0.563	2.948	-0.214
5	0.5	0.589	3.692	-0.221	0.571	3.147	-0.218
9	0.5	0.487	3.147	-0.130	0.466	1.245	-0.106
9	5.5	0.642	4.493	-0.194	0.607	3.810	-0.192
9	15.5	0.759	5.047	-0.193	0.692	4.649	-0.195

Upon further investigation of the different magnetic cores of Fe (e.g., Fe_2O_3 compared to Fe_3O_4), it was observed that the different states of Fe did not have significant effect on the SP band (Figure 6.3.5.3). The only significant changes observed in the SP spectra occurred in the near IR region. These findings also have implications to other systems, including different monolayer shells, different metals (e.g., Cu, and alloys)

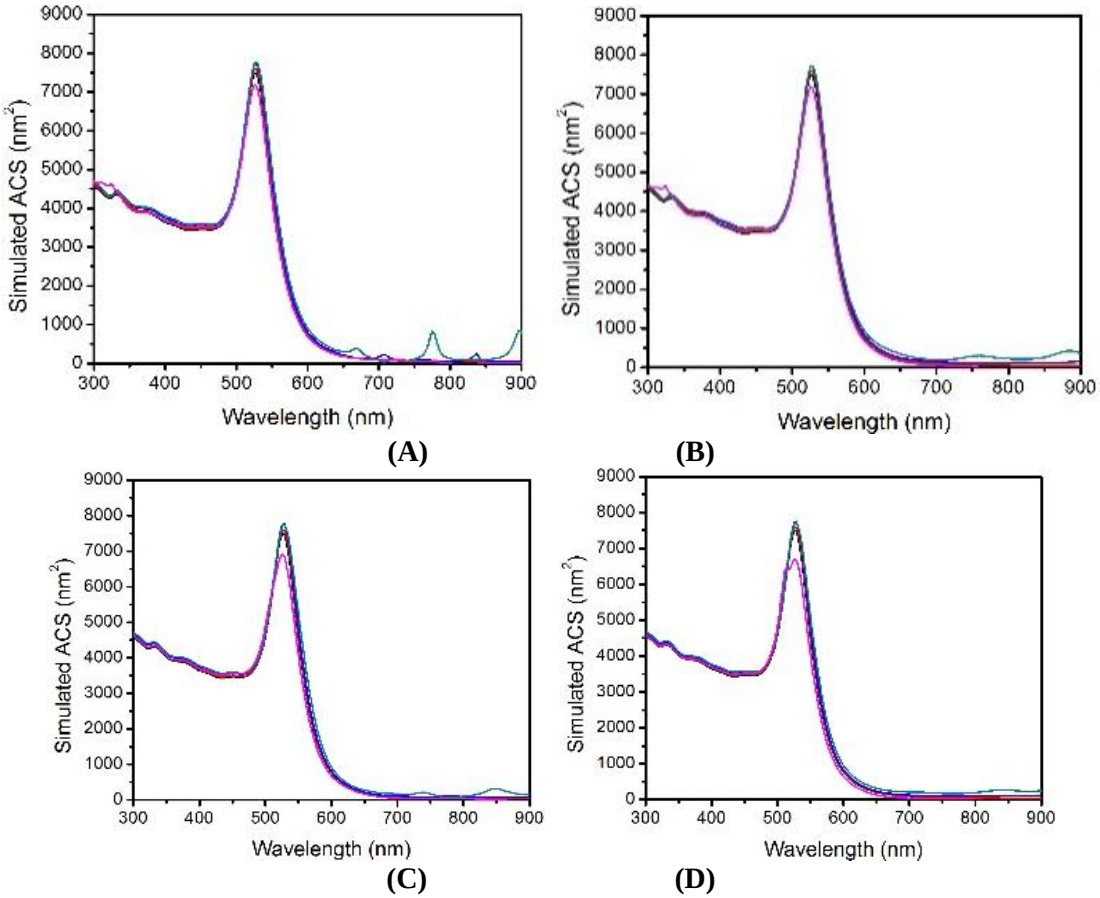

Figure 6.3.5.3. Comparison of simulated ACS Intensity of different Fe oxide magnetic cores (Fe_2O_3 (A, B) and Fe_3O_4 (C, D)) when coated with 0.5 nm shell thickness of Au (A, C) and Ag (B, D).

The investigation of Ag and Au coated NPs with different metal cores have exhibited similar plasmonic coupling as that found in Ag and Au coated NPs with iron oxide cores (Figure 6.3.5.4) when gap distance between dimer particles were decreased. In many of these cases, there appeared a red-shift in the near IR region at 1 nm gap and there was evidence of an even farther red-shift in the IR region at 0 nm.

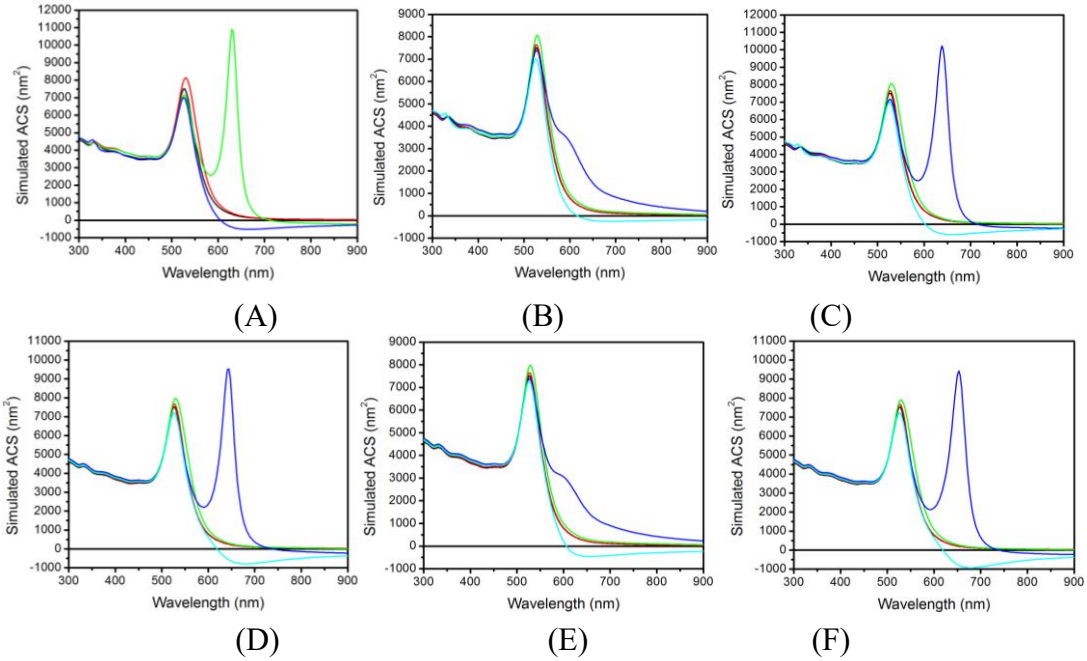

Figure 6.3.5.4. Simulated ACS spectra of Ag coated (A-C) and Au coated (D-F) NPs with different metal cores: Co (A, D), Fe (B, E), and Ni (C, F) when gap distances are 22, 12, 2, 1, and 0 nm.

6.4 Conclusion

These results have provided some important new insights into the interparticle spatial characteristics of DNA-linked core-shell type nanoparticles consisting of magnetic cores and plasmonic gold or silver shells in terms of the theoretical-experimental correlation. In comparison with Au nanoprobes, the simulated results of the SERS enhancement for the DNA-linked dimers of plasmonic-magnetic M@Au nanoprobes show a similar agreement with the experimental data in terms of the 'squeezed' interparticle spacing characteristic. Remarkably, for M@Ag nanoprobes, the agreement between the simulated and experimental results for DNA-linked dimers of M@Ag and Au nanoprobes is achieved at an interparticle spacing of essentially zero, implying an important role played by the magnetic interaction in the interparticle interactions. The results presented show that shell

thickness and magnetic core have a significant role on the plasmonic coupling of the NPs. These observations are remarkable, suggesting that both the gap and the chemical nature of the materials in the nanoparticles play an important role in the relative strength of interparticle plasmonic coupling. These findings are also supported by studies of other core shell NPs showing significantly-reduced interparticle gap distance.[14] These findings also have implications to other systems for the manipulation of biomolecules in detection systems.

References

1. Cheng, H. W.; Luo, J.; Zhong, C. J. SERS nanoprobes for bio-application. *Front. Chem. Sci. Eng.* **2015**, *9* (4), 428–441 DOI: 10.1007/s11705-015-1536-0.
2. Jamshaid, T.; Neto, E. T. T.; Eissa, M. M.; Zine, N.; Kunita, M. H.; El-Salhi, A. E.; Elaissari, A. Magnetic particles: From preparation to lab-on-a-chip, biosensors, microsystems and microfluidics applications. *TrAC - Trends Anal. Chem.* **2016**, *79*, 344–362 DOI: 10.1016/j.trac.2015.10.022.
3. De Crozals, G.; Bonnet, R.; Farre, C.; Chaix, C. Nanoparticles with multiple properties for biomedical applications: A strategic guide. *Nano Today* **2016**, *11* (4), 435–463 DOI: 10.1016/j.nantod.2016.07.002.
4. Nam, J.-M.; Oh, J.-W.; Lee, H.; Suh, Y. D. Plasmonic Nanogap-Enhanced Raman Scattering with Nanoparticles. *Acc. Chem. Res.* **2016**, acs.accounts.6b00409 DOI: 10.1021/acs.accounts.6b00409.
5. Skeete, Z.; Cheng, H.; Crew, E.; Lin, L.; Zhao, W.; Joseph, P.; Shan, S.; Cronk, H.; Luo, J.; Li, Y.; et al. Design of Functional Nanoparticles and Assemblies for Theranostic Applications. *ACS Appl. Mater. Interfaces* **2014**, *6* (24), 21752–21768 DOI: 10.1021/am502693t.
6. Rong, Z.; Wang, C.; Wang, J.; Wang, D.; Xiao, R.; Wang, S. Magnetic immunoassay for cancer biomarker detection based on surface-enhanced resonance Raman scattering from coupled plasmonic nanostructures. *Biosens. Bioelectron.* **2016**, *84*, 15–21 DOI: 10.1016/j.bios.2016.04.006.
7. Fan, C.; Zhu, S.; Xin, H.; Tian, Y.; Liang, E. Tunable and enhanced SERS activity of magneto-plasmonic Ag–Fe 3 O 4 nanocomposites with one pot synthesize method. *J. Opt.* **2017**, *19* (1), 15401 DOI: 10.1088/2040-8986/19/1/015401.
8. Lin, L.; Crew, E.; Yan, H.; Shan, S.; Skeete, Z.; Mott, D.; Krentsel, T.; Yin, J.; Chernova, N. a.; Luo, J.; et al. Bifunctional nanoparticles for SERS monitoring and magnetic intervention of assembly and enzyme cutting of DNAs. *J. Mater. Chem. B* **2013**, *1* (34), 4320 DOI: 10.1039/c3tb20446d.
9. Li, J.; Skeete, Z.; Shan, S.; Yan, S.; Kurzatkowska, K.; Zhao, W.; Ngo, Q. M.; Holubovska, P.; Luo, J.; Hepel, M.; et al. Surface Enhanced Raman Scattering Detection of Cancer Biomarkers with Bifunctional Nanocomposite Probes. *Anal. Chem.* **2015**, *87* (21), 10698–10702 DOI: 10.1021/acs.analchem.5b03456.
10. Wang, L.; Luo, J.; Shan, S.; Crew, E.; Yin, J.; Zhong, C. J.; Wallek, B.; Wong, S. S. S. Bacterial inactivation using silver-coated magnetic nanoparticles as functional antimicrobial agents. *Anal. Chem.* **2011**, *83* (22), 8688–8695 DOI: 10.1021/ac202164p.
11. Lim, D.-K.; Jeon, K.-S.; Kim, H. M.; Nam, J.-M.; Suh, Y. D. Nanogap-engineerable Raman-active nanodumbbells for single-molecule detection. *Nat. Mater.* **2010**, *9* (1), 60–67 DOI: 10.1038/nmat2596.
12. Skeete, Z.; Cheng, H.-W.; Ngo, Q. M.; Salazar, C.; Sun, W.; Luo, J.; Zhong, C.-J. "Squeezed" interparticle properties for plasmonic coupling and SERS characteristics of duplex DNA conjugated/linked gold nanoparticles of homo/hetero-sizes. *Nanotechnology* **2016**, *27* (32), 325706 DOI: 10.1088/0957-4484/27/32/325706.
13. Lee, J. H.; Nam, J. M.; Jeon, K. S.; Lim, D. K.; Kim, H.; Kwon, S.; Lee, H.; Suh, Y. D. Tuning and maximizing the single-molecule surface-enhanced Raman scattering

from DNA-tethered nanodumbbells. *ACS Nano* **2012**, *6* (11), 9574–9584 DOI: 10.1021/nn3028216.

14. Lee, H. M.; Lee, J.-H.; Kim, H. M.; Jin, S. M.; Park, H. S.; Nam, J.-M.; Suh, Y. D. High-precision measurement-based correlation studies among atomic force microscopy, Rayleigh scattering, and surface-enhanced Raman scattering at the single-molecule level. *Phys. Chem. Chem. Phys.* **2013**, *15* (12), 4243–4249 DOI: 10.1039/c3cp43817a.
15. Ci, X.-T.; Wu, B.-T.; Song, M.; Chen, G.-X.; Liu, Y.; Wu, E.; Zeng, H.-P. Deep-ultraviolet surface plasmon resonance of Al and Al_{core} /Al_2O_{3shell} nanosphere dimers for surface-enhanced spectroscopy. *Chinese Phys. B* **2014**, *23*, 97303 DOI: 10.1088/1674-1056/23/9/097303.
16. Lee, J. H.; You, M. H.; Kim, G. H.; Nam, J. M. Plasmonic nanosnowmen with a conductive junction as highly tunable nanoantenna structures and sensitive, quantitative and multiplexable surface-enhanced Raman scattering probes. *Nano Lett.* **2014**, *14* (11), 6217–6225 DOI: 10.1021/nl502541u.
17. Pileni, M. P. Inorganic nanocrystals self ordered in 2D superlattices: how versatile are the physical and chemical properties? *Phys. Chem. Chem. Phys.* **2010**, *12* (38), 11821 DOI: 10.1039/c0cp00456a.
18. Saikia, K.; Sen, D.; Mazumder, S.; Deb, P. Reassembling nanometric magnetic subunits into secondary nanostructures with controlled interparticle spacing. *RSC Adv.* **2015**, *5* (1), 694–705 DOI: 10.1039/C4RA12115E.
19. Srivastava, S.; Samanta, B.; Jordan, B. J.; Hong, R.; Xiao, Q.; Tuominen, M. T.; Rotello, V. M. Integrated Magnetic Bionanocomposites through Nanoparticle-Mediated Assembly of Ferritin. *J. Am. Chem. Soc.* **2007**, *129* (38), 11776–11780 DOI: 10.1021/ja073163x.
20. Crew, E.; Yan, H.; Lin, L.; Yin, J.; Skeete, Z.; Kotlyar, T.; Tchah, N.; Lee, J.; Bellavia, M.; Goodshaw, I.; et al. DNA assembly and enzymatic cutting in solutions: a gold nanoparticle based SERS detection strategy. *Analyst* **2013**, *138* (17), 4941 DOI: 10.1039/c3an00683b.
21. Nicewarner-Pena, S. R.; Freeman, R. G.; Reiss, B. D.; He, L.; Pena, D. J.; Walton, I. D.; Cromer, R.; Keating, C. D.; Natan, M. J. *Science*, **2001**, *294*, 137.
22. Njoki, P. N.; Lim, I.-I. S.; Mott, D.; Park, H. Y.; Khan, B.; Mishra, S.; Sujakumar, R.; Luo, J.; Zhong, C. J. *J. Phys. Chem. C*, **2007,** *111*, 14664.
23. Njoki, P. N.; Luo, J.; Kamundi, J. M. M.; Lim, S., Zhong, C. J. *Langmuir*, **2010**, *26*, 13622.
24. Lim, I.-I. S.; Chandrachud, U.; Wang, L.; Gal, S.; Zhong, C. J. *Anal. Chem.*, **2008**, *80*, 6038.
25. Hostetler, M. J.; Templeton, A. C.; Murray, R. W. *Langmuir*, **1999**, *15*(11), 3782 DOI: 10.1021/la981598f.

Chapter 7

Summary and Future Work

This work focused on the functionalization of gold- and silver-based nanoparticles as nanoprobes for the detection of different biomolecules. The results have demonstrated the significance of the role played by the interparticle interactions on plasmonic coupling of the functional nanoprobes responsible for LSPR and SERS characteristics which are exploited for the detection of different molecules. The major findings are summarized here.

First, the aggregation of dye molecules has been demonstrated as a model system for probing the plasmonic coupling via the π–π^* stacking interaction. The correlation between the experimental results and the theoretical simulations for both LSPR and SERS has provided insights into the effect of interparticle distance on plasmonic coupling. The J-aggregation of the dye molecules defined the spatial parameters and provides spectroscopic signatures for establishing a strong correlation between LSPR and SERS. The insight into the interparticle interactions that produce the spectroscopic signatures has significant implications for the detection molecules.

Secondly, the antigen-antibody recognition by protein A and goat anti-rabbit IgG has been studied as a model system for defining the interparticle plasmonic coupling

between NPs in solution. The effect of the interparticle interactions on the SERS characterization in this model were analyzed using different antigen concentrations. Through the analysis of different antigen concentrations, the antibody-conjugated nanoprobes showed promising results using Raman-labeled nanoprobes for SERS detection of protein A in solution with low concentrations. The findings in this model system in terms of experimental - theoretical correlation have implications for the design of nanoprobes for exploring SERS technique towards point-of-care applications.

Thirdly, the study of duplex DNA mediated assembly of AuNPs by both experimental measurements and theoretical simulations has new insights into the understanding the effect of the interparticle interactions on the spectroscopic signal amplification. The theoretical simulation of the plasmonic coupling and electromagnetic field enhancement of homo- and hetero-size NP dimers has provided useful information for assessing LSPR and SERS features in relation to the nanoparticle size and interparticle gap distance. A major finding from this system was the interparticle squeezing to a distance smaller than the expected for the conventional perception of the duplex DNA linkage. This finding has significant implications for understanding DNA-mediated NP assembly and exploring nanoprobe-enhanced SERS detection of DNA in solution.

Lastly, magnetic core – gold or silver shell NPs have been investigated as a multifunctional nanoprobes for the detection of DNA through experimentation and computational modeling to understand the effect of interparticle properties on the spectroscopic characteristics of LSPR and SERS. The interparticle interaction of metallic shells in the presence of the magnetic cores has been shown to further squeeze the interparticle distance. This is attributed to the magnetic attraction of the cores which

decreases the interparticle distances. The results have demonstrated the significant role played by the effective shell thickness and magnetic core sizes in the interparticle plasmonic coupling. These results have implications for the design of multifunctional nanoprobes with enhanced SERS and LSPR properties for biomolecular detection.

The findings presented in this work provide a great deal of answers to questions previously asked on the effect of the interparticle properties on the spectroscopic signatures involved in these systems. However, they have also generated new questions to answer, one of which was derived from the theoretical simulation of different size NP dimers in the squeezing effect of the DNA on the NPs. Since the magnetic core – Au or Ag shell NPs exhibit a gap distance of approximately 0 nm, the labels were pushed toward the peripheral contact region of the hotspot, posing the question on which particle should the Raman label (RL) be conjugated to in hetero-sized dimers in order to increase the NP enhancement. The theoretical data provided some insight that the RL may form a hotter hotspot on the smaller NP or near the smaller NP. This further understanding could aid the design of nanoprobes that produce a larger enhancement, allowing for the detection of molecules in lower concentrations.

Further experimentation is needed to obtain a more detailed understanding of the interparticle interactions on the intensity observed from the assembly of NPs with proteins. More studies need to be performed in the analysis of antigen-antibody binding orientation, to understand how the dehydration process affects the protein structure upon NP squeezing. Techniques such as FTIR, NMR, NanoSight Tracking, and Dynamic Light Scattering should be used to monitor bond formation and changes to surface potentials and

interparticle properties. Similarly, it would be interesting to observe the theoretical results with the utilization of larger computing power to produce better resolved simulations.

Concurrently with these methods for the further understanding of the systems, it would be interesting to expand the preliminary work on the application of the metallic nanoprobes in microfluidic systems, like flow cells or on paper substrates. This will allow for the analysis of other methods for simple, reusable and disposable methods of the point-of-care analysis. Some of these methods may also include the printing of NP inks used for disease detection on economical devices, like glass or paper substrates. Further research needs to be conducted to allow for the detection of biomolecules using different optical and electrical techniques simultaneously on these low-cost substrates. The results will provide useful information for the development of portable, highly specific, and non-invasive sensors for the ability to monitor ones' health without visiting a medical center.

In summary, significant progress has been made towards harnessing the metal nanoparticles and assemblies as an effective strategy to create multifunctional properties for detection, targeting, recognition and diagnostics. Many of the examples of the multifunctional nanoprobes in this work focus on the optical, spectroscopic, electrical and magnetic properties for signal transduction or process intervention in a wide range of molecular or biomolecular applications such as amino acids, peptides, proteins, DNA, miRNA, bacteria, and biomarkers as well. These multifunctional properties are often linked to the interparticle interactions and reactivities at the interfaces between the nanoparticles and the targeted biomolecules. The examples illustrate the importance of understanding the detailed nanostructural parameters such as size, composition and surface properties in correlation with their optical, spectroscopic, electrical and magnetic

properties. The fundamental understanding of the design parameters in nanoengineering of the functional nanoparticles in terms of the desired (e.g., specific targeting) and undesired (e.g., nanotoxicity effect) properties would allow for the development of practically-viable devices or technologies for diseases and cancer biomarker detection. The importance is reflected by many emerging research activities focusing on point-of-care detection devices and low-cost printable and flexible sensing devices. The progress in these fronts will provide both fundamental and practical knowledge for advancing nanoparticle based theranostic applications. There are also other nanostructural parameters such as shape and interatomic distance or geometry and other material properties such as catalytic and thermoelectric properties which can regulate the interfacial interactions and reactivities for the nanotransduction and nanointervention, which are not discussed in this thesis but are actively investigated by many researchers, including our group in previous and on-going efforts.